UNIVERSITY OF SOUTHAMPTON

FACULTY OF ENGINEERING SCIENCE AND MATHEMATICS

Institute of Sound and Vibration Research

Smart double panel with decentralised active damping units for the control of sound transmission

by

Neven Alujević

A thesis submitted for the award of

Doctor of Philosophy

August 2008

UNIVERSITY OF SOUTHAMPTON

Ova disertacija posvećena je mojem ocu, te barba Mati, barba Borisu i barba Frani.
Oni su, dok sam bio mali, za mene zavidavali vide i zabijali brokve,
i sa mnom izrađivali male brodiće na struju,
tako da sam odlučio postati inženjer.

UNIVERSITY OF SOUTHAMPTON

ABSTRACT

FACULTY OF ENGINEERING AND APPLIED SCIENCE

INSTITUTE OF SOUND AND VIBRATION RESEARCH

Doctor of Philosophy

SMART DOUBLE PANEL WITH DECENTRALISED ACTIVE DAMPING UNITS FOR THE CONTROL OF SOUND TRANSMISSION

by Neven Alujević

This thesis presents a comprehensive study of a smart aircraft double panel for active vibroacoustic control. The control of the double panel vibration is implemented using Multi-Input-Multi-Output (MIMO) decentralised velocity feedback loops. The loops are applied via an array of electrodynamic force actuators and collocated velocity sensors. The actuators are located in an air cavity between the two panels such that they can react against the two panels. Two velocity sensors per actuator are used. Either sensor is located at the source and radiating panel footprint of an actuator. The error velocity is formed by subtracting weighted sensor outputs.

In the introductory part of the thesis a survey of aircraft interior noise is given, and state-of-the-art passive and active noise control methods are presented. In Chapter two the mathematical model for the theoretical analysis of the smart double panel is formulated and a parametric study of passive sound transmission is performed using the mathematical model. In Chapter three the performance of decentralised feedback control systems using absolute and relative velocity is analysed theoretically. In Chapter four the stability and performance of decentralised feedback control systems using reactive actuators driven with weighted velocity error signals is analysed theoretically. In Chapter five the stability of decentralised feedback control systems using weighted velocity error signals and electrodynamic reactive actuators is analysed experimentally. In Chapter six the performance of decentralised feedback control systems using weighted velocity error signals and reactive actuators is analysed experimentally.

Table of contents

ABSTRACT iii
Table of contents iv
List of illustrations vi
List of tables xiii
List of symbols xiv
Acknowledgements xix
1 Introduction 1
1.1 Aircraft cabin noise 1
1.2 Passive control of aircraft cabin noise 5
1.3 Active control of aircraft cabin noise 7
1.4 Recent advances in cabin noise active control 10
1.5 Smart panels for active structural acoustic control 12
1.6 Scope and objective 16
1.7 Structure and organisation 18
1.8 Contributions 20
2 Model problem and the parametric study of passive sound transmission 21
2.1 Smart double panel with decentralised control units 21
2.2 Mathematical model 22
2.2.1 Mobility matrix model 22
2.3 Parametric study of passive sound transmission 32
2.3.1 Effects of the radiating panel surface density 35
2.3.2 Effects of the radiating panel bending stiffness 40
2.3.3 Effects of the cavity depth 42
2.3.4 Effects of the stiffness of the mounting system 44
2.4 Summary 47
3 Decentralised absolute and relative velocity feedback control 48
3.1 Feedback control laws 48
3.2 Radiating panel direct velocity feedback using skyhook forces 50
3.3 Source panel direct velocity feedback using skyhook forces 52
3.4 Source and radiating panel direct velocity feedback using skyhook forces 55
3.5 Relative velocity feedback using ideal reactive actuators 57

3.6 Frequency averaged reductions 60
3.7 Summary 62
4 Decentralised feedback control using reactive actuators and weighted velocity signals 63
4.1 Feedback configuration 63
4.2 Control performance 67
4.3 Stability 72
4.4 Parametric study of the stability of the feedback loops 77
4.5 Summary 84
5 Design and testing of the smart double panel 85
5.1 The smart double panel design 85
5.2 Stability analysis of individual feedback loops using the Nyquist criterion 90
5.3 Stability analysis of the nine feedback loops using generalised Nyquist criterion 102
5.4 Summary 105
6 Global control effects of the smart double panel 107
6.1 Experimental procedure 107
6.2 Passive sound radiation of the smart panel 111
6.3 Relative velocity feedback – effects of different feedback gains 114
6.4 Weighted velocity feedback – effects of different velocity weighting factors 119
6.5 Results with optimal weighting factors and feedback gains 122
6.6 Comparison between active and passive control 127
6.7 Summary 129
7 Conclusions 131
Recommendations for future work 134
Appendix A: Mobility and impedance functions 135
Appendix B: Convergence 148
Appendix C: Data sheets for sensor and actuator transducers 153
List of references 166

List of illustrations

Figure 1: The distribution of the pressure amplitudes on the aircraft fuselage skin generated by the passing blades of the propeller. (Courtesy of ISVR, University of Southampton) 3

Figure 2: An example of a propeller aircraft (Bombardier Q400- Dash 8) equipped with an ANVC control active control system. Courtesy of Ultra Electronics (http://www.ultraquiet.com/)..... 8

Figure 3: The distribution of A-weighted sound pressure level in the Q400 airplane, active control off (left hand side) and on (right hand side plot). Courtesy of Ultra Electronics (http://www.ultraquiet.com/). 9

Figure 4: Kinetic energy (left) and the sound transmission ration (right) of a smart panel with 16 decentralised velocity feedback units. The solid lines-no control, dashed lines –small feedback gains, dotted lines-optimal feedback gains, and dash-dotted lines-extensive feedback gain. (From Ref. 53)..... 13

Figure 5: A smart panel with sixteen decentralised velocity feedback units, using rectangular piezoelectric patches and matched velocity sensors. (From Ref. 56) 14

Figure 6: Nyquist plot of the frequency response function between the sensor-actuator pair, without phase lag compensator (left hand side plot); and (b) with phase lag compensator (right hand side plot). (From Ref. 55)..... 14

Figure 7: Smart double panel with an array of decentralised control units 22

Figure 8: Mobility model scheme..... 23

Figure 9: Surface density and bending stiffness curves for (a) polymer honeycomb, (b) aluminium and (c) steel radiating panels..... 34

Figure 10: Effects of the variation of the radiating panel surface density. The top plot shows the source panel kinetic energy, the middle plot shows the radiating panel kinetic energy, and the bottom plot shows the sound power transmission ratio. Solid line is for design (a), dashed line design (b), and the dotted line design (c). The straight lines in the sound transmission plots show the predictions using Equations (61-64). Black line is for the design (a), blue line is for the design (b) and green line is for the design (c). The vertical dash dotted lines indicate mass-air-mass resonant frequencies calculated using Equation (61) for the three designs. 36

Figure 11: Scaled deflection shapes at three different resonant frequencies. 37

Figure 12: Effects of the variation of the radiating panel bending stiffness. The top plot shows the source panel kinetic energy, the middle plot shows the radiating

panel kinetic energy, and the bottom plot shows the sound power transmission ratio. Solid line indicates the design (a), dashed line design (d), and the dotted line design (e) (Table 1). 41

Figure 13: Effects of the variation of the depth of the air cavity between the two panels. The top plot shows the source panel kinetic energy, the middle plot shows the radiating panel kinetic energy, and the bottom plot shows the sound power transmission ratio. Solid line indicates the design (a), dashed line design (f), and the dotted line design (g). The straight lines in the sound transmission plots show the predictions using Equations (61-64). Black line is for the design (a), green line is for the design (f) and blue line is for the design (g). The vertical dash dotted lines indicate mass-air-mass resonant frequencies calculated using Equation (61) for the three designs. 43

Figure 14: Effect of increasing of elastic mounts stiffness on the source and radiating panel deflection shape at frequency of 36 Hz; for designs (a) k=0 N/m, (h) k=5891 N/m, and (i) k=58910 N/m 44

Figure 15: Effects of the variation of the mounting system elastic constant. The top plot shows the source panel kinetic energy, the middle plot shows the radiating panel kinetic energy, and the bottom plot shows the sound power transmission ratio. Solid line indicates the design (a), dashed line design (h), and the dotted line design (i). 46

Figure 16: Direct velocity feedback systems 49

Figure 17: Feedback arrangements 49

Figure 18: Radiating panel direct velocity feedback using skyhook forces. The top plot shows the source panel kinetic energy, the middle plot shows the radiating panel kinetic energy, and the bottom plot shows the sound power transmission ratio. Solid line – no control, dashed – low feedback gains, dotted – intermediate feedback gains, dash-dotted – high feedback gains. . 51

Figure 19: Source panel direct velocity feedback using skyhook forces. The top plot shows the source panel kinetic energy, the middle plot shows the radiating panel kinetic energy, and the bottom plot shows the sound power transmission ratio. Solid line – no control, dashed – low feedback gains, dotted – intermediate feedback gains, dash-dotted – high feedback gains. . 54

Figure 20: Source and radiating panel direct velocity feedback using skyhook forces, applied simultaneously. The top plot shows the source panel kinetic energy, the middle plot shows the radiating panel kinetic energy, and the bottom plot shows the sound power transmission ratio. Solid line – no control, dashed – low feedback gains, dotted – intermediate feedback gains, dash-dotted – high feedback gains. 56

Figure 21: Relative velocity feedback using reactive control forces. The top plot shows the source panel kinetic energy, the middle plot shows the radiating panel kinetic energy, and the bottom plot shows the sound power transmission

ratio. Solid line – no control, dashed – low feedback gains, dotted – intermediate feedback gains, dash-dotted – high feedback gains. 59

Figure 22: Normalised kinetic energy of the radiating panel (left) and sound transmission ratio (right), integrated from 0 Hz to 3 kHz, plotted against the control gain, for the four control strategies: source panel direct velocity feedback (dashed lines) with skyhook control forces, radiating panel direct velocity feedback (dash-dotted lines) with skyhook control forces, relative velocity feedback using reactive actuators (solid lines) and both source and radiating panel direct velocity feedback using skyhook control forces applied simultaneously (dotted lines). 60

Figure 23: Configuration of the error signal..... 65

Figure 24: Direct velocity feedback using reactive control forces with velocity weighting factor equal to α=0.375. The top plot shows the source panel kinetic energy, the middle plot shows the radiating panel kinetic energy, and the bottom plot shows the sound power transmission ratio. Solid line – no control, dashed – low feedback gains, dotted – intermediate feedback gains, dash-dotted – high feedback gains. 68

Figure 25: Scaled deflection shapes of the two panels at the 1st (column A), 5th (column B) and 23rd (column C) resonances of the system. First row depicts the resonances with no control, centre row with optimal gain, and the bottom row with large feedback gain (α=0.375). The scaling within a column is equal; the scaling between columns is not. 69

Figure 26: Normalised kinetic energy of the radiating panel (A) and sound transmission ratio (B), integrated from 0 Hz to 3 kHz, plotted against the control gain, for the different α-factor values: α=0.875 (solid faint line), α=0.75 (dashed faint line), α=0.625 (dotted faint line), α=0.5 (dash-dotted faint line) and α=0.375 (solid line) and for a decentralised MIMO feedback system that uses 16 ideal skyhook actuators and velocity sensors on the radiating panel (dashed line). 70

Figure 27: Maximum reductions of the: a) sound transmission ratio (solid line), b) normalised total kinetic energy of the source panel (dashed line), c) normalised kinetic energy of the radiating panel (dotted line)..... 71

Figure 28: Bode (plot A) and Nyquist (plot B) plots of the open loop sensor-actuator FRF for the velocity weighting factors of α=0.5. 73

Figure 29: Bode (plot A) and Nyquist (plot B) plots of the open loop sensor-actuator FRF for the velocity weighting factors of α=0.1 with (solid line) and without (dashed line) air coupling..... 73

Figure 30: δ_0 value plotted against the velocity weighting factor α when the acoustical coupling between the two panels is (solid line) or is not (dashed line) taken into account in the model. 74

Figure 31: Critical α-factor distribution plotted over the surface of the double panel in case of fully coupled configuration (plot A), in case when structural coupling is neglected (plot B), and in case when acoustical coupling is neglected (plot C). 76

Figure 32: a) δ_0 plotted against the velocity weighting factor (plots A and B), b) critical velocity weighting factor (plots C and D) plotted against the varied parameter, c) δ_0 in case when $\alpha = 0$ plotted against the varied parameter (plots E and F). The parameters varied in this figure are the source panel mass density (plots A, C, and E) and the source panel elastic modulus (plots B, D, and F). The vertical lines on plots C-F indicate the location of the reference case (a) (Table 1) on the parameter axis..... 78

Figure 33: a) δ_0 plotted against the velocity weighting factor (plots A and B), b) critical velocity weighting factor (plots C and D) plotted against the varied parameter, c) δ_0 in case when $\alpha = 0$ plotted against the varied parameter (plots E and F). The parameters varied in this figure are the radiating panel mass density (plots A, C, and E) and the radiating panel elastic modulus (plots B, D, and F). The vertical lines on the plots C-F indicate the location of the reference case (a) (Table 1) on the parameter axis). 80

Figure 34: a) δ_0 plotted against the velocity weighting factor (plots A and B), b) critical velocity weighting factor (plots C and D) plotted against the varied parameter, c) δ_0 in case when $\alpha = 0$ plotted against the varied parameter (plots E and F). The parameters varied in this figure are the stiffness of the elastic mounts (plots A, C, and E) and the mass density of the air in the cavity between the plates (plots B, D and F). The vertical lines on the plots in the second and third row indicate the location of the reference case (a) (Table 1) on the parameter axis). 82

Figure 35: The effect of the l_z dimension of the air cavity to the δ_o versus α curve. Three cavity l_z dimensions have been considered here (0.02m, 0.03m, 0.04m), but the curves overlap. 83

Figure 36: A schematic representation of the prototype smart double panel with nine velocity feedback loops. 86

Figure 37: The prototype smart double panel experimental test facility; A) the lower clamping frame mounted on top of the thick-walled Perspex box, B) the source panel mounted, C) the upper clamp mounted, and D) the radiating panel mounted using the four corner mounts. 87

Figure 38: Left hand side photograph: the miniature voice-coil actuator (H2W, NCC01-04-001) shown in comparison to a US$ quarter coin. 87

Figure 39: The front panel of the nine channel controller unit. 88

Figure 40: Electric scheme of a controller channel 88

Figure 41: Bode plots of the open loop sensor-actuator FRF for piezoelectric accelerometers and different MEMS accelerometer signal conditioners..... 91

Figure 42: Nyquist plots of the open loop sensor-actuator FRF for: a) time integrated output of the two piezoelectric accelerometers with reference to the actuator current (left hand side), b) time integrated output of the two MEMS accelerometers with a 2.5 kHz low-pass filter with reference to the actuator voltage. 93

Figure 43: Nyquist plots of nine open loop sensor-actuator FRFs, with the velocity weighting factor α =0.5. 95

Figure 44: Amplitude Bode plots of nine open loop sensor-actuator FRFs, with the velocity weighting factor α =0.5. 96

Figure 45: Phase Bode plots of nine open loop sensor-actuator FRFs, with the velocity weighting factor α =0.5. 97

Figure 46: Phase Bode plots of nine open loop sensor-actuator FRFs, with the velocity weighting factor α =0. 98

Figure 47: Nyquist plots of nine open loop sensor-actuator FRFs, with the velocity weighting factor α =0. 99

Figure 48: The maximum negative real parts of the open loop sensor-actuator FRFs, δ_0, plotted against the velocity weighting factor α. Solid lines show the results when the frequency range between 10 and 2400 Hz is considered, and the faint lines show the results when the full frequency range (10-6400 Hz) is considered. 101

Figure 49: The locus of $D(j\omega) = \det[\mathbf{I} + \mathbf{H}(j\omega)\mathbf{G}(j\omega)]$. The velocity weighting factor equals to α = 0.5. The top plot shows the locus with reference to the actuator current, and bottom plot shows the locus with reference to the actuator voltage. The value of the nine open loop feedback gains *g* is 0.1..... 105

Figure 50: The experimental test facility for the measurements of the radiated sound power in the anechoic chamber. 108

Figure 51: The experimental test setup for the measurements of the radiated sound power in the anechoic chamber. 109

Figure 52: The experimental test setup for the measurements of the radiating panel vibration using the laser vibrometer. 110

Figure 53: Radiated sound power plotted against frequency in case of the deep cavity arrangement (top) and the shallow cavity arrangement (bottom). Blue lines are in the case of the Honeycomb radiating panel, red lines are in the case of the aluminium radiating panel, and green lines are in case of the Perspex radiating panel. 112

Figure 54: Radiated sound power plotted against frequency in case Honeycomb (top) and Perspex (bottom) radiating panels. The blue lines are in the case of the deep cavity arrangement and the red lines are in the case of the shallow cavity arrangement. 113

Figure 55: Radiated sound power plotted against frequency in case when Honeycomb (top), aluminium (centre) and Perspex (bottom) radiating panels are used with the deep air cavity. Sound power spectra are shown for increasing feedback gains in mV/V (see legends). Velocity weighting factors equal 0.5. 116

Figure 56: Radiated sound power plotted against frequency in case when Honeycomb (top), aluminium (centre) and Perspex (bottom) radiating panels are used with the shallow air cavity. Sound power spectra are shown for increasing feedback gains in mV/V (see legends). Velocity weighting factors equal 0.5. 117

Figure 57: Radiated sound power plotted against frequency in case when Honeycomb (top), aluminium (centre) and Perspex (bottom) radiating panels are used with the deep air cavity. Sound power spectra are shown for velocity weighting factors, α, increasing from 0 to 0.5 (dashed coloured lines) and from 0.5 to 1 (solid coloured lines). Feedback gains equal 100 mV/V. The black lines are when the control is off. 120

Figure 58: Radiated sound power plotted against frequency in case when Honeycomb (top), aluminium (centre) and Perspex (bottom) radiating panels are used with the shallow air cavity. Sound power spectra are shown for velocity weighting factors, α, increasing from 0 to 0.5 (dashed coloured lines) and from 0.5 to 1 (solid coloured lines). Feedback gains equal 100 mV/V. The black lines are when the control is off. 121

Figure 59: Radiated sound power spectra (top plot) and the spectra of mean velocity of the radiating panel (bottom plot) for the configuration with Honeycomb radiating panel and deep air cavity. Green lines: without sensors and actuators, blue lines: with sensors and actuators open loop, red lines: with sensors and actuators closed loop. 123

Figure 60: Radiated sound power spectra (top plot) and the spectra of mean velocity of the radiating panel (bottom plot) for the configuration with Honeycomb radiating panel and shallow air cavity. Green lines: without sensors and actuators, blue lines: with sensors and actuators open loop, red lines: with sensors and actuators closed loop. 124

Figure 61: Radiated sound power spectra for Perspex radiating panel with deep cavity (top plot), and Perspex radiating panel with shallow cavity (bottom plot). Green lines: without sensors and actuators, blue lines: with sensors and actuators open loop, red lines: with sensors and actuators closed loop. 126

Figure 62: Radiated sound power spectra for aluminium radiating panel with deep cavity (top plot), and aluminium radiating panel with shallow cavity (bottom

plot). Green lines: without sensors and actuators, blue lines: with sensors and actuators open loop, red lines: with sensors and actuators closed loop. 127

Figure 63: The high density polyamide foam used to asses the effectiveness of a typical passive treatment on the attenuation of the smart panel radiated sound power. The dimensions of the foam are dimensions 414×314×25 mm. The mass of the foam is 0.370 kg. 128

Figure 64: The sound power radiation of the smart double panel with no sensors and actuators (blue line), with the passive sound absorbing foam (red line) and with the active control without the foam (green line). Measurements are performed with the aluminium radiating panel and with the deep air cavity. 129

List of tables

Table 1: Values of the varied parameters..... 34

Table 2: Values of the fixed parameters 35

Table 3: The physical properties and the geometry of the prototype smart double panel. 89

List of symbols

Abbreviations

j	imaginary unit ($j = \sqrt{-1}$)	[-]
$\mathbf{I}$	identity matrix	[-]
FRF	Frequency Response Function	[various]
n	index of mode shape	[-]
m	index of mode shape	[-]
π	Ludolf's number	[-]

Parameters

$\phi_{m,n}$	plate mode shape function	[-]
$\omega_{m,n}$	plate natural frequencies	[s^{-1}]
η	plate loss factor	[-]
λ_n	plate mode normalisation factor	[-]
I_s	panel second moment of area	[m^3]
ν_r	Poisson's ratio	[-]
φ_m	characteristic beam function	[-]
A_e	area of the surface element	[m^2]
A_n	cavity mode normalisation factor	[-]
ψ_{n_1,n_2,n_3}	air cavity natural mode shape function	[-]
ζ	air cavity loss factor	[-]
$\omega^{cav}_{n_1,n_2,n_3}$	air cavity natural frequency	[s^{-1}]
n_1, n_2, n_3	cavity mode numbers for, *x*,*y*, and *z* directions	[-]
c	viscous damping factor	[Nsm^{-1}]
l_x	panel length	[m]

l_y	panel width	[m]
l_{xe}	panel element length	[m]
l_{ye}	panel element width	[m]
l_z	cavity depth	[m]
k	elastic constant, acoustic wavenumber, number of elements	[Nm^{-1},m^{-1},-]
k_x	acoustical wavenumber in *x*-direction	[m^{-1}]
k_y	acoustical wavenumber in *y*-direction	[m^{-1}]
x_j	*x*-coordinate of panel element geometrical centre	[m]
y_j	y-coordinate of panel element geometrical centre	[m]
P	acoustical pressure of the plane wave	[Pa]
$\mathbf{H}$	diagonal matrix with feedback control gains	[Nsm^{-1}]
$\mathbf{R}$	radiation resistance matrix	[Nsm^{-1}]
E_r	kinetic energy of the radiating panel	[J]
E_s	kinetic energy of the source panel	[J]
E	Young's modulus	[GPa]
E_R	radiating panel Young's modulus	[GPa]
E_s	source panel Young's modulus	[GPa]
ρ_s	source panel mass density	[kgm^{-3}]
ρ_r	radiating panel mass density	[kgm^{-3}]
ρ_0, ρ_{air}	air mass density	[kgm^{-3}]
ω	circular frequency	[s^{-1}]
ω_0	mass-air-mass resonance circular frequency	[s^{-1}]
ω_c	mass-air-mass resonance circular frequency	[s^{-1}]
g	single channel feedback gain	[Nsm^{-1}]
h_s	source panel thickness	[m]
h_r	radiating panel thickness	[m]
B	panel bending stiffness	[Nm]
m	panel surface density	[kgm^{-2}]
T	sound transmission ratio	[dB]

W_r	radiated sound power	[W]
W_i	incident sound power	[W]
c, c_0	speed of sound	[ms^{-1}]
θ	elevation angle of incidence	[rad]
ϕ	azimuthal angle of incidence	[rad]
α	velocity weighting factor	[-]
α_{crit}	critical velocity weighting factor	[-]
δ_0	maximum FRF negative real part	[various]
i	electrical current	[A]
U	voltage	[V]
R	electrical resistance	[Ω]
L	inductance	[H]
ψ	voice coil constant	[NA^{-1},Vsm^{1}]

Phasors

$\mathbf{v}_m$	vector of velocity phasors at mounts locations	[ms^{-1}]
$\mathbf{f}_m$	vector of force phasors at mounts locations	[N]
$\dot{w}_j$	complex amplitude of the linear transverse velocity	[ms^{-1}]
N_{zj}	complex amplitude of the linear transverse force	[N]
$\mathbf{v}_c$	vector of velocity phasors at control locations	[ms^{-1}]
$\mathbf{f}_c$	vector of force phasors at control locations	[N]
$\mathbf{v}_e$	vector of velocity phasors at centres of elements	[ms^{-1}]
v_E	complex amplitude of the error signal	[ms^{-1}]
$\mathbf{v}_{re}$	vector of velocity phasors at centres of radiating panel elements	[ms^{-1}]
$\mathbf{v}_{se}$	vector of velocity phasors at centres of source panel elements	[ms^{-1}]
$\mathbf{f}_e$	vector of force phasors at centres of elements	[N]
$\mathbf{v}_s$	source panel velocity vector	[ms^{-1}]
$\mathbf{f}_s$	source panel force vector	[N]

$\mathbf{v}_r$	radiating panel velocity vector	[ms^{-1}]
$\mathbf{f}_r$	radiating panel force vector	[N]
$\mathbf{v}_t$	transmission system velocity vector	[ms^{-1}]
$\mathbf{f}_t$	transmission system force vector	[N]
$\mathbf{f}_p$	primary excitation force vector	[N]
$\mathbf{f}_f$	flanking excitation force vector	[N]
$\mathbf{f}_{pf}$	primary-flanking excitation force vector	[N]
$\mathbf{v}_{sr}$	source-radiating panel velocity vector	[ms^{-1}]
$\mathbf{f}_{sr}$	source-radiating panel force vector	[N]
f_c	complex amplitude of the control force	[N]
f_{rc}	complex amplitude of the radiating panel control force	[N]
f_{sc}	complex amplitude of the source panel control force	[N]
v_{rc}	complex amplitude of the radiating panel control velocity	[ms^{-1}]
v_{sc}	complex amplitude of the source panel control velocity	[ms^{-1}]
F_c	reactive actuator control force	[N]
f	force	[N]

Impedances and mobilities

$\mathbf{Y}_{sj}$	source panel mobility matrix	[ms^{-1}N^{-1}]
$\mathbf{Y}_{rj}$	radiating panel mobility matrix	[ms^{-1}N^{-1}]
$\mathbf{Y}_{srj}$	source-radiating panel mobility matrix	[ms^{-1}N^{-1}]
$\mathbf{Y}_{cj}$	mobility matrix at the control locations	[ms^{-1}N^{-1}]
$\mathbf{Y}_{csj}$	mobility matrix at the source panel control locations	[ms^{-1}N^{-1}]
$\mathbf{Y}_{crj}$	mobility matrix at the radiating panel control locations	[ms^{-1}N^{-1}]
$\mathbf{Z}_t$	impedance matrix of the transmission system	[Nsm^{-1}]
$\mathbf{T}_{cp}$	double panel control-primary mobility matrix	[ms^{-1}N^{-1}]
$\mathbf{T}_{cc}$	double panel control-control mobility matrix	[ms^{-1}N^{-1}]

T_{cc}	double panel control-control mobility function	$[ms^{-1}N^{-1}]$
$\mathbf{G}$	plant response matrix	$[ms^{-1}N^{-1}]$
$\mathbf{G_R}$	radiating panel plant response matrix	$[ms^{-1}N^{-1}]$
$\mathbf{G_S}$	radiating panel plant response matrix	$[ms^{-1}N^{-1}]$
D	determinant of the return difference matrix	[-]

Acknowledgements

First and foremost I express my deep and sincere gratitude for the guidance and continuous support of Professor Paolo Gardonio. I have greatly benefited from his wide and comprehensive knowledge and experience. Professor Gardonio has always encouraged me to make my work more efficient and meaningful through his numerous advices on the subject and beyond.

I would like to thank to Dr Ken Frampton for co-supervision of my work and for proof reading of my thesis. Dr Frampton has always been very supportive and constructive.

I would like to thank to Professor Stephen J. Elliot for giving me opportunity to work in the very motivating environment of the SPCG group of the ISVR.

In addition, I thank to Professor Stephen J. Elliot and Professor Brian R. Mace for continuously monitoring my progress via regular review meetings, and for pointing the possible directions of the research.

I thank to prof. dr. sc. Željko Domazet for giving me opportunity to study abroad for such a long period, and to prof. dr. sc. Lovre Krstulović-Opara for kindly agreeing to take my teaching obligations at the Faculty of Mechanical Engineering, Electrical Engineering and Naval Architecture (FESB) of University of Split. I also thank to doc. dr. Nastia Degiuli and dr. sc. Hrvoje Kozmar for friendship and support.

The ISVR technical support team was extremely helpful. Really big thanks go to Dennis White for building complicated mechanical components of the prototype. Thanks to Rob Stansbridge, Anthony Wood, Allan Waddilove and Andy Westerman for building the electrical components of the prototype. Thanks to Nigel Davies for carefully analysing safety issues related to my experiments, and then giving appropriate advices.

I am indebted to my colleagues as well. Jens Rohlfing was always there to give a hand with the tedious process of assembling the different arrangements of the prototype smart panel, during the measurements in the anechoic chamber. I am very grateful for that.

Yoko Aoki was always willing to share her know-how in the lab. Dr. Olie Baumann was very patient while sharing his considerable experience. Cristóbal González-Díaz's help and advices are also appreciated. In addition, I thank to all other colleagues at the ISVR for many precious moments during the tree years study.

I thank to my mum and my brother for their care and love. I thank to Karolina for her love and generosity.

Financial support during the three years was provided by a Marie Curie Early Stage Training (MC EST) fellowship, within the research and training network "European Doctorate in Sound and Vibration Studies (EDSVS)". Financial supports of the Ministry of Science, Education and Sport of Republic of Croatia and FESB are also acknowledged.

1 Introduction

In this thesis a decentralised Multi-Input-Multi-Output velocity feedback system is applied for active vibroacoustic control of a model aircraft double panel. The double panel model consists of a source and a radiating panel, coupled acoustically and structurally. The active control is implemented via an array of force actuators with collocated velocity sensors. A novel sensor-actuator configuration is proposed. Electrodynamic actuators that react against the two panels, which are equipped with weighted source/radiating panels velocity error sensors, are used.

The double panel system is a simplified model of a real aircraft fuselage structure. First, it only counts for a section of an aircraft fuselage skin confined between two adjacent frames and two adjacent stringers. Second, the tensioning effect that is generated on the aircraft skin by aircraft pressurization system is neglected. Third, the curvatures of the aircraft skin and trim panels are neglected.

Performance of the active control systems is assessed in terms of reductions of sound power radiated by the double panel, and reductions of the radiating panel vibration. Stability properties of the proposed feedback control systems are evaluated theoretically and experimentally using Nyquist criteria.

In the following sections a review of aircraft cabin noise and its passive and active control is presented. In particular the control of broadband disturbances with decentralised feedback control loops is reviewed. The objectives and content of the rest of the thesis is then laid out.

1.1 Aircraft cabin noise

The interest in noise and vibration research in aircraft industry has increased significantly in the past fifty years. This is primarily caused by a steady increase in aircraft engine power and the consequent increase in Mach numbers of a typical cruise flight. The increased interior noise levels generated a need for better understanding of noise transmission mechanisms into the aircraft cabin, and for the development of

advanced noise reduction techniques, in order to maintain acceptable interior noise levels and passenger comfort.

In general, interior aircraft noise is generated by two principal sources[1-3]:

- the power plant, including the propeller and engine, either turbine or reciprocating, and
- Turbulent Boundary Layer (TBL).

Noise from internal sources, such as air-conditioning systems, may also be important[1-3]. The higher cruise Mach numbers resulted in a significant increase in TBL generated noise in past decades. Similarly, the increase of engine power has led to an increase in acoustic power generated by the power plant. However, the emergence of modern jet engines with a secondary (bypass) stream resulted in lower jet velocities, and thus also in relatively lower acoustic outputs when compared to traditional single stream engines having equal thrusts. This effect puts the emphasis on the increase in the TBL generated noise.

The interior noise in aircraft is normally classified according to two transmission paths through which the noise spreads from its source to the aircraft cabin; these include the airborne and the structure-borne paths[1-3]. The airborne path is characterised by acoustic or aerodynamic excitation of the fuselage skin which then radiates sound to the interior. The structure-borne path is instead characterised by vibration excitation of the fuselage frame structure and skin which radiates sound to the interior of the aircraft. Noise from the power plant and the TBL sources is mainly transmitted via airborne paths[1-3]. The structure-borne paths can also contribute to the interior noise level significantly, particularly in aircraft with rear mounted engines[1-4], however, mostly at discrete frequencies[1]. In fact, the structure borne paths are mainly associated with the engine, either reciprocating or turbine.

In case of propeller-driven aircraft, the cabin noise is dominated by tones at the propeller blade-passing frequency and its higher harmonics[1,2,5]. The propeller noise is mainly transmitted through the fuselage into the passenger compartment. The propeller

generates large pressure variations at the fuselage exterior (Figure 1), which effectively excite fuselage panels which then radiate the noise into the aircraft interior. An important parameter which influences the propeller noise is the minimal distance between the propeller blade tip and the adjacent fuselage section[1,6]. The direction of the propeller rotation is important for the cabin noise and contributes to asymmetries in the interior sound pressure levels in twin engine propeller airplanes. In general, a down-going blade generates higher sound pressure levels[4,7-9]. There are two main reasons for the importance of the propeller rotation direction. The first is the fact that down-going and up-going blades have different aerodynamic angles of attack and are influenced differently by the wing vortex sheet (the circulation around the wing). The second is the fact that the aircraft floor in the passenger compartment influences noise transmission differently for the down-going and up-going blades.

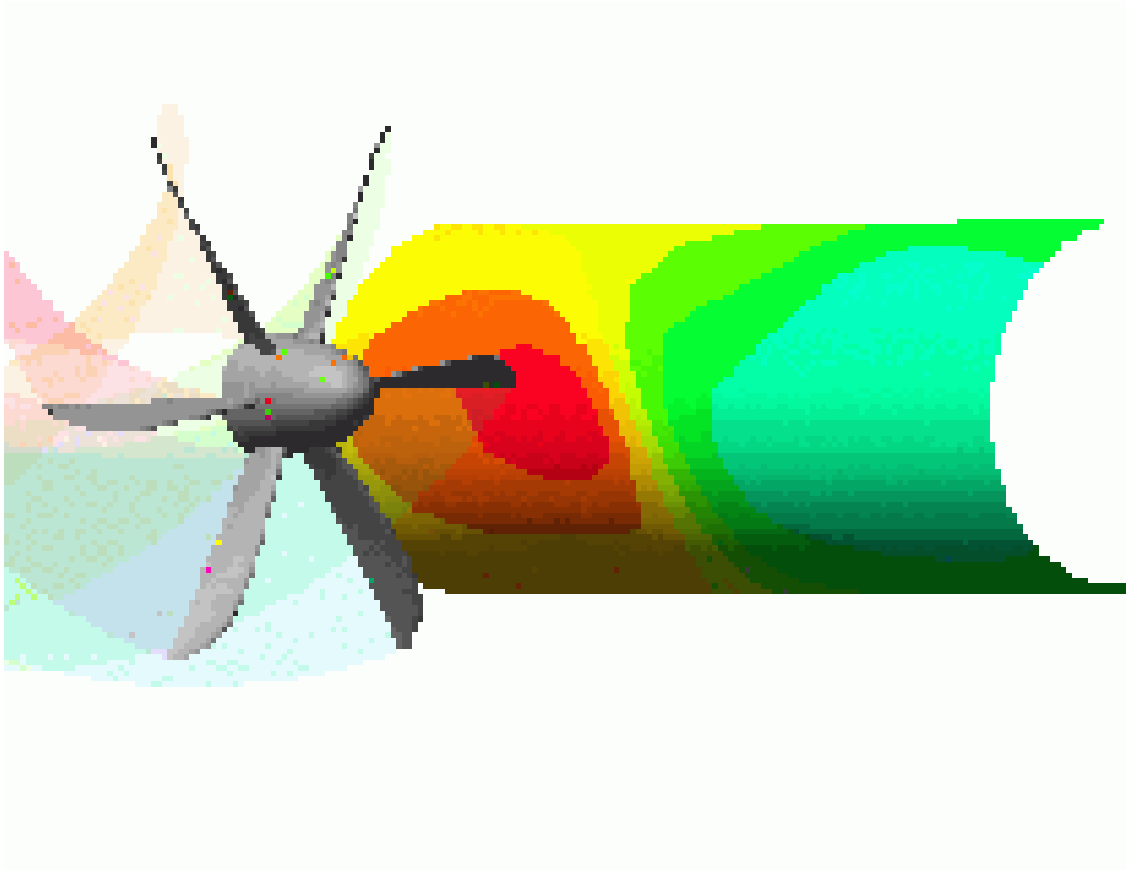

Figure 1: The distribution of the pressure amplitudes on the aircraft fuselage skin generated by the passing blades of the propeller. (Courtesy of ISVR, University of Southampton)

In case of turbine engines, high-speed gas flow out of the engine exhaust is an important noise source (the jet noise). Although the jet noise has a limited influence in cruise conditions, it can dominate the interior noise in low speed climb conditions[10].

This is because in the latter case the TBL noise is less important due to the low Mach numbers during the climb. Jet noise may dominate the sound field in the rear passenger compartment even during cruise conditions in case of aircraft with engines mounted in wing nacelles close to the fuselage[1,2]. The frequency bands where the jet noise contributes the most are those between 125 Hz and 400 Hz[11]. The velocity of the engine exhaust jet is an important parameter, and modern high-bypass turbofans with a secondary low-velocity stream tend to be quieter.

The structurally transmitted engine noise is caused by unbalanced forces present both in turbine and reciprocating engines. The resulting vibrations excite the aircraft structure and are transmitted to the interior walls which radiate sound directly into the passenger compartment[12,13]. In particular, this type of noise transmission is important in case of airplanes with engines mounted on the rear of the fuselage as they are closely coupled to the fuselage structure without the benefit of the isolation provided by a massive wing structure with fuel load[4]. However, structure-borne engine noise has been observed even in aircraft with engines mounted on the wings; particularly when the engines are close to the fuselage[1,2].

TBL noise has gained importance since the introduction of commercial turbojet aircraft with high cruise speeds. The airflow over the fuselage surface is characterised by a fluctuating pressure which excites the fuselage skin. The nature of this excitation is random both in frequency and spatial domains. The boundary layer pressure field is convected in the direction of the airflow. The convection speed is proportional to the aircraft speed such that at certain cruise speeds “hydrodynamic coincidence” occurs[3]. In this case the phase of the boundary layer induced pressure matches the phase of the bending wave vibration of the fuselage skin. The consequent large vibration amplitudes of the fuselage skin results in large sound pressure levels in the aircraft cabin.

In general, the interior noise generated by the TBL source is important at mid and high frequencies, and it dominates the interior noise field at frequencies which are in the range between 400 Hz and 2 kHz[14-16]. The most important parameter for the interior sound pressure level due to the TBL is the Mach number. In-flight measurements of TBL noise can be performed by descend flights with engines shut down[15], or by using only one out of two engines on a twin engine aircraft[7,14].

In modern commercial airplanes, propelled by jet engines, the TBL noise source is the main contributor to the aircraft cabin noise during typical cruise conditions[2].

1.2 Passive control of aircraft cabin noise

Interior noise levels in aircraft are traditionally controlled using passive methods. Over the last 50 years many different passive methods have been used on commercial aircraft. The most common concept involves the use of additional trim panels which together with the aircraft outer skin panel form a double panel system with an air cavity between the two panels. The air cavity is suitable for placing one or more layers of porous material, typically a high density fibreglass blankets, and an intervening sheet of heavy flexible material[17-21]. The principal restrictions on such a passive treatment are the weight, including that of the air moisture trapped in the porous insulating material, the available space and the cost. The effectiveness of the treatment deteriorates at low frequencies, normally below 500 Hz. This is due to two principal reasons. First, the sound transmission loss of double panels is high only above the mass-air-mass resonance[22,23]. Second, the sound insulation effectiveness of the sound absorbing layer decreases at lower frequencies due to the limited thickness of the layer[24].

Damping materials can also be used, typically in the form of constrained layer damping tape with a viscoelastic adhesive and an aluminium backing layer[17,20,21]. Normally, damping layers are applied to fuselage skin panels. In new aircraft designs the damping layers are also applied on trim panels[20,25,26]. This is because the modern trim panels are made of lightweight materials, often in the form of thin Honeycomb sandwich panels, with high stiffness to density ratio. This yields a lower acoustic coincidence frequency of the trim panel where the wavelength in the structure matches the acoustic wavelength and thus the efficiency of the sound radiation is rather high. In general, the drawback of the constrained damping layer method is that it is only effective at frequencies above the panel fundamental resonance, and that additional weight is added to the aircraft.

In case of propeller aircraft, since the primary noise source is characterised by the discrete tonal components which are related to the blade passing frequency, Helmholtz resonators can be used as a passive noise reduction method. They are particularly aimed

at increasing the sound transmission loss of the sound proofing treatment[27,28]. Therefore they are placed in the cavity between the aircraft fuselage skin and interior trim panels. The resonators are tuned to the propeller blade passing frequency. Reductions of up to 15 dB were predicted in theory, up to 11 dB reductions were measured in the laboratory and 5-6 dB reductions were measured in flight tests[28], but without optimizing the installation in the aircraft.

Another method for reducing noise at discrete frequencies includes tuned vibration absorbers (TVA) and tuned dampers. Although the effect of both devices is limited to a relatively narrow bandwidth, the tuned dampers provide reductions over a broader frequency range at a cost of degraded performance at the resonant frequency of the device (the impedance effect is smaller)[1]. The dynamic absorbers have proven to be effective for the reduction of tonal noise components in the Douglas DC-9 commercial aircraft with two rear-mounted engines. The two tones at 120 and 180 Hz, originating from two fan stages of the engine, were suppressed by more than 10 dB[4]. It is important to mention that the effectiveness of the treatment highly depends on changes of engine rotational speed and is therefore limited to applications where the speed variations during the cruise conditions are small. Because of this concern, tuned dampers were used in case of the Saab 340, in order to give larger reductions with variations of the propeller speed and to provide some control at the second harmonic as well[29].

Engine mounts offer a possibility to intercept the structural vibration transmission path by a careful balance between the static and dynamical stiffness of the mounts. A good passive engine mount is a compromise between the requirements on the two stiffnesses. This is because the engine thrust and weight require a high static stiffness to support the engine, whereas for the vibration isolation purposes low dynamic stiffness is required. These requirements are usually met by custom designs using, for example, visco-elastic materials. Laboratory tests performed with fuselage and simulated engine for a single-engine airplane indicate that reductions up to 10 dB are possible[30].

An interesting passive noise reduction method in multi-engine propeller aircraft is propeller syncrophasing[9]. The synchronisation of propellers has been an effective method for controlling the beats generated by the slightly different rotational speeds of different propellers. However, the improved engine speed control systems now permit

selecting and maintaining the relative phase angle between the propellers. This enables reduction of sound pressure levels in the cabin due to a mutual cancellation effect of the multiple noise sources. A study[31] indicated that there are more possibilities for the cancellation in four propeller aircraft than in two propeller aircraft, such that the corresponding average sound pressure level reductions are 8 dB and 1.5 dB, respectively. However, the different propellers may not equally contribute to the sound pressure level at a certain cabin location, in which case the reduction is less that optimum.

In order to improve upon the efficiency of the passive methods, particularly at low frequencies, a lot of effort has been put into research of active noise control methods for aircraft cabin noise, with the major breakthroughs occurring in the past two decades[3].

1.3 Active control of aircraft cabin noise

The first active control methods were developed for the reduction of tonal noise components in propeller aircraft interior. There are three active control approaches to tonal aircraft cabin noise[3]:

- Active Noise Control (ANC),
- Active Noise and Vibration Control (ANVC), and
- Active Boundary Control (ABC).

The ANC approach uses secondary acoustic sources – loudspeakers - that are driven to create a control acoustic field which destructively interferes with the existing primary field in the enclosed space of the aircraft cabin[32-35]. The ANVC control approach uses structural actuators, such as electrodynamic shakers or strain actuators (typically PZT patches) which can generate vibrations of the fuselage structure such that the interior sound is attenuated[36]. The ABC approach uses smart trim panels that have stiff segments which are driven to suppress near field radiation of the trims themselves[37-40]. It is important to note that all three methods can be used to control the sound in the enclosed cabin space regardless of the primary noise source transmission path (airborne, structure-borne), i.e. they can generate attenuations even if the noise is not transmitted through the fuselage walls or the aircraft structure. The sensors used in the ANC and

ANVC methods are exclusively acoustic microphones, deployed at appropriate locations in the aircraft interior. The number of the microphones is typically larger than the number of the loudspeakers. The ABC method however uses structural sensors, typically seismic accelerometers, in addition to the acoustic sensors.

Considering now the generation of control signals, the three control techniques utilize a reference signal of the engine speed taken from the main engine shaft[33-36,41]. This signal is used to provide a reference for a centralised feed-forward controller which employs adaptive algorithms for generating control signals[32,42-44]. The controller also comprises a plant model, i.e. frequency response functions between all sensors and actuators. The control signals are used to drive the actuators in order to minimise the sum of squared error signals measured by the error sensors. Figure 2 shows the twin engine Bombardier Q400- Dash 8 in flight, which has been equipped with an ANVC control system.

Figure 2: An example of a propeller aircraft (Bombardier Q400- Dash 8) equipped with an ANVC control active control system. Courtesy of Ultra Electronics (http://www.ultraquiet.com/).

Figure 3 shows the distribution of sound pressure levels in the Q400 cabin when an ANVC system (produced by Ultra Electronics) is either switched on or off. As shown on the right hand side of Figure 3 the active control system provides excellent reductions of up to 20 dB in A-weighted sound pressure levels.

Active control methods can also be used for vibration isolation purposes and the reduction of structurally transmitted engine vibrations. For example, instead of passive tuned vibration absorbers, adaptive tuneable vibration absorbers (ATVA) can be used.

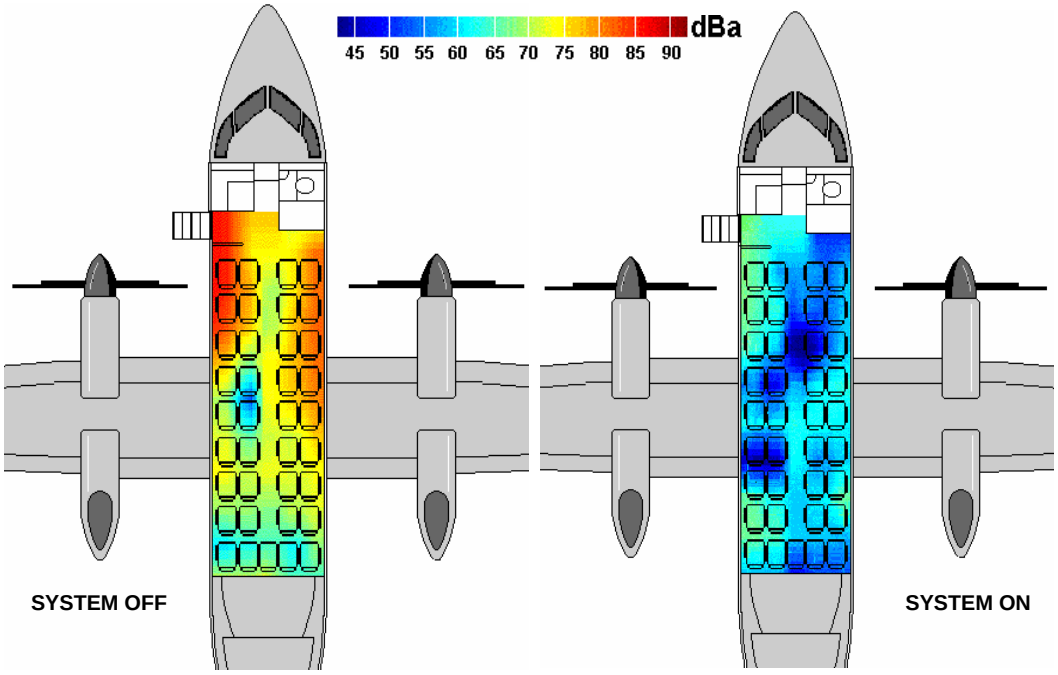

Figure 3: The distribution of A-weighted sound pressure level in the Q400 airplane, active control off (left hand side) and on (right hand side plot). Courtesy of Ultra Electronics (http://www.ultraquiet.com/).

They can bypass the tuning problems of the passive devices by constantly matching the tuning frequency to the disturbance tone. ATVA devices are set to minimise a cost function that approximates the sound level in the cabin, and are thus rearranging the fuselage vibration in order to minimise the radiated sound rather than to minimise the structural vibration itself[45]. In fact, when the passive tuned vibration absorbers[4] applied on the Douglas DC-9 were replaced by the active ones (ATVA), both tones (originating from two fan stages of the engine) decreased at the noisiest seat by 25 dB over the engine rpm range of 65-100% when switching the active system on[46,47].

Active control can also be used to avoid the problems related to conflicting requirements on the static and dynamic stiffnesses of aircraft engine mounts. As mentioned before, the engine mounts should be statically stiff (to connect the engine to the aircraft structure) and dynamically soft (to isolate the engine from the aircraft structure)[48]. As one would expect, for operational and safety reasons this clash of the requirements is usually resolved in favour of the static stiffness which leads to rather poor vibration

isolation. However, by using active or semi-active mounts, the transmitted vibrations can be effectively reduced even with stiff mounting elements.

An active mount consists of a reactive or proof-mass actuator, a sensor system and a controller. In the case of a reactive actuator, the control force is chosen such that the total transmitted dynamic force due to the active and the passive component is zero. Then the receiving structure is not excited and the source structure (engine) vibrates as if it were floating freely in space[49]. The reactive actuator can be mounted either in parallel or in series with the connecting element. If it is mounted in series it has to be able to support the static load of the engine. If it is mounted in parallel, the actuator must be able to overcome the stiffness of the connecting element[48,50]. The sensor systems usually measure the transmitted force or the relative displacement[49].

If a proof-mass (inertial) actuator is used, then it is attached to the mount connection point of the aircraft structure. Usually, the inertial actuator is driven to cancel the velocity measured at the connection point of the aircraft structure. The control capability can be limited by the amplitude of the required control force at the resonance or the engine-mount system[51]. If the primary excitation has predominantly tonal characteristics, a feedforward system can be used which utilizes a reference signal well-correlated to the disturbance.

1.4 Recent advances in cabin noise active control

In case of broadband, random disturbances, such as the disturbances generated by the TBL and the turbofan jet stream, passive and feedforward active control methods can not provide large interior sound level reductions at low frequencies.

Passive double panel arrangements with the sound-proof material in the cavity give good reductions of the transmitted sound only at the mid and high frequency range, above the mass-air-mass resonance of the double panel. The transmitted sound is attenuated particularly well at high frequencies because:

- above the mass-air-mass resonance the sound transmission is governed by the mass law, and therefore decreases with increase of frequency; and

- the efficiency of the sound absorbing layer (high density fibreglass blankets in the air cavity between the panels) increases as the wavelength decreases.

However, at frequencies below the mass-air-mass resonance, the sound transmission ratio is rather high and is controlled by the resonances of the double panel system. Also, the wavelength is large in comparison to the sound-proof layer thickness such that the sound absorption efficiency is rather low[22-24].

On the other hand, the active methods (ANC, ANVC, and ABC) heavily rely on the availability of reference signals[32-44], which are almost impossible to obtain in case of random (TBL or jet noise) disturbances. This limits the applicability of the described feedforward control architectures to the attenuation of tonal noise components with available reference signals well correlated to the primary disturbance.

For these reasons, a lot of research has been focused onto the development of feedback active control systems[52-58] which do not require reference signals and which could potentially deal with the random low frequency noise transmitted through the fuselage structure. A control architecture that includes actuators and sensors embedded into the structural walls has been considered, in order to suppress the noise transmitted by the vibration of the fuselage walls. This technique is called Active Structural Acoustic Control (ASAC)[59-61]. In contrast to ANC systems, ASAC systems aim to minimise the sound transmission through a partition by modifying its response using the structural actuators and sensors rather than by acoustic actuators and sensors distributed in the enclosure. The ASAC control action focused on the walls enclosing the cabin reduces the number of dimensions of controlled system by one, with reference to ANC and ANVC. This is because only out of plane, two dimensional vibrations of the fuselage skin are important for the sound transmitted into the cabin, while ANC and ANVC systems act directly on the three dimensional acoustic field. Although ASAC systems can be implemented within the feedforward framework[22,45], only feedback ASAC systems are considered here because of their suitability for the control of the broadband noise transmission. ASAC systems can be deployed in a centralised and decentralised manner. A centralised ASAC feedback system would require information of the frequency response functions between many sensors and many structural actuators, which limits the robustness of the control. For this reason, Multi-Input-Multi-Output

(MIMO) decentralised feedback systems have been considered, which do not require reference signals or system transfer function models[53-56]. In addition, a comparison of a centralised and decentralised ASAC system has shown surprisingly similar performances in some arrangements[52].

Decentralised MIMO systems exhibit unconditional stability if the sensors and actuators are dual and collocated[62-64]. For example, a velocity sensor and a force actuator form a dual and collocated pair. If such a pair implements a negative velocity feedback loop then an active damping effect is produced. As a consequence, the resonant response of the structure is reduced as is the transmitted sound power[52-59,65,66,69,70]. This is particularly important because the broadband sound transmission through thin partitions at low frequencies is controlled by well separated resonances[22], which can be effectively controlled by a damping action. Furthermore, the decentralised control architecture provides the necessary robustness, because a failure of one control unit does not cause the failure of the system as a whole.

The challenges of velocity feedback control approaches include the development of transducer arrangements which provide good duality and collocation properties of the sensor-actuator pairs. The difficulties are mainly related to the dynamics of the actuation and sensing mechanisms of practical sensors and actuators. The non-perfect duality and collocation may yield stability problems and may preclude the implementation of the desired feedback gains[55,57,58].

In the following section, a brief survey of recent work on smart panels for active structural acoustic control, based on velocity feedback is given. Particular attention is given to feedback loop stability as a function of the different sensing and actuation mechanisms used.

1.5 Smart panels for active structural acoustic control

A theoretical analysis of a smart panel for the control of sound transmission can be found in Ref. 53. The authors have considered a thin rectangular aluminium panel, simply supported along its edges, equipped with sixteen MIMO decentralised velocity feedback loops. Idealised point force actuators with collocated ideal velocity sensors

were considered as a benchmark for the maximum performance of the proposed control arrangement. The performance results based on the theoretical study are shown in Figure 4.

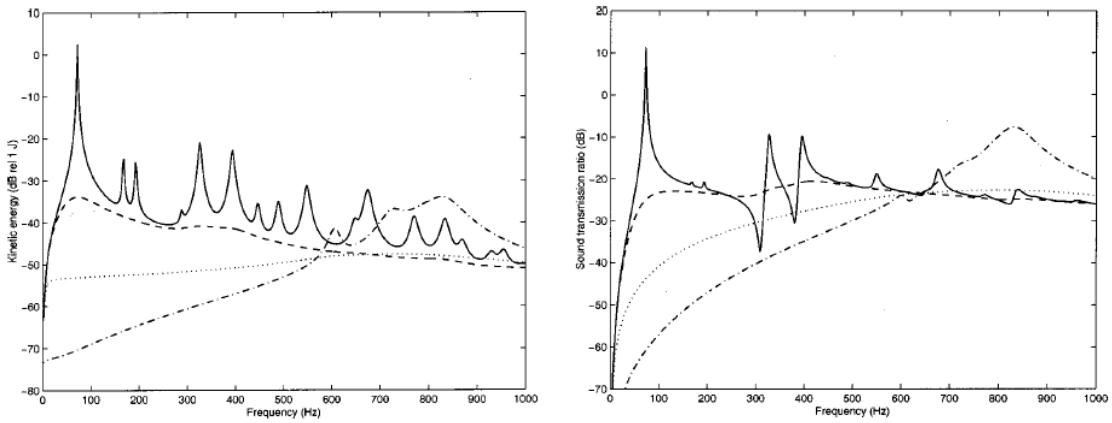

Figure 4: Kinetic energy (left) and the sound transmission ration (right) of a smart panel with 16 decentralised velocity feedback units. The solid lines-no control, dashed lines – small feedback gains, dotted lines-optimal feedback gains, and dash-dotted lines-extensive feedback gain. (From Ref. 53)

Significant reductions in both the spatially averaged kinetic energy of the panel and in its radiated sound power can be obtained for an optimal value of feedback gain, although higher values of feedback gain can induce extra resonances in the system and degrade the control performance. The feedback controller in that case was unconditionally stable, allowing the implementation of desired feedback gains (around 100 Nms^{-1}). An experimental study was also performed and practical transducer pairs were used, each consisting of a piezoelectric patch and a velocity sensor located at the centre of the piezoelectric patch[54-56]. The experimental setup is shown in Figure 5.

The measured open loop sensor-actuator Frequency Response Function (FRF) suggested that the feedback loop was conditionally stable, and the implementation of very high feedback gains was not possible. Figure 6 shows Nyquist plots of the open loop sensor-actuator frequency response function.

The Nyquist plots show that at higher frequencies (around 20 kHz) the locus enters the negative real quadrants and crosses the real axis. According to the Nyquist criterion, such a feedback loop is conditionally stable. The frequency of the crossing of the negative real axis corresponded to the frequency where the structural wavelength became comparable to the piezoelectric patch dimensions.

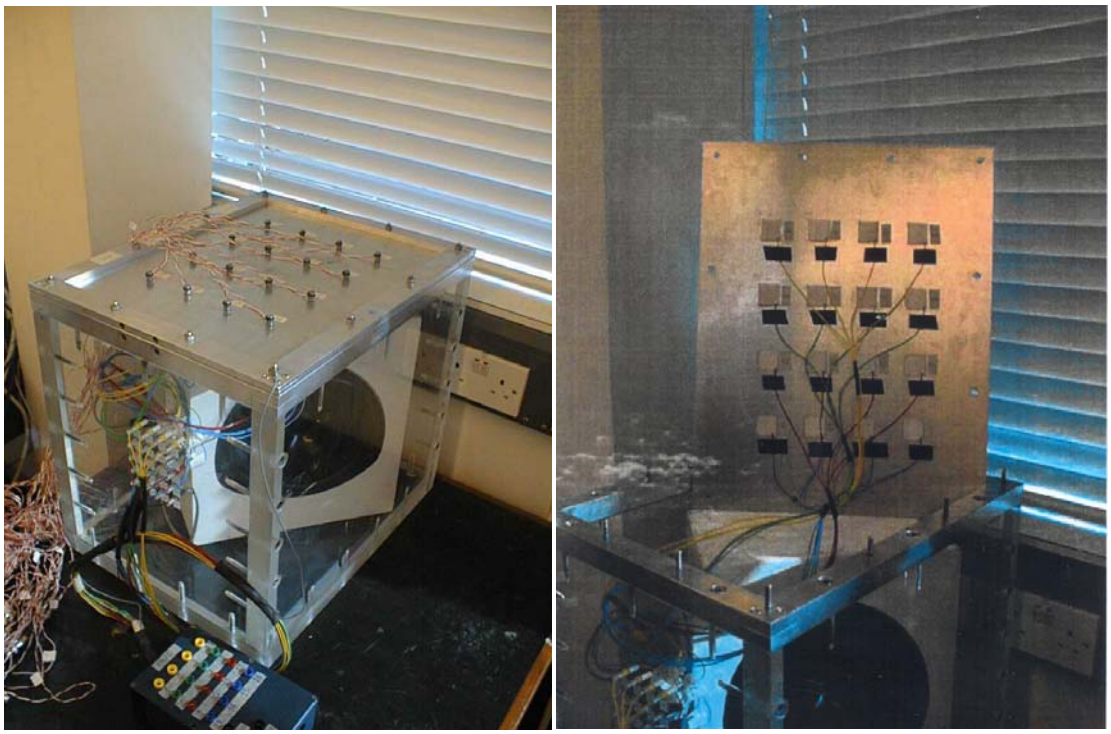

Figure 5: A smart panel with sixteen decentralised velocity feedback units, using rectangular piezoelectric patches and matched velocity sensors. (From Ref. 56)

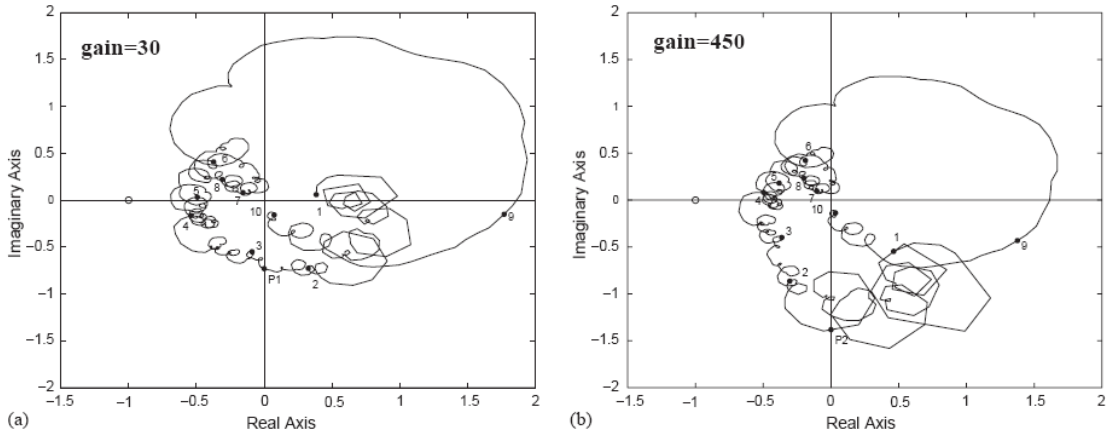

Figure 6: Nyquist plot of the frequency response function between the sensor-actuator pair, without phase lag compensator (left hand side plot); and (b) with phase lag compensator (right hand side plot). (From Ref. 55)

Therefore the conditional stability of the velocity feedback loop may be explained by the fact that the piezoelectric patch and a velocity sensor behaved as dual and collocated pairs only at frequencies lower than the actuator-plate "coincidence" frequency. Nevertheless, when a phase lag compensator was used; it enabled the implementation of higher gains (Figure 6, right hand side plot), and very good reductions of the panel vibration and the radiated sound power[56]. Recent work by Aoki et al.[67] aimed to improve

the stability properties of such transducer pairs by using different shaping of piezoelectric actuators.

An interesting arrangement had been proposed by Gardonio et al.[58], who tested theoretically and experimentally a smart panel equipped with matched volume velocity sensor and a uniform force actuator for the control of volumetric modes of a rectangular plate. Volumetric vibratory modes of panels are important due to their large far-field radiation efficiency. Polyvinylidene fluoride films 0.5 mm thick with a quadratically shaped electrode were bonded to either side of the plate, to form the matched volume velocity sensor and the uniform force actuator pair. However several problems were encountered with the measurement of the transfer function between the sensor and actuator. The most important problems were the unwanted coupling between the sensor and actuator via in-plane plate vibration; and the high-frequency effects produced by the non-perfect shaping of the actuator and sensor electrodes.

An alternative to the piezoelectric actuator is an inertial (proof mass, seismic) actuator[22,68-73]. An inertial actuator applies the control force onto the structure by reacting against a proof mass. The mass is attached to the structure by an elastic member. In parallel with the elastic member an actuating member is used. The actuating member is often an electromagnetic (voice coil) actuator which generates a Lorentz force. The permanent magnet of the actuating member usually acts as the proof mass.

Inertial actuators exhibit second order dynamics and their control authority is consequently limited to frequencies above the fundamental mass-spring resonance. For that reason a requirement on the actuator design is that the fundamental resonance is as low as possible. This means that the stiffness of the elastic member should be very low if the proof mass is to be kept within reasonable limits. This can generate problems related to excessive static deflections in presence of static accelerations, like for example, gravity. A possible solution to these problems is the use of self levelling inertial actuators with local displacement feedback control[68].

The dynamics of the actuator is also a limiting factor to the performance and stability properties of smart panels which use inertial actuators. For example, González Díaz et al.[69,70] studied a smart panel with five proof-mass actuators and collocated seismic

accelerometer sensors for the vibration control of a thin rectangular plate. The sensor-actuator pairs behaved as dual and collocated only at frequencies between the actuator fundamental resonance and the sensor fundamental resonance. The feedback control loops were conditionally stable, and the stability was guaranteed only when feedback gains smaller than a critical value were applied. In addition, a spillover effect was observed at the frequency of the actuator fundamental resonance. These problems can be addressed by damping down the actuator fundamental resonance[71], via implementation of a local velocity feedback loop. A detailed description of the design of a lightweight, miniature inertial actuator, including the scaling study can be found in Ref. 72.

The described problems with the actuator dynamics were the motivation for this study which investigates a novel smart panel. The new smart panel comprises two single panels, such that electrodynamic actuators can be used which react between the two panels. In such a way it might be possible to avoid stability problems due to local dynamics of inertial actuators.

1.6 Scope and objective

This PhD dissertation presents theoretical and experimental study of decentralised active control of sound transmission through a simplified model of an aircraft double panel. The model aircraft panel consists of two plates which are coupled acoustically by the air in the cavity between them and structurally by four elastic mounts. The source panel is made from a 1 mm thick aluminium sheet, and represents the fuselage skin, whereas the radiating panel is made from a 3mm thick Honeycomb polymer plate, and represents the interior (trim) panel. Active vibroacoustic control is implemented on the double panel using decentralised velocity feedback loops. A novel actuation arrangement is used such that the control forces are applied using a regular array of voice-coil actuators located in the cavity, which can react between the two plates. Each actuator end is equipped with a velocity sensor. The two velocity sensors can be used to close absolute and relative velocity feedback loops. Furthermore, the two junction-velocity signals can be weighted and combined into error signals. By changing the weighting factor, a variety of error signals can be created, which emphasise either the source or the radiating panel velocity in the error signal.

The model double panel studied in this thesis is notably simplified in comparison to real aircraft fuselages in a following way:

- First, it only counts for a section of the fuselage skin confined between two adjacent frames and two adjacent stringers. Thus, for very low frequencies, where the longitudinal and circumferential wavelength are longer than the stiffener spacing, the calculated and measured sound transmission results may be inaccurate.
- Second, in pressurized aircraft, a pressure difference between the aircraft interior and exterior is maintained by the cabin pressurization system. This effectively applies a tension to the source panel and causes a consistent upward shift of the source panel resonance frequencies with reference to a non-tensioned panel.
- Third, the aircraft skin and trim panels are curved, and the model used for the study in this study considers flat panels. The curvature has an impact to the sound transmission which is neglected here.

In summary, the model problem used for this study performs best in the intermediate frequency range from about 100 Hz up to 3 kHz. Although some mechanisms of sound excitation, transmission and radiation of the fuselage double wall of an aircraft have been neglected with this model, it is thought by the author that it contains the most important features of the problem and should therefore provide a good understanding of the phenomena occurring when active control with reactive actuators is applied.

The main objectives of this thesis are:

- to investigate the active control of noise transmitted through a double panel using an array of reactive actuators and velocity sensors
- pairs that implement decentralised velocity feedback loops;
- to design, build and implement a smart double panel experimental demonstrator; and
- to asses the performance and stability properties of a smart double panel demonstrator with reference to either absolute velocity feedback, relative velocity feedback, and the feedback using weighed velocities.

A fully-coupled model has been formulated for the theoretical analysis of the smart double panel system passive behaviour, as well as its stability and control performance. A parametric study of the passive response and sound power transmission ratio has been performed theoretically. Also, an experimental parametric study of the passive response and sound radiation has been performed.

The stability of the feedback loops is investigated theoretically and experimentally by using the Nyquist criterion for the analysis of the open loop frequency response function for one of the feedback units. In particular, the stability of the feedback unit has been investigated with respect to different weighting factors of the velocity error sensor. In addition, a generalised Nyquist stability criterion has been used to investigate experimentally the cross-talk effects between the decentralised feedback units on the global stability properties of the smart panel.

The effectiveness of the decentralised active control system has been demonstrated theoretically and experimentally in terms of reductions of the trim panel mean kinetic energy and the radiated sound power.

Finally, the active control effects are compared to the passive effects produced by a sound absorbing foam sheet, located in the air cavity between the two panels. The sound absorbing foam sheet has a weight comparable to the weight added by the sensor and actuator elements.

1.7 Structure and organisation

The thesis is organised into two principal parts: theoretical and the experimental. The theoretical part comprises chapter two, three and four, whereas the experimental part is consisted of chapters five and six.

In Chapter two the model problem is described in detail, including the development of the mathematical model for the numerical simulations of the response and the sound transmission without and with active control. In addition, the physics of the passive structure-borne and airborne sound transmission through the smart double panel is

studied with reference to a set of key mechanical parameters of the structure. The mathematical model is validated by a comparison of simulated and analytical sound transmission ratio. Also a convergence study is performed in order to avoid possibilities of numerical inaccuracies of the mathematical model used.

In Chapter three the performance of sixteen-channel decentralised velocity feedback using skyhook actuators with collocated velocity sensors acting either on the source or radiating panels is analysed first. The performance analysis is carried out with reference to reductions of the spatially averaged kinetic energy and the sound transmission ratio due to the active control. Then the control effects of reactive actuators driven with relative velocity signals are studied.

In Chapter four, decentralised feedback control using weighted velocity signals is analysed. In particular, the stability and performance of the smart double panel are analysed with reference to the velocity weighting factor used. In addition, a parametric study of the stability of the feedback loops has been performed in order to investigate the sensitivity of the stability margins with reference to the mechanical parameters of the system under control.

In Chapter five the design and experimental testing of a smart double panel demonstrator is presented. In this case active vibroacoustic control is implemented on the double panel using nine direct velocity feedback loops. Miniature voice coil actuators that react between the two panels with collocated Micro Electro Mechanical Systems (MEMS) accelerometer sensors are used for the decentralised velocity feedback control. The study involved two types of experiments. First, the sensor-actuator frequency response function of a single control unit was measured with reference to different input/output signal conditioners using two types of accelerometer sensors. The Nyquist stability criterion was then used to determine the configuration which guarantees the best stability properties of a single control unit. Second, a 9×9 matrix of point and transfer mobilities were measured in order do investigate the global stability properties of the smart panel, using the generalised Nyquist criterion.

In Chapter six, an experimental parametric study of the sound radiation has been performed with reference to different materials of the radiating panel. Global control

effects of the smart double panel are assessed in terms of reductions of the radiated sound power and the radiating panel kinetic energy.

1.8 Contributions

The original contributions of this thesis are:

- A theoretical performance analysis of absolute and relative decentralised velocity feedback configurations for the active control of noise transmitted through a model aircraft double panel, using skyhook and reactive actuators.
- A theoretical and experimental stability investigation of a single velocity feedback loop for the vibration control of a model aircraft double panel when a reactive force actuator is driven by two weighted velocity signals.
- A theoretical performance investigation of a 16-channel decentralised feedback control applied on a smart double panel using reactive force actuators driven by weighted velocity signals.
- An experimental investigation of the stability and performance of a 9-channel decentralised feedback control applied on a prototype smart double panel using reactive force actuators driven by weighted velocity signals.
- An experimental validation of the velocity weighting factor effect.

The findings which are presented in Chapters 2-4 have been published in recent issues of American Institute for Aeronautics and Astronautics (AIAA) Journal[65,66], whereas the content of Chapters 5 and 6 have been used for publications submitted to AIAA Journal and Journal of Acoustical Society of America (JASA).

2 Model problem and the parametric study of passive sound transmission

The introductory chapter presented a description of the mechanisms of the sound transmission into the aircraft interior and a survey of available passive and active control methods. The potential of MIMO decentralised feedback control as a possible solution for broadband low-frequency noise transmission of aircraft double panels was also discussed.

The aim of this chapter is to give an overall picture and a detailed description of the model problem analysed in this thesis. Also, the mathematical model used to determine the smart double panel response and sound transmission is presented in detail. Although the double panel is a simplified model, it captures the basic sound transmission properties of double panels in aircraft for mid to high frequencies. Finally, a parametric study is performed by varying the key mechanical properties of the double panel system and by analysing the effects of the parameter change onto the sound transmission and response of the double panel.

2.1 Smart double panel with decentralised control units

The double panel considered in this study consists of two plates, which are, as shown in Figure 7, structurally and acoustically coupled respectively via elastic mounts and the air in the cavity between the plates.

In this study the source panel is excited by an acoustic plane wave, while the radiating panel radiates sound into free-field. The source panel is assumed to be simply supported along all the edges. It is modelled as a 414x314x1 mm^3 aluminium panel, in order to represent a section of an outer skin of an aircraft between two adjacent frames and two adjacent stringers. In order to excite all the vibratory modes of the source panel, the acoustic plane wave excitation has azimuthal and elevation angles of 45^o and 45^o.

The radiating panel is modelled as a plate with free boundary conditions along the four edges, structurally connected to the source panel by means of four rubber mounts. The

radiating panel has the same x and y dimensions as the source panel, but it is made of a honeycomb polymer material with 3 mm thickness. These properties have been chosen so as to emulate a typical aircraft trim panel.

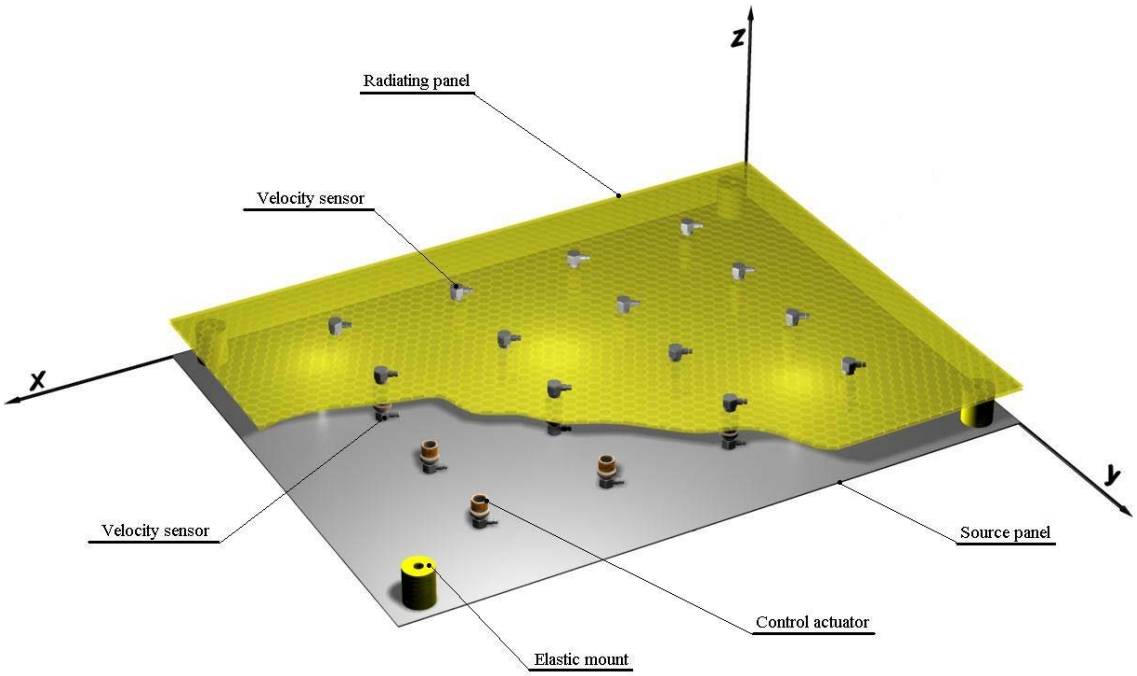

Figure 7: Smart double panel with an array of decentralised control units

As shown in Figure 7, both source and radiating panels are equipped with a 4x4 array of collocated ideal point force actuators and velocity sensors which can be used to generate direct velocity feedback loops on either panel or relative velocity feedback between the two panels. The array of decentralised control system elements have been equally spaced along the x and y directions in such a way that the distances between actuators (sensors) are equal to double the distance between the edge of the plate and a perimeter actuator (sensor).

2.2 Mathematical model

2.2.1 Mobility matrix model

In the mobility matrix model it is assumed that the system is divided into three elements: the source panel, the radiating panel and the structure-borne and airborne transmission paths. The structure-borne transmission path is due to the sound transmission via the

elastic mounts, while the airborne path is due to the sound transmission via the air confined between the radiating and the source panel. Each of these elements is modelled using point and transfer mobility or impedance functions. The airborne transmission path is modelled using transfer impedances between a finite number of cavity elements that are adjacent to the surfaces of the panels. The excitation of the source panel by the incident acoustic wave and the radiated sound power from the radiating panel are also calculated by assuming that the two panels are divided into the same number of elements. This number is obtained by choosing element dimensions to be $l_{x,e}=l_x/(4M)$ and $l_{y,e}=l_y/(4N)$ where M and N are higher modal orders used in calculations. The mobility model scheme is given in Figure 8.

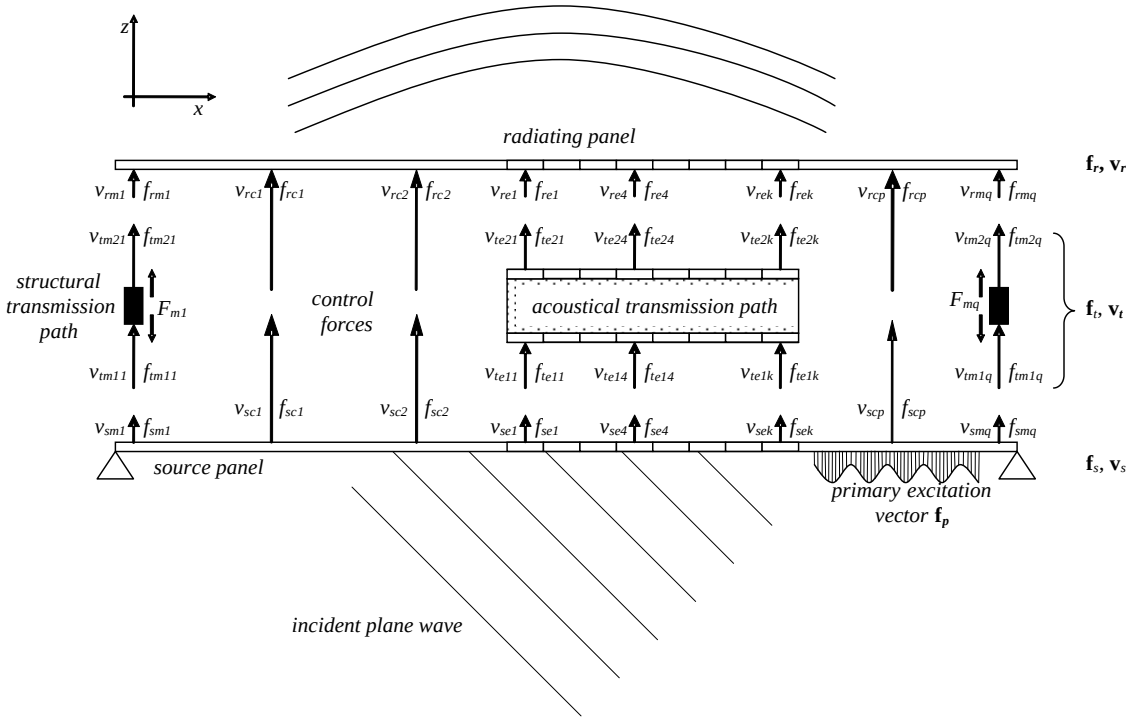

Figure 8: Mobility model scheme

The model considers only out of plane displacements/velocities and forces at the various types of junctions and at the centres of the plates and cavity elements. The time harmonic displacement or force are given by $w(t)=\mathrm{Re}\{w(\omega)e^{j\omega t}\}$ or $f(t)=\mathrm{Re}\{f(\omega)e^{j\omega t}\}$, where ω is the circular frequency in $[\mathrm{rad/s}]$ and $j=\sqrt{-1}$. Thus $w(t)$ and $f(t)$ are the time-harmonic displacement and force functions while $w(\omega)$ and $f(\omega)$ are the complex frequency-dependent displacement and force phasors. In order to simplify the mobility formulation used in this study, the time harmonic dependence is

implicitly assumed in the mathematical expressions which are therefore formulated in terms of the frequency-dependent phasors. Also, the first and second derivative of the time-harmonic functions, for example the linear out of plane velocity, $\dot{w}(t) = \mathrm{Re}\{j\omega w(\omega) e^{j\omega t}\}$ or linear out of plane acceleration $\ddot{w}(t) = \mathrm{Re}\{-\omega^2 w(\omega) e^{j\omega t}\}$ are represented by velocity and acceleration frequency dependent phasors $\dot{w}(\omega) = j\omega w(\omega)$ and $\ddot{w}(\omega) = -\omega^2 w(\omega) = j\omega \dot{w}(\omega)$.

The transmission path via the elastic mounts is modelled as an elastic out of plane force, so that point impedances can be used to model this coupling at the mount locations. This path consists of q=4 distributed elastic mounts. The mounts connect the two panels at four locations close to the corners of the plates, as it is usually the case with aircraft trim panel mounting systems, although in practice the mounts are fixed on the frame structure rather then on the fuselage skin. At each mount junction the vibration and the transmitted forces are characterised by one complex function that corresponds to the out of plane (z) translational degree of freedom. Other vibration degrees of freedom, such as, for example, in plane displacements or out of plane rotations, are neglected in this model.

The velocity and force phasors at mount locations are grouped in the following column vectors:

$$\mathbf{v}_m \equiv \left\{\dot{w}_1, \dot{w}_2, \ldots \dot{w}_j, \ldots \dot{w}_{q-1}, \dot{w}_q\right\}^T, \tag{1}$$

$$\mathbf{f}_m \equiv \left\{N_{z1}, N_{z2}, \ldots N_{zj}, N_{zq-1}, N_{zq}\right\}^T, \tag{2}$$

where $\dot{w}_j$ is the complex amplitude of the linear velocity along the z axis, and N_{zj} is the complex amplitude of the force in the z direction, at the j-th elastic mount. The two panels are also excited by means of p control forces. The velocity and control force phasors at the control positions in the source and radiation panels are grouped in the following two column vectors:

$$\mathbf{v}_c \equiv \left\{\dot{w}_1, \dot{w}_2, ... \dot{w}_j, ... \dot{w}_{p-1}, \dot{w}_p\right\}^T, \tag{3}$$

$$\mathbf{f}_c \equiv \left\{N_{z1}, N_{z2}, ... N_{zj}, N_{zp-1}, N_{zp}\right\}^T. \tag{4}$$

The double panel is also characterised by an acoustical transmission path, which occurs via the air in the cavity between the two plates. As shown in Figure 8, the surface boundaries that the cavity shares with the source and the radiating plate are modelled using a finite number of small elements *k*, such that the element dimensions are considerably smaller than the shortest acoustic wavelength in the cavity. The lateral surfaces of the air cavity are assumed to be rigid walls. Each of the top and bottom surface elements can only vibrate in the direction normal to the surfaces themselves and their velocities and forces are defined at the geometrical centres of the elements.

The velocity and force phasors at the centres of the elements are grouped in the following two column vectors:

$$\mathbf{v}_e \equiv \left\{\dot{w}_1, \dot{w}_2, ... \dot{w}_j, ... \dot{w}_{k-1}, \dot{w}_k\right\}^T, \tag{5}$$

$$\mathbf{f}_e \equiv \left\{N_{z1}, N_{z2}, ... N_{zj}, N_{zk-1}, N_{zk}\right\}^T. \tag{6}$$

With reference to the notation shown in Figure 8, these junction vectors are grouped together to form four combined vector pairs. These four groups are: the source velocity vector $\mathbf{v}_s$ and the source force vector $\mathbf{f}_s$; the radiating velocity vector $\mathbf{v}_r$ and the radiating force vector $\mathbf{f}_s$; the transmission system velocity vector $\mathbf{v}_t$ and the transmission system force vector $\mathbf{f}_t$; and finally, the control velocity vector $\mathbf{v}_c$ and the control force vector $\mathbf{f}_c$. The four groups of vectors are given by:

$$\mathbf{v}_s \equiv \begin{Bmatrix} \mathbf{v}_{sm} \\ \mathbf{v}_{se} \end{Bmatrix} \equiv \begin{Bmatrix} v_{sm1} \\ v_{sm2} \\ \vdots \\ v_{smq} \\ v_{se1} \\ v_{se2} \\ \vdots \\ v_{sek} \end{Bmatrix} \quad \mathbf{v}_r \equiv \begin{Bmatrix} \mathbf{v}_{rm} \\ \mathbf{v}_{re} \end{Bmatrix} \equiv \begin{Bmatrix} v_{rm1} \\ v_{rm2} \\ \vdots \\ v_{rmq} \\ v_{re1} \\ v_{re2} \\ \vdots \\ v_{rek} \end{Bmatrix} \quad \mathbf{v}_t \equiv \begin{Bmatrix} \mathbf{v}_{tm1} \\ \mathbf{v}_{te1} \\ \mathbf{v}_{tm2} \\ \mathbf{v}_{te2} \end{Bmatrix} \equiv \begin{Bmatrix} v_{tm11} \\ \vdots \\ v_{tm1q} \\ v_{te11} \\ \vdots \\ v_{te1k} \\ v_{tm21} \\ \vdots \\ v_{tm2q} \\ v_{te21} \\ \vdots \\ v_{te2k} \end{Bmatrix} \quad \mathbf{v}_c \equiv \begin{Bmatrix} \mathbf{v}_{sc} \\ \mathbf{v}_{rc} \end{Bmatrix} \equiv \begin{Bmatrix} v_{sc1} \\ v_{sc2} \\ \vdots \\ v_{scp} \\ v_{rc1} \\ v_{rc2} \\ \vdots \\ v_{rcp} \end{Bmatrix} \tag{7-10}$$

$$\mathbf{f}_s \equiv \begin{Bmatrix} \mathbf{f}_{sm} \\ \mathbf{f}_{se} \end{Bmatrix} \equiv \begin{Bmatrix} f_{sm1} \\ f_{sm2} \\ \vdots \\ f_{smq} \\ f_{se1} \\ f_{se2} \\ \vdots \\ f_{sek} \end{Bmatrix} \quad \mathbf{f}_r \equiv \begin{Bmatrix} \mathbf{f}_{rm} \\ \mathbf{f}_{re} \end{Bmatrix} \equiv \begin{Bmatrix} f_{rm1} \\ f_{rm2} \\ \vdots \\ f_{rmq} \\ f_{re1} \\ f_{re2} \\ \vdots \\ f_{rek} \end{Bmatrix} \quad \mathbf{f}_t \equiv \begin{Bmatrix} \mathbf{f}_{tm1} \\ \mathbf{f}_{te1} \\ \mathbf{f}_{tm2} \\ \mathbf{f}_{te2} \end{Bmatrix} \equiv \begin{Bmatrix} f_{tm11} \\ \vdots \\ f_{tm1q} \\ f_{te11} \\ \vdots \\ f_{te1k} \\ f_{tm21} \\ \vdots \\ f_{tm2q} \\ f_{te21} \\ \vdots \\ f_{te2k} \end{Bmatrix} \quad \mathbf{f}_c \equiv \begin{Bmatrix} \mathbf{f}_{sc} \\ \mathbf{f}_{rc} \end{Bmatrix} \equiv \begin{Bmatrix} f_{sc1} \\ f_{sc2} \\ \vdots \\ f_{scp} \\ f_{rc1} \\ f_{rc2} \\ \vdots \\ f_{rcp} \end{Bmatrix}, \tag{11-14}$$

where:

- v_{smj}, f_{smj} and v_{sej}, f_{sej} represent the complex velocities and forces at the source junction for the *j*-th mount and for the *j*-th acoustic element,
- v_{rmj}, f_{rmj} and v_{rej}, f_{rej} represent the complex velocities and forces at the radiating junction for the *j*-th mount and for the *j*-th acoustic element,
- v_{tm1j}, f_{tm1j} and v_{te1j}, f_{te1j} represent the complex velocities and forces for the *j*-th mount and for the *j*-th acoustic element on the source panel,
- v_{tm2j}, f_{tm2j} and v_{te2j}, f_{te2j} represent the complex velocities and forces for the *j*-th mount and for the *j*-th acoustic element on the radiating panel,
- v_{scj}, f_{scj} and v_{rcj}, f_{rcj} represent the control system complex velocities and forces for the *j*-th control force at the *j*-th control point either on the source or radiating panels.

The dynamics of the source and radiating panels are modelled using a mobility matrix formulation, so that velocity and force vectors can be expressed in the form:

$$\mathbf{v}_s = \mathbf{Y}_{s1}\mathbf{f}_s + \mathbf{Y}_{s2}\mathbf{f}_p + \mathbf{Y}_{s3}\mathbf{f}_c, \qquad \mathbf{v}_r = \mathbf{Y}_{r1}\mathbf{f}_r + \mathbf{Y}_{r2}\mathbf{f}_f + \mathbf{Y}_{r3}\mathbf{f}_c, \qquad (15,16)$$

where $\mathbf{Y}_{s1}$, $\mathbf{Y}_{s2}$, $\mathbf{Y}_{s3}$ and $\mathbf{Y}_{r1}$, $\mathbf{Y}_{r2}$, $\mathbf{Y}_{r3}$ are mobility matrices of the source and the radiating panel, and $\mathbf{f}_p$, $\mathbf{f}_c$, $\mathbf{f}_f$ are the primary excitation vector, control force vector and flanking excitation vector, respectively. The details of the mobility matrices used in Equations (15,16) and also of the mobility and impedance matrices introduced in the forthcoming part of the formulation are defined in Appendix A. For example a plate mobility function between points P_1 and P_2 has a form[22] $Y_{\dot{w},N_z}(\omega) = j\omega\sum_{m=1}^{\infty}\sum_{n=1}^{\infty}\frac{\phi_{m,n}(x_{P2},y_{P2})\phi_{m,n}(x_{P1},y_{P1})}{\rho\, h\, l_x l_y\left[(\omega_{m,n})^2(1+j\eta)-\omega^2\right]}$, where $\phi_{m,n}$ are the plate mode shape functions, ρ is the mass density of the plate material, h_s is the plate thickness, l_x is the plate length, l_y is the plate width, $\omega_{m,n}$ are the plate natural frequencies, and η is the plate loss factor.

The primary and flanking excitation vector are given by:

$$\mathbf{f}_p \equiv \begin{Bmatrix} f_{p1} \\ f_{p2} \\ \vdots \\ f_{pk} \end{Bmatrix}, \qquad \mathbf{f}_f \equiv \begin{Bmatrix} f_{f1} \\ f_{f2} \\ \vdots \\ f_{fk} \end{Bmatrix}, \qquad (17,18)$$

The flanking excitation vector $\mathbf{f}_f$ acting on the radiating panel could be caused by a subsystem connected to it or by an additional flanking path connecting the source panel to the radiating panel. The flanking excitation has not been considered throughout the study covered by this thesis, so that the flanking excitation vector is assumed to be a vector with all the elements equal to zero.

If the source plate is excited by a plane acoustic wave then the components of the primary excitation vector are determined by pressure field generated by the plane wave over the surface of the source panel:

$$f_{pj}(x_j, y_j, \omega) = \frac{l_x l_y}{k} P e^{-j\left(k_x x_j + k_y y_j\right)} \tag{19}$$

where P is the amplitude of the plane wave which has an acoustic wave number in the x direction given by $k_x = k\sin(\theta)\cos(\phi)$ and in the y direction given by $k_y = k\sin(\theta)\sin(\phi)$, where k is the wave number, θ and ϕ are azimuthal and elevation angles, while x_j and y_j are coordinates of the geometrical centre of corresponding element of the source panel. The term $Pe^{-j\left(k_x x_j + k_y y_j\right)}$ in Equation (19) is the pressure at the geometrical centre of an element while the term $\frac{l_x l_y}{k}$ is the area of the element. Therefore the excitation is modelled by assuming that the pressure field over the surface of the element can be approximated by the pressure at the centre of the element.

The dynamics of the transmission system is expressed using the following impedance matrix expression:

$$\mathbf{f}_t = \mathbf{Z}_t \mathbf{v}_t, \tag{20}$$

where $\mathbf{Z}_t$ is an impedance matrix of the transmission system. A detailed description of the elements of this matrix is given in Appendix A. The elements in the $\mathbf{Z}_t$ matrix, which are due to mounting system stiffness are diagonal, while the elements in the $\mathbf{Z}_t$ matrix due to acoustical coupling are fully populated, because the velocity at one element will generate a force, which is caused by pressure fluctuations at the centres of all the other elements, on both source and radiating plates. An example of an impedance function between points P1 and P2 of the rectangular cavity is given by[22] $Z_{N_z,\dot{w}}^{P1,P2}(\omega) = \frac{A_e^2 \rho_{air} \omega c_0^2}{l_x l_y l_z} \sum_{n_1=1}^{\infty}\sum_{n_2=1}^{\infty}\sum_{n_3=1}^{\infty} \frac{\psi_{n_1,n_2,n_3}^{P2} \psi_{n_1,n_2,n_3}^{P1}}{2\zeta\omega_n^{cav}\omega + j\left[\omega^2 - \left(\omega_{n_1 n_2,n_3}^{cav}\right)^2\right]}$, where A_e is the area of the

surface element, ρ_{air} is the air mass density, c_0 is speed of sound in the air, l_z is the cavity depth (distance between panels' inner surfaces), $\psi^{P1}_{n_1,n_2,n_3}$ is the natural mode shape function at point $P1$, $\psi^{P2}_{n_1,n_2,n_3}$ is the natural mode shape function at point $P2$, ζ is the air cavity loss factor, $\omega^{cav}_{n_1,n_2,n_3}$ are the air cavity natural frequencies, and n_1, n_2, n_3 are mode numbers for, *x*,*y*, and *z* directions.

The source and radiating panel Equations (15) and (16) can be grouped together in one equation:

$$\mathbf{v}_{sr} = \mathbf{Y}_{sr1}\mathbf{f}_{sr} + \mathbf{Y}_{sr2}\mathbf{f}_{pf} + \mathbf{Y}_{sr3}\mathbf{f}_c\,, \tag{21}$$

where the mobility matrices and the excitation vector have the form:

$$\mathbf{Y}_{sr1} = \begin{bmatrix} \mathbf{Y}_{s1} & \mathbf{0} \\ \mathbf{0} & \mathbf{Y}_{r1} \end{bmatrix}, \qquad \mathbf{Y}_{sr2} = \begin{bmatrix} \mathbf{Y}_{s2} & \mathbf{0} \\ \mathbf{0} & \mathbf{Y}_{r2} \end{bmatrix}, \qquad \mathbf{Y}_{sr3} = \begin{bmatrix} \mathbf{Y}_{s3} \\ \mathbf{Y}_{r3} \end{bmatrix}, \tag{22,23,24}$$

$$\mathbf{f}_{pf} = \begin{Bmatrix} \mathbf{f}_p \\ \mathbf{0} \end{Bmatrix}, \tag{25}$$

and the junction velocity and force vectors are given by:

$$\mathbf{v}_{sr} \equiv \begin{Bmatrix} \mathbf{v}_s \\ \mathbf{v}_r \end{Bmatrix}, \qquad \mathbf{f}_{sr} \equiv \begin{Bmatrix} \mathbf{f}_s \\ \mathbf{f}_r \end{Bmatrix}, \tag{26,27}$$

where $\mathbf{v}_{sr}$ and $\mathbf{f}_{sr}$ are respectively the source-radiating velocity vector and the source-radiating force vector. The source-radiating vectors are related to the corresponding coupling system vectors so as to satisfy the continuity (for the velocity vectors) and equilibrium (for the force vectors) principles at each junction:

$$\mathbf{v}_t = \mathbf{v}_{sr}\,, \qquad \mathbf{f}_t = -\mathbf{f}_{sr}\,. \tag{28,29}$$

If Equations (28) and (29) are substituted into Equation (20) the source-radiating force vector and force radiating velocity vector can be related through the following impedance expression:

$$\mathbf{f}_{sr} = -\mathbf{Z}_t \mathbf{v}_{sr} . \tag{30}$$

Substitution of Equation (30) into Equation (21) yields:

$$\mathbf{v}_{sr} = -\mathbf{Y}_{sr1}\mathbf{Z}_t \mathbf{v}_{sr} + \mathbf{Y}_{sr2}\mathbf{f}_{pf} + \mathbf{Y}_{sr3}\mathbf{f}_c , \tag{31}$$

$$\mathbf{v}_{sr} = (\mathbf{I} + \mathbf{Y}_{sr1}\mathbf{Z}_t)^{-1}\left(\mathbf{Y}_{sr2}\mathbf{f}_{pf} + \mathbf{Y}_{sr3}\mathbf{f}_c\right), \tag{32}$$

$$\mathbf{v}_{sr} = (\mathbf{I} + \mathbf{Y}_{sr1}\mathbf{Z}_t)^{-1}\mathbf{Y}_{sr2}\mathbf{f}_{pf} + (\mathbf{I} + \mathbf{Y}_{sr1}\mathbf{Z}_t)^{-1}\mathbf{Y}_{sr3}\mathbf{f}_c , \tag{33}$$

$$\mathbf{v}_{sr} = \mathbf{Q}_{tp}\mathbf{f}_{pf} + \mathbf{Q}_{tc}\mathbf{f}_c , \tag{34}$$

where the matrices $\mathbf{Q}_{tp}$ and $\mathbf{Q}_{tc}$ are given by:

$$\mathbf{Q}_{tp} = (\mathbf{I} + \mathbf{Y}_{sr1}\mathbf{Z}_t)^{-1}\mathbf{Y}_{sr2} , \qquad \mathbf{Q}_{tc} = (\mathbf{I} + \mathbf{Y}_{sr1}\mathbf{Z}_t)^{-1}\mathbf{Y}_{sr3} . \tag{35,36}$$

Using now Equation (30) with Equation (34) gives the source-radiating force vectors:

$$\mathbf{f}_{sr} = -\mathbf{Z}_t\mathbf{Q}_{tp}\mathbf{f}_{pf} - \mathbf{Z}_t\mathbf{Q}_{tc}\mathbf{f}_c , \tag{37}$$

$$\mathbf{f}_{sr} = \mathbf{R}_{tp}\mathbf{f}_{pf} + \mathbf{R}_{tc}\mathbf{f}_c , \tag{38}$$

where $\mathbf{R}_{tp}$ and $\mathbf{R}_{tc}$ are given by:

$$\mathbf{R}_{tp} = -\mathbf{Z}_t\mathbf{Q}_{tp} , \qquad \mathbf{R}_{tc} = -\mathbf{Z}_t\mathbf{Q}_{tc} . \tag{39,40}$$

Similar to Equation (21), the control velocity vector can also be expressed using the mobility method:

$$\mathbf{v}_c = \mathbf{Y}_{c1}\mathbf{f}_{sr} + \mathbf{Y}_{c2}\mathbf{f}_{pf} + \mathbf{Y}_{c3}\mathbf{f}_c , \tag{41}$$

where the mobility matrices have the form:

$$\mathbf{Y}_{c1} = \begin{bmatrix} \mathbf{Y}_{cs1} & \mathbf{0} \\ \mathbf{0} & \mathbf{Y}_{cr1} \end{bmatrix}, \qquad \mathbf{Y}_{c2} = \begin{bmatrix} \mathbf{Y}_{cs2} & \mathbf{0} \\ \mathbf{0} & \mathbf{Y}_{cr2} \end{bmatrix}, \qquad \mathbf{Y}_{c3} = \begin{bmatrix} \mathbf{Y}_{cs3} & \mathbf{0} \\ \mathbf{0} & \mathbf{Y}_{cr3} \end{bmatrix}. \tag{42,43,44}$$

$\mathbf{Y}_{cs1}$, $\mathbf{Y}_{cs2}$, $\mathbf{Y}_{cs3}$ and $\mathbf{Y}_{cr1}$, $\mathbf{Y}_{cr2}$, $\mathbf{Y}_{cr3}$ are mobility matrices of the source and the radiating panel, at the control locations. A detailed description of the elements of these matrices can be found in Appendix A.

Substitution of Equation (38) into Equation (41) yields:

$$\mathbf{v}_c = \mathbf{Y}_{c1}\mathbf{R}_{tp}\mathbf{f}_{pf} + \mathbf{Y}_{c1}\mathbf{R}_{tc}\mathbf{f}_c + \mathbf{Y}_{c2}\mathbf{f}_{pf} + \mathbf{Y}_{c3}\mathbf{f}_c , \tag{45}$$

$$\mathbf{v}_c = \left(\mathbf{Y}_{c1}\mathbf{R}_{tp} + \mathbf{Y}_{c2}\right)\mathbf{f}_{pf} + \left(\mathbf{Y}_{c1}\mathbf{R}_{tc} + \mathbf{Y}_{c3}\right)\mathbf{f}_c , \tag{46}$$

$$\mathbf{v}_c = \mathbf{T}_{cp}\mathbf{f}_{pf} + \mathbf{T}_{cc}\mathbf{f}_c , \tag{47}$$

where $\mathbf{T}_{cp}$ and $\mathbf{T}_{cc}$ are given by:

$$\mathbf{T}_{cp} = \mathbf{Y}_{c1}\mathbf{R}_{tp} + \mathbf{Y}_{c2} , \tag{48}$$

$$\mathbf{T}_{cc} = \mathbf{Y}_{c1}\mathbf{R}_{tc} + \mathbf{Y}_{c3} . \tag{49}$$

With feedback control, the control force vector $\mathbf{f}_c$ is related to the control velocity vector $\mathbf{v}_c$ by means of an arbitrary matrix **H**:

$$\mathbf{f}_c = -\mathbf{H}\mathbf{v}_c , \tag{50}$$

so that the control velocities can be calculated using Equation (47) as follows:

$$\mathbf{v}_c = \mathbf{T}_{cp}\mathbf{f}_{pf} + \mathbf{T}_{cc}\left(-\mathbf{H}\mathbf{v}_c\right), \tag{51}$$

$$\mathbf{v}_c = \left(\mathbf{I} + \mathbf{T}_{cc}\mathbf{H}\right)^{-1}\mathbf{T}_{cp}\mathbf{f}_{pf}, \tag{52}$$

while the source and radiating panel forces are determined by Equation (38). Finally, the source and radiating velocities are then given by Equation (21).

The sound power radiated by the radiating panel can then be evaluated using the velocities of the radiating elements[22,73] which are a subset of $\mathbf{v}_{sr}$, Equation (8), as:

$$W(\omega) = \mathbf{v}_{re}^H \mathbf{R} \mathbf{v}_{re}, \tag{53}$$

where $\boldsymbol{R}$ is the radiation resistance matrix[22,73] and $(\ )^H$ denotes the Hermitian transpose (the complex conjugate).

Kinetic energy of either source or radiating panel can be calculated using the following expressions[22]:

$$\begin{aligned} E_s(\omega) &= \frac{1}{4}\rho_s h_s l_{xe} l_{ye} \mathbf{v}_{se}^H \mathbf{v}_{se}, \\ E_r(\omega) &= \frac{1}{4}\rho_r h_r l_{xe} l_{ye} \mathbf{v}_{re}^H \mathbf{v}_{re}, \end{aligned} \tag{54,55}$$

where ρ_s, h_s, ρ_r, h_r are mass densities and thicknesses of the source and radiating panel, respectively.

2.3 Parametric study of passive sound transmission

The double panel model problem has been chosen in order to reflect the vibroacoustic properties of double panels in aircraft. The primary aim of this section is twofold. The first is to investigate how the vibroacoustic response varies when key parameters of the components of the model are changed. This type of study facilitates the interpretation of the physical phenomena for the airborne and structure-borne sound transmission through

the double panel. The second is to validate the model by comparing the simulations with other results obtained from well established analytical models[22].

It is known that for double partitions, important parameters can be the material properties of the panels, their dimensions, the distance between them, and the stiffness of elastic mounts which structurally connect the two panels. In order to perform a realistic study, the variation of these properties is selected with reference to materials and dimensions representative of a transportation aircraft skin. Normally the material properties and construction geometry of the bodywork of transportation vehicles are chosen by designers to meet functionality and safety requirements. In contrast, trim panels are designed for noise reduction and other constraints such as functionality, style, thermal insulation etc. Therefore, for the purpose of the parametric study the thickness and material of the radiating panel have been varied, whereas the source panel properties have been held fixed. The parametric study also included the radiating panel materials which are normally not suitable for aerospace applications, such as for example steel radiating panels. These materials have been included in order to extend the parametric study to a wider range of the material properties that would enable a better analysis. In this way it is provided that clear trends can be observed with the parameter change.

Three different radiating panels have been investigated: 1) light and stiff polymer honeycomb plate, 2) heavier but less stiff aluminium plate, and 3) heavy steel plate with low stiffness. The bending stiffness of a rectangular isotropic plate is given by[75]:

$$B = E\frac{h^3}{12}, \tag{56}$$

where h is thickness of the plate, and E is Young modulus, while the surface density of the plate (mass of the plate per unit area) is given by[75]:

$$m = \rho h, \tag{57}$$

where ρ is mass density of the plate material. Thus, for a given material, the bending stiffness and surface density are linked by the following law:

$$B = \frac{E}{\rho^3} m \,, \tag{58}$$

which is plotted in Figure 9 for the three materials considered in this study.

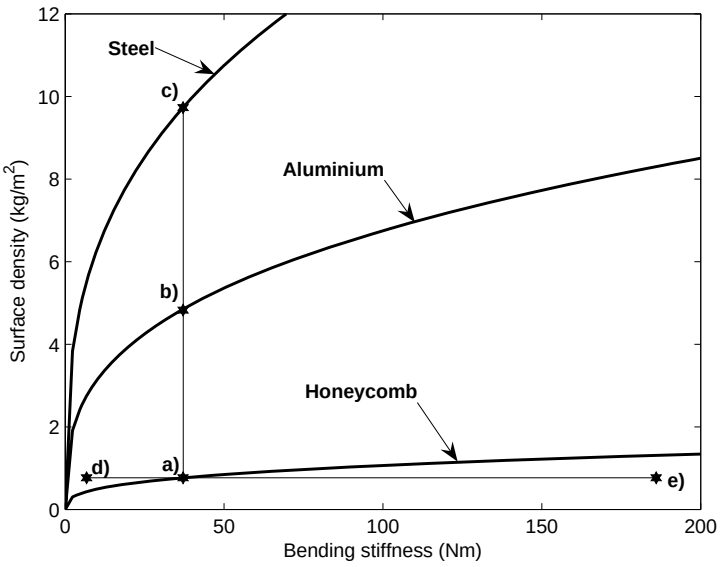

Figure 9: Surface density and bending stiffness curves for (a) polymer honeycomb, (b) aluminium and (c) steel radiating panels

All variations considered are summarised in Table 1. Designs (a), (b) and (c) represent three materials with constant bending stiffness and surface density between 0.765 kg/m^2 and 9.75 kg/m^2.

Table 1: Values of the varied parameters

	design	(a)	(b)	(c)	(d)	(e)	(f)	(g)	(h)	(i)
Mount stiffness	k_m (N/m)	5891	5891	5891	5891	5891	5891	5891	0	58910
Cavity depth	l_z (m)	0.03	0.03	0.03	0.03	0.03	0.02	0.04	0.03	0.03
Radiating panel	m_r (kg/m^2)	0.765	4.81	9.75	0.765	0.765	0.765	0.765	0.765	0.765
	B_r (Nm)	33.6	33.6	33.6	6.72	168	33.6	33.6	33.6	33.6
	E_r (Pa)	$15{\cdot}10^9$	$71{\cdot}10^9$	$210{\cdot}10^9$	-	-	$15{\cdot}10^9$	$15{\cdot}10^9$	$15{\cdot}10^9$	$15{\cdot}10^9$
	ρ_r (kg/m^3)	255	2720	7800	-	-	255	255	255	255
	h_r (m)	0.003	0.00177	0.00125	-	-	0.003	0.003	0.003	0.003

Also the effect of different bending stiffness of the radiating panel have been investigated, while keeping the surface density constant, as indicated by sets (a), (d) and (e) in Figure 9. The remaining parameters that have been varied are the air gap thickness and the stiffness of the four elastic mounts. The column which contains the parameters related to the reference case is highlighted in green. Table 2 gives the parameters that have been kept constant in all simulations.

Table 2: Values of the fixed parameters

Radiating panel	Air properties			Source panel						Elastic mounts
η_r	ρ_{air} (kg/m^3)	c_0 (m/s)	η_{air}	m_s (kg/m^2)	B_s (Nm)	E_s (Pa)	ρ_s (kg/m^3)	h_s (m)	η_s	η_m
0.03	1.19	343	0.1	2.72	5.9167	$71\cdot10^9$	2720	0.001	0.02	0.05

2.3.1 Effects of the radiating panel surface density

The effects of the radiating panel surface density are analysed considering the designs (a), (b) and (c) indicated in Figure 9. The three designs have the same radiating panel stiffness, but different surface densities as listed in Table 1. The cavity depth for all the simulations was 30 mm. The source panel kinetic energy and the radiating panel kinetic energy per unit amplitude of the incident wave (Equations (54,55)), and the sound transmission ratio are shown in Figure 10 against the frequency. The sound transmission ratio is calculated as the ratio of radiated sound power to incident sound power so that:

$$T = \frac{W_r}{W_i}, \tag{59}$$

where $W_r(\omega)$ is the radiating sound power, determined according to Equation (58). The sound power of the incident plane wave can be calculated using the following expression[53]:

$$W_i = \left|P^2\right| \frac{l_x l_y}{2\rho c} \cos\theta \quad , \tag{60}$$

where P is the acoustical pressure of the incident wave (Equation (19)) which is P=1 Pa throughout this thesis.

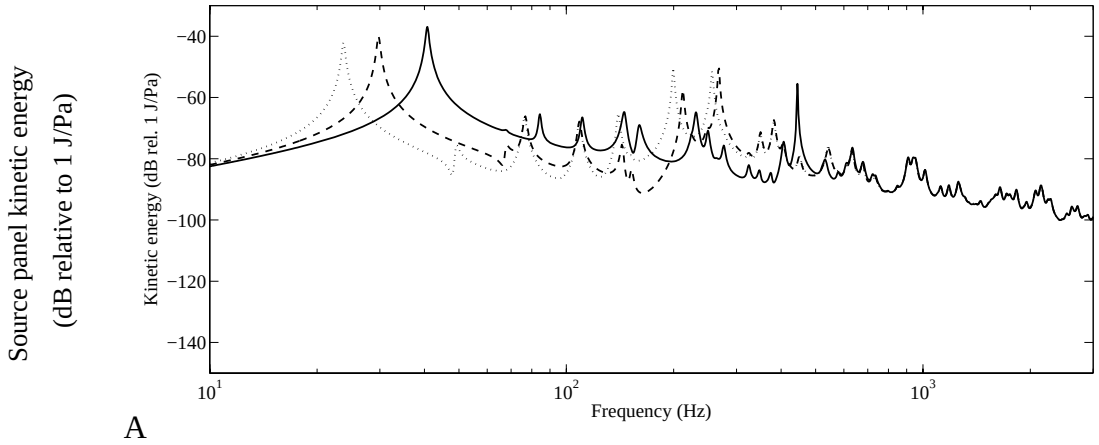

A

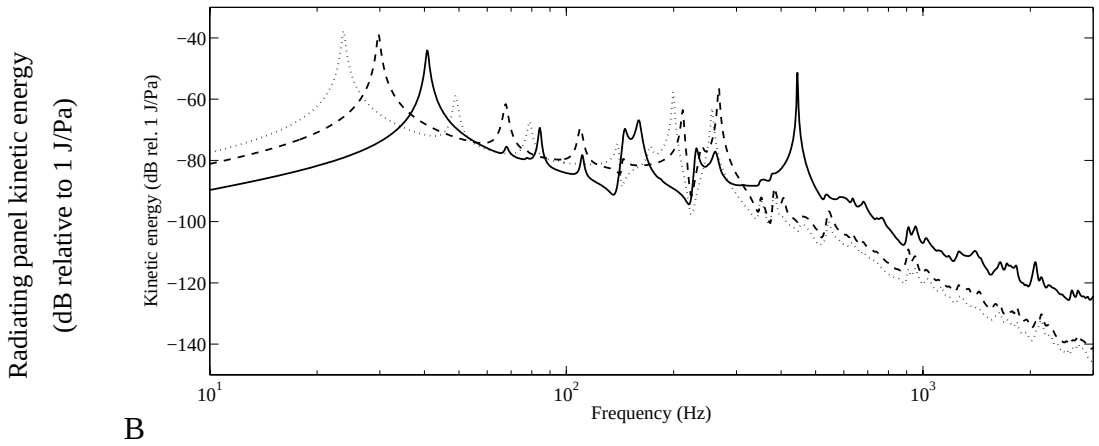

B

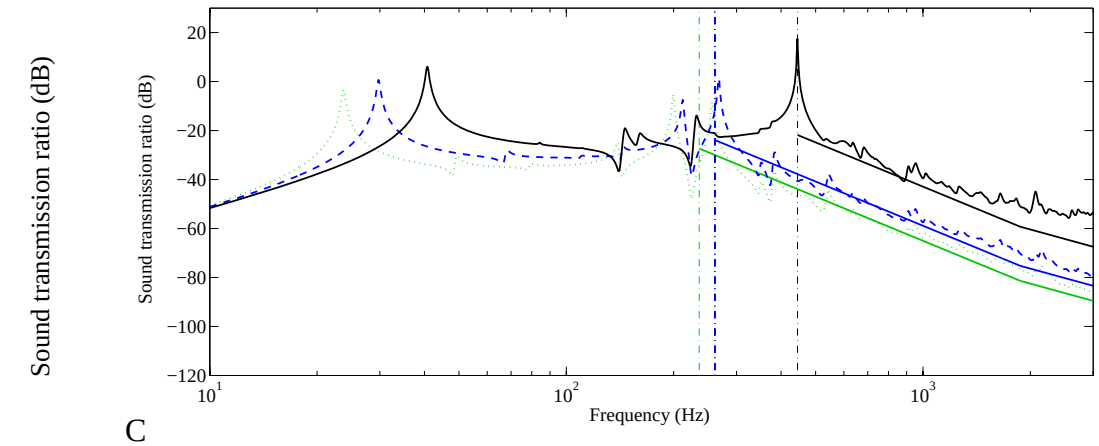

C

Figure 10: Effects of the variation of the radiating panel surface density. The top plot shows the source panel kinetic energy, the middle plot shows the radiating panel kinetic energy, and the bottom plot shows the sound power transmission ratio. Solid line is for design (a), dashed line design (b), and the dotted line design (c). The straight lines in the sound transmission plots show the predictions using Equations (61-64). Black line is for the design (a), blue line is for the design (b) and green line is for the design (c). The vertical dash dotted lines indicate mass-air-mass resonant frequencies calculated using Equation (61) for the three designs.

Considering first the system design (a) with the honeycomb radiating panel, below about 444 Hz the response and sound radiation are characterised by well separated resonances. These resonances are due to the coupled response of the two panels via the four mounts and the air in the cavity. The cavity air acts as an additional distributed relative spring since the first cavity resonance occurs at about 415 Hz. Therefore these modes are characterised by a plate-spring-plate type of coupled mode where the source plate is typified by volumetric flexural deformations with shape similar to the (1,1), (2,1), (1,2) modes of a simply supported plate and the radiating plate is characterised by rigid body volumetric deformations similar to a) the (0,0) even mode, b) the (1,0) and (0,1) beam-type modes and c) (1,1), (2,1), (1,2) flexible modes of a freely suspended plate. Plots A and B in Figure 11 depict deflection shapes at the first and fifth resonant frequency, respectively.

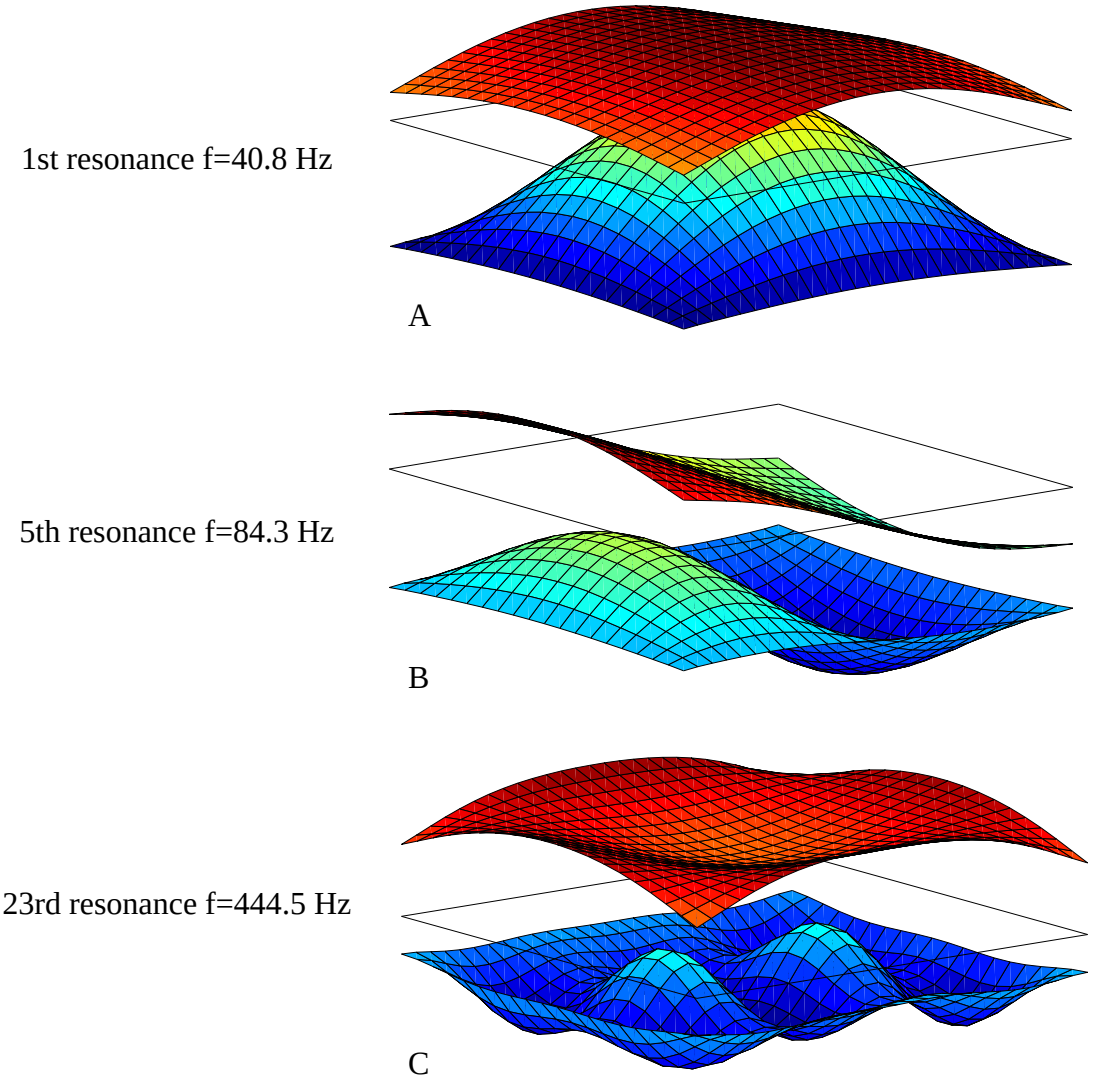

Figure 11: Scaled deflection shapes at three different resonant frequencies.

Note that the two plates move in phase since they are strongly coupled by the stiff air spring which forces the radiating plate to undergo motion similar to that of the source panel.

The kinetic energy plots (A and B) in Figure 10 are characterised by more resonances than the sound transmission ratio plot (C). This is due to the fact that the modes with small volumetric component, (i.e. even-even, odd-even, or even-odd modes, such as for example the fifth mode (plot B in Figure 11), have smaller radiation efficiency than the odd-odd modes. In any case these resonances have small amplitudes since the air coupling between the two panels is also weakened when non-volumetric modes are involved. At 444 Hz there is a strong resonance noticeable in all the plots in Figure 10. This resonance is usually referred to as the mass-air-mass type resonance[22], and the deflection shape is characterised by out of phase motion of the two plates (plot C in Figure 11). Since for design (a) the first cavity resonance occurs at 415 Hz, the cavity mode interferes with the shape of the mass-air mass-mode. At frequencies above the mass-air-mass resonance the response is characterised by the typical mass-law[22] with an initial descend of the sound radiation of 18 dB per octave band. Also, the modal density is much bigger since, together with the modes controlled by the two plates there are also modes controlled by the cavity. Thus, the rising modal overlap effect and the increasing damping action on the two panels smoothes out the spectra of the response and sound radiation which no longer shows well separated, lightly damped resonance peaks.

According to the simplified model given by Fahy and Gardonio[22] the mass-air-mass resonant frequency for unbounded plates depends upon the surface densities of the two plates, and the stiffness of the air, where the latter is determined by the depth of the cavity, by the air density and speed of sound:

$$\omega_0 = \left[\left(\frac{\rho_{air} {c_0}^2}{l_z} \right) \left(\frac{m_1 + m_2}{m_1 \cdot m_2} \right) \right]^{0.5}, \tag{61}$$

where l_z is the distance between the two plates, ρ_{air} is the mass density of air, c_0 is the speed of sound., while m_1 and m_2 are surface densities (kg/m^2) of the source and the

radiating panel respectively. For example, the natural frequency of the mass-air-mass resonant mode calculated using Equation (61) is equal to 423 Hz, while the simulated value equals to 444Hz. The simulated value can be considered as in a good correspondence with theory, taking into account the fact that Equation (61) is valid for unbounded plates, coupled only by the air between them.

Above the mass-air-mass resonance, the sound transmission ratio is mass controlled, so that the minima of the sound transmission ratio for this frequency range can be approximated using the following expression[22]:

$$T = -20\log\left[\frac{(m_1 + m_2)\omega}{2\pi}\right] - 40\log\frac{\omega}{\omega_0} + 42, \tag{62}$$

which is valid up to a critical frequency[22] :

$$\omega_c = \frac{10^{-1.8} \cdot \rho_{air} \cdot {c_0}^2}{2\pi d}. \tag{63}$$

Above the critical frequency ω_c the theoretical minima of the sound transmission ratio descend with rate of 12 dB per octave band, following the equation[22]:

$$\mathrm{T} = -20\log\left(\frac{m_1 \cdot \omega}{2\pi}\right) - 20\log\left(\frac{m_2 \cdot \omega}{2\pi}\right) + 78. \tag{64}$$

Considering now the simulations using aluminium and steel radiating panels, with the same bending stiffnesses but increased surface density, the sound transmission plot C and the kinetic energy plots A and B show a clear reduction of resonant frequencies of double panel modes, as the surface density is increased. The mean value of the sound transmission ratio goes down as the density per unit surface goes up. This phenomenon shows a marked mass effect, because it affects both the coupled response of the double panel as well as the sound radiation by the radiating panel. The predictions using formulae (61,64) are shown on the sound transmission ratio plot (C) using coloured

lines. Considering the mass variation effect of the radiating plate, there is a good agreement between the simulated and predicted sound transmission ratio trends.

2.3.2 Effects of the radiating panel bending stiffness

The effects of the radiating panel stiffness are analysed considering designs (a), (d) and (e) indicated in Figure 9, which have the same radiating panel density per unit area, but different bending stiffnesses as listed in Table 1. The cavity depth for all the simulations was 30 mm. The source panel kinetic energy, the radiating panel kinetic energy and the sound transmission ratio are shown in Figure 12 against the frequency for the three cases.

Considering all the system designs (d), (e), and (a), below about 440 Hz the response and sound radiation are characterised by well separated resonances just as observed in the previous subsection. The response and sound transmission ratio is also characterised by the mass law at the frequencies above about 440 Hz (the mass-air-mass mode). In fact, the natural frequency of this mode does not change with stiffness of the radiating plate, as one might expect, because the mode is mainly determined by out of phase motion of the two plates coupled by the air spring. At frequencies above the mass-air-mass resonance, where the response is mass controlled, the sound transmission ratio seems to be higher for stiffer radiating panels.

Clear changes in the sound transmission ratio and kinetic energies occur at lower frequencies, for example, below the first resonance of the coupled system (approx. 40 Hz), where the response is stiffness controlled. The natural frequency of the first mode tends to go down as the stiffness of the radiating plate is reduced. Similar behaviour occurs for all the resonant frequencies below the mass-air-mass resonance. The sound transmission ratio in the whole frequency band tends to descend when reducing the radiating plate stiffness.

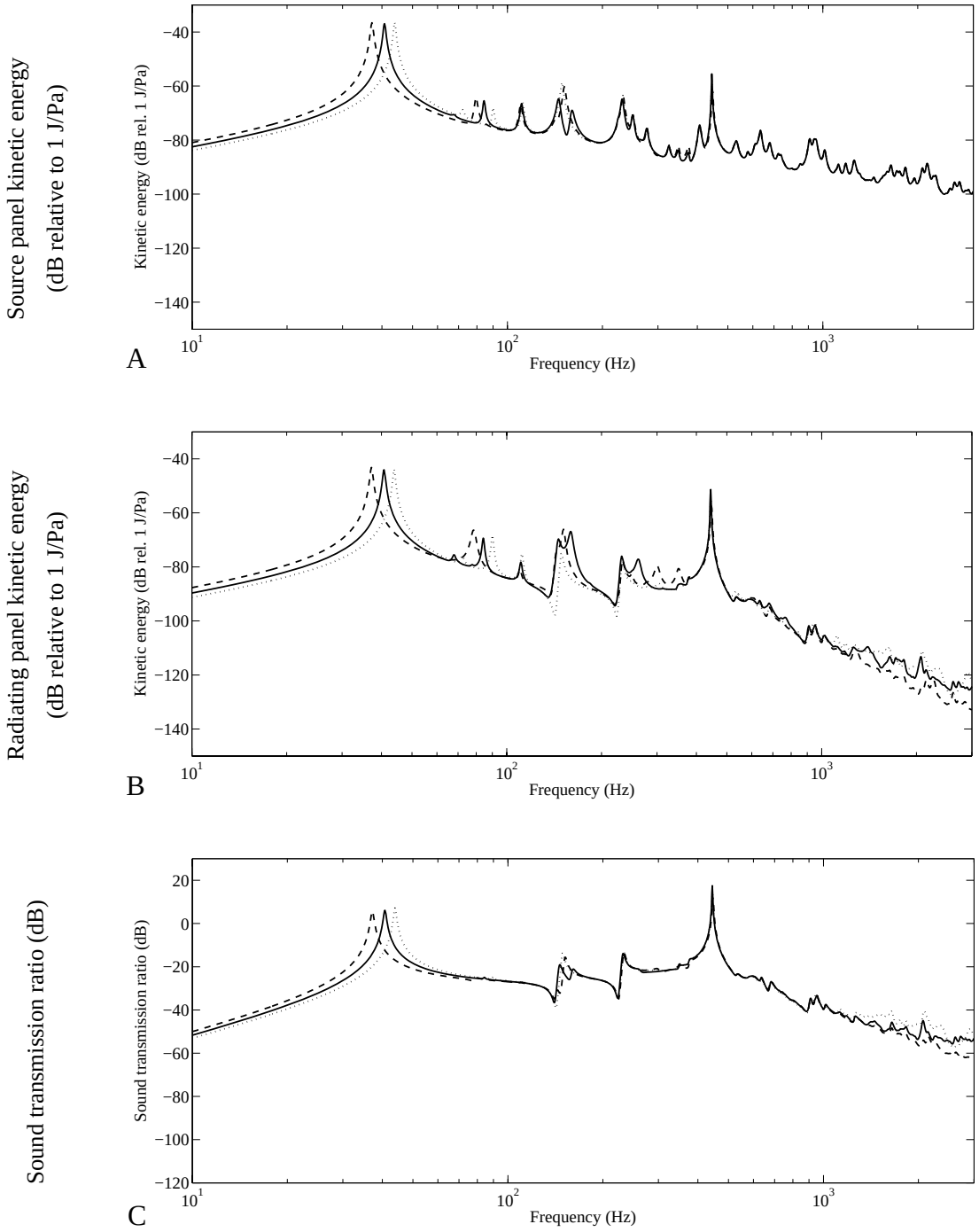

Figure 12: Effects of the variation of the radiating panel bending stiffness. The top plot shows the source panel kinetic energy, the middle plot shows the radiating panel kinetic energy, and the bottom plot shows the sound power transmission ratio. Solid line indicates the design (a), dashed line design (d), and the dotted line design (e) (Table 1).

2.3.3 Effects of the cavity depth

The effect of cavity depth is shown in Figure 13 for distances depths of 20, 30 and 40 mm. The stiffness of the mounts as well as other double panel parameters have been kept constant, as listed in Table 1, designs (f) and (g). Both total kinetic energy and sound transmission ratio plots show little variation below the mass-air-mass resonant frequency as the air gap is increased. The principal variation occurs at the mass-air-mass resonance which decreases from 444 Hz to 400 Hz as the cavity depth increases. This is because the air stiffness becomes smaller as the gap between the two panels increases. This cavity depth effect is in agreement with Equation (61).

The low frequency response, for example near the first resonant frequency of the double panel, remains almost unaltered by the variation in the depth of the air cavity. This is because at such low frequencies the air in the cavity is controlled by the (0,0,0) volumetric mode which behaves as a stiff distributed spring. As a result the modal stiffness of the 40 Hz mode remains unaltered with variations of the air gap. The modal mass is barely affected by an increased mass of the cavity air (as the cavity depth increases) due to the relatively low air mass density. The basic simulation trends are in agreement with predictions based on Equation (61-64), as shown on the sound transmission ratio plots by straight lines.

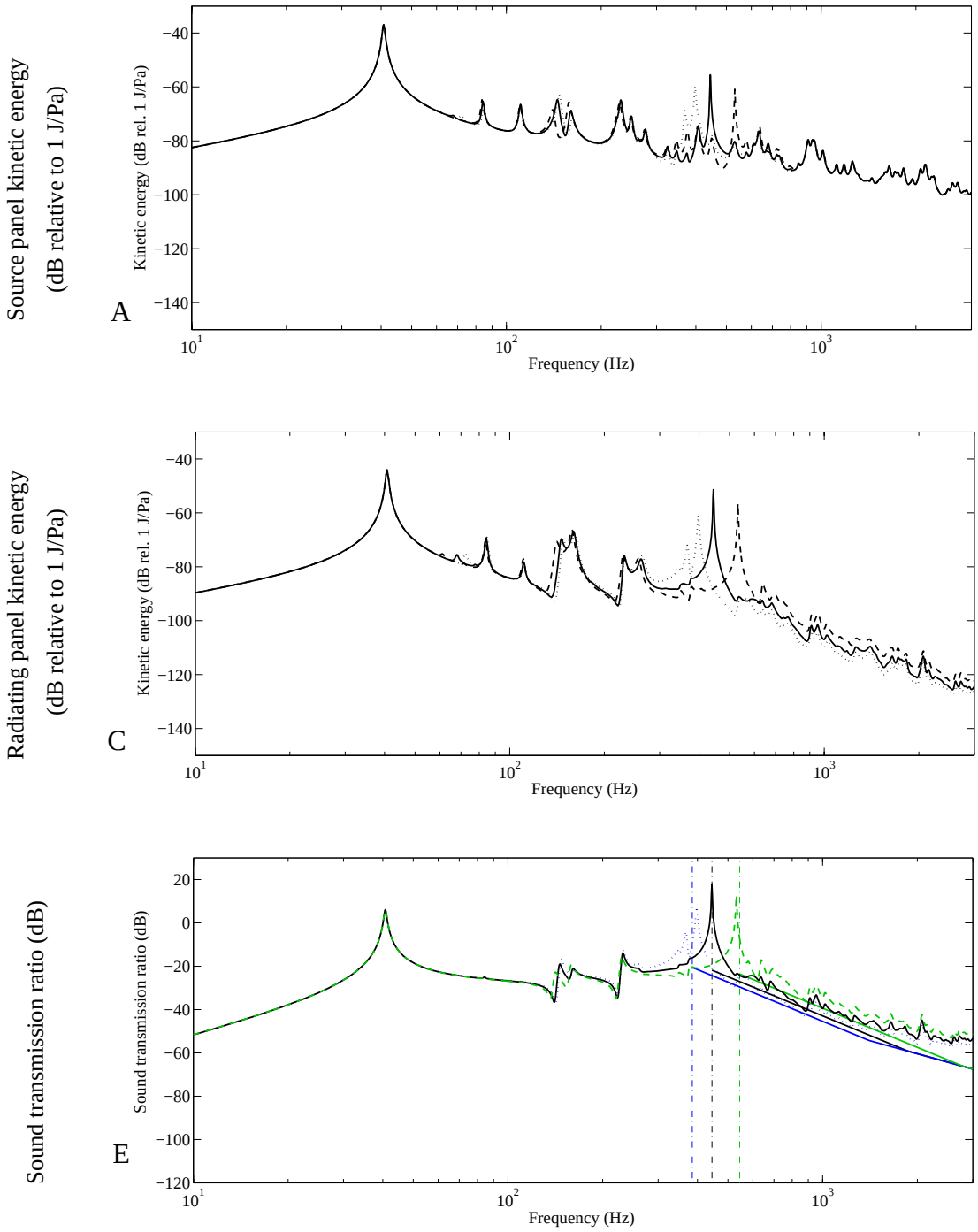

Figure 13: Effects of the variation of the depth of the air cavity between the two panels. The top plot shows the source panel kinetic energy, the middle plot shows the radiating panel kinetic energy, and the bottom plot shows the sound power transmission ratio. Solid line indicates the design (a), dashed line design (f), and the dotted line design (g). The straight lines in the sound transmission plots show the predictions using Equations (61-64). Black line is for the design (a), green line is for the design (f) and blue line is for the design (g). The vertical dash dotted lines indicate mass-air-mass resonant frequencies calculated using Equation (61) for the three designs.

2.3.4 Effects of the stiffness of the mounting system

The elastic mount stiffness effect is introduced in Figure 14 by showing the panel deflection shapes at 36 Hz, which is slightly below the first resonant frequency (40 Hz). Considering first the top plot (the case with no springs), the source panel vibrates like a (1,1) mode of a simply supported plate while the radiating panel vibrates as a (0,0) translational rigid body mode of a free plate.

Design (a)

(no mounts)

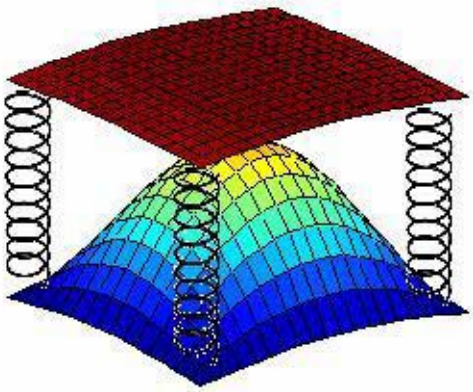

Design (h)

(Standard mounts)

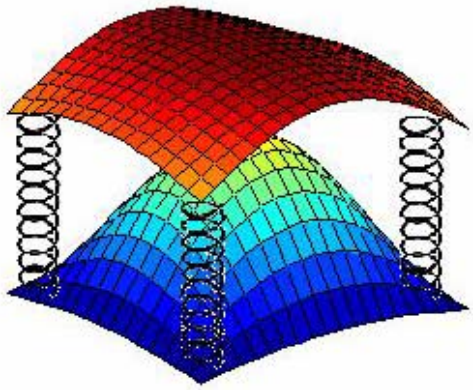

Design (i)

(Stiff mounts)

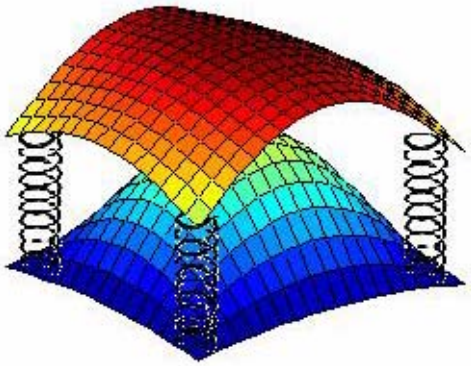

Figure 14: Effect of increasing of elastic mounts stiffness on the source and radiating panel deflection shape at frequency of 36 Hz; for designs (a) k=0 N/m, (h) k=5891 N/m, and (i) k=58910 N/m

When the stiffness of the four mounts is increased so that it becomes comparable or exceeds the bending stiffness of the radiating panel, the deflection shape of the radiating panel gradually changes towards the (1,1) mode of a panel pinned at the four corners. Also the natural frequencies of the modes tend to shift to the natural frequencies of the modes that correspond to the new boundary condition, (Figure 15, dotted lines).

In general the spectra of the radiating panel total kinetic energy and the sound transmission ratio show little variation as the stiffness of the four mounts are increased. The most important effect corresponds to the first system resonance at about 40Hz which, as shown in Figure 15, tends to rise as the stiffness of the mounting system increases. This is due to the fact that, for soft mounts, the volumetric displacement of the source panel is absorbed by the rigid body motion of the radiating panel and the stiffness effect is controlled by the source panel and mounts' stiffnesses only. In contrast, when stiff mounts are used, the volumetric displacement of the source panel is absorbed by the (1,1) flexural mode of the radiating panel so that there is an effective increase in modal stiffness.

The mass-air-mass resonant frequency is affected slightly by the mount elastic constant variation. The air stiffness effect is much more important and the modal stiffness contributed by the mounts is relatively small.

The kinetic energy of the radiating plate and the sound transmission ratio (plots B and C) at the mass-air mass resonance are affected by the stiffness of the mounts. This is due to the fact that more rigid mounts, located close to the simply supported boundary of the source panel, constrain the vibration of the radiating panel, especially its rigid body motion.

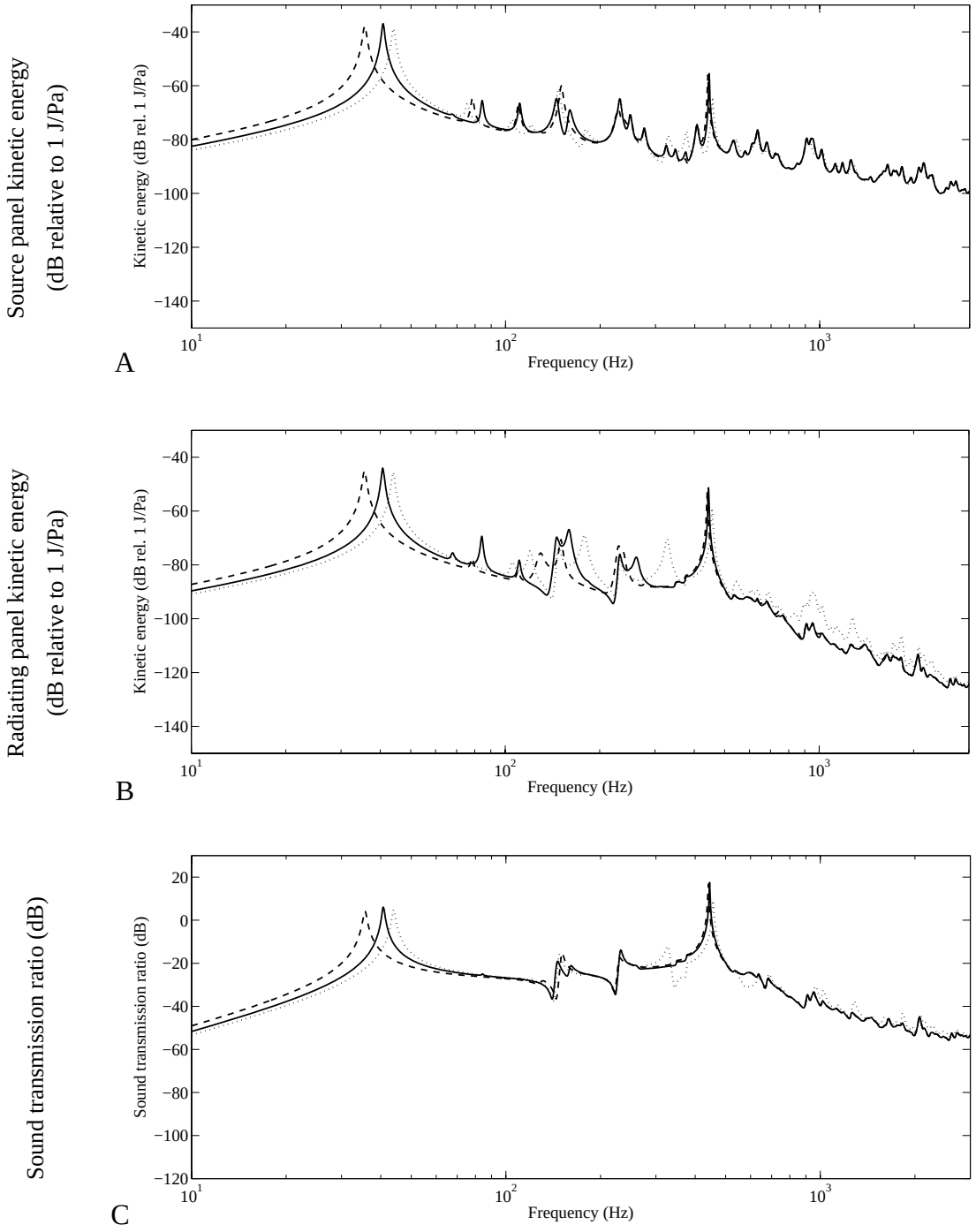

Figure 15: Effects of the variation of the mounting system elastic constant. The top plot shows the source panel kinetic energy, the middle plot shows the radiating panel kinetic energy, and the bottom plot shows the sound power transmission ratio. Solid line indicates the design (a), dashed line design (h), and the dotted line design (i).

2.4 Summary

In Chapter 2 the double panel model problem is described. A mathematical model for the theoretical analysis of the passive and active sound transmission through the double panel model is formulated. The mathematical model is based on the mobility and impedance matrix method which counts for acoustically and structurally fully coupled double panels.

A parametric study of passive sound transmission is then performed using the formulated mathematical model. The mass and stiffness of the radiating panel, the depth of the air cavity between the source and the radiating panel and the stiffness of structural mounts were varied. The effects of the variation of each parameter on the sound transmission and the response of the double panel were analysed.

The passive sound transmission through double panels was characterised by a mass-air-mass resonance effect. Below the mass-air-mass resonance effect, the sound transmission ratio was rather high and is governed by well-separated resonances. In contrast, above the mass-air-mass resonance the sound transmission ratio was governed by the mass law, such that it rolls-off quickly with increasing frequency. The mass-air-mass resonant frequency can therefore be considered as a cut-off point between the low frequency range with high sound transmission ratios, and the high-frequency range where the passive sound insulation properties of double panels are enhanced. The mass-air-mass resonant frequency was found to be sensitive to the variations of the radiating panel surface density and the depth of the air cavity between the two panels. The variation of the radiating panel and mount stiffness caused the low frequency resonances of the double panel to shift.

The rather high low frequency sound transmission below the mass-air-mass resonance is a motivation for the analysis in the next chapter. In order to reduce the resonant low frequency sound transmission, decentralised velocity feedback control systems which apply active damping are considered next.

3 Decentralised absolute and relative velocity feedback control

The results of the parametric study in the previous chapter indicated high sound transmission ratio and kinetic energy of the radiating plate in low frequency bands, up to a characteristic cut-off frequency (the mass-air-mass resonant frequency). This behaviour has been observed for all designs (Table 1), including the reference case (the design (a) in Table 1), which suggests that the low frequency noise transmission can be a major problem for double panels excited by broadband disturbances. This is indeed the case with aircraft which are inevitably excited by a turbulent boundary layer (TBL) excitation, among other noise sources. As mentioned in the introductory chapter, this sort of excitation is broadband and has random characteristics. The facts that low frequency noise is efficiently transmitted through the double panel and that the source panel is excited be the TBL, make feedback active control an attractive alternative to passive methods. Moreover the simulation results in Chapter 3 indicated that the sound transmission ratio is characterised by well separated low frequency resonances. If active damping systems are used then the low frequency resonant response (and the resonant transmission of sound) could be reduced. In addition, a decentralised system could provide the necessary robustness and simplicity. Therefore this chapter is dedicated to the implementation of decentralised velocity feedback strategies. Four velocity feedback approaches are analysed within the study presented in the following chapter. First, the active control is applied on the radiating panel only, using skyhook force actuators with collocated ideal velocity sensors on the radiating panel. Second, the control of the source panel applied using skyhook actuators and ideal velocity sensors. Then a simultaneous control of the source and the radiating panels are considered. Finally, a feedback control that uses reactive actuators which are attached between the two panels, fed with relative radiating/source velocity signals is analysed.

3.1 Feedback control laws

Direct velocity feedback control, implemented using Multiple-Input-Multiple-Output (MIMO) decentralised loops, is considered in this chapter. The velocity sensors and force actuators are collocated, which guarantees unconditional stability of the feedback

loops, if ideal sensors and actuators are assumed[62,63,64]. A direct velocity feedback control scheme is depicted in Figure 16, which is unconditionally stable for passive plant response $\mathbf{T}_{cc}(\omega)$, and a passive controller $\mathbf{H}(\omega)$.

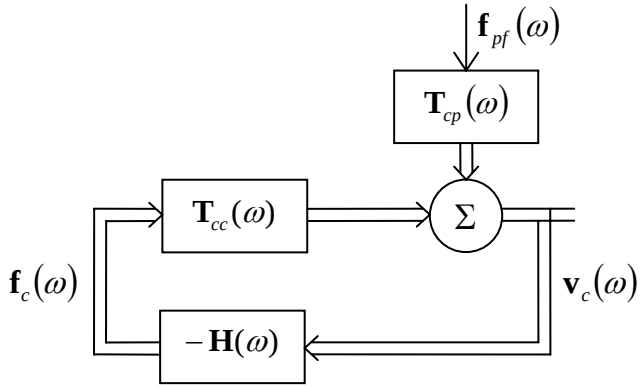

Figure 16: Direct velocity feedback systems

Four control arrangements are investigated in this chapter. The first two consist of a 4x4 array of decentralised velocity feedback control systems using collocated velocity sensors and idealised skyhook force actuators on the source and radiating panels. The third arrangement applies a 16 channel MIMO system on the two panels. The fourth control system considers reactive actuators between the two panels, while the error signal is the relative velocity between the two panels at the control locations.

Radiating panel DVFB	Source panel DVFB	Source and radiating panel DVFB	Relative source/radiating DVFB
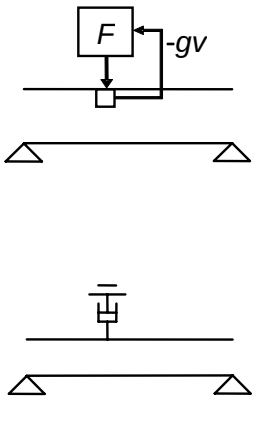	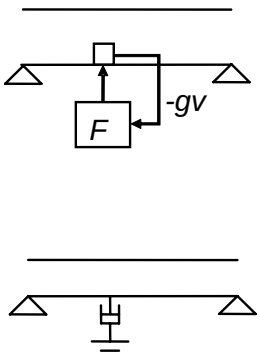	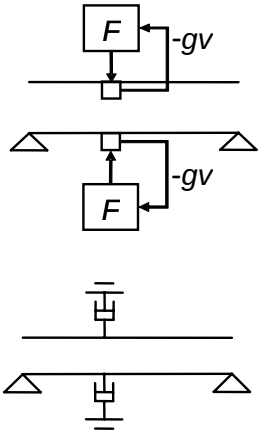	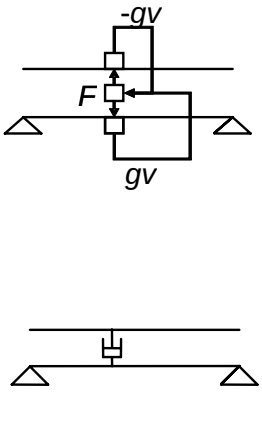
Skyhook actuators			Reactive actuators

Figure 17: Feedback arrangements

Figure 17 schematically shows the four feedback arrangements studied in this chapter. Simulations for each control approach have been performed up to 3 kHz with different feedback gain levels. The material properties of the radiating panel correspond to design (a) in Table 1.

3.2 Radiating panel direct velocity feedback using skyhook forces

In order to implement a MIMO direct velocity feedback on the radiating panel, using skyhook forces, the matrix **H** in Equation (50) is formed so as to fill only the last sixteen spaces of its diagonal, which relates the radiating panels velocities at the control locations to the radiating panel control forces by means of a scalar feedback gain *g*. All other elements of this 32×32 matrix are equal to zero as indicated in Equation (65):

$$\mathbf{H} = \begin{bmatrix} 0 & 0 & \cdots & & & \cdots & 0 \\ 0 & 0 & \cdots & & & \cdots & 0 \\ \vdots & \vdots & \ddots & & & & \vdots \\ & & & 0 & & & \\ & & & & g & & \\ & & & \vdots & & g & \\ \vdots & \vdots & & & & \ddots & \vdots \\ 0 & 0 & \cdots & & & \cdots & g \end{bmatrix}. \tag{65}$$

In this way ideal skyhook dampers are modelled with the mobility matrix model presented in Chapter 2. The simulation results are depicted in Figure 18 using three different feedback gain values. The figures follow a standard layout presented earlier in this thesis: from top to the bottom Figure 18 shows the kinetic energy of the source panel, the kinetic energy of the radiating panel, and the sound transmission ratio. The four curves plotted represent responses of the system with increasing control gains. As the control gains are increased the active damping action rises so that, as shown by the dashed lines, the response of the radiating panel, and thus the sound radiation, tend to decrease at radiating panel low-order resonance frequencies. However, when very large control gains are used, the radiating panel tends to be pinned[53] at the control position by

the skyhook dampers resulting in very large reductions of radiating panel kinetic energy and sound transmission ratio.

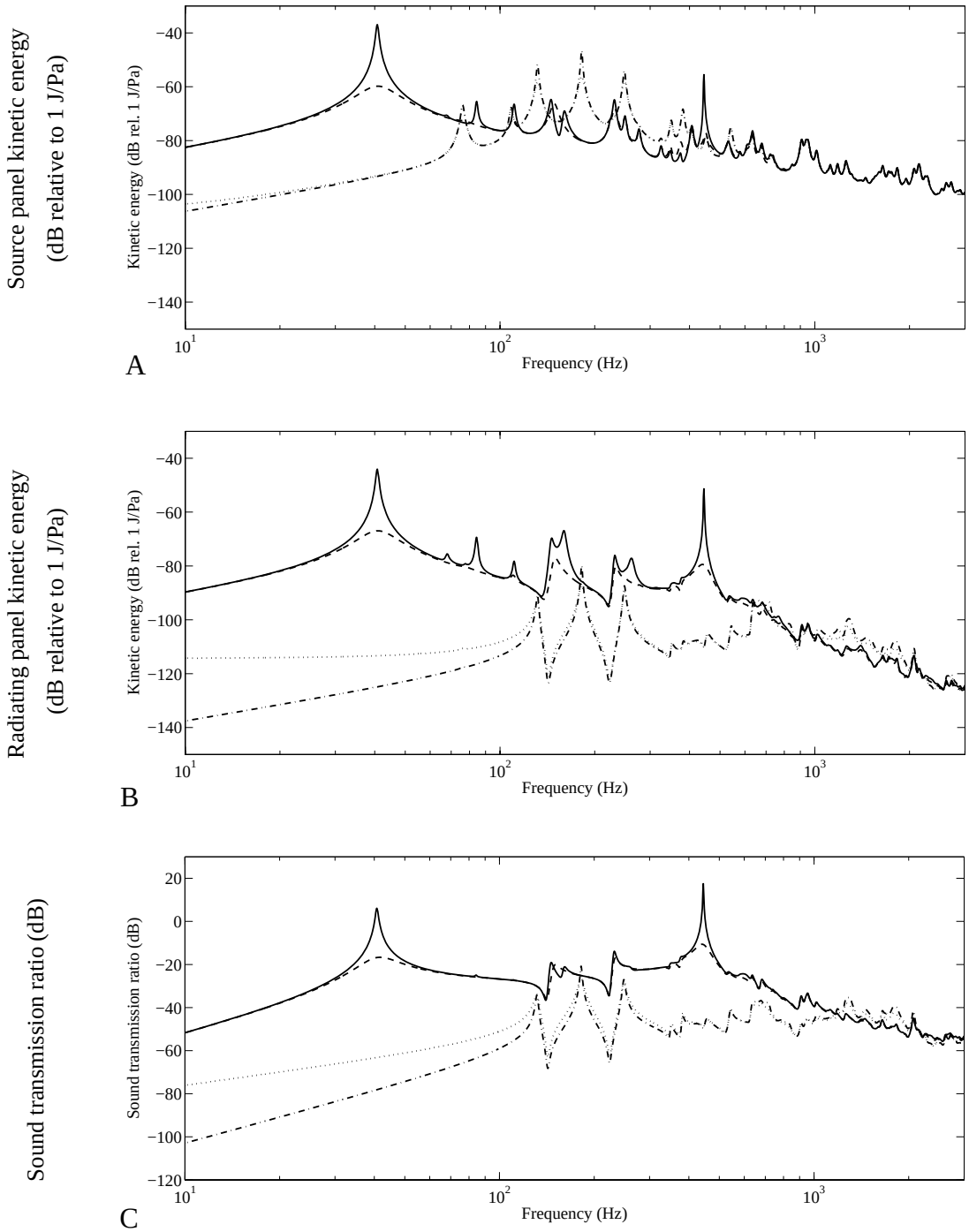

Figure 18: Radiating panel direct velocity feedback using skyhook forces. The top plot shows the source panel kinetic energy, the middle plot shows the radiating panel kinetic energy, and the bottom plot shows the sound power transmission ratio. Solid line – no control, dashed – low feedback gains, dotted – intermediate feedback gains, dash-dotted – high feedback gains.

It must be emphasised that these results are valid provided the feedback control system is stable. This is indeed the case when collocated velocity sensors and ideal skyhook force actuators are used. When more practical actuators such as piezoelectric strain actuators, or electro-dynamic actuators that react against a proof mass or against the source panel, are used then stability is an open issue which may prevent the implementation of those feedback control gains which are necessary to get high reductions of the radiating panel kinetic energy and sound transmission ratio. A similar study[53] carried out on a single panel with a 4x4 array of decentralised velocity feedback control systems using collocated velocity sensors and point forces has shown that when very large feedback gains are implemented the pinning effect produces two consequences. First, the response of the panel is characterised by a new set of modes defined by the new pinning boundary conditions introduced by the feedback control loops. Second, the response is characterised by lightly damped resonances, since having the control positions pinned prevents the generation of active damping. Therefore new resonances of the panel occur at higher frequencies. This type of phenomenon can be seen in Figure 18 (plots B and C) where the new resonances of the radiating panel occur above approximately 1 kHz. In other words, the broadband sound transmission of the panel is increased for very high feedback gains, as will be demonstrated in Section 3.6.

3.3 Source panel direct velocity feedback using skyhook forces

In order to implement MIMO direct velocity feedback on the source panel only, using skyhook forces, the matrix **H** in Equation (50) is formed so as to fill only the first sixteen spaces of its diagonal, which relates the source panel velocities at the control locations and the source panel control forces by means of a scalar feedback gain *g*. All other elements of this 32×32 matrix are equal to zeros as indicated in Equation (66):

$$\mathbf{H} = \begin{bmatrix} g & 0 & 0 & \cdots & & & \cdots & 0 \\ 0 & g & 0 & \cdots & & & \cdots & 0 \\ 0 & 0 & \ddots & & & & & \vdots \\ \vdots & \vdots & & g & & & & \\ & & & & 0 & & & \\ & & & & & 0 & & \\ \vdots & \vdots & & & & & \ddots & \vdots \\ 0 & 0 & \cdots & & & & \cdots & 0 \end{bmatrix}. \tag{66}$$

In this way ideal skyhook dampers are modelled with the mobility matrix model presented in Section 2.2.

The simulation results are depicted in Figure 19 using three different feedback gains. From top to the bottom Figure 19 shows the kinetic energy of the source panel, the kinetic energy of the radiating panel, and the sound transmission ratio. Also in this case, when the control gains are raised from zero, the response of the radiating panel and the sound transmission decrease at the low frequency resonances. However, for very large control gains, although very large reductions are achieved at the first few resonance frequencies, the new lightly damped resonances become prominent (plots B and C). Active damping of the source panel does not reduce the sound radiation near the mass-air-mass resonance (plots B and C), since the radiating panel is free to vibrate independently of the highly constrained source panel.

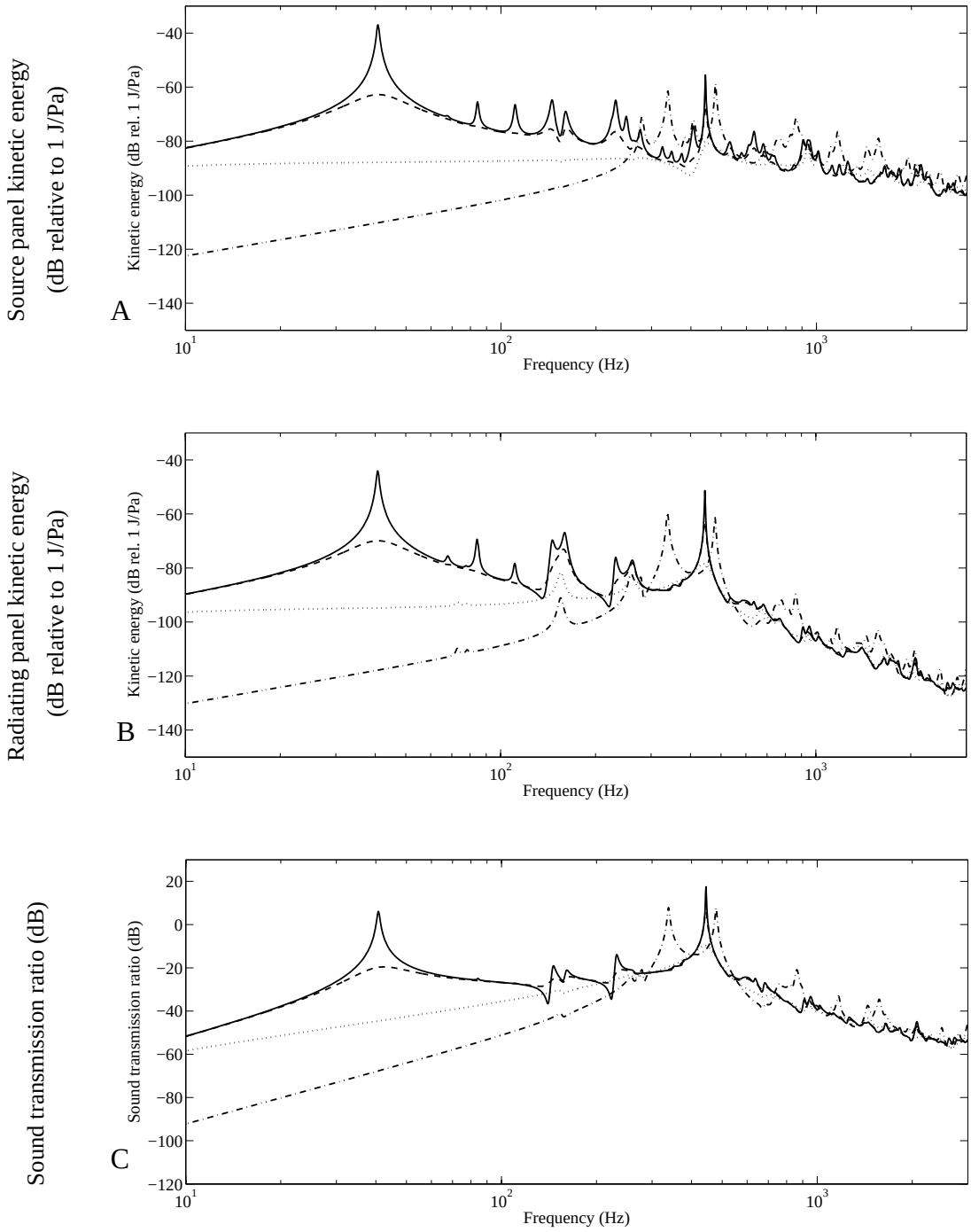

Figure 19: Source panel direct velocity feedback using skyhook forces. The top plot shows the source panel kinetic energy, the middle plot shows the radiating panel kinetic energy, and the bottom plot shows the sound power transmission ratio. Solid line – no control, dashed – low feedback gains, dotted – intermediate feedback gains, dash-dotted – high feedback gains.

3.4 Source and radiating panel direct velocity feedback using skyhook forces

In order to implement MIMO direct velocity feedback on the source and on the radiating panel simultaneously, using skyhook forces, the matrix **H** in Equation (50) is formed so as to fill its diagonal, which relates the radiating panels velocities at the control locations and the radiating panel control forces as well as the source panel control velocity and the source panel control forces by means of a scalar feedback gain, *g*. All other elements of this 32×32 matrix are equal to zeros as indicated in Equation (67):

$$\mathbf{H} = \begin{bmatrix} g & 0 & \cdots & & \cdots & 0 \\ 0 & g & \cdots & & \cdots & 0 \\ \vdots & \vdots & \ddots & & & \vdots \\ & & & & & \\ & & & & & \\ & & & & & \\ \vdots & \vdots & & & \ddots & \vdots \\ 0 & 0 & \cdots & & \cdots & g \end{bmatrix}. \tag{67}$$

In this way ideal skyhook dampers are modelled with the mobility matrix model presented in Section 2.2. The simulation results are depicted in Figure 20 using three different feedback gains. The plots in Figure 20 show the control effects that would result when the two control arrangements act simultaneously on the source and radiating panels. Comparing these results with those plotted for the control system acting on the radiating panel (Figure 18), it is clear that relatively larger control effects are generated when the two control systems act simultaneously. However it must be emphasised that this is actually 32 channel control in comparison to the 16 channel control of previous two arrangements. For very high feedback gains there is still a pinning effect which causes the new lightly-damped resonances above approximately 1 kHz.

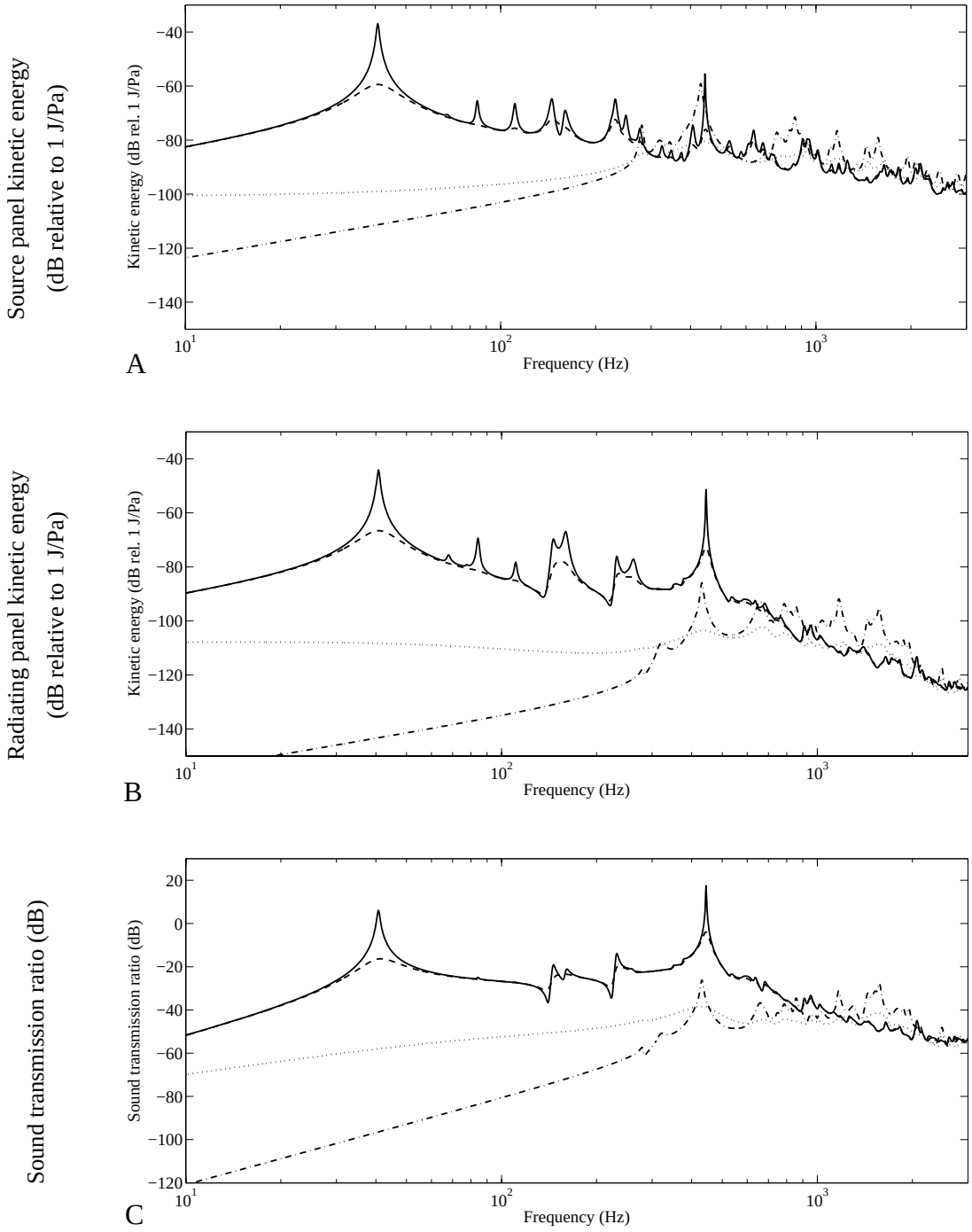

Figure 20: Source and radiating panel direct velocity feedback using skyhook forces, applied simultaneously. The top plot shows the source panel kinetic energy, the middle plot shows the radiating panel kinetic energy, and the bottom plot shows the sound power transmission ratio. Solid line – no control, dashed – low feedback gains, dotted – intermediate feedback gains, dash-dotted – high feedback gains.

3.5 Relative velocity feedback using ideal reactive actuators

In order to implement MIMO direct velocity feedback using the relative velocity of the source and radiating panel at the control locations, and reactive control actuators, the matrix **H** in Equation (50) is formed so as to fill its main diagonal by scalar gains. Furthermore, the upper and the lower sixteenth diagonals are populated by negative scalar gains so as to subtract the absolute velocities of the radiating and source panels in order to obtain the relative velocity. In this way the reactive dampers, driven by relative radiating/source panel velocity signals, are modelled using the following control matrix with the mobility matrix model presented in Section 2.2.

$$\mathbf{H} = \begin{bmatrix} g & 0 & \dots & 0 & -g & 0 & \dots & 0 \\ 0 & g & & & 0 & -g & & \\ \vdots & & \ddots & 0 & \vdots & & \ddots & \vdots \\ 0 & \dots & 0 & g & 0 & \dots & 0 & -g \\ -g & 0 & \dots & 0 & g & 0 & & 0 \\ 0 & -g & & \vdots & 0 & g & & \\ \vdots & & \ddots & 0 & & & \ddots & \vdots \\ 0 & \dots & 0 & -g & 0 & & \dots & g \end{bmatrix}. \tag{68}$$

In order to clarify this modelling strategy, the control forces that result from the gain matrix arranged this way are calculated. If Equation (68) is substituted to Equation (50), which relates the control forces with control velocities using the gain matrix **H**, the following expression is obtained:

$$\begin{Bmatrix} f_{sc1} \\ f_{sc2} \\ \vdots \\ f_{sc16} \\ f_{rc1} \\ f_{rc2} \\ \vdots \\ f_{rc16} \end{Bmatrix} = -\begin{bmatrix} g & 0 & \dots & 0 & -g & 0 & \dots & 0 \\ 0 & g & & & 0 & -g & & \\ \vdots & & \ddots & 0 & \vdots & & \ddots & \vdots \\ 0 & \dots & 0 & g & 0 & \dots & 0 & -g \\ -g & 0 & \dots & 0 & g & 0 & & 0 \\ 0 & -g & & \vdots & 0 & g & & \\ \vdots & & \ddots & 0 & & & \ddots & \vdots \\ 0 & \dots & 0 & -g & 0 & & \dots & g \end{bmatrix} \begin{Bmatrix} v_{sc1} \\ v_{sc2} \\ \vdots \\ v_{scp} \\ v_{rc1} \\ v_{rc2} \\ \vdots \\ v_{rcp} \end{Bmatrix}, \tag{69}$$

so that the elements of the control force vector are given by:

$$\begin{aligned}
f_{sc1} &= -\left(g \cdot v_{sc1} - g \cdot v_{rc1}\right) = g\left(v_{rc1} - v_{sc1}\right) \\
f_{sc2} &= -\left(g \cdot v_{sc2} - g \cdot v_{rc2}\right) = g\left(v_{rc2} - v_{sc2}\right) \\
&\vdots \\
f_{sc16} &= -\left(g \cdot v_{sc16} - g \cdot v_{rc16}\right) = g\left(v_{rc16} - v_{sc16}\right) \\
f_{rc1} &= -\left(-g \cdot v_{sc1} + g \cdot v_{rc1}\right) = -g\left(v_{rc1} - v_{sc1}\right) \\
f_{rc2} &= -\left(-g \cdot v_{sc2} + g \cdot v_{rc2}\right) = -g\left(v_{rc2} - v_{sc2}\right) \\
&\vdots \\
f_{rc16} &= -\left(-g \cdot v_{sc16} + g \cdot v_{rc16}\right) = -g\left(v_{rc16} - v_{sc16}\right)
\end{aligned} \quad . \tag{70}$$

It is clear from Equation (70) that the source panel and the radiating panel reactive control forces f_{scj} and f_{rcj} are proportional to the relative velocities $\left(v_{rcj} - v_{scj}\right)$. Also, the source panel control forces and the radiating panel control forces satisfy the equilibrium condition for the *j*-th reactive actuator:

$$f_{scj} + f_{rcj} = g\left(v_{rcj} - v_{scj}\right) - g\left(v_{rcj} - v_{scj}\right) = 0\,. \tag{71}$$

because the two (source and radiating) force components are of equal magnitude with opposite sign.

The simulation of the control performance is depicted in Figure 21 using three different feedback gains. As the control gains are raised from zero, active damping is generated so that the response at the low frequency resonances goes down. However, comparing the plots in Figure 21 to those of Figure 18 and Figure 20, the maximum control effectiveness that could be obtained is much lower. Moreover, in this case the pinning effect when very large control gains are implemented causes the two panels to move together as if they were connected by infinitely rigid studs. Therefore the original low frequency resonances are shifted up. This effect is particularly noticeable on the first resonance of the system at 40 Hz. By the implementation of the large feedback gains the double panel becomes a sort of thick and light single panel with a high stiffness-mass ratio. The next important feature is a significantly reduced response and sound

transmission at the mass-air-mass resonant frequency (plots B and C). The relative dampers seem to successfully restrict the typical out of phase motion of the two plates.

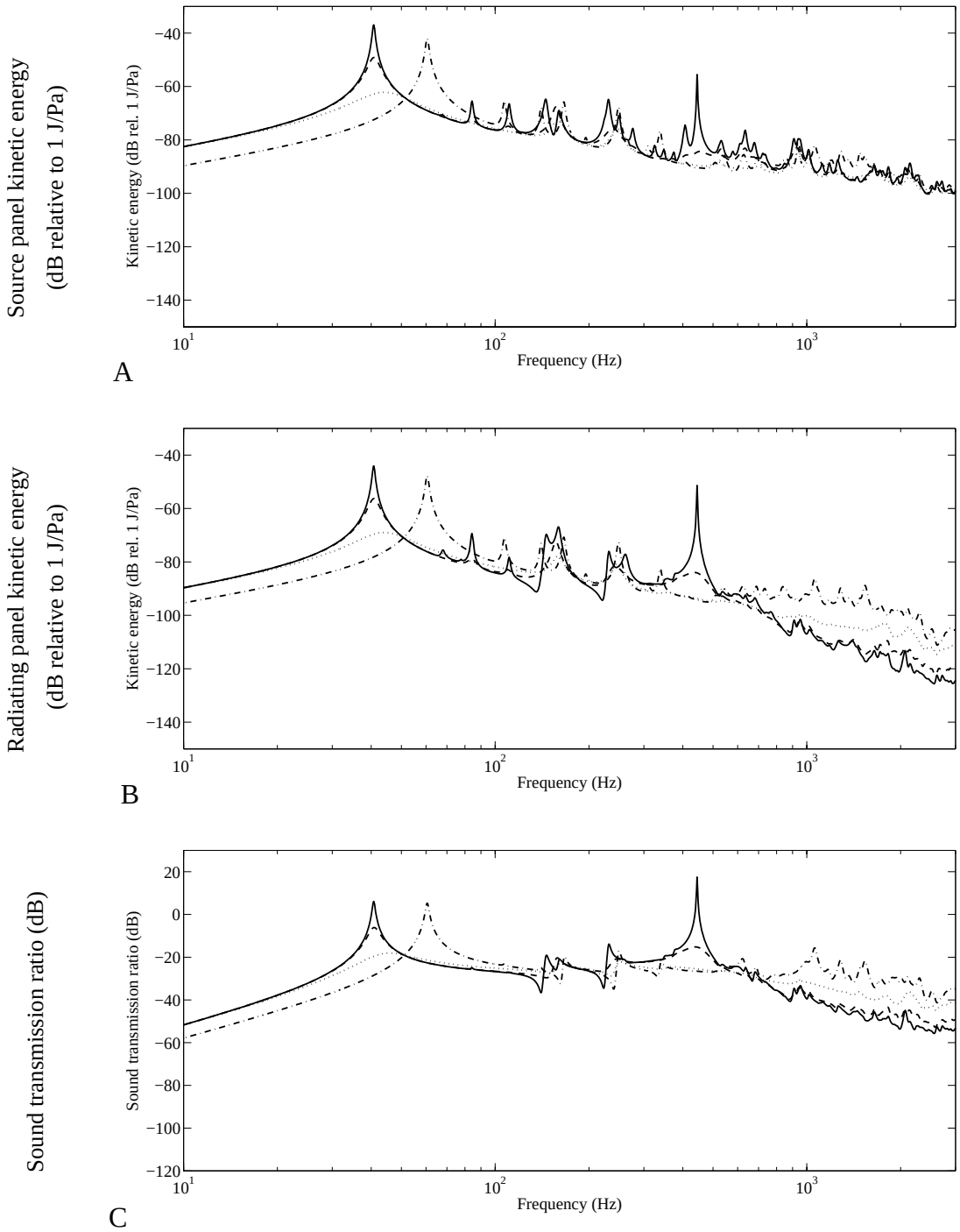

Figure 21: Relative velocity feedback using reactive control forces. The top plot shows the source panel kinetic energy, the middle plot shows the radiating panel kinetic energy, and the bottom plot shows the sound power transmission ratio. Solid line – no control, dashed – low feedback gains, dotted – intermediate feedback gains, dash-dotted – high feedback gains.

However, above the mass-air-mass resonance sound transmission is increased by the control system and the beneficial mass law that governs the passive response is compromised. This is again because of the pinning effect (the double panel under large feedback gains behaves like a single panel) due to large control forces that restrict relative motion of the two panels. Thus, the overall stiffness/mass ratio of the double panel is greatly increased. As a result, the sound transmission ratio in the mass-controlled frequency range decreases by 6 dB per octave band, which is a characteristic of single panels[22], rather the by 12 dB per octave band, which is a characteristic of double panels[22].

3.6 Frequency averaged reductions

The two plots in Figure 22 show the kinetic energy of the radiating panel (plot A) and the sound transmission ratio (plot B), integrated from 0 Hz to 3 kHz and normalised with respect to the case without control, for the four control strategies: active damping of the radiating panel (dash-dotted lines), active damping of the source panel (dashed lines), both radiating and source active damping, (dotted lines) and relative active damping (solid lines).

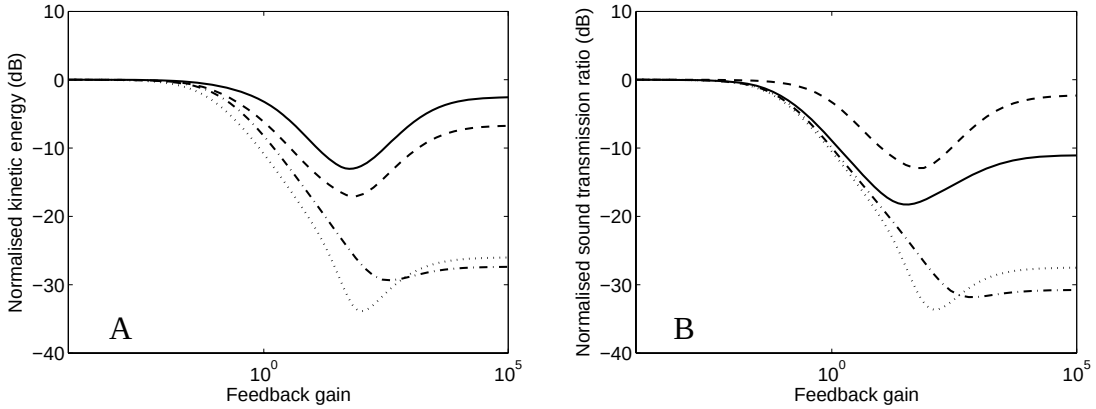

Figure 22: Normalised kinetic energy of the radiating panel (left) and sound transmission ratio (right), integrated from 0 Hz to 3 kHz, plotted against the control gain, for the four control strategies: source panel direct velocity feedback (dashed lines) with skyhook control forces, radiating panel direct velocity feedback (dash-dotted lines) with skyhook control forces, relative velocity feedback using reactive actuators (solid lines) and both source and radiating panel direct velocity feedback using skyhook control forces applied simultaneously (dotted lines).

Either the kinetic energy of the radiating panel and the sound transmission ratio monotonically decrease as the sixteen control gains are raised, so that a maximum reduction respectively of about 29 dB and 32 dB are generated for the radiating panel

active damping strategy (dash-dotted lines). For higher control gains the reduction of kinetic energy and sound transmission ratio degrades because of the pinning effect that introduces a modal response characterised by lightly damped new resonances.

The reductions for the case of source panel control (dashed lines) are much lower in comparison to those obtained with the 16 channel control system on the radiating panel. In fact, the radiating panel kinetic energy is brought down by a maximum of about 17 dB, while the sound transmission ratio goes down by only 12 dB. In this case, for very large control gains, the pinning effect on the source panel rearranges the response of the double panel in such a way that the normalised sound transmission ratio is similar to that of the non-controlled system.

The dotted lines in Figure 22 show the control effects that would be generated when the two control arrangements act simultaneously on the source and radiating panels. Comparing these results with those plotted for the control system acting on the radiating panel, it is clear that relatively larger reductions are generated when the two control systems act simultaneously. However, the dotted lines in Figure 22 indicate that the maximum reduction of the kinetic energy and the sound transmission ratio are increased only by a few dB. Thus it should be possible to achieve much larger reductions by arranging the 32 control units on the radiating panel.

In conclusion, as shown by the solid lines in Figure 22, the maximum reductions of the radiating panel normalised kinetic energy and normalised sound transmission ratio for the case of reactive actuators driven by relative velocity signals are about 15 and 18 dB. Although the reductions with skyhook control forces acting on the radiating panel are almost twice as much, the reactive actuators are a more feasible actuation solution. In contrast, the skyhook control forces can be produced in practice only if an inertial reference system is available. Alternatively, it is possible to react from a mass suspended by a spring, which however acts as the inertial reference only at frequencies above the fundamental resonance of the mass-spring system.

3.7 Summary

In Chapter 3 a theoretical analysis of four decentralised velocity feedback arrangements for the active control of the sound transmission through the double panel was presented. First, an array of skyhook actuators with idealised, collocated velocity sensors were applied for the vibroacoustic control of the radiating panel. Second, the array was applied on the source panel. Third, a sixteen channel sensor-actuator array was applied on either panel. It was found that relatively the best performance is obtained with the active control of the radiating panel, considering the number of channels of the control systems.

However, skyhook actuation is difficult to implement in practice. For that reason, the fourth decentralised velocity feedback system was considered. An array of reactive control actuators with relative radiating/source panel velocity sensors was applied between the two panels. In this case the reductions of the sound transmission ratio and the radiating panel kinetic energy were lower than the reductions obtained with skyhook active damping of the radiating panel. The reductions in the sound transmission ratio were, however, better than those obtained with the source panel active damping. In particular, the reactive actuation arrangement could be applied in practice, for example by using miniature electrodynamic actuators that react between the two panels.

Therefore the reactive actuation control arrangement is considered in the next Chapter of this thesis. Yet, in order to improve the performance of the active control with reactive actuators, a new error signal is considered in Chapter 4. Weighted source and radiating signals are used to form the error velocity signal.

4 Decentralised feedback control using reactive actuators and weighted velocity signals

This chapter is concerned with theoretical stability and performance analysis of a smart double panel with 16 weighted velocity feedback loops. The loops are applied via an array of reactive force actuators and collocated velocity sensors. The actuators are located in an air cavity between the two panels such that they can react against the two panels. Two velocity sensors per actuator are used. Either sensor is located at the source and radiating panel footprint of an actuator. The error velocity is formed by subtracting weighted sensor outputs.

The performance of the active control is first analysed in terms of the reductions of the radiating panel kinetic energy and the sound transmission ratio. Second, the stability of the feedback loops is analysed using the Nyquist criterion on the open loop sensor-actuator frequency response functions. It is shown that both the stability and performance depend on the velocity weighting factor used. In fact there are critical values of the velocity weighting factor where the stability of the loops change from unconditional to conditional. A parametric study is performed in order to understand how the critical velocity weighting factors depend upon the mechanical properties of the double panel.

4.1 Feedback configuration

An ideal reactive actuator (neglecting actuator electro-dynamical and mechanical response) is dual and collocated with an ideal relative velocity sensor (neglecting sensor electro-dynamical and mechanical response). This guarantees unconditional stability of the direct velocity feedback loop. Therefore the approach described in the previous Chapter (relative velocity error signals and reactive actuators) does not need particular stability analysis as long as ideal reactive actuators with ideal velocity sensors are considered.

The reduction in the sound transmission ratio, as well as in the kinetic energy of the radiating plate were, however, much less than the reductions obtained using, for example, the skyhook actuators acting on the radiating plate. For this reason different control laws are discussed in this Chapter.

In order to improve the performance of the MIMO direct velocity feedback loops using a reactive actuation scheme, the velocities that are collected from the radiating and the source panel sensors are weighted by a factor, as shown in Equation (72), so that:

$$v_E = v_{rc}(1-\alpha) - v_{sc}\alpha\,, \tag{72}$$

where v_E is the error signal, which is amplified and fed back to the reactive actuator, v_{rc} and v_{sc} are the velocities measured on the radiating and source panel for one of the decentralised control systems, and α is the velocity weighting factor.

If α =0, the error signals are formed purely from the radiating panel velocities at the control locations. In contrast, if α =1, the error signals are formed purely from the source panel velocities. If α =0.5, the error signals are then proportional to the relative velocity of the panels at the control locations. By changing the weighting factor from zero to one it is possible to smoothly transform the error signal from a pure radiating panel velocity, passing by the relative radiating/source velocity towards a pure source panel velocity.

A single actuator produces a reactive force designated as f_c (control force) which is applied to the radiating panel, $f_{rc} = f_c$, and to the source panel, $f_{sc} = -f_c$, (Figure 23). The minus sign before f_c comes from the equilibrium condition which requires that $f_{rc} = -f_{sc}$, and from the fact that positive *z*-axis is directed from the source towards the radiating plate. Due to the acoustical/structural coupling of the panels, each of the control force components, f_{rc} and f_{sc}, contributes to the motion of each panel at both (source and radiating) control locations. For example, as shown in the block diagram in Figure 23, radiating panel control force component f_{rc} contributes to the radiating panel

velocity at the radiating panel sensor location v_{rc} via the corresponding point mobility function $T_{cc}^{r,r}(\omega)$, but it also contributes to the source panel velocity at the sensor location (v_{sc}) via the corresponding transfer mobility function $T_{cc}^{r,s}(\omega)$ of the coupled system.

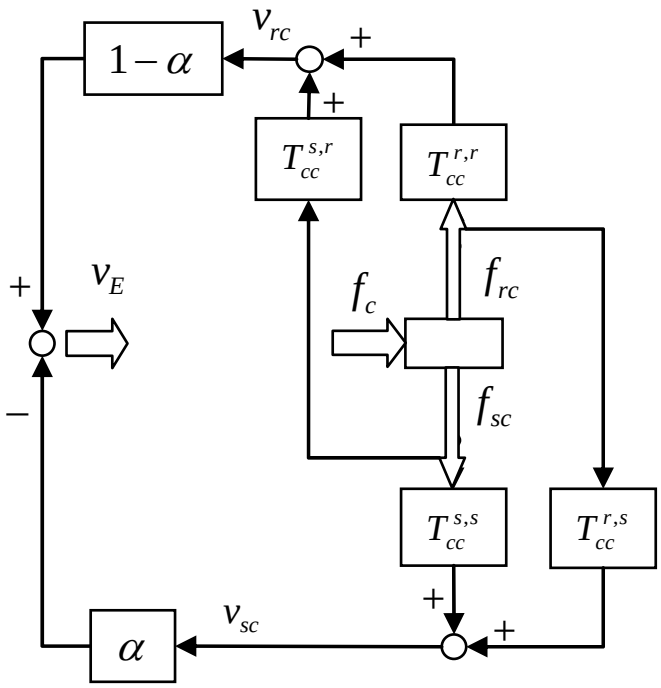

Figure 23: Configuration of the error signal

On the other hand, the block diagram in Figure 23 also shows that the source panel secondary force component f_{sc} contributes to the source panel velocity at the sensor location v_{sc} via the corresponding point mobility function $T_{cc}^{s,s}(\omega)$, and it also contributes to the radiating panel velocity at the sensor location (v_{rc}) via the corresponding transfer mobility function $T_{cc}^{s,r}(\omega)$ of the coupled system. Therefore, use of the reactive actuation scheme includes indirect actuation paths, which are realised through structural and acoustical coupling of the two plates. The superscripts $(\,)^{r,r}$ $(\,)^{s,s}$, $(\,)^{sr}$ and $(\,)^{r,s}$ are used to indicate the point and the transfer mobilities of the double panel system at control locations. They designate respectively radiating to radiating, source to source, source to radiating, and radiating to source mobilities between the two points of interest (Figure 23). The point mobilities $T_{cc}^{s,s}(\omega)$ and $T_{cc}^{r,r}(\omega)$ are the elements located on the main diagonal of the $\mathbf{T}_{cc}$ matrix (Equation (49)), while the transfer mobilities $T_{cc}^{s,r}(\omega)$ and $T_{cc}^{r,s}(\omega)$ are located on the sixteenth upper and lower diagonal of the $\mathbf{T}_{cc}$

matrix respectively, in the case when sixteen loops are used. The point mobility functions $T_{cc}^{s,s}(\omega)$ and $T_{cc}^{r,r}(\omega)$ model direct actuation paths whereas the transfer mobility functions $T_{cc}^{s,r}(\omega)$ and $T_{cc}^{r,s}(\omega)$ describe indirect actuation paths. The existence of the indirect actuation paths can affect the stability of the control system if the α factor is different from 0.5 (dual and collocated case).

The effects of the control systems that use weighted velocities to form the error signals, and reactive control actuators, can be simulated via the matrix **H** in Equation (50). The **H** matrix is formed in the following way: its main diagonal and the sixteenth upper and lower diagonals are populated with appropriate weighting factors, as given in Equation (73):

$$\mathbf{H} = g\begin{bmatrix} \alpha & 0 & \dots & 0 & \alpha-1 & 0 & \dots & 0 \\ 0 & \alpha & & & 0 & \alpha-1 & & \\ \vdots & & \ddots & 0 & \vdots & & \ddots & \vdots \\ 0 & \dots & 0 & \alpha & 0 & \dots & 0 & \alpha-1 \\ -\alpha & 0 & \dots & 0 & 1-\alpha & 0 & & 0 \\ 0 & -\alpha & & \vdots & 0 & 1-\alpha & & \\ \vdots & & \ddots & 0 & & & \ddots & \vdots \\ 0 & \dots & 0 & -\alpha & 0 & & \dots & 1-\alpha \end{bmatrix}. \tag{73}$$

If Equation (73) is substituted into Equation (50), which relates the control forces with control velocities, using the matrix **H**, the following expression is obtained:

$$\begin{Bmatrix} f_{sc1} \\ f_{sc2} \\ \vdots \\ f_{sc16} \\ f_{rc1} \\ f_{rc2} \\ \vdots \\ f_{rc16} \end{Bmatrix} = g\begin{bmatrix} \alpha & 0 & \dots & 0 & \alpha-1 & 0 & \dots & 0 \\ 0 & \alpha & & & 0 & \alpha-1 & & \\ \vdots & & \ddots & 0 & \vdots & & \ddots & \vdots \\ 0 & \dots & 0 & \alpha & 0 & \dots & 0 & \alpha-1 \\ -\alpha & 0 & \dots & 0 & 1-\alpha & 0 & & 0 \\ 0 & -\alpha & & \vdots & 0 & 1-\alpha & & \\ \vdots & & \ddots & 0 & & & \ddots & \vdots \\ 0 & \dots & 0 & -\alpha & 0 & & \dots & 1-\alpha \end{bmatrix}\begin{Bmatrix} v_{sc1} \\ v_{sc2} \\ \vdots \\ v_{scp} \\ v_{rc1} \\ v_{rc2} \\ \vdots \\ v_{rcp} \end{Bmatrix}. \tag{74}$$

so that the elements of the control force vector are given by:

$$
\begin{aligned}
f_{sc1} &= g\left[\alpha \cdot v_{sc1} + (\alpha - 1) \cdot v_{rc1}\right] = -g\left[(1-\alpha)v_{rc1} - \alpha v_{sc1}\right] \\
f_{sc2} &= g\left[\alpha \cdot v_{sc2} + (\alpha - 1) \cdot v_{rc2}\right] = -g\left[(1-\alpha)v_{rc2} - \alpha v_{sc2}\right] \\
&\vdots \\
f_{sc16} &= g\left[\alpha \cdot v_{sc16} + (\alpha - 1) \cdot v_{rc16}\right] = -g\left[(1-\alpha)v_{rc16} - \alpha v_{sc16}\right] \\
& \qquad . \qquad (75) \\
f_{rc1} &= g\left[-\alpha \cdot v_{sc1} + (1-\alpha) \cdot v_{rc1}\right] = g\left[(1-\alpha)v_{rc1} - \alpha v_{sc1}\right] \\
f_{rc2} &= g\left[-\alpha \cdot v_{sc2} + (1-\alpha) \cdot v_{rc2}\right] = g\left[(1-\alpha)v_{rc2} - \alpha v_{sc2}\right] \\
&\vdots \\
f_{rc16} &= g\left[-\alpha \cdot v_{sc16} + (1-\alpha) \cdot v_{rc16}\right] = g\left[(1-\alpha)v_{rc16} - \alpha v_{sc16}\right]
\end{aligned}
$$

Also, the source panel and radiating panel control forces satisfy the equilibrium condition for a reactive actuator *j*:

$$
f_{scj} + f_{rcj} = -g\left((1-\alpha)v_{rcj} - \alpha v_{scj}\right) + g\left((1-\alpha)v_{rcj} - \alpha v_{scj}\right) = 0 . \qquad (76)
$$

since the two force components are of equal magnitude with opposite signs.

4.2 Control performance

Control performance results are shown in Figure 24 using three different feedback gain values. The velocity weighting factor used in these simulations was α=0.375, which slightly emphasises the radiating panel velocity signals. The double panel system properties correspond to system design (a) (Table 1). Previous simulations that have been carried out with skyhook forces have shown that the best control action is achieved when the sixteen feedback control loops are formed by the error velocity signals measured at the radiating panel only, using the skyhook actuators. However, as will be discussed in following section, if this feedback configuration is used with the reactive actuators, it has severe stability limitations which preclude the implementation of large feedback control gains required to generate the desired active damping effects. A careful stability analysis (given in the following section) indicates that unconditionally stable feedback control loops can be obtained when the velocity feedback loops are implemented with a weighting factor of at least α=0.375, which emphasises the velocity signals from the radiating panel.

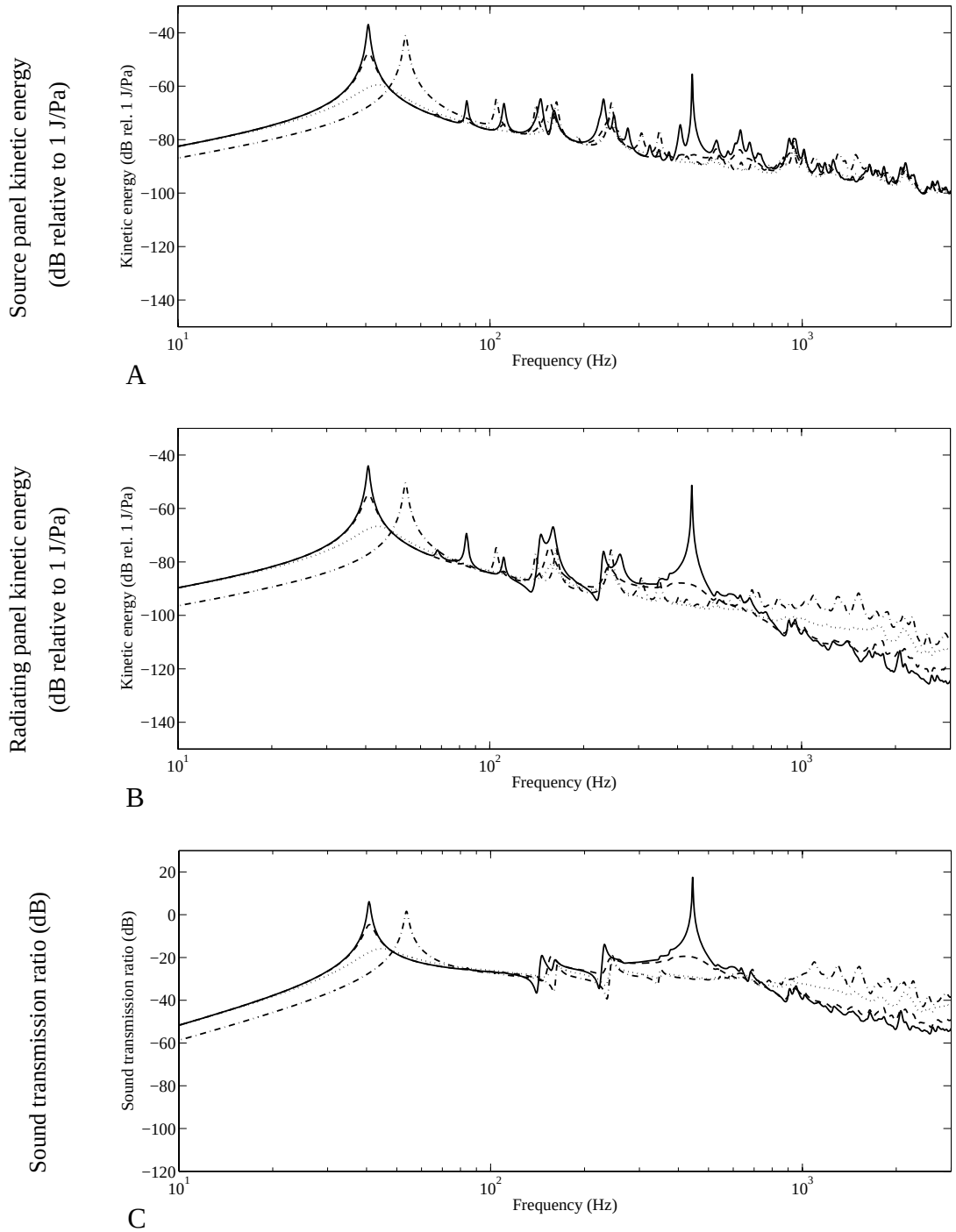

Figure 24: Direct velocity feedback using reactive control forces with velocity weighting factor equal to α =0.375. The top plot shows the source panel kinetic energy, the middle plot shows the radiating panel kinetic energy, and the bottom plot shows the sound power transmission ratio. Solid line – no control, dashed – low feedback gains, dotted – intermediate feedback gains, dash-dotted – high feedback gains.

The solid lines on all graphs in Figure 24 represent either the sound transmission ratio or kinetic energy of the panels without control. Considering feedback control loops with

α =0.375, as the feedback control gains are turned up, active damping action rises so that, as shown by dashed and dotted lines in Figure 24, the response of the radiating panel, and thus the sound radiation, tend to decrease at the low-order mode resonant frequencies. If very large gains are applied, the response of the radiating panel is characterised by a new set of modes. These modes are defined by the control forces that bring the two panels to move together as if they were connected by very rigid fasteners, since the α value is quite close to 0.5. Thus a new set of resonances are produced at slightly higher frequencies and with relatively higher amplitudes. In other words the double panel tends to become a sort of thick and light single panel with a higher stiffness-mass ratio. The response is then characterised by lightly damped resonances, since having the control positions of the source and the radiating panel connected by the rigid links prevents the generation of active damping.

Figure 25 illustrates the response of the panel at three resonant frequencies when there is no control (top row) and when the sixteen control units either implement the control gains that give the largest active damping effect (centre row) or implement very large control gains so that the two panels are linked together at the sixteen control positions (bottom row).

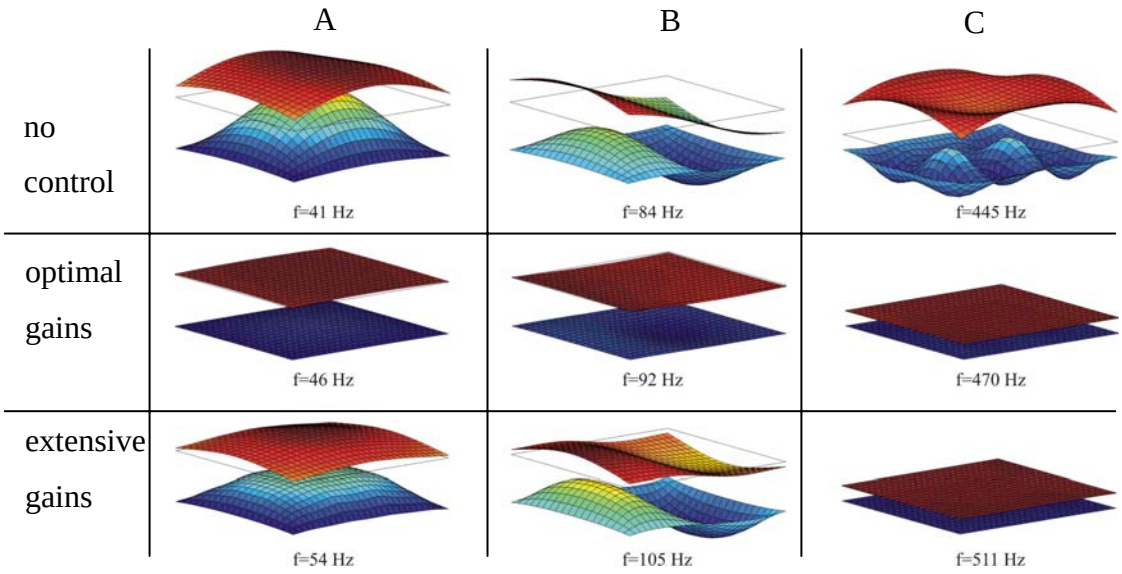

Figure 25: Scaled deflection shapes of the two panels at the 1st (column A), 5th (column B) and 23rd (column C) resonances of the system. First row depicts the resonances with no control, centre row with optimal gain, and the bottom row with large feedback gain (α =0.375). The scaling within a column is equal; the scaling between columns is not.

The mode shape designated by (A) is characterised by a (1,1) volumetric mode of the source panel which induces an even rigid body mode of the resiliently mounted radiating panel (the first mode of the double panel). The four flexible mounts change the vibration field of the radiating panel in such a way that it looks like a (1,1) flexible mode which is pinned at the four mounting points. The mode shape designated by (B) is characterised by a (2,1) mode of the source panel which induces a rocking rigid body mode of the resiliently mounted radiating panel. Also, in this case, the four mounts constrain the vibration of the radiating panel at the corners. Finally the deflection shape (C), (mass-air-mass), besides the air acting like a spring between two masses, is characterised by a strong coupling between the two panels via the first cavity mode (1,0,0) which resonates. As a result the responses of the two panels are influenced by the cavity mode which induces a cosinusoidal field in *x*-direction on the source panel. In this case, the sixteen control units tend to prevent the excitation of the resonant cavity mode and the relative out of phase motion of the two plates. Thus, when the control gains are raised the response of the two panels monotonically falls off at the mass-air-mass resonance even for very large control gains (Figure 25, column C at the bottom).

The two plots in Figure 26 show the normalised kinetic energy of the radiating panel (plot A) and sound transmission ratio (plot B), integrated from 0 Hz to 3 kHz and plotted against feedback gain.

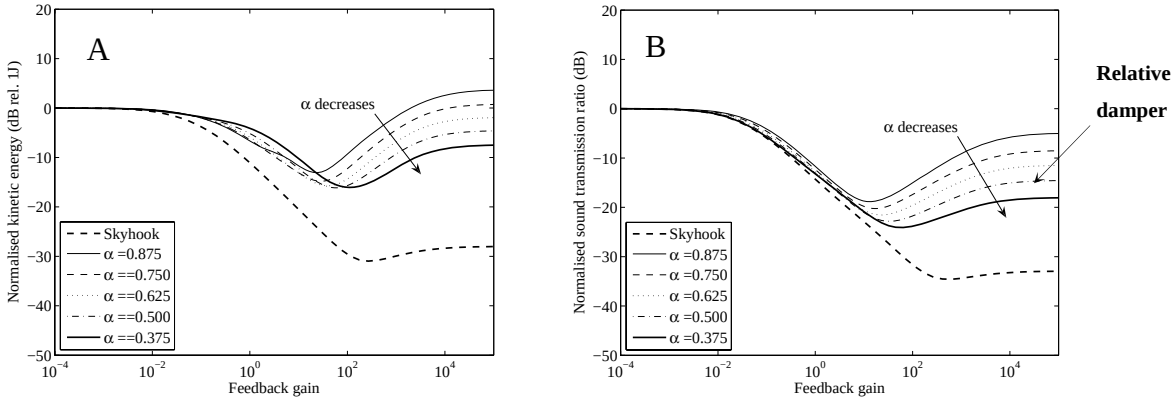

Figure 26: Normalised kinetic energy of the radiating panel (A) and sound transmission ratio (B), integrated from 0 Hz to 3 kHz, plotted against the control gain, for the different α -factor values: α =0.875 (solid faint line), α =0.75 (dashed faint line), α =0.625 (dotted faint line), α =0.5 (dash-dotted faint line) and α =0.375 (solid line) and for a decentralised MIMO feedback system that uses 16 ideal skyhook actuators and velocity sensors on the radiating panel (dashed line).

The curves in each plot have been derived by varying the sensor weighting factor α between 0.875 and 0.375, where $\alpha = 0.375$ is the smallest value of α for which the system is unconditionally stable. Also, the dash-dotted curves have been added which represent the reductions which would be generated by a decentralised MIMO feedback system that uses ideal skyhook actuators and velocity sensors on the radiating panel (Chapter 4.1.5). The results indicate that the latter is by far the best arrangement. The response and sound radiation reductions are twice that obtained with the best reactive force feedback configuration. However, it must be emphasised that in practice it is normally necessary to have a reactive arrangement in order to obtain a pure force actuation. Alternatively, as discussed previously, it could be obtained with proof mass actuators. But in this case the feedback loop is only conditionally stable and does not permit control gains necessary to obtain the large control effects predicted by the dash-dotted lines in Figure 26. Therefore the reactive control scheme is discussed next.

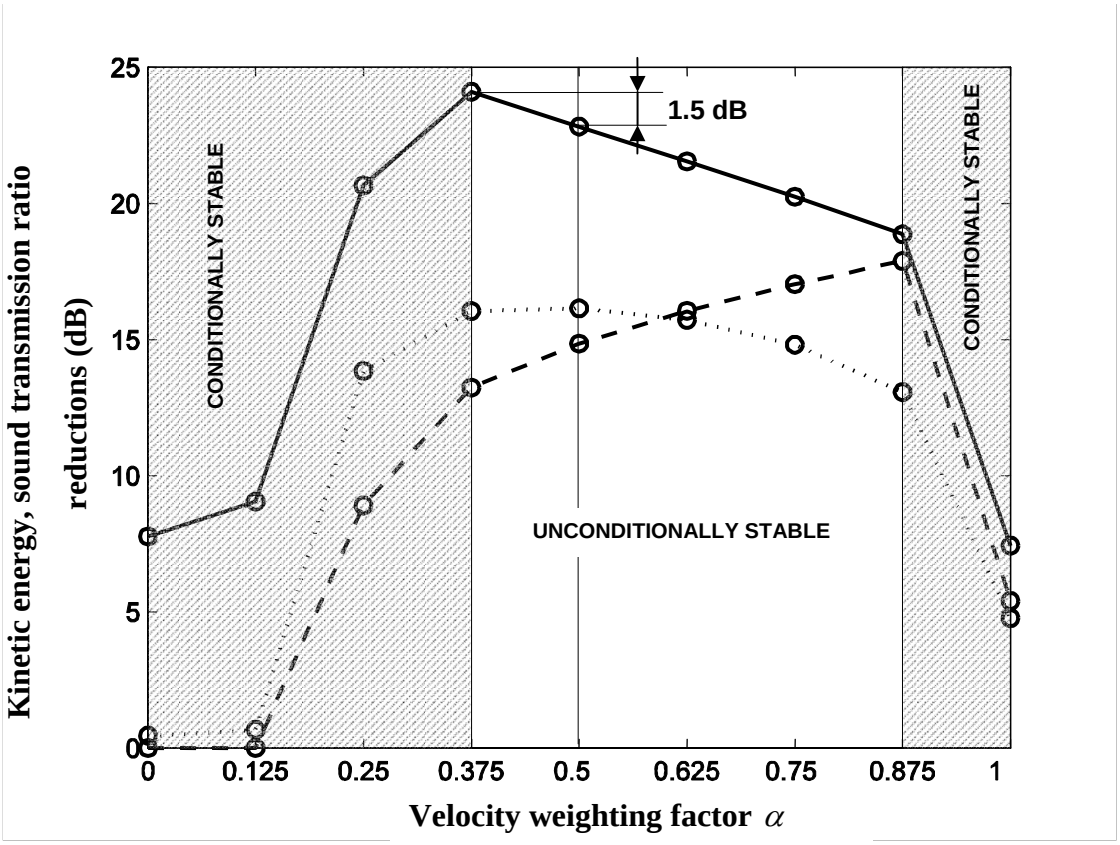

Figure 27: Maximum reductions of the: a) sound transmission ratio (solid line), b) normalised total kinetic energy of the source panel (dashed line), c) normalised kinetic energy of the radiating panel (dotted line).

For all the α values the kinetic energy of the radiating panel and the sound transmission ratio monotonically decrease as the sixteen control gains are raised from zero to

approximately 10 Ns/m - 100 Ns/m. This results in a maximum reduction respectively of about 16 dB (plot A) and 24 dB (plot B) for optimal control gains and for optimal (the smallest) velocity weighting factor α =0.375. For higher control gains the reduction of kinetic energy and sound transmission ratio degrades because the control systems tend to connect the panels at the control positions: this effect prevents active damping and introduces a modal response characterised by lightly damped new resonances.

Figure 27 shows that the best reductions of sound transmission ratio and kinetic energy of the radiating panel are obtained when the error signals of the sixteen control loops are tuned in such a way as to weight the radiating panel velocities more. In contrast, as one would expect, the best reduction of source panel kinetic energy is obtained when the error signals are tuned in such a way as to weight the source panel velocities more.

4.3 Stability

As was mentioned before, indirect actuation paths are relevant if reactive actuators with "unbalanced" velocity sensors pairs are used on the double panel system considered in this thesis. As a result the implementation of large control gains can be limited by stability issues. In this study, the Nyquist criterion is used to assess the stability of a single control loop. In practice the stability of all sixteen control loops should be assessed with a generalised form of the Nyquist criterion[42,76,77]. However the stability analysis of a single control unit can be better interpreted in terms of the physics of the system. Moreover any instability of a single unit is likely to affect the stability of the whole sixteen channel control system. Thus the stability of a single control unit can be assumed as a necessary, although not sufficient condition for the stability of the whole sixteen channel control system, and will be analysed first.

Figure 28 shows Bode (left hand side) and Nyquist (right hand side) plots of a sensor-actuator open loop frequency response function assuming the velocity weighting factor α =0.5. The feedback loop considered here is one of the inner four feedback loops (Figure 7). The open loop sensor-actuator FRF phase is confined between ±90º, thus there is no negative real part in the Nyquist plot and the feedback loop is bound to be unconditionally stable. Also a decrease in the open loop sensor-actuator FRF amplitude

is noticeable, as the frequency rises, which shows that the control effectiveness at higher frequencies is reduced.

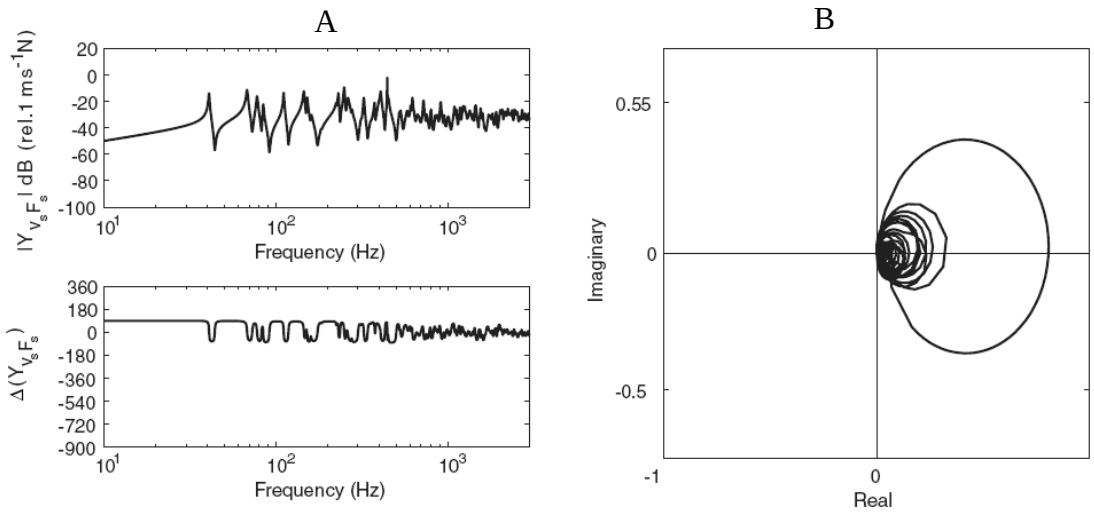

Figure 28: Bode (plot A) and Nyquist (plot B) plots of the open loop sensor-actuator FRF for the velocity weighting factors of α =0.5.

One may expect intuitively that this case of α =0.5 would be stable because it is a case of pure relative damping; i.e. the reactive control force is proportional to the opposite of the relative velocity of the panels at the actuators position.

Further simulations have shown that this condition applies for values of α down to 0.375. If the velocity weighting factor is further decreased, to a value as low as α =0.1, then, as shown in Figure 29 by solid lines, the system becomes conditionally stable.

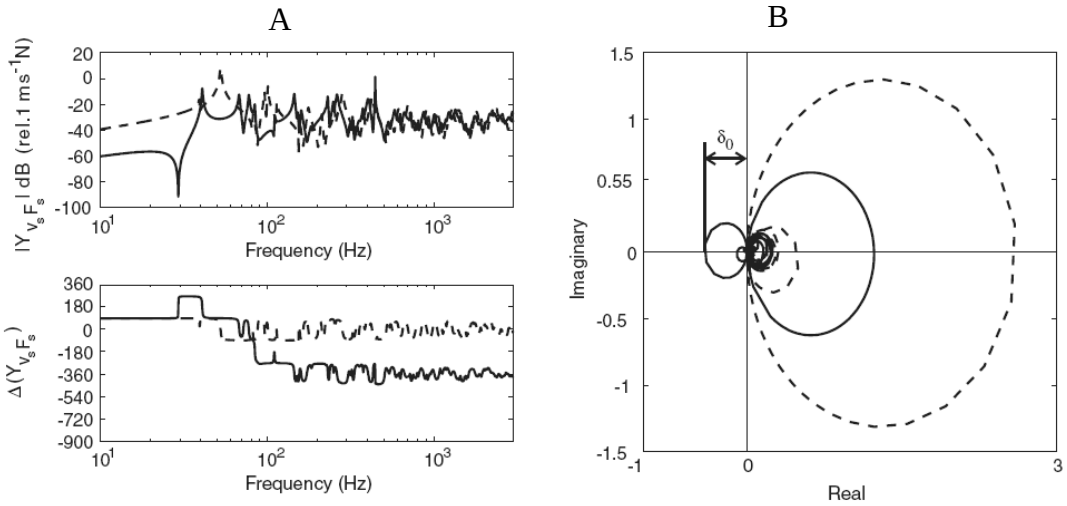

Figure 29: Bode (plot A) and Nyquist (plot B) plots of the open loop sensor-actuator FRF for the velocity weighting factors of α =0.1 with (solid line) and without (dashed line) air coupling.

This is due to two 180^o phase lags at approximately 40 Hz and at 84 Hz. These phase lags occur at the resonances of the 1^{st} and 5^{th} modes of the double panel. At these frequencies the indirect actuation paths (from the source panel to the radiating panel and vice versa) produce error signals in opposite phase to those of the direct paths, so that, since the resonances of these two modes are particularly effective, the sensor-actuator open loop frequency response functions undergoes a -180˚ phase lag. The two modes are characterised by a radiating panel vibration field that is forced to follow the source panel motion via the acoustical coupling (plots A and B in Figure 25). In order to illustrate the importance of acoustical indirect actuation path, a simulation has been performed, which neglects the acoustical coupling of the two panels. The corresponding results are depicted in Figure 29 by the dashed lines. The control system in that case would be stable as the phase of the open loop sensor-actuator FRF is constrained between $\pm 90^o$ and thus the locus stays in the positive real quadrants.

Figure 30 shows the maximum value of δ_o in Figure 29B plotted against the velocity weighting factor, α, for cases with and without acoustical coupling.

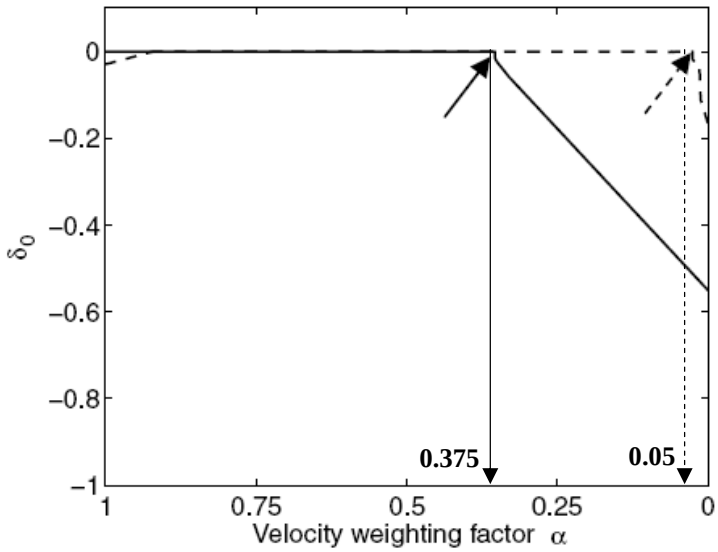

Figure 30: δ_0 value plotted against the velocity weighting factor α when the acoustical coupling between the two panels is (solid line) or is not (dashed line) taken into account in the model.

According to the Nyquist criterion, if $\delta_o = 0$ then the system is unconditionally stable. In contrast, if $\delta_o < -1$ the system is unstable. Finally, if $-1 < \delta_o < 0$ then the system is conditionally stable, although control spillover effects are likely to occur at some

frequencies. It can be seen that acoustical coupling between the panels is the major cause of conditional stability for the control with α-factor lower than approximately 0.375. This value corresponds to the knee location in Figure 30, as designated by an arrow. The α-factor of the knee, where the system switches from conditional to unconditional stability, is considered the critical velocity weighting factor (α_{crit}) throughout this thesis.

Elastic mounts are another path for indirect actuation. Indeed it is the coupling via the elastic mounts that limits the stability in the case where no acoustic coupling is considered between the two panels (dashed line). In summary the velocity weighting factor of approximately α=0.375 can be considered a threshold for unconditional stability of feedback control with reactive actuators for the double panel system design (a) (Table 1) and for the feedback loop considered here.

So far the considered frequency response function was for one of the inner four control loops of the array with sixteen control units (Figure 7). However, the location of the feedback unit might also be an important factor. For example, the source panel is simply supported along its edges. If a control unit is located exactly at an edge, the velocity v_{sc} equals to zero, as well as mobilities $T_{cc}^{s,s}(\omega)$, $T_{cc}^{s,r}(\omega)$ and $T_{cc}^{r,s}(\omega)$ shown in Figure 23. Only the point mobility $T_{cc}^{r,r}(\omega)$ is different from zero. Therefore the indirect actuation paths do not exist and the error velocity is purely determined by the radiating panel control force component f_{rc}. As a consequence, even for $\alpha = 0$ a control loop located at edges should be unconditionally stable. This suggests that there must be a spatial distribution of the critical velocity weighting factor α.

In order to investigate this effect, simulations have been performed with control units located all over the double panel surface: in total 34×34 *x* and *y* coordinates have been investigated, and for each location the critical velocity weighting factor has been determined. The results are depicted in Figure 31, which shows contour plots of the critical α over the panel's surface. Plot A indicates that the highest α factors are necessary near the centre of the plate to ensure unconditional stability. As expected, zero values are required at the edges. Very high values can also be observed near the mounts.

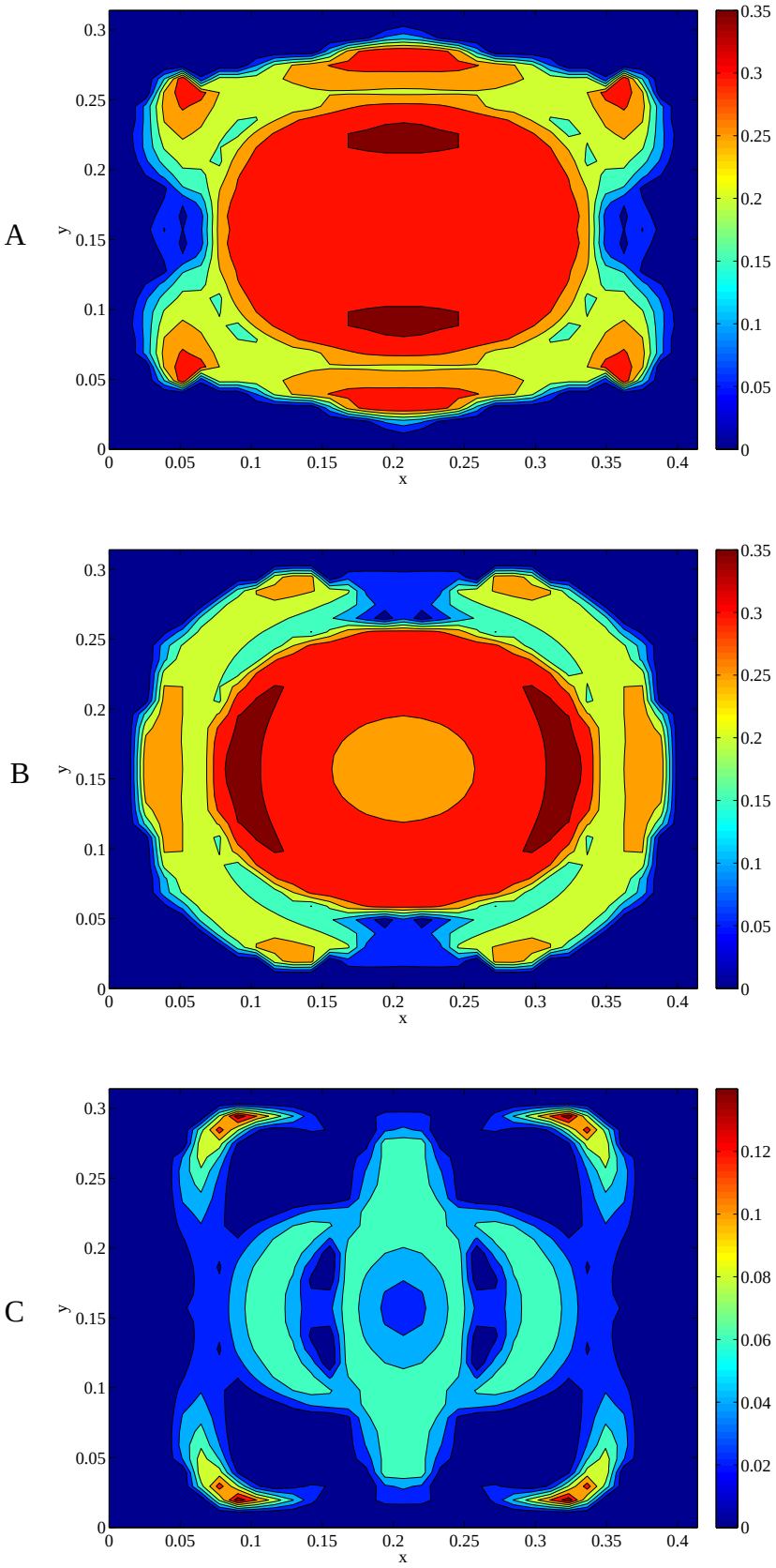

Figure 31: Critical α-factor distribution plotted over the surface of the double panel in case of fully coupled configuration (plot A), in case when structural coupling is neglected (plot B), and in case when acoustical coupling is neglected (plot C).

If the mounts are removed this effect vanishes as shown in plot B in Figure 31. High values are still present in the centre of the panel. Finally, if the air coupling is neglected, the critical α value drops significantly all over the panel, except in the vicinity of the mounts (plot C). This indicates that the acoustical coupling is the most important path for the indirect actuation when using reactive actuators in the model double panel considered here.

4.4 Parametric study of the stability of the feedback loops

In order to assess the effect of the physical properties on the control system stability, a parametric study has been performed. The following properties have been varied: a) mass density (surface density) of the source panel, b) Young's modulus (bending stiffness) of the source panel, c) mass density (surface density) of the radiating panel, d) Young's modulus (bending stiffness) of the radiating panel, e) elastic mount stiffness, and f) mass density of the air in the cavity. During variation of each of the parameters, all other properties of the double panel were kept equal to the properties of design (a) in Table 1. Since it was observed that the centre of the double panel represented the most critical location (Figure 31), this location has been chosen to assess the stability of the feedback loop for this parametric study.

For each parametric study the variation of δ_o has been derived for different velocity weighting factors in the range 0-1. In this way it was possible to determine the critical velocity weighting factor, which was observed in the previous section of this thesis, with respect to the varied parameters. Therefore the range of α factors for which the loop remains in the unconditionally stable regime has been considered. Also the value of δ_o in the case when α =0 have been determined for each parameter. This value is important because it gives an idea of the maximum feedback gain which is available to conditionally stable systems with velocity sensors located on the radiating panel only.

Figure 32 shows the results of the parametric study with respect to the variation of the source panel material properties including: mass density (left hand plots) and Young's modulus (right hand plots). These properties directly influence the surface density of a plate and its bending stiffness, as shown by Equations (56,57).

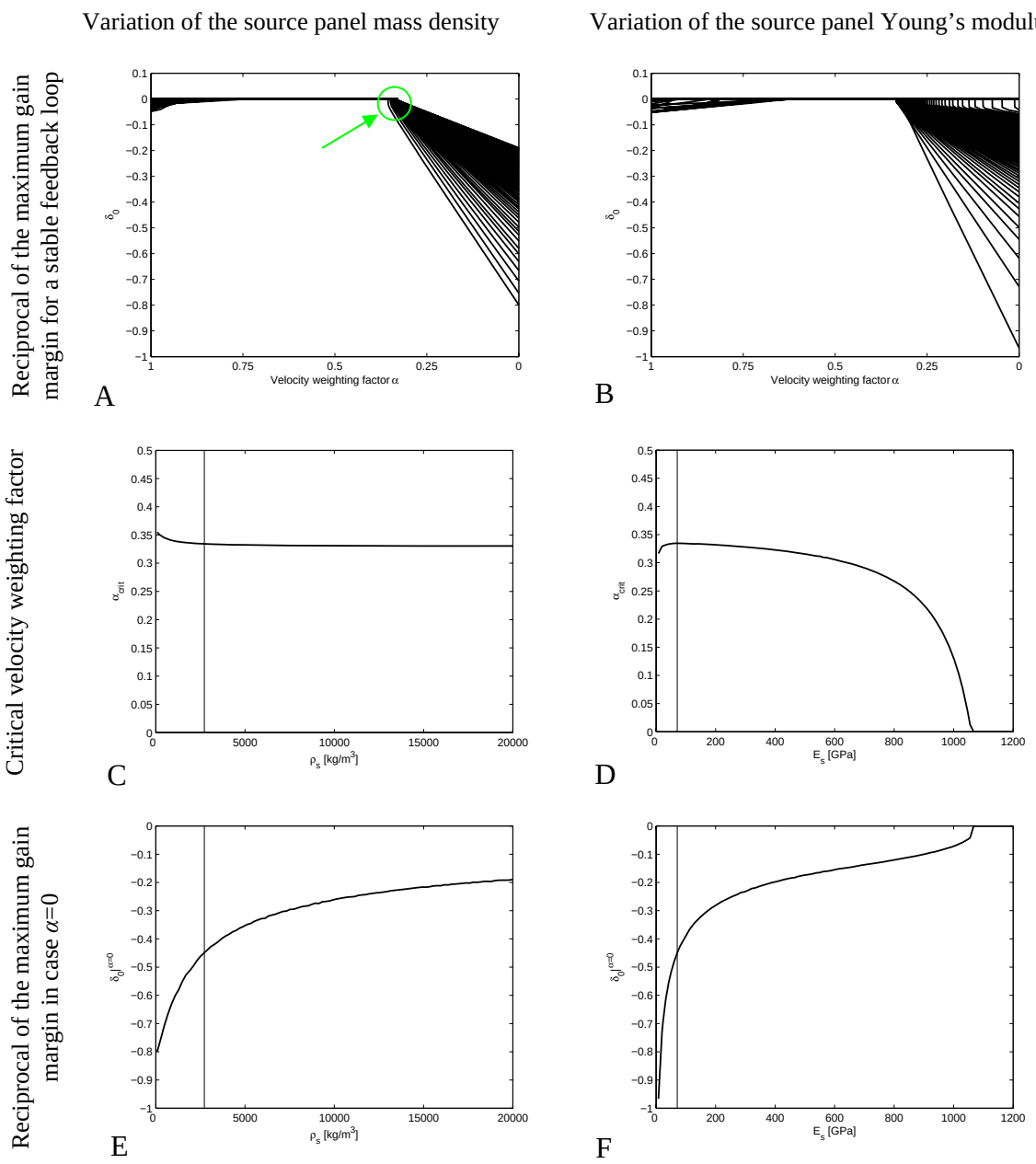

Figure 32: a) δ_0 plotted against the velocity weighting factor (plots A and B), b) critical velocity weighting factor (plots C and D) plotted against the varied parameter, c) δ_0 in case when $\alpha = 0$ plotted against the varied parameter (plots E and F). The parameters varied in this figure are the source panel mass density (plots A, C, and E) and the source panel elastic modulus (plots B, D, and F). The vertical lines on plots C-F indicate the location of the reference case (a) (Table 1) on the parameter axis.

Plots A and C indicate that the critical α value is only a little influenced by the mass density of the source panel. (The critical α is the knee location indicated by arrow in Figure 30.) On the other hand, δ_o in case when α =0 shows sensitivity to the variation since the available gain margin tends to change substantially (plot E). Moreover plot E

clearly indicates that very heavy source panels provide more gain margin in the range of conditional stability.

In contrast, variation of source panel stiffness causes the critical velocity weighting factor to change substantially, and, in the case of extremely stiff source panels, the value approaches zero (plot D). Also, δ_o in case when α=0, decreases as the source panel bending stiffness increases, giving more gain margin for conditionally stable feedback loops (plot F).

The sensitivity of α_{crit} to variation of either stiffness or mass of the source plate around the reference case (vertical lines in plots) is small (plots C and D). This indicates that there is not much room for affecting the critical velocity weighting factor without considerably changing the mass and the stiffness of the source panel. On the other hand the sensitivity of the gain margin for conditionally stable systems around the reference case is considerable (plots E and F). However, the desirable feedback gain of approximately 100 Ns/m (Figure 26) is not achievable for reasonable values of mass and stiffness.

Figure 33 shows stability parametric study results for variations in radiating panel mass density (left hand plots) and Young's modulus (right hand plots). It can be observed that the critical α value is insensitive to changes in mass density of the radiating panel (plots A and C). This statement also extends to δ_o in the case when α=0, since the gain margin does not change substantially (plot E). In contrast, an increase in radiating panel stiffness causes the critical velocity weighting factor to decrease in the vicinity of the reference case (plot D). But, even in case of extremely stiff radiating panels, this value does not decrease to zero. Considering now δ_o in case when α=0, it decreases with increase in radiating panel bending stiffness (plot F), giving more gain margin for conditionally stable feedback loops. However the increase of the gain margin is not high enough to permit implementation of desirable feedback gains.

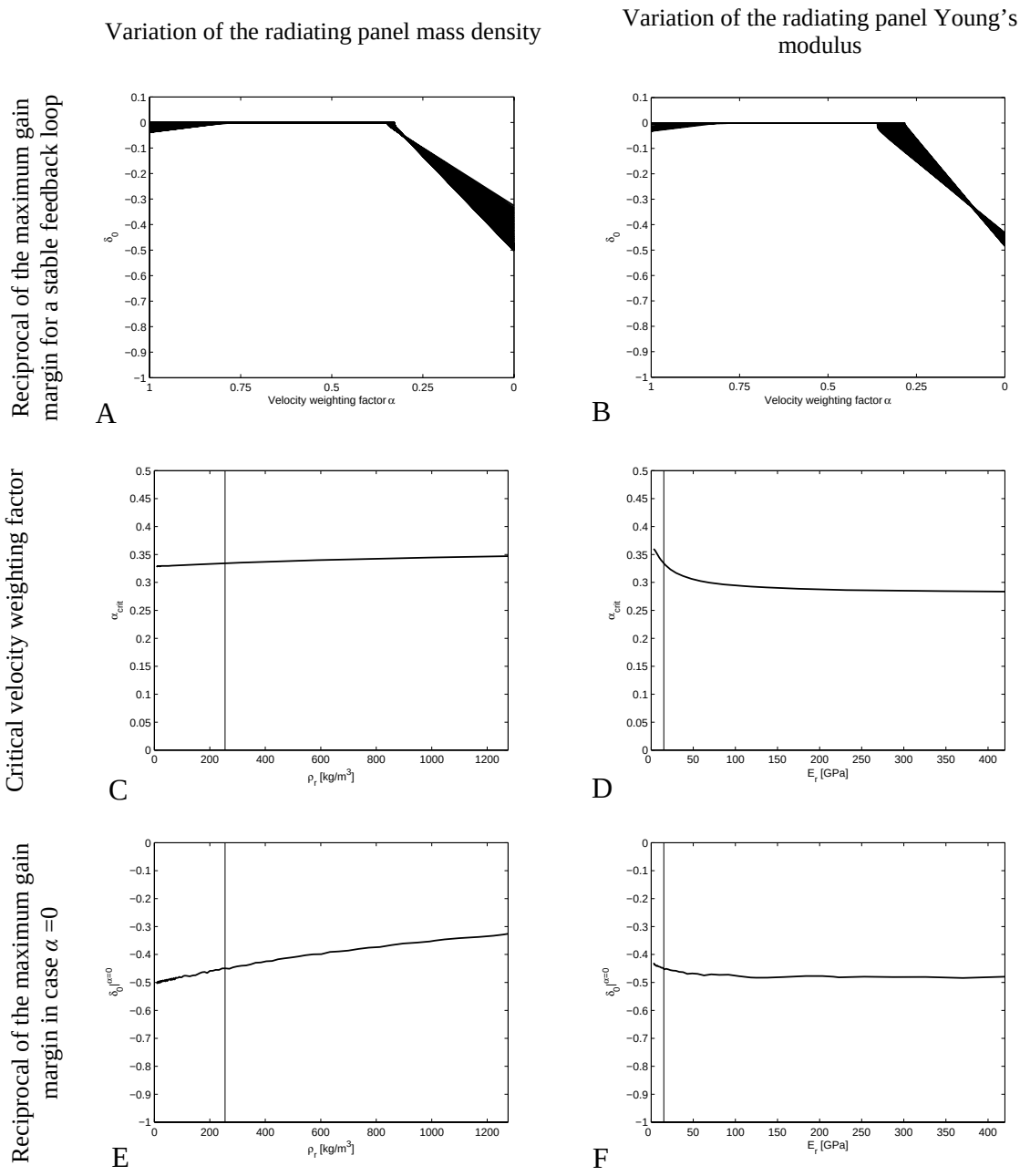

Figure 33: a) δ_0 plotted against the velocity weighting factor (plots A and B), b) critical velocity weighting factor (plots C and D) plotted against the varied parameter, c) δ_0 in case when $\alpha = 0$ plotted against the varied parameter (plots E and F). The parameters varied in this figure are the radiating panel mass density (plots A, C, and E) and the radiating panel elastic modulus (plots B, D, and F). The vertical lines on the plots C-F indicate the location of the reference case (a) (Table 1) on the parameter axis).

In conclusion, the study of radiating panel material properties indicates that the stability properties are only significantly influenced by the variation of the bending stiffness (Young's modulus) of the radiating panel. This could have an impact on the stability if

the panel had very low stiffness, as indicated by the slope of the curve plot D of Figure 33.

The variation of elastic mounts stiffness, depicted in plots A, C, and E of Figure 34 is now considered. This parameter has a modest influence on critical velocity weighting factor and gain margin for conditionally stable systems. Even in case when the stiffness of the mounts is varied between 0 and 100 kN/m, α_{crit} changes are bounded between 0.28 and 0.37 (plot C), while δ_o with α =0 changes are limited between -0.33 and -0.46 (plot E). However, it is worth noting the overall trend in the α_{crit} dependence upon mount stiffness since it increases with increase of stiffness. This outcome is not surprising because the structural coupling of the two plates is a path for the indirect actuation effect. It is also worth noting that there are only four elastic mounts and they are near the edge of the plate, where the mobility functions of the source panel have low amplitudes. This limits the influence of the structural indirect actuation in a first place, so that varying its strength does not significantly affect the stability limits. The stability limits are predominantly determined by the very strong acoustical indirect actuation path.

In fact, in the previous section the simulations with and without the air in the cavity indicated the importance of the acoustical indirect actuation path. Figure 29 and Figure 30 showed how the absence of the air can dramatically reduce the α_{crit}. These results were motivation to study the stability with respect to the air density which, for this parametrical study was varied between 0 (total vacuum) and the air density under the standard atmospheric conditions ($\rho_{air} = 1.19\,\mathrm{kg/m^3}$). α_{crit} was very sensitive to air density, but the shape of the curve in Figure 34D, shows that the principal variation occurs at very high levels of vacuum. In other words, the slope of the curve is very small around the reference case ($\rho / \rho_0 = 1$). It is interesting to compare plot B in Figure 34 to plot B in Figure 32 where the source panel stiffness variation is shown. These two plots show different curve shapes in the conditionally stable region. The stiffness of the source panel primarily acts by increasing the available gain margin, whereas the density of the air in the cavity shifts the knee (α_{crit} value) to the right.

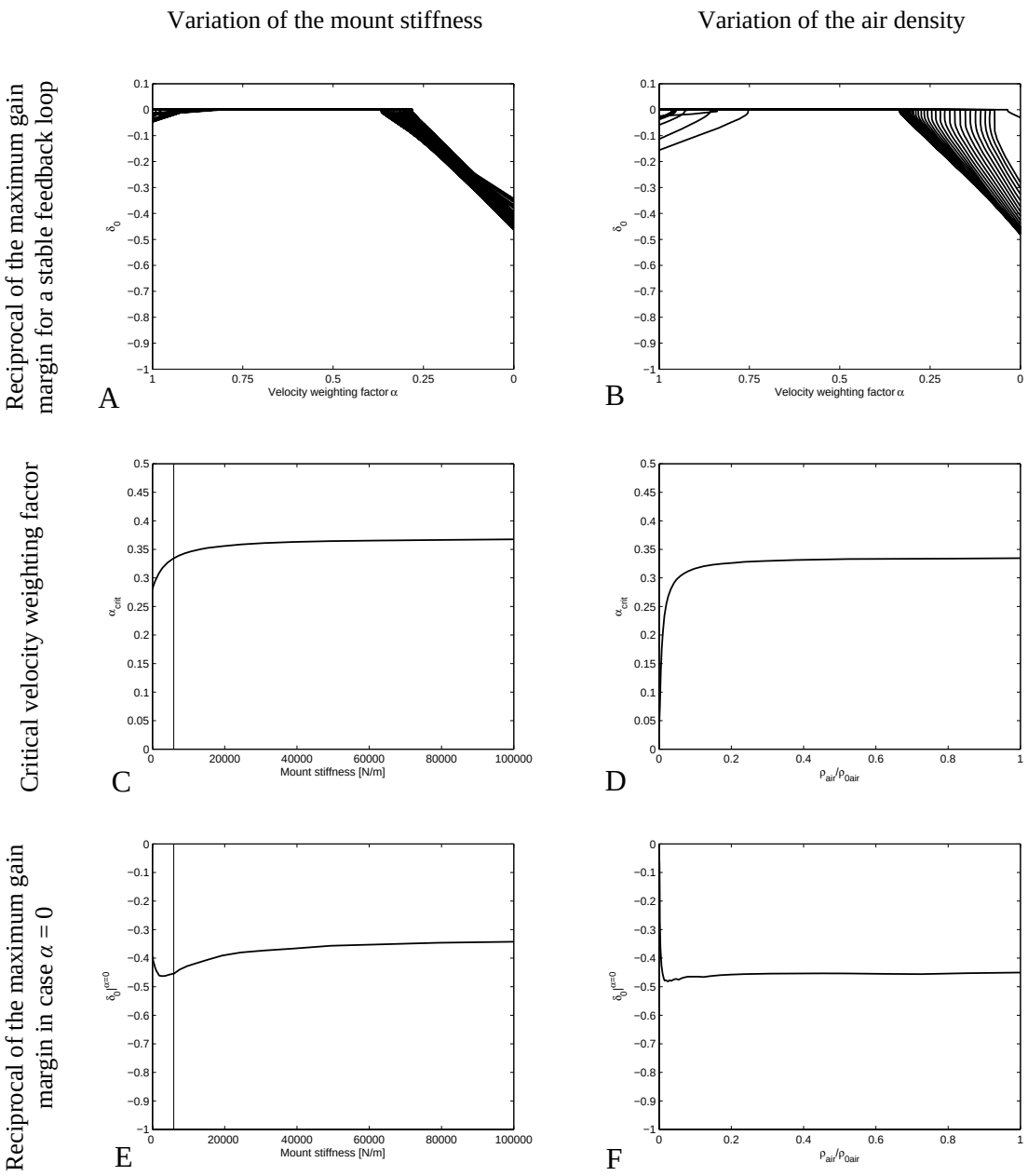

Figure 34: a) δ_0 plotted against the velocity weighting factor (plots A and B), b) critical velocity weighting factor (plots C and D) plotted against the varied parameter, c) δ_0 in case when $\alpha = 0$ plotted against the varied parameter (plots E and F). The parameters varied in this figure are the stiffness of the elastic mounts (plots A, C, and E) and the mass density of the air in the cavity between the plates (plots B, D and F). The vertical lines on the plots in the second and third row indicate the location of the reference case (a) (Table 1) on the parameter axis).

The final parameter considered is the air cavity depth (l_z). Three depths were considered including: 0.02m, 0.03m, 0.04m The influence on the stability properties is negligible, as shown in Figure 35 (the three curves overlap).

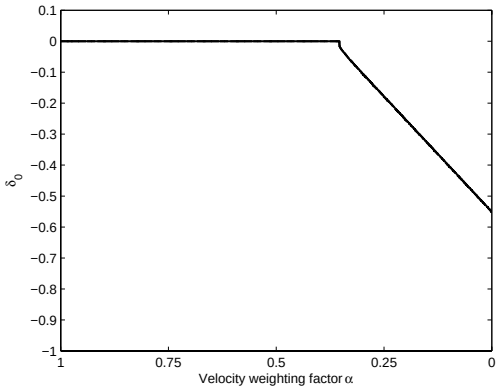

Figure 35: The effect of the l_z dimension of the air cavity to the δ_o versus α curve. Three cavity l_z dimensions have been considered here (0.02m, 0.03m, 0.04m), but the curves overlap.

This outcome can be explained by considering the physics of the acoustical coupling at the lowest resonant frequency of the double panel (approximately 40 Hz). At this frequency the mode shape is dominated by volumetric, in phase motion of the two panels (Figure 25A). The cavity air only couples the two plates like a very stiff distributed spring. This is important for the stability since the most important phase lag for conditionally stable systems occurs at this frequency (40Hz). This lag is characterised by the largest resonant amplitude of the open loop sensor-actuator FRFs (Figure 29). Therefore δ_o is observed at the lowest resonance of the double panel system (Figure 29B). The air in the cavity has very limited influence on the vibration amplitude or natural frequency of the mode (Figure 13). In fact, the natural frequency of the mode is mostly determined by the two panels' mass and stiffness properties, while the air constrains the motion of the two plates without contributing to the modal mass or stiffness.

In conclusion, the parameters of the double panel system that strongly affect the stability of the feedback loops are the strength of the acoustical coupling effect, and the stiffness of the source plate. However the influence does not occur in the vicinity of the reference case (the design (a) in Table 1). In addition, the strength of the acoustical coupling can probably be affected by means other than the density of the air, such as, by changing the air cavity boundary conditions.

4.5 Summary

In Chapter 4 a theoretical stability and performance analysis of a smart double panel with 16 weighted velocity feedback loops was performed. The loops were applied via an array of reactive force actuators and collocated velocity sensors. The actuators are located in an air cavity between the two panels such that they can react against the two panels. Two velocity sensors per actuator are used. Either sensor is located at the source and radiating panel footprint of an actuator. The error velocity is formed by subtracting weighted sensor outputs.

The performance of the active control is analysed first, in terms of the reductions of the radiating panel kinetic energy and the sound transmission ratio. Second, the stability of the feedback loops is analysed using the Nyquist criterion on the open loop sensor-actuator frequency response functions.

The performance analysis has shown that for the double panel under analysis better reductions were obtained with the velocity weighting factors $\alpha < 0.5$ that emphasize the radiating panel velocity signals. On the other hand, the stability analysis has shown that the feedback loops with the velocity weighting factors $\alpha = 0$ that use radiating panel velocities only, are not unconditionally stable. In fact there are critical values of the velocity weighting factor where the stability of the loops change from unconditional to conditional.

Finally, a parametric study has been performed in order to understand how the critical velocity weighting factors depend upon the mechanical properties of the double panel. It was found that the stiffness of the source panel and the cavity air density can influence the value of the critical velocity weighting factor. The increase in source panel stiffness resulted in a decrease in the value of the critical velocity weighting factor. The decrease in the cavity air density led to a decrease in the critical velocity weighting factor.

5 Design and testing of the smart double panel

In this chapter the design and experimental testing of a prototype smart panel demonstrator is described. The prototype smart panel is equipped with nine decentralised velocity feedback units.

Electrical components of the experimental demonstrator include:

- nine miniature, lightweight voice coil actuators;
- eighteen miniature, low-cost Micro Electro Mechanical Systems (MEMS) accelerometers; and
- a nine channel analogue feedback controller.

The mechanical components of the demonstrator include:

- the source and radiating panels with sensor and actuator junctions;
- a rigid clamping system; and
- a Perspex box.

Using this setup, the stability properties anticipated in the theoretical study were experimentally verified in this chapter, by measuring sensor-actuator open loop frequency response functions. The Nyquist criterion was used to examine the stability properties of each feedback loop with respect to the different velocity weighting factors. In addition, the generalised Nyquist criterion was used to demonstrate the stability of the nine feedback loops operating simultaneously.

5.1 The smart double panel design

The smart double panel demonstrator built for this study consists of two rectangular plates with dimensions 0.414×0.314 m^2. The source panel is built from a 1 mm thick aluminium plate whereas the radiating panel is built from a 3 mm thick polymer honeycomb plate. The radiating panel is attached to the source panel by four corner

mounts, such that the distance between the two plates is 0.03 m. As shown schematically in Figure 36, miniature voice coil actuators, consisting of a coil and a permanent magnet, are placed in the air cavity between the two panels. For practical reasons, coils are attached to the source panel, whereas the permanent magnets are attached to the radiating panel. In this way it was easier to align the coil and magnet pairs and provide clearance between them. Each coil and magnet is equipped with a MEMS accelerometer sensor. The sensor-actuator control units are arranged such that they form a regular 3×3 array. The distance between perimeter units and the edge of the plate equals the distance between any two adjacent units of the array, both lengthwise and widthwise.

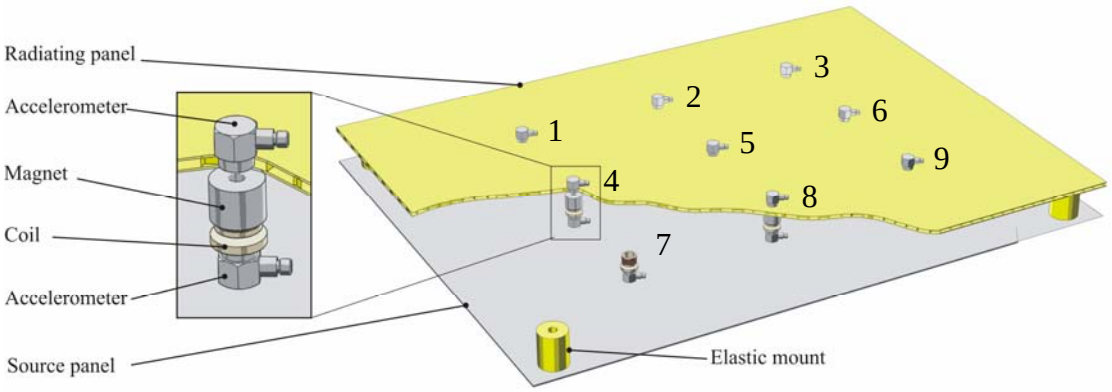

Figure 36: A schematic representation of the prototype smart double panel with nine velocity feedback loops.

Figure 37 shows the experimental test rig. As shown in Figure 36C, the source panel is clamped between two rigid aluminium frames. Both frames have a width of 25 mm, but they have different thicknesses: 25mm for the bottom frame and 40mm for the top one. The dimensions of the plate used to build the source panel have been chosen to match the width and length of the clamping frame so that $l_{xs}\times l_{ys}\times h_s$=464×364×1mm^3. The radiating panel is attached to the source panel using four corner mounts such that the outer surface of the radiating panel is slightly below the upper clamp level (Figure 37D). The clamping frame and the two panels are mounted on the open side of a Perspex box in order to measure the sound radiated by the radiating panel when the source panel is excited by a shaker located in the box (Figure 37A). The results of these measurements are presented in Chapter 6.

The miniature voice coil actuator (H2W Technologies, model NCC01-04-001) is shown in Figure 38A, and the MEMS accelerometer (Analog Devices, model ADXL103) is

shown in Figure 38B. The detailed properties of the voice coil actuator can be found in Ref. 78, and the properties of the MEMS accelerometer can be found in Ref. 79, and also in Appendix C.

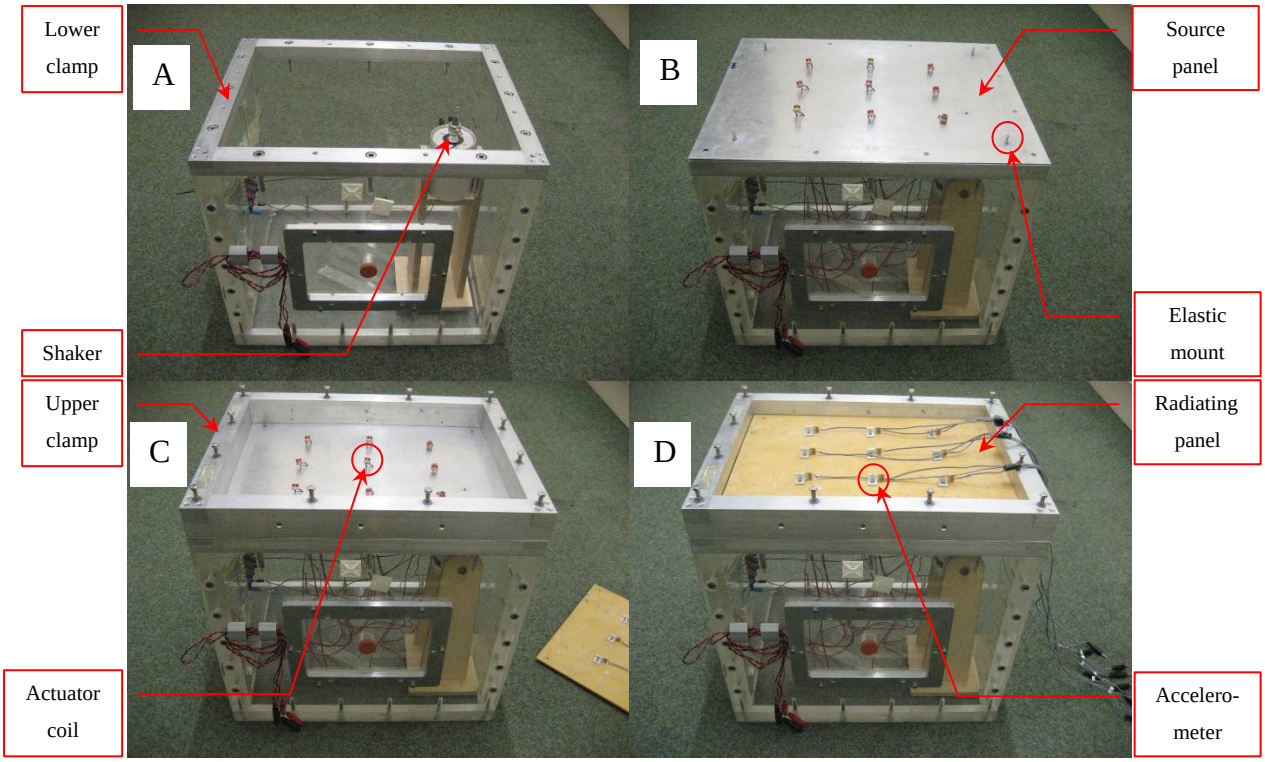

Figure 37: The prototype smart double panel experimental test facility; A) the lower clamping frame mounted on top of the thick-walled Perspex box, B) the source panel mounted, C) the upper clamp mounted, and D) the radiating panel mounted using the four corner mounts.

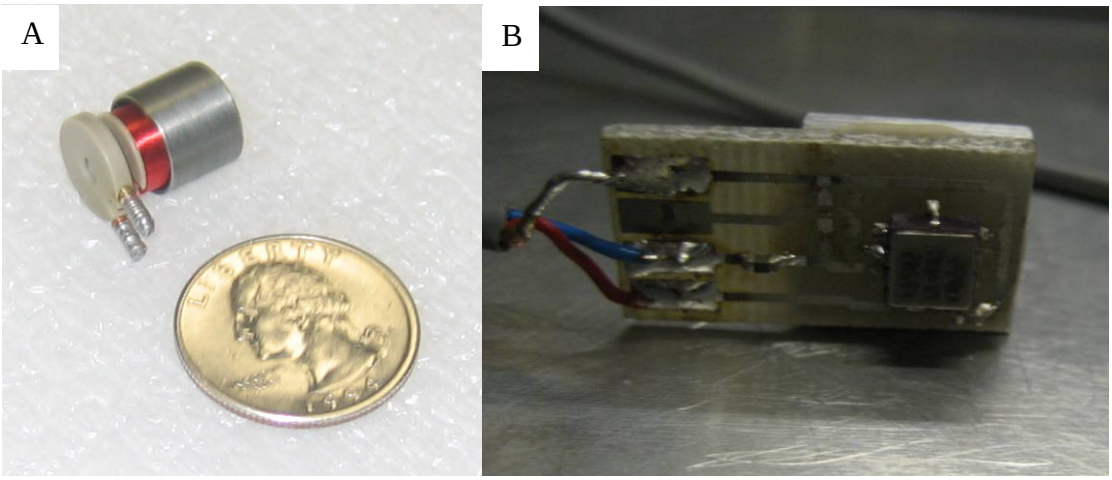

Figure 38: Left hand side photograph: the miniature voice-coil actuator (H2W, NCC01-04-001) shown in comparison to a US$ quarter coin.
Right hand side photograph: the MEMS accelerometer chip connected to a 10×20 mm^2 board.

A nine channel controller has been designed and manufactured in order to process the sensor outputs and generate the actuator inputs. When the feedback control loops are closed, the output signals of the source and radiating panel accelerometers are first independently amplified in order to implement the weighting of the two acceleration signals and then subtracted in order to obtain the error acceleration signal. For example, if the two acceleration signals are amplified with equal gains, then a relative acceleration between the coil and the magnet of each actuator unit is obtained. Or alternatively, by varying source and radiating accelerometer gains, error acceleration signals with weighting factors between 0 and 1 can be obtained. The electrical scheme of a controller channel is shown in Figure 40.

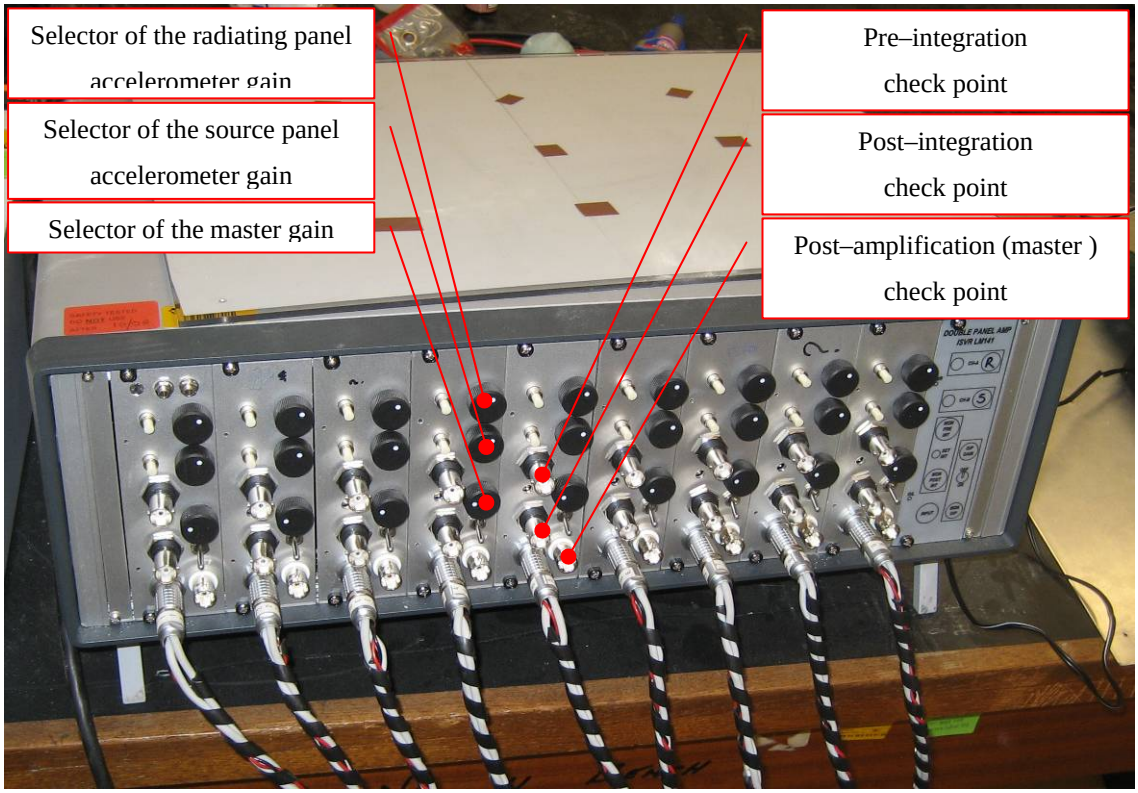

Figure 39: The front panel of the nine channel controller unit.

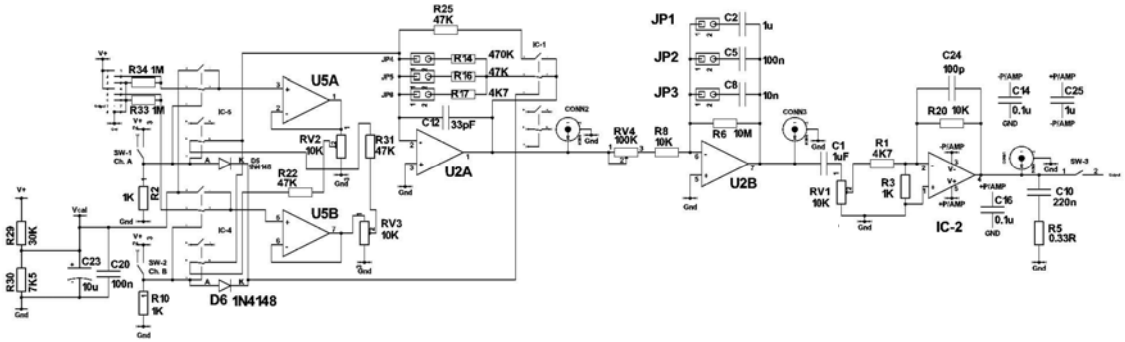

Figure 40: Electric scheme of a controller channel

The nine error acceleration signals are fed to analogue integrators with an identical amplification gain in order to provide the error velocity signals. The resulting error velocity signal therefore represents the weighted error velocity as defined in Equation (72). The error signal is then amplified by power amplifiers with an identical amplification gain in order to drive the voice coil actuators. Each control channel has three checkpoints for monitoring the three stages in each feedback loop: pre-integration, post-integration, and final, post-amplification check point (Figure 39).

Table 3: The physical properties and the geometry of the prototype smart double panel.

Parameter		Value
Dimension (mm)		414×314
Source panel	Thickness (mm)	1.0
	Density (kg/m3)	2700
	Young's modulus (GPa)	70
	Poisson's ratio	0.33
Radiating panel	Thickness (mm)	3.0
	Density (kg/m3)	255
	Young's modulus (GPa)	15
	Poisson's ratio	0.3
Mounts	*x*-position (mm)	21, 393
	y-position (mm)	16, 298
	Stiffness (N/m)	32000
Cavity depth (mm)		30
Box wall thickness (mm)		30
Shaker position (x, y) , (mm)		86.1, 111.4
Box inner dimension (mm)		414×314×400

5.2 Stability analysis of individual feedback loops using the Nyquist criterion

In the first experiment reported in this chapter, the source and radiating accelerometer signals are amplified by the same gain before the subtraction. Thus, the relative acceleration between the two force actuator ends is measured. It is then integrated, inverted and amplified by a control unit, such that a relative velocity is fed back to the reactive actuator. This corresponds to the use of a velocity weighting factor equal to 0.5 in Equation (72). Theoretically, such a collocated relative velocity sensor is dual with the reactive actuator and should thus result in unconditionally stable feedback loops which generate relative active damping. However, in practice the electrodynamic response of the transducers may prevent unconditional stability of the feedback loops and thus limit the feedback gains. Thus, the purpose of this study is to examine the stability of the relative damping control approach, described in Chapter 3, when real actuators and sensors are used.

The reactive force actuators are made of a miniature coil and magnet pairs. MEMS accelerometers with analogue integration circuits are used to measure the velocities at the two ends of the reactive actuators. Both the actuators and the sensors exhibit local electrodynamic and electromechanical effects. For example, the actuator dynamics can be modelled using the following expressions[73]:

$$i(t) = \frac{U(t)}{R} - \frac{L}{R}\frac{di}{dt} - \frac{\Psi}{R}\frac{dx}{dt}, \tag{76}$$

$$f(t) = \Psi i(t), \tag{77}$$

where $U(t)$ is the voltage between the coil ends, R is the resistance of the coil, L is the coil inductance, Ψ is the voice coil constant, and $\frac{dx}{dt}$ is the relative velocity between the magnet and the coil. According to Equation (77) the current through the actuator coil $i(t)$ can be used as an approximation of the actuator force $f(t)$.

The Nyquist criterion is used to assess the stability of a control loop. Strictly, the stability of all nine control loops should be assessed with a generalised form of the Nyquist criterion[42]. However, the stability analysis of a single control unit can be better interpreted in terms of the physics of the system. Additionally, instability of a one unit usually affects the stability of the nine channel control system. Thus the stability of a single control unit is assumed again as a necessary condition for the stability of the whole nine channel control system. The control unit considered here is located slightly off the centre of the double panel. The master gain of the controller units is set to 100 mV/V. Figure 41 shows Bode plots of the measured sensor-actuator open loop Frequency Response Function (FRF). In order to identify the control configuration that offers the best stability properties, the response functions were taken for two sensing configurations. The first uses two miniaturised piezoelectric accelerometers (Brüel&Kjaer type 4375) and the second uses two MEMS accelerometers. For the second configuration, three input/output signal conditioning configurations were also considered.

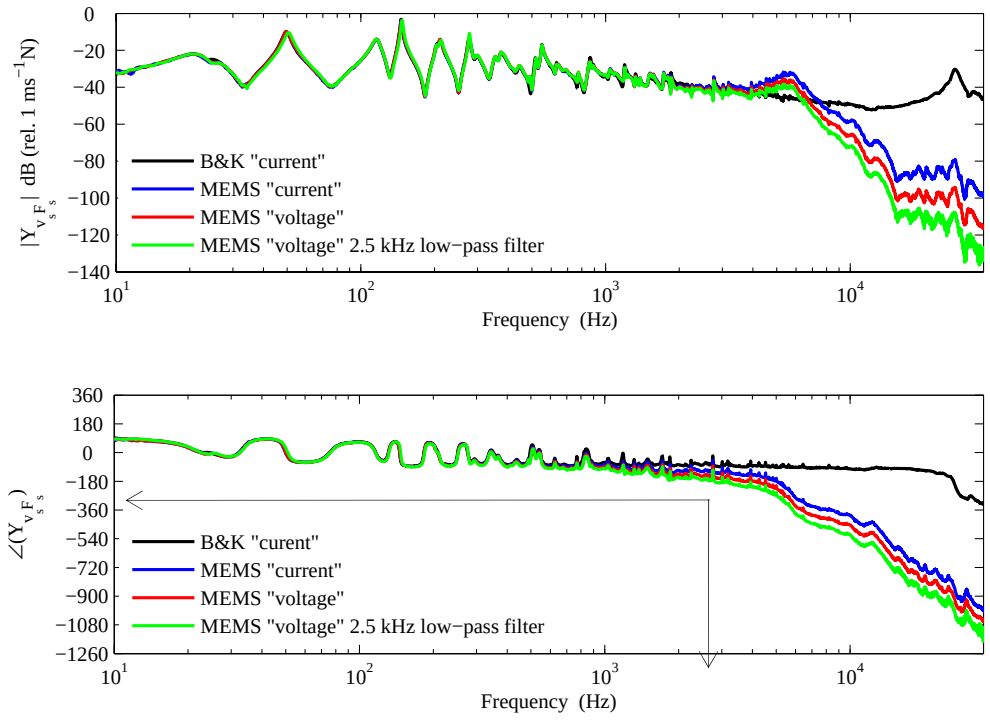

Figure 41: Bode plots of the open loop sensor-actuator FRF for piezoelectric accelerometers and different MEMS accelerometer signal conditioners. The master gain of the controller units is set to 100 mV/V.

The black line in Figure 41 shows the open loop sensor-actuator FRF with reference to the actuator current when a pair of high quality B&K piezoelectric accelerometers is

used instead of the MEMS accelerometers. The aim of using the high quality accelerometers is to provide a benchmark for the stability analysis. The phase plot shows that the phase of the open loop sensor-actuator FRF is limited between -90˚ and 90˚ up to 20 kHz. Therefore up to that frequency the two sensors and the actuator behave as dual and collocated pairs. However, at frequencies around 35 kHz there is an abrupt increase in the open loop sensor-actuator FRF amplitude and a 180˚ phase lag. The 35 kHz amplitude peak corresponds to the natural frequencies of the two seismic accelerometers. Plot A in Figure 42 shows the Nyquist plot for this case. The majority of the loops, originating from the plate resonances, are located in the two positive real quadrants. However the small loop, originating from the accelerometer resonance, crosses the real axis in the negative two quadrants. This indicates that the available gain margin is finite and the feedback loop is conditionally stable due to the dynamics of the sensor. In addition, control spillover can be expected at frequencies where the locus enters the circle with unit radius and centre at -1+0*j*.

Considering now the MEMS accelerometers, the blue lines in Figure 41 indicate that the open loop sensor-actuator FRF has positive real parts only up to approximately 1 kHz. Around approximately 5.5 kHz there is an increase of the open loop sensor-actuator FRF amplitude and a 180˚ phase lag. Again, this is due to the accelerometer fundamental resonance, which now occurs at lower frequency and is relatively more damped. Nevertheless, in the frequency range of interest (approximately up to 500 Hz), the outputs of the two types of relative velocity sensors are nearly identical. Considering now the red lines, which show the open loop sensor-actuator FRF with reference to the actuator voltage, an additional amplitude roll-off and a phase lag can be noted. These may be caused by the eddy currents in the voice coil magnet generated by the variable electromagnetic field of the coil. The green lines in Figure 41 show the open loop sensor-actuator FRF including a first order Butterworth filter with the cut-off frequency of 2.5 kHz, applied directly at the two accelerometer sensor outputs. The filter was used to further reduce the effect of the sensor resonance and to increase the available gain margin. The Bode plots indicate a further amplitude roll-off and a phase lag caused by the filter implementation. The three open loop sensor-actuator FRFs measured with the MEMS accelerometers indicate that it is preferable to drive the actuator with voltage and also to add the 2.5 kHz low-pass filter. In this way the peak at the fundamental

resonance of the accelerometers, which causes the stability problems, is effectively attenuated so that larger feedback gains can be implemented.

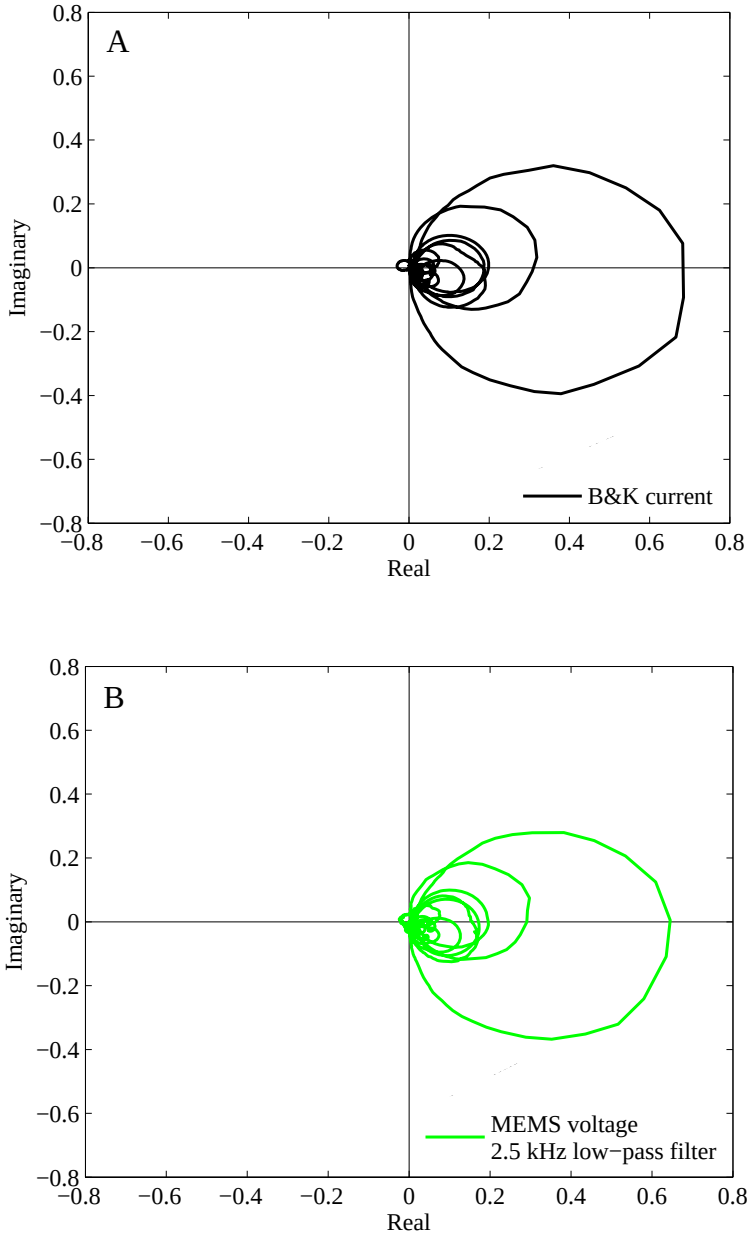

Figure 42: Nyquist plots of the open loop sensor-actuator FRF for: a) time integrated output of the two piezoelectric accelerometers with reference to the actuator current (left hand side), b) time integrated output of the two MEMS accelerometers with a 2.5 kHz low-pass filter with reference to the actuator voltage. The master gain of the controller units is set to 100 mV/V.

Plot B in Figure 42 shows the open loop sensor-actuator FRF Nyquist plot for the case when MEMS sensors with filtered outputs are used with reference to the actuator voltage. The loop in the negative real quadrants, which crosses the real axis, is again caused by the fundamental resonance of the two sensors. However, the zero-crossing

frequency is actually lower than the resonant frequency of the two accelerometers due to the additional phase lags caused by the actuator dynamics and the effects of the filter. The zero crossing frequency is approximately 2600 Hz, as indicated by the arrows in the phase diagram in Figure 41. In fact, the open loop sensor-actuator FRF amplitude at the zero crossing frequency is slightly smaller than that obtained with the high quality accelerometers (Figure 40A). The stability analysis using the Nyquist criterion indicates that the feedback loop is conditionally stable with gain margin of 34 dB. Moreover, control spillover can be expected at frequencies around 2600 Hz.

In the second experiment, nine sensor-actuator open loop frequency response functions for all feedback units of the smart panel were measured. MEMS accelerometers were chosen because of their low cost and comparatively acceptable stability properties. The low pass filter with 2500 Hz cut-off frequency was used and included in the open loop sensor-actuator FRF measurements. The open loop sensor-actuator FRFs are measured with reference to actuator current, and the integration of the output of the accelerometers was performed off-line using an ideal integrator, i.e. by multiplying the measured accelerations by $1/(j\omega)$. The upper frequency limit of the measurements was chosen to be 6400 Hz in order to include the resonant frequency of the MEMS accelerometers. Figure 43 shows Nyquist plots of nine sensor-actuator frequency response functions for all feedback units of the smart panel, numerated as in Figure 36.

Each Nyquist plot again shows majority of the circles in the right hand side of the real – imaginary plane, which are due to resonances of the double panel, and a small circle in the left hand side, which is due to the resonances of the two accelerometers. Although there are differences between individual feedback units, in general they show similar behaviour. The differences in the Nyquist plots of, for example, units 1,3,7, and 9, which should ideally be the same, indicate that there are asymmetries in the test rig and the sensor-actuator transducers, and/or non-homogeneous material properties of the panels.

Figure 44 shows the amplitudes of the nine sensor-actuator frequency response functions. The shapes of the nine open loop sensor-actuator FRF amplitudes show well separated low-frequency resonances which are due to the two panels' low order modes.

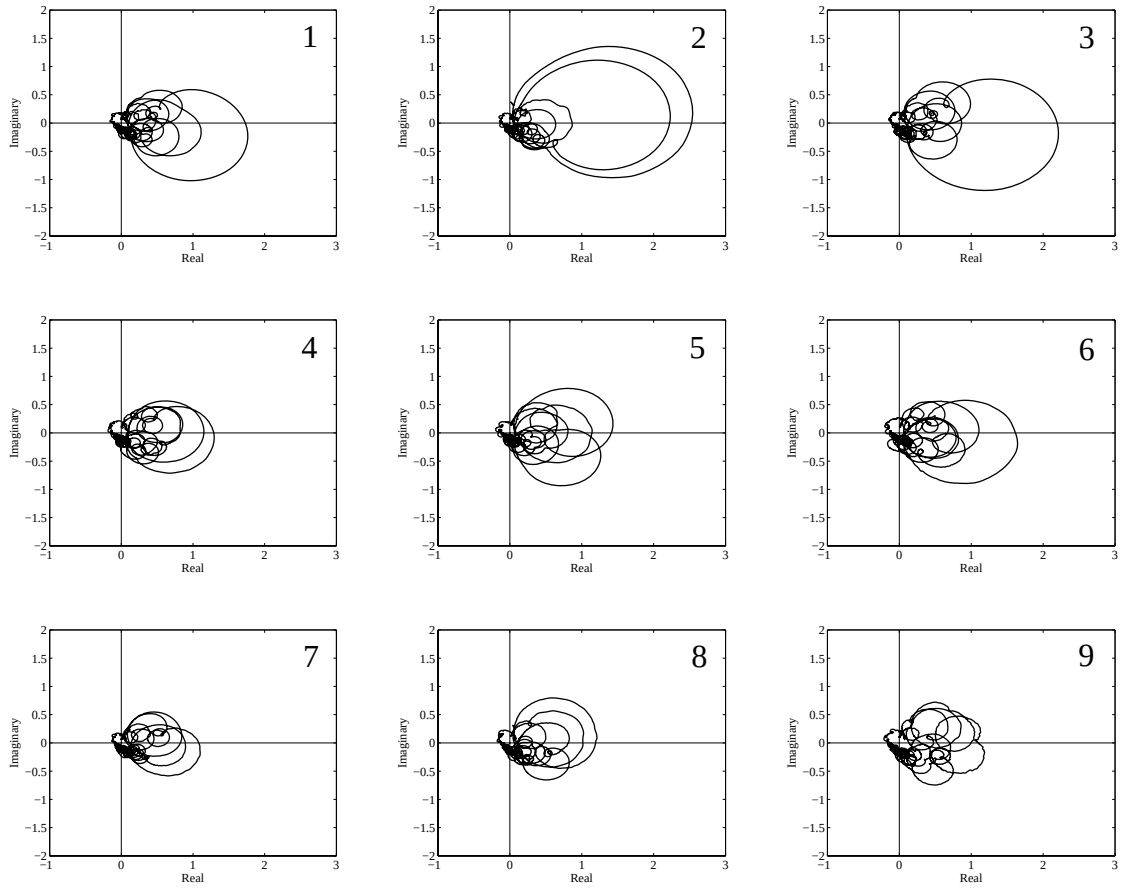

Figure 43: Nyquist plots of nine open loop sensor-actuator FRFs, with the velocity weighting factor α =0.5. The master gain of the controller units is set to 100 mV/V.

The highest amplitude values are typically between 100-200 Hz, and then roll off as the frequency increases. This effect can be attributed to the mass law which governs the response of the smart double panel, and thus the shape of the open loop sensor-actuator FRF amplitude.

However, at 5.5 kHz there is a marked increase in the amplitude of each open loop sensor-actuator FRF. This is due to the increased output of the accelerometers at their resonant frequency. On the other hand, at very low frequencies (below 100 Hz), the resonance peaks due to double panel low order modes, are somewhat lower in amplitude. This indicates that the low order mode passive damping may be relatively higher than predicted in simulations in Chapter 4.

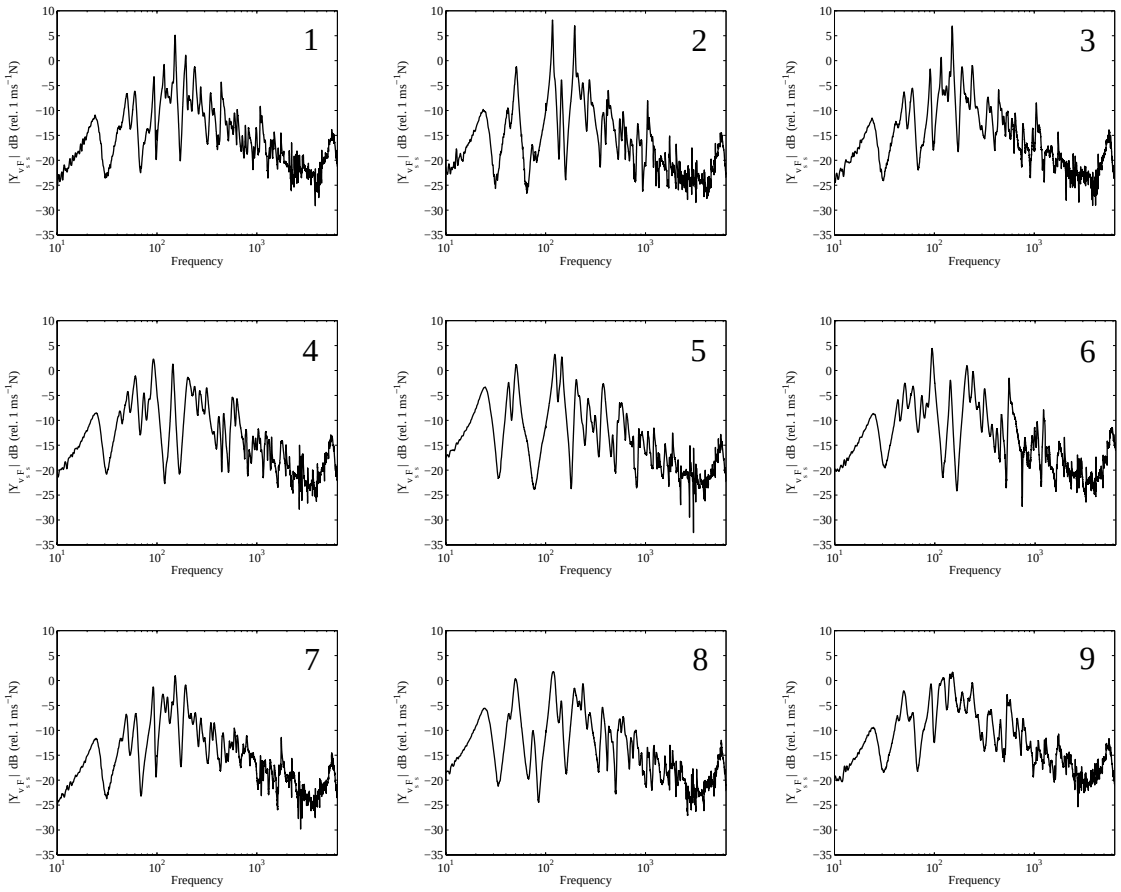

Figure 44: Amplitude Bode plots of nine open loop sensor-actuator FRFs, with the velocity weighting factor α =0.5. The master gain of the controller units is set to 100 mV/V.

Figure 45 shows the nine open loop sensor-actuator FRF phase angles. The plots show that at low frequencies the open loop sensor-actuator FRF phases are contained between -90 and 90 degrees, but at the resonant frequency of the accelerometers (5.5 kHz) the phase abruptly lags by 180 degrees for all nine feedback units. Also, there is a slow phase lag starting from 0 Hz to ∞ due to low-pass filter effects. There are no 180 degree phase lags at lower frequencies because the units feed the relative velocity back to the actuators (the velocity weighting factors equal to α =0.5).

However, if the pre-amplification gain of the source panel accelerometers is set to zero, then the feedback loops use only the radiating panel velocities. This corresponds to the case of $\alpha = 0$, and should, in accordance to the findings presented in the previous chapter, result in low frequency phase lags.

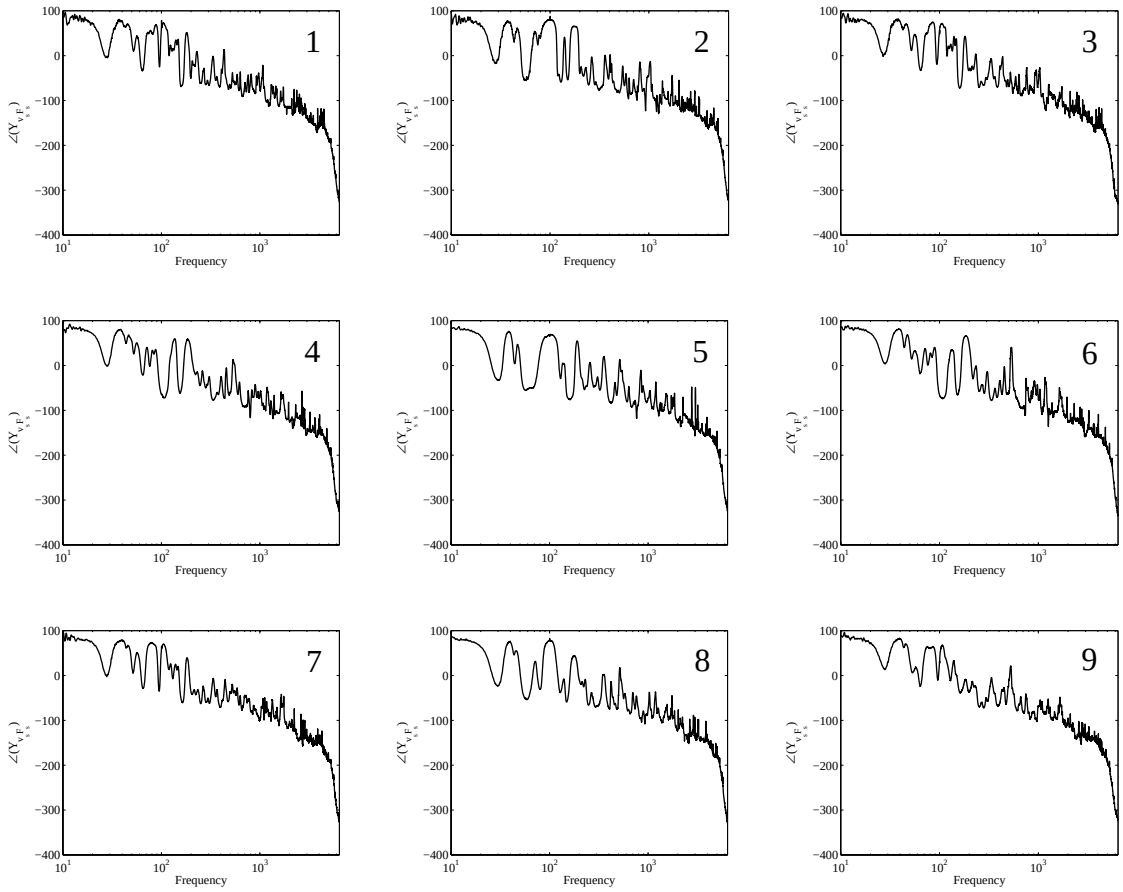

Figure 45: Phase Bode plots of nine open loop sensor-actuator FRFs, with the velocity weighting factor α =0.5. The master gain of the controller units is set to 100 mV/V.

This is indeed the case, as demonstrated in Figure 46. The nine phase plots show that the each of the nine feedback loops exhibits two successive lags of 180 degrees. The two lags occur at frequencies between 80 and 100 Hz. This can lead to the severe stability problems and the feedback gains can be further restricted due to the high amplitudes of the open loop sensor-actuator FRFs at low frequencies. In addition, a negative real part of the open loop sensor-actuator FRF at lower frequencies can cause spillover effects in the frequency range where control is aimed to reduce the response and the sound radiation of the double panel.

In order to asses the impacts of the phase lags shown in Figure 46 on the stability of the feedback loops, Nyquist plots of the nine open loop sensor-actuator FRFs are analysed next.

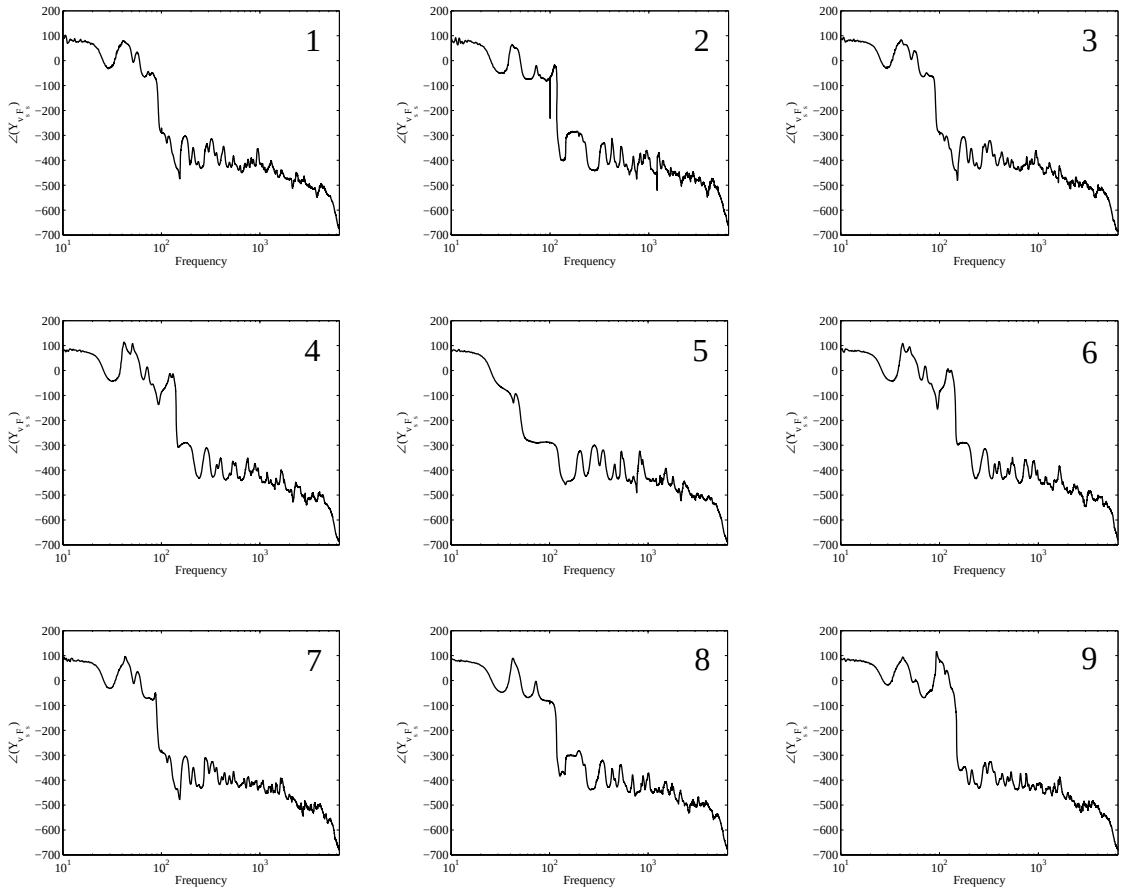

Figure 46: Phase Bode plots of nine open loop sensor-actuator FRFs, with the velocity weighting factor α =0. The master gain of the controller units is set to 100 mV/V.

.

As shown in Figure 47, the Nyquist plots for those units which are close to the edges of the clamped source panel do not show increased amplitudes of the negative real parts of the open loop sensor-actuator FRF. But if the unit number 5 is considered, which is located in the centre of the double panel, it is clear that the loop left of the ordinate axis is considerably larger than that in case with relative damping. In fact, it is large enough to restrict the feedback gain to approximately 2 Nms^{-1}. Thus, there are differences between the units located close to the edges and the centre unit.

The difference between the units close to the panel boundary and the unit in the centre of the panel can be explained by the fact that the amplitudes of the source panel point mobilities increase as the feedback unit location is changed from the clamped edge (where they are zero) to the panel centre. In other words, an actuator which reacts against the source panel close to a panel edge reacts against a rather stiff base. Therefore the velocity measured by the source panel sensor is almost zero, and does not contribute to the error signal. In contrast, an actuator which reacts against the source panel close to

the panel centre is reacting against a flexible panel, whose vibrations are then transmitted to the radiating panel sensor location via the acoustical and structural flanking paths and do contribute to the error signal. These flanking paths can be modelled as transfer mobility functions. In general, transfer mobilities do not have positive real parts only, such that the corresponding open-loop sensor-actuator FRF may also have negative real parts. This behaviour of the open-loop sensor-actuator FRF and resulting stability issues are also predicted by the theoretical model discussed in Chapter 4 (see Figure 29 and Figure 31).

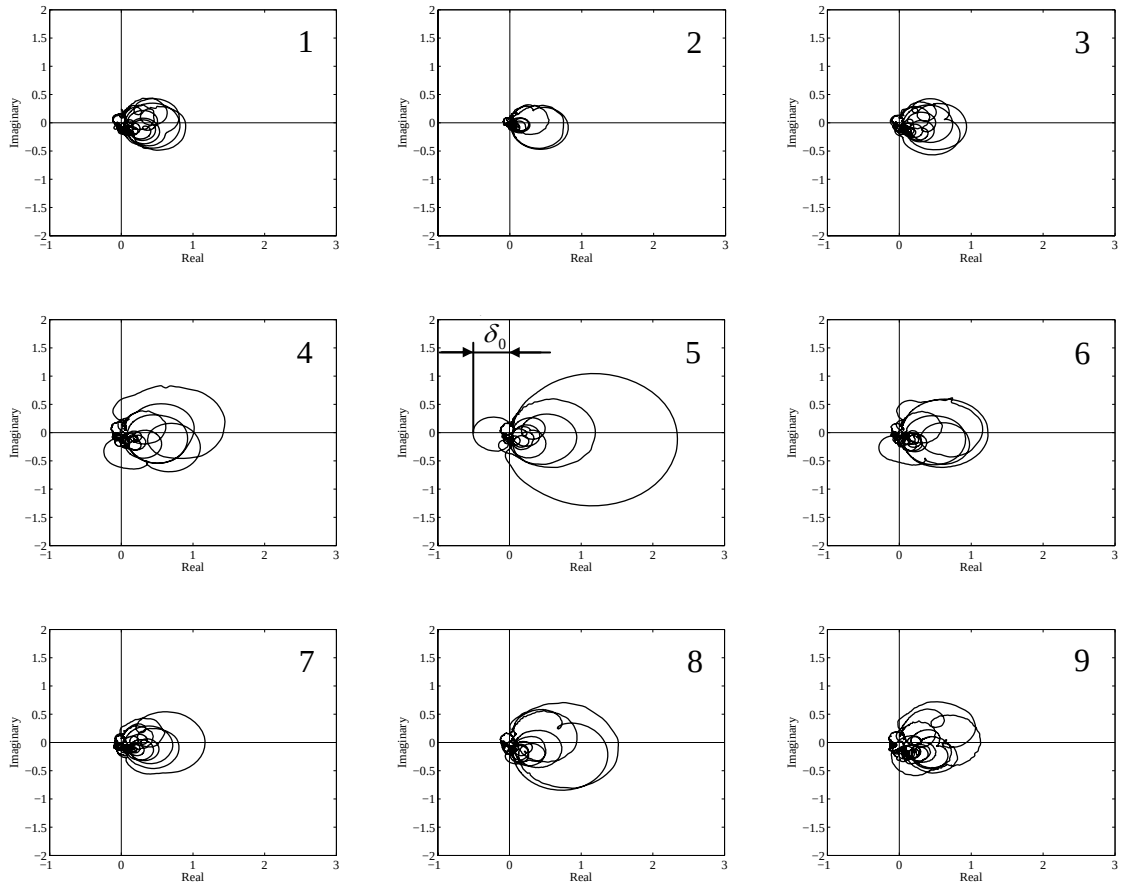

Figure 47: Nyquist plots of nine open loop sensor-actuator FRFs, with the velocity weighting factor α =0. The master gain of the controller units is set to 100 mV/V.

In order to more clearly demonstrate the effects of the velocity weighting factor on the available gain margin, additional two sets of measurements were performed. The first set involved measurements of nine radiating panel velocity signals with reference to nine corresponding reactive actuator forces, $\left(\frac{v_{rc}}{F_C}(j\omega)\right)_{1,1}, \left(\frac{v_{rc}}{F_C}(j\omega)\right)_{2,2}, \ldots \left(\frac{v_{rc}}{F_C}(j\omega)\right)_{9,9}$.

The second set involved a measurement of nine source panel velocity signals with reference to nine corresponding reactive actuator forces $\left(\frac{v_{rc}}{F_C}(j\omega)\right)_{1,1}, \left(\frac{v_{rc}}{F_C}(j\omega)\right)_{2,2}, \ldots \left(\frac{v_{rc}}{F_C}(j\omega)\right)_{9,9}$. The eighteen FRFs were used for an off-line reconstruction of the open loop sensor-actuator FRFs with arbitrary velocity weighting factors according to the following expressions. The error velocity in case of weighted velocities is given by:

$$v_E = v_{rc}(1-\alpha) - v_{sc}\alpha \ , \tag{78}$$

If Equation (78) is divided by the reactive actuator net force $F_C(j\omega)$ then it yields:

$$\frac{v_E}{F_C}(j\omega) = \left[\frac{v_{rc}}{F_C}(j\omega)\right](1-\alpha) - \left[\frac{v_{sc}}{F_C}(j\omega)\right]\alpha \ , \tag{79}$$

Therefore, if the frequency response functions $\frac{v_{rc}}{F_C}(j\omega)$, and $\frac{v_{sc}}{F_C}(j\omega)$ in Equation (79) are known then it is possible to reconstruct off-line the sensor actuator open loop frequency response functions $\frac{v_E}{F_C}(j\omega)$ for an arbitrary velocity weighting factor.

The nine open loop sensor-actuator FRFs were reconstructed using the results of the two sets of measurements according to Equation (79). Then the maximum negative real parts of the nine open loop sensor-actuator FRFs were calculated and plotted against the velocity weighting factor α in Figure 48. Each of the plots in Figure 48 shows two types of results. The faint lines show the maximum negative real part of the open loop sensor-actuator FRFs, indicated by δ_0 in the centre plot of Figure 47, plotted against the velocity factors ranging for zero to one, for the full frequency range 10-6400 Hz. Therefore the available gain margins $1/\delta_0$, for each feedback unit can be calculated as a function of velocity weighting factor. However, it is not clear from such a representation whether the maximum negative real parts occur at low frequencies (due to the velocity weighting factor used), or at high frequencies (due to the dynamics of the sensors). For

that reason the sensor-actuator frequency response functions were evaluated up to 2400 Hz, and the maximum negative real parts were determined for that frequency range, in order to capture the low frequency behaviour only.

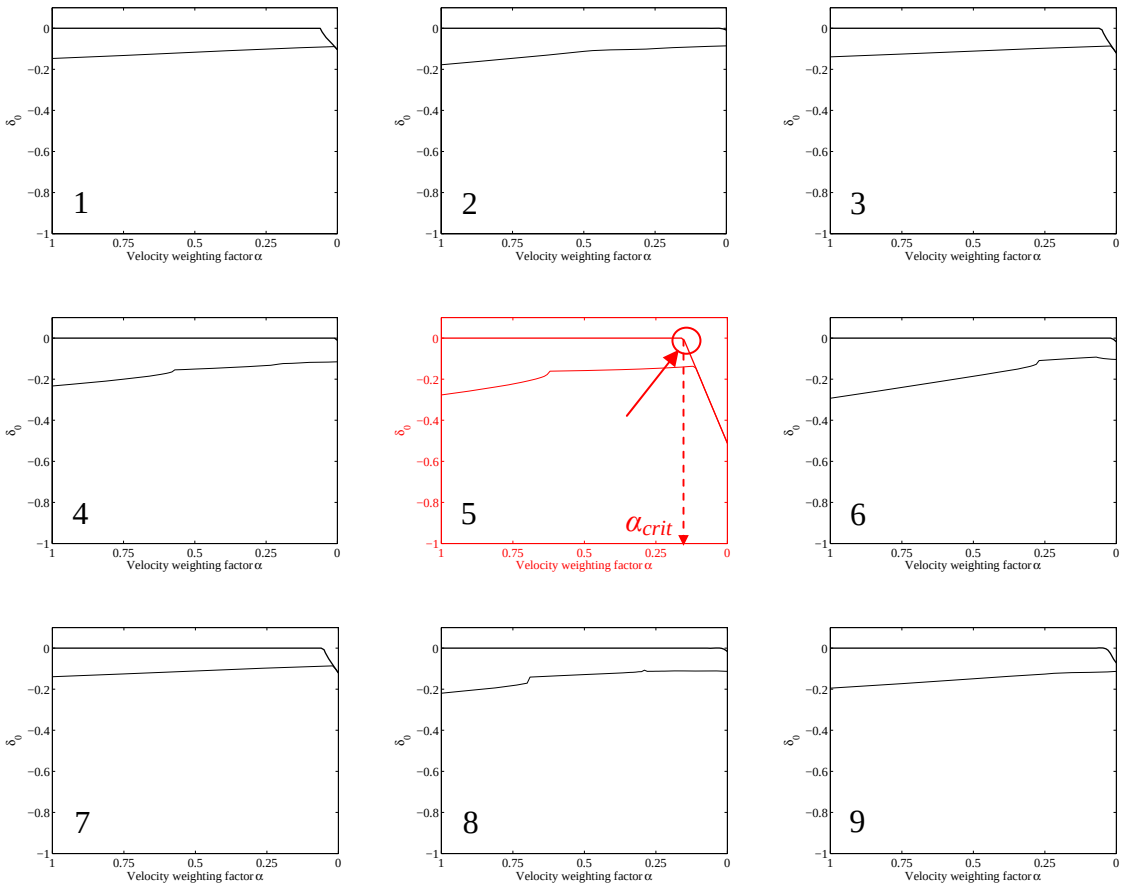

Figure 48: The maximum negative real parts of the open loop sensor-actuator FRFs, δ_0, plotted against the velocity weighting factor α, as calculated from experimental results. Solid lines show the results when the frequency range between 10 and 2400 Hz is considered, and the faint lines show the results when the full frequency range (10-6400 Hz) is considered.

For the low frequency case, as shown by the solid line in plots in Figure 48, the graphs illustrate the phenomenon more clearly. As the velocity weighting factor α decreases from one to zero, the δ_0 equals zero down to the critical velocity weighting factor, α_{crit} (see the centre plot in Figure 48). As the velocity weighting factors decrease further, δ_0 linearly decreases down to negative values. The effect is particularly visible at control unit number 5, because it is located at the centre of the panel. The knee-shaped plots are very similar to those obtained theoretically in Chapter 4, depicted in Figure 30. However, when comparing Figure 48 to Figure 30, the critical velocity weighting factor

obtained experimentally (0.2) is considerably lower than that obtained theoretically (0.375). This may be due to internal damping in each of the voice-coil actuators, which is generated by the viscous air flow through a small ring-shaped orifice between the actuator coil and magnet. The relative damping in the coil-magnet pairs effectively introduces an additional damper with a velocity weighting factor of $\alpha = 0.5$. This results in an increased value of the true velocity weighting factor in comparison to the apparent velocity weighting factor. The effects related to the passive damping of the coil-magnet pairs are discussed in more details in Chapter 6.

Considering now the remaining feedback units, the values of the critical velocity weighting factors are even lower. This may be attributed to the proximity of the clamped edges of the source panel, which tends to reduce the values of the α_{crit}. Such findings qualitatively agree with the simulated values of α_{crit}, plotted in Figure 31 over the surface of the double panel.

In conclusion, the stability analysis of the individual feedback loops indicates that, in order to avoid the low frequency phase lags of the open loop sensor-actuator FRFs, and to increase the gain margin, it is necessary to use an error signal comprised of two weighted sensor outputs per each reactive actuator.

5.3 Stability analysis of the nine feedback loops using generalised Nyquist criterion

In the third experiment performed within the scope of the stability investigation, the full 9×9 matrix of the sensor actuator frequency response functions is analysed using the generalised Nyquist criterion[42] for different velocity weighting factors. In order to perform such an analysis, two 9×9 matrices of the frequency response functions were measured. The first matrix, $\mathbf{G_R}(j\omega)$, is a fully populated matrix of the frequency response functions between the nine radiating panel velocity sensors and the nine reactive actuators:

$$\mathbf{G_R}(j\omega)=\begin{bmatrix} \left(\frac{v_{rc}}{F_C}(j\omega)\right)_{1,1} & \left(\frac{v_{rc}}{F_C}(j\omega)\right)_{1,2} & \cdots & \left(\frac{v_{rc}}{F_C}(j\omega)\right)_{1,9} \\ \left(\frac{v_{rc}}{F_C}(j\omega)\right)_{2,1} & \left(\frac{v_{rc}}{F_C}(j\omega)\right)_{2,2} & \cdots & \left(\frac{v_{rc}(j\omega)}{F_C(j\omega)}\right)_{2,9} \\ \vdots & \vdots & \ddots & \vdots \\ \left(\frac{v_{rc}}{F_C}(j\omega)\right)_{9,1} & \left(\frac{v_{rc}}{F_C}(j\omega)\right)_{9,2} & \cdots & \left(\frac{v_{rc}}{F_C}(j\omega)\right)_{9,9} \end{bmatrix} \tag{80}$$

where $\left(\frac{v_{rc}}{F_C}(j\omega)\right)_{i,j}$ is the frequency response function between the *i*-th radiating panel sensor and the *j*-the reactive actuator.

The second matrix, $\mathbf{G_S}(j\omega)$, is a fully populated matrix of the frequency response functions between the nine source panel velocity sensors and the nine reactive actuator forces:

$$\mathbf{G_S}(j\omega)=\begin{bmatrix} \left(\frac{v_{sc}}{F_C}(j\omega)\right)_{1,1} & \left(\frac{v_{sc}}{F_C}(j\omega)\right)_{1,2} & \cdots & \left(\frac{v_{sc}}{F_C}(j\omega)\right)_{1,9} \\ \left(\frac{v_{sc}}{F_C}(j\omega)\right)_{2,1} & \left(\frac{v_{sc}}{F_C}(j\omega)\right)_{2,2} & \cdots & \left(\frac{v_{sc}}{F_C}(j\omega)\right)_{2,9} \\ \vdots & \vdots & \ddots & \vdots \\ \left(\frac{v_{sc}}{F_C}(j\omega)\right)_{9,1} & \left(\frac{v_{sc}}{F_C}(j\omega)\right)_{9,2} & \cdots & \left(\frac{v_{sc}}{F_C}(j\omega)\right)_{9,9} \end{bmatrix} \tag{81}$$

where $\left(\frac{v_{sc}}{F_C}(j\omega)\right)_{i,j}$ is the frequency response function between the *i*-th source panel sensor and the *j*-the reactive actuator.

The full 9×9 matrix of the sensor-actuator frequency response functions for a given velocity weighting factor can thus be calculated as:

$$\mathbf{G}(j\omega)=(1-\alpha)\mathbf{G_R}-\alpha\mathbf{G_S} \tag{82}$$

Assuming that the plant and the controller are individually stable, the generalised Nyquist criterion states that the closed loop system is stable if and only if, for a stable open loop system, the locus of the determinant of the measured return difference matrix, $D(j\omega) = \det[\mathbf{I} + \mathbf{H}(j\omega)\mathbf{G}(j\omega)]$, does not encircle or passes through the origin, as the angular frequency, ω, varies between $-\infty$ and $+\infty$.

The matrices $\mathbf{G_R}$ and $\mathbf{G_S}$ were taken for two different feedback signal cases. The first case included FRF measurements with reference to the actuator currents, including the low-pass filters with 2.5 kHz cut-off frequency, but using ideal off-line integrators. In the second case the FRF measurements were taken with reference to the actuator voltages, including the 2.5 kHz low pass filters, but also including the real controller units (integrators and amplifiers). In the forthcoming text the first case is referred to as "the current command" case, whereas the second case is referred to as "the voltage command" case. The matrix $\mathbf{G}(j\omega)$ was calculated for the two cases by using Equation (82). The $D(j\omega)$ was calculated using the gain matrix $\mathbf{H}(j\omega) = g \cdot \mathbf{I}$, where the value of g was 0.1, which corresponds to the master gain settings of 100mV/V for each channel of the controller.

The stability analysis using generalised Nyquist criterion is not as straightforward as that for the single channel feedback loops presented in Section 5.2. In fact, the locus of $\det[\mathbf{I} + \mathbf{H}(j\omega)\mathbf{G}(j\omega)]$ does not simply get bigger as the nine feedback gains are increased. It also changes shape as the maximum feedback gains g of the decentralised feedback control system are altered[42]. Thus it is not easy to obtain a clear geometric guide to the relative stability of the system[42].

Figure 49 shows the locus of $D(j\omega)$ for the current command and voltage command cases, assuming the velocity weighting factor $\alpha = 0.5$. For the feedback gains used, the nine channel system is stable as the locus of the determinant of the return difference matrix does not encircle the origin nor passes through the origin. By increasing the gains of the nine feedback loops it is possible to change the locus of the determinant such that the Nyquist stability criterion is just about to be violated, in which case the maximum gain limit of the nine feedback loops is reached. However, for practical reasons the maximum gains used during the experimental tests presented in Chapter 6 were selected

low enough to avoid spillover effects rather then by plotting and analysing the locus of the $D(j\omega)$, which can vary as the measurement conditions change.

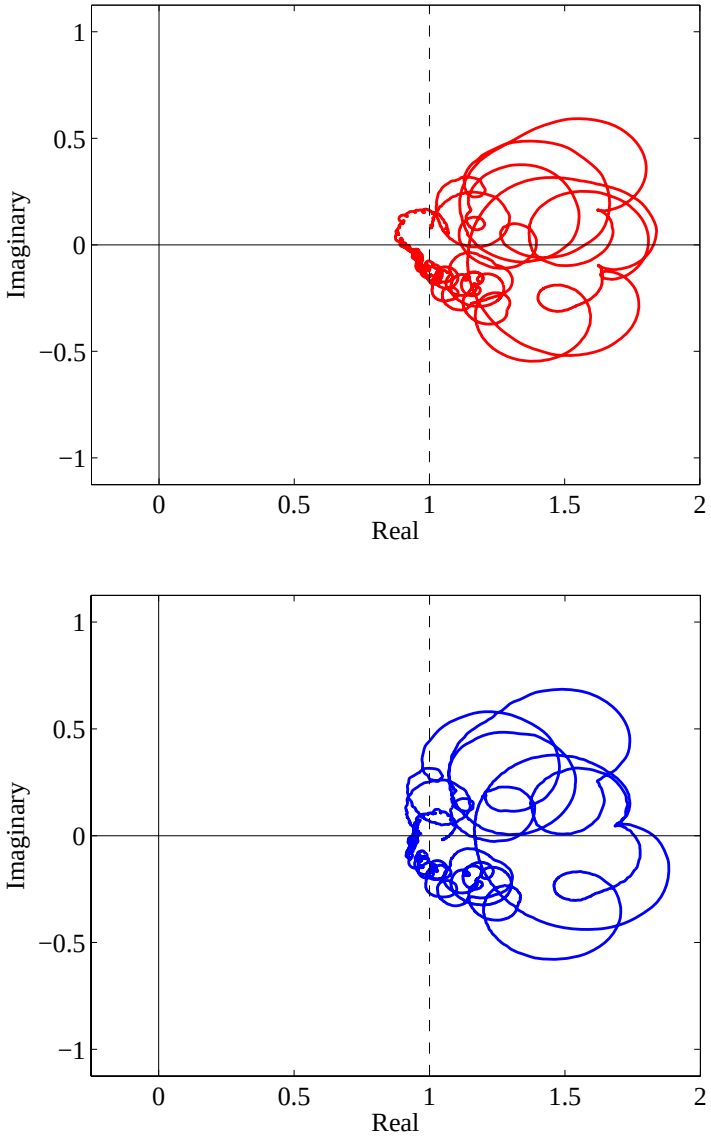

Figure 49: The locus of $D(j\omega) = \det[\mathbf{I} + \mathbf{H}(j\omega)\mathbf{G}(j\omega)]$. The velocity weighting factor equals to α = 0.5. The top plot shows the locus with reference to the actuator current, and bottom plot shows the locus with reference to the actuator voltage. The value of the nine open loop feedback gains g is 0.1.

5.4 Summary

In Chapter 5 the design and experimental testing of a prototype smart panel demonstrator is described. The prototype smart panel is equipped with nine decentralised velocity feedback units. Electrical components of the experimental

demonstrator included nine miniature, lightweight voice coil actuators; eighteen miniature, low-cost Micro Electro Mechanical Systems (MEMS) accelerometers; and a nine channel analogue feedback controller. The mechanical components of the demonstrator included the source and radiating panels with sensor and actuator junctions; a rigid clamping system; and a Perspex box.

Using this setup, the stability properties anticipated in the theoretical study were experimentally verified, by measuring sensor-actuator open loop frequency response functions. The Nyquist criterion was used to examine the stability properties of each feedback loop with respect to the different velocity weighting factors. In addition, generalised Nyquist criterion was used to show the stability of the nine channel system.

It was shown that the indirect actuation paths, which are due to acoustical and structural coupling of the two panels, cause stability problems with feedback loops that use only one sensor per reactive actuator. It was found that it is necessary to use both source and radiating panel sensors with appropriate velocity weighting factors, in order to avoid low frequency phase lags in the sensor-actuator open loop frequency response functions. However, even if the feedback loops are closed using the correct velocity weighting factors, the maximum feedback gains were limited due to internal resonance of the sensors. The effect of the sensor dynamics was reduced by applying low-pass filtering of the sensor outputs and by using a voltage command to the actuators rather then a current command.

6 Global control effects of the smart double panel

This chapter presents the experiments carried out in order to test the effectiveness of the smart panel active control in terms of the reductions in radiating panel mean velocity and sound power radiation.

The experimental procedure is described first. Second, the passive sound radiation is discussed with reference to three different radiating panels and two different cavity depths in the frequency range up to 3200 Hz. Third, the effectiveness of the active control system in reducing the radiated sound power up to 500 Hz is assessed as a function of feedback gains for the case with relative velocity feedback. Fourth, the impact of the velocity weighting factor on the radiated sound power is analysed. Fifth, the broad band (0-3200 Hz) effects of the active control system on the radiated sound power and the mean velocity of the radiating panel are presented for optimal feedback gains and velocity weighting factors. Finally, the noise reduction performance of the active control system is compared to the performance of a traditional passive treatment of comparable weight.

6.1 Experimental procedure

In order to assess the performance of the control system in terms of attenuation of the sound power radiation, the double panel was mounted on a Perspex box, which, as shown in Figure 50, has a shaker inside that generates the primary disturbance on the source panel. As shown in Figure 50, a pair of rigid aluminium frames is used to clamp the smart panel on the open side of the box. The box is made with relatively thick plates of Perspex so that the transmission of sound generated inside the box is minimised by the heavy and thick walls. The thickness of the Perspex plates was chosen to be 30 mm and below 5 kHz the sound transmission through thin panels mounted on the box top is at least 10–20 dB higher than the flanking component radiated by the Perspex walls[56]. In this way it is ensured that the majority of the exterior sound is generated by the structure-borne and airborne sound transmission through the smart double panel. With this arrangement it is therefore possible to assess the reduction of sound radiation through the smart panel even when the control system is working and possibly

attenuates the passive sound transmission by up to 5–15 dB. As can be noticed in Figure 50, a set of electric connectors is arranged on one wall of the box to enable the electrical connection between the nine source panel sensors and nine actuators and with the controller unit.

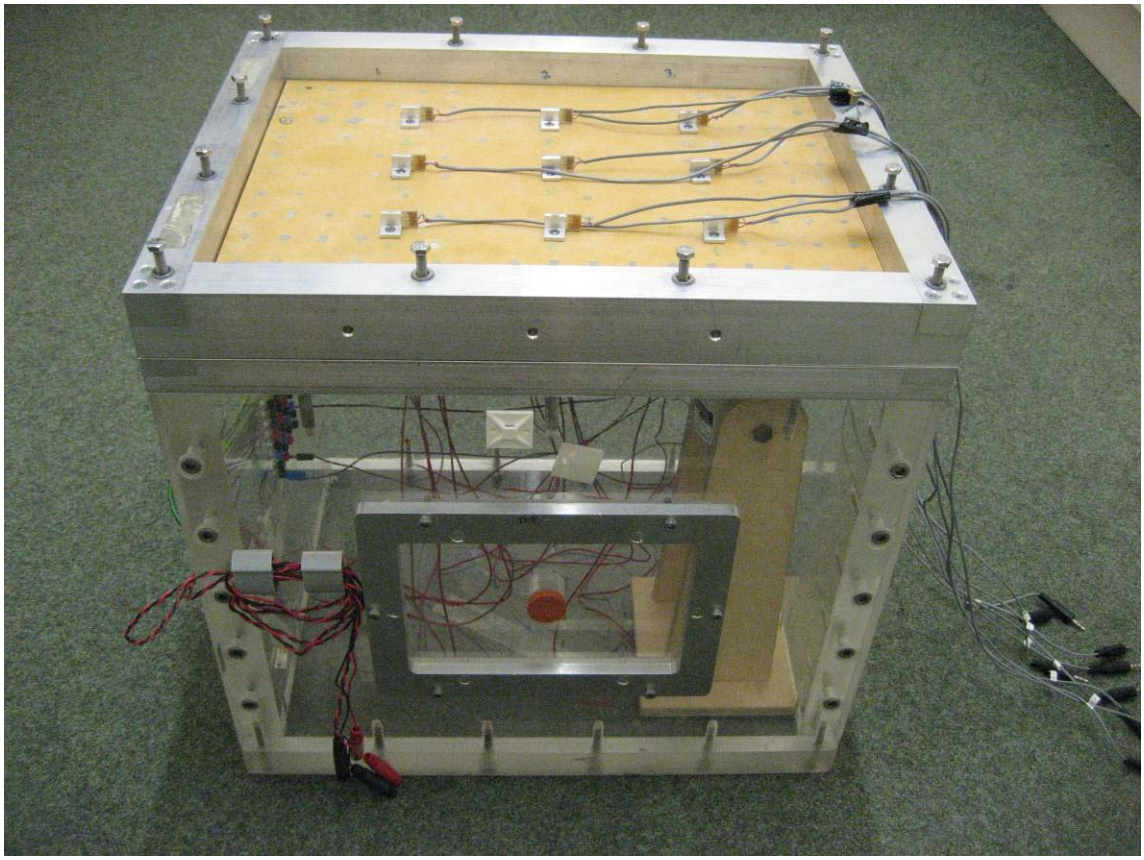

Figure 50: The experimental test facility for the measurements of the radiated sound power in the anechoic chamber.

Using the box in this manner can introduce certain problems with the measurement results. These are due to the coupling of the source panel with the box acoustical cavity. This can affect the measurement at the acoustic resonant frequencies[56]. Nevertheless, the smart panel was tested using the box method because this configuration enables a good estimate of the panel sound radiation using the anechoic chamber sound power measurement method. The method has been used in the past for testing of similar types of smart panels[56,67,70]. Thus, it is possible to compare results with the previously obtained test data.

As shown in Figure 51, the double panel was mounted on the testing facility in an anechoic chamber and was excited by a structural disturbance provided by a shaker

attached to the source panel. Random, white noise excitations were applied in frequency bands 0-500 Hz and 0 to 3.2 kHz. The testing facility was placed on a wooden floor made with a set of panels in order to approximate the sound radiation effect of a baffled panel. The nine-channel controller described in Chapter 5 was used with different feedback control gains and velocity weighting factors in ranges that guaranteed the feedback control system stability.

Figure 51: The experimental test setup for the measurements of the radiated sound power in the anechoic chamber.

In order to estimate the total radiated sound power from the panel with and without control, the sound pressure level was measured in nine positions around the box, according to the standard procedure described by the ISO 3744. The measurements are analysed in terms of narrow band frequency response functions between the averaged sound pressure measured by the nine microphones and the excitation force of the primary disturbance source (shaker) in the frequency range 0-500 Hz and 0–3.2 kHz.

Measurements of the spatially averaged mean velocity of the radiating panel were also performed using a laser vibrometer for selected cases. The experiments were carried out in order to evaluate how much and in which way the smart panel vibrations vary when the nine decentralized control units are turned on. As for the experiment in the anechoic chamber, the panel was mounted on the test box and was excited by a structural disturbance provided by a shaker attached to the source panel (Figure 52).

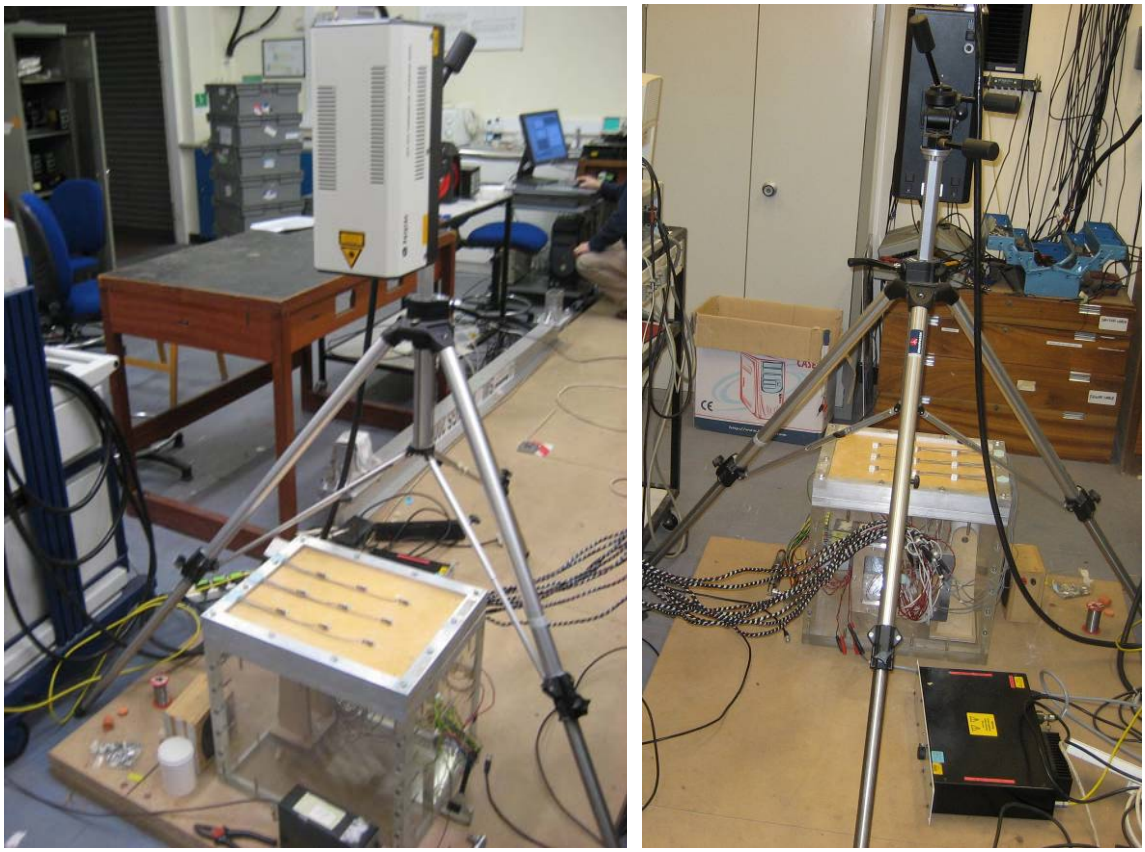

Figure 52: The experimental test setup for the measurements of the radiating panel vibration using the laser vibrometer.

White noise shaker excitations were used in the frequency band between 0 and 3.2 kHz. The laser vibrometer was equipped with a scanning system which enabled the

measurement of the panel transverse vibration over an evenly distributed grid of 187 points. In this way 187 frequency response functions were measured which give the spatially averaged transverse velocity of the radiating panel per unit excitation of the shaker with and without the nine control units turned on. The 9 channel controller described in Chapter 5 was used with 9 equal feedback control gains and velocity weighting factors that were found to produce the best reductions of the radiated sound power in the frequency band 0-3.2 kHz.

6.2 Passive sound radiation of the smart panel

The purpose of the experimental study presented in this section is to demonstrate passive properties of the tested double panels which may be important for the performance of the active control arrangement. As discussed in Chapter 2, sound transmission through double panels is characterised by the mass-air-mass resonance effect[22]. The mass-air-mass resonant frequency, ω_0, for unbounded plates is given by Equation 61. Below the mass-air-mass resonant frequency the sound transmission is rather high and characterised by well separated resonances[22,23]. Above the mass-air-mass resonance frequency the sound transmission decreases with increasing of frequency, (Equations (62,64)).

Figure 53 shows the measured narrow band total radiated sound power per unit structural primary excitation input. The spectra were measured by using the experimental procedures described in the previous section. In this experiment the radiating panel material was varied in order to investigate the influence of the different properties of the radiating panel on the spectrum of the radiated sound power. In addition to the Honeycomb radiating panel, an aluminium and a Perspex radiating panels were also tested. The geometry and mechanical properties of the aluminium panel are the same as those of the source panel. The Perspex panel is 3 mm thick, with Young's modulus of 4 GPa and mass density of 1180 kg/m^3. The cavity depth was also varied in order to investigate its influence to the spectrum of the radiated sound power. Therefore, in addition to the 30 mm deep air cavity, a shallow cavity was also used with the depth of 13 mm in combination with each radiating panel material.

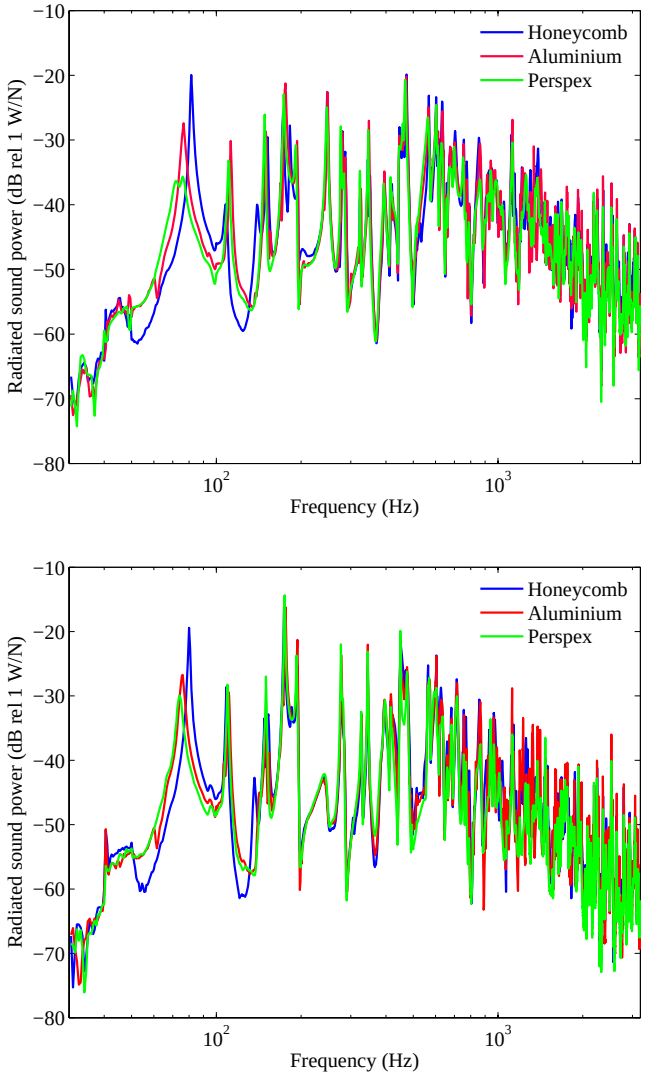

Figure 53: Radiated sound power plotted against frequency in case of the deep cavity arrangement (top) and the shallow cavity arrangement (bottom). Blue lines are in the case of the Honeycomb radiating panel, red lines are in the case of the aluminium radiating panel, and green lines are in case of the Perspex radiating panel.

The results with the deep cavity are shown in the top plot, whereas the results using the shallow cavity are shown on the bottom plot in Figure 53. The sound power radiation spectra show well separated resonances at frequencies below approximately 500 Hz, which are due to the lightly damped low-order modes and the mass-air-mass resonance effect of the double panel. At higher frequencies, above approximately 500 Hz, the sound radiation is governed by the mass law, such that the radiated sound power decreases with increase of frequency by 12 dB per octave band.

The effects produced by the variation of radiating panel material are most notable at the lowest resonant frequency of the system, which decreases with the increase in the weight of the radiating panel. Thus the Honeycomb radiating panel with high stiffness to density ratio yields the highest first natural frequency, whereas the use of a Perspex radiating panel with low stiffness to density ratio results in the lowest first natural frequency. In addition, the sound radiation at the lowest natural frequency decreases as the mass of the radiating panel is increased.

The two plots in Figure 54 show the effect of the cavity depth for Honeycomb and Perspex radiating panels.

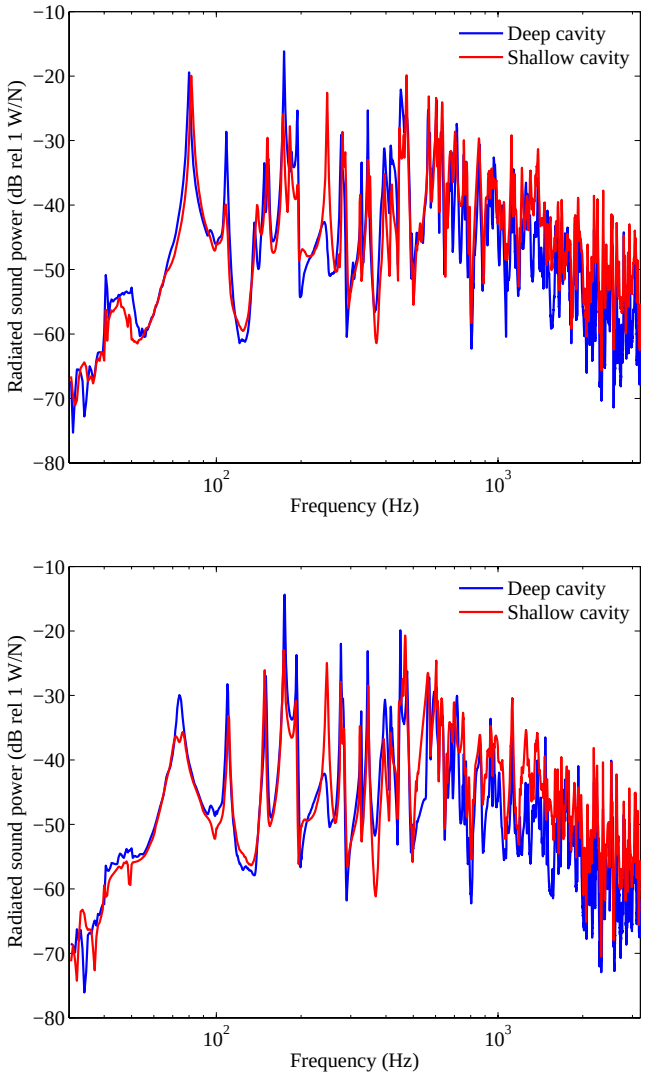

Figure 54: Radiated sound power plotted against frequency in case Honeycomb (top) and Perspex (bottom) radiating panels. The blue lines are in the case of the deep cavity arrangement and the red lines are in the case of the shallow cavity arrangement.

The results with the shallow and the deep cavity are rather similar at low frequencies. However, at high frequencies, where the sound radiation is governed by the mass law, the deep cavity configurations radiate approximately 5 dB less sound power (blue lines) than the shallow cavity configurations (red lines). This is related to the influence of the cavity depth on the mass-air-mass resonance. The deep cavity mass-air-mass resonance is at 280 Hz for the Perspex plate and 450 Hz for the Honeycomb plate. In case of the shallow cavity they are at 420 Hz for the Perspex plate and 680 Hz for the Honeycomb plate. The higher is the mass-air-mass resonant frequency, the wider is the low-frequency range where the sound radiation is controlled by damping. As a result, the sound transmission in the mass controlled high-frequency range is shifted upwards for the shallow cavity arrangements.

Considering now the characteristics of the sound radiation for all six cases, the following conclusions can be drawn. The largest sound radiation occurs at the low frequencies, below the mass-air mass resonant frequencies. This low frequency range can be approximated as the range between 30 Hz and 500 Hz for all six cases. In addition, the low frequency noise is characterised by resonant sound radiation, primarily due to the lightly damped modes of the radiating panel mounted on the flexible springs. For this reason, decentralised MIMO control systems of the smart panel, which generate active damping, are targeted at control below the mass-air-mass resonance frequency, in the frequency range 0-500 Hz.

6.3 Relative velocity feedback – effects of different feedback gains

The aim of the study presented in this section is to illustrate the effects of the control system on low frequency sound radiation by varying the feedback gain of the nine control units. The source and radiating panel accelerometer signals were used with the same pre-amplification gains, such that the effective velocity weighting factor is 0.5.

The performance of the active control systems is assessed in terms of the reduction in total radiated sound power. The nine feedback gains are set such that each feedback loop

operates using the same feedback gain. Since, as described in Chapter 5, the feedback loops are conditionally stable, the implementation of high feedback gains could lead to control spillover at higher frequencies. For that reason the upper limit for the feedback gains had to be chosen low enough to not cause large spillover effects or instability. Because the most significant sound radiation occurs at frequencies up to approximately 500 Hz, as indicated in the previous section, the measurements were taken up to this frequency.

The measurements were performed with three different radiating panel materials and two different air cavity depths. The same materials and cavity depths were used as in the tests of passive sound radiation presented in Section 6.2.

Figure 55 shows the narrow band spectra of total radiated sound power for three deep cavity arrangements. The top plot in Figure 55 shows the results with the Honeycomb radiating panel, the middle plot is for the aluminium radiating panel, and the bottom plot is for the Perspex radiating panel.

The mechanical properties and the geometry of the Perspex and aluminium radiating panels are given in the previous section. The blue lines in all plots show the radiated sound power with the sensor and actuator components mounted onto the source and radiating panels when the active control system is switched off. The additional coloured lines in plots show the radiated sound power with the active control system switched on for different values of the nine feedback gains. In the plot legends the feedback gains are represented in terms of mV/V of the amplification factor of the final stage of each of the controller channels. Therefore they do not represent the dimensional velocity feedback gains in Nsm^{-1}; however they do provide relative relations between the different gains applied.

Figure 56 shows the narrow band spectra of total radiated sound power for three shallow cavity arrangements. The top plot in Figure 56 shows the results with the Honeycomb radiating panel, the middle plot is for the aluminium radiating panel, and the bottom plot is for the Perspex radiating panel.

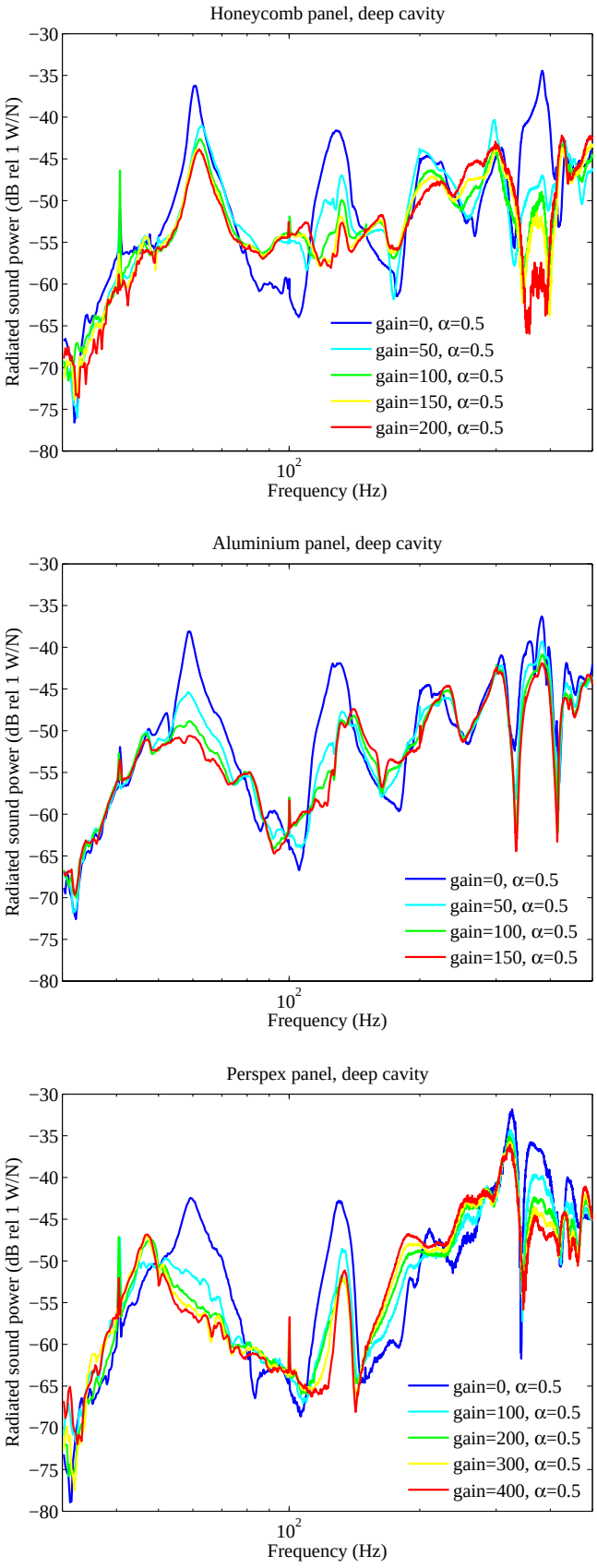

Figure 55: Radiated sound power plotted against frequency in case when Honeycomb (top), aluminium (centre) and Perspex (bottom) radiating panels are used with the deep air cavity. Sound power spectra are shown for increasing feedback gains in mV/V (see legends). Velocity weighting factors equal 0.5.

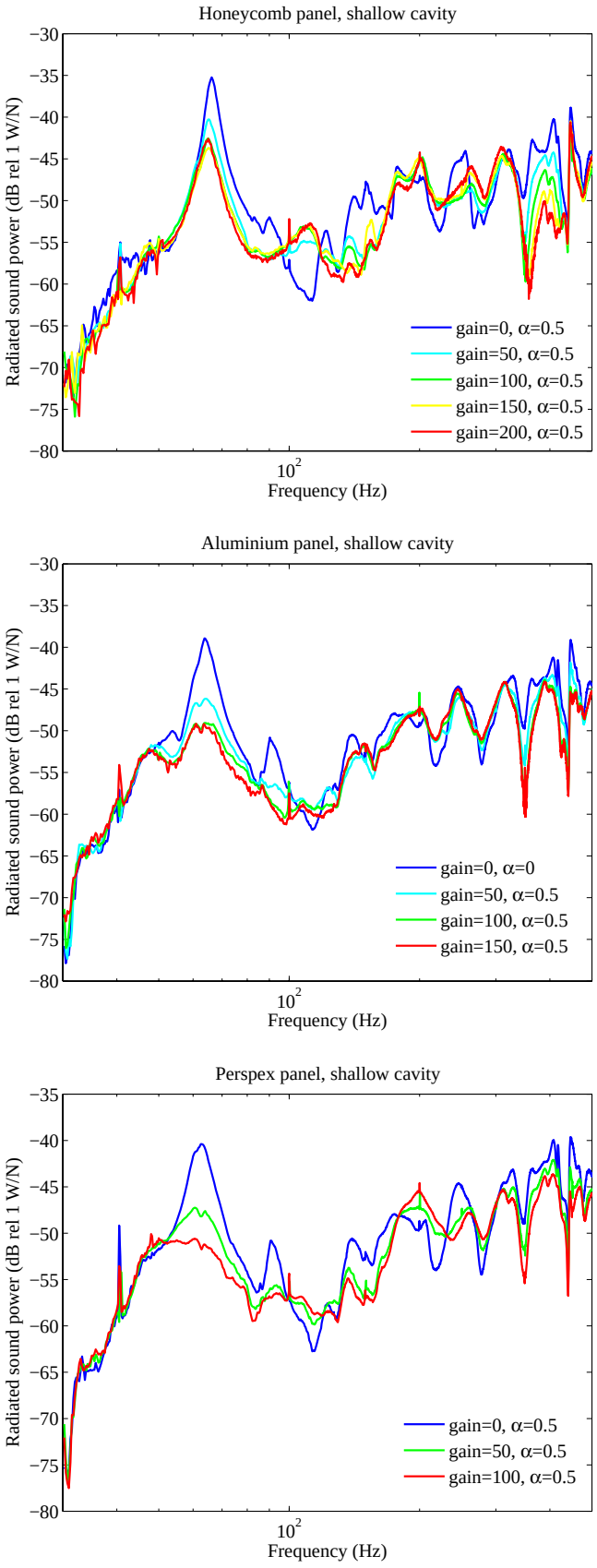

Figure 56: Radiated sound power plotted against frequency in case when Honeycomb (top), aluminium (centre) and Perspex (bottom) radiating panels are used with the shallow air cavity. Sound power spectra are shown for increasing feedback gains in mV/V (see legends). Velocity weighting factors equal 0.5.

In general all results shown in Figure 55 and Figure 56 illustrate similar trends when the active control systems are switched on. As the feedback gains are increased from zero, the sound radiation tends to decrease by about 6-10 dB at the lowest resonance of the double panel system. The lowest resonance occurs between 60 and 65 Hz for all tested configurations. In addition, large reductions are obtained at frequencies around 400 Hz. For example, for the deep cavity and Honeycomb radiating panel configuration the reduction of the radiated sound power at 380 Hz is almost 25 dB. It is worth mentioning that the theoretical mass-air-mass resonant frequency for this configuration is 374 Hz. (As the sensors and actuators are mounted onto the panels, an additional mass is added to the system such that the mass-air-mass resonant frequency shifts down to 374 Hz from 440 Hz.) The explanation for this good control performance is that the mass-air-mass mode is characterised by the out of phase motion of the two plates (see Figure 11C), such that the relative dampers of the active control system can couple well with the dominant mode which is characterised by the out of phase vibration of the two panels.

However, the active damping approach tends to increase the response at anti-resonances of the sound transmission spectra. For example, in the deep cavity and Honeycomb radiating panel case there is an increase of the radiated sound power at 100 Hz due to the active control by about 10 dB.

It must be emphasised that the performance results illustrated in Figure 55 and Figure 56 do not represent the ultimate control capability of the proposed active control system because the value of the velocity weighting factor was fixed at 0.5 for this experiment. It is thus possible that different velocity weighting factor may lead to improved control performance. For this reason, in the next part of this chapter, the impact of the velocity weighting factor to the control performance is studied.

6.4 Weighted velocity feedback – effects of different velocity weighting factors

In this section the radiated sound power measurements were performed with respect to the control effects generated by the use of different velocity weighting factors. The results are plotted in Figure 57 and Figure 58.

Figure 57 shows the narrow band spectra of total radiated sound power for three deep cavity arrangements. The top plot in Figure 57 shows the results with the Honeycomb radiating panel, the middle plot is for the aluminium radiating panel, and the bottom plot is for the Perspex radiating panel. The measured sound power spectra for three shallow cavity arrangements are plotted in Figure 58, following the same layout as in Figure 57.

The feedback gain was kept constant during the measurements by maintaining the final stage amplification factor (master gain) of each controller channel to 100 mV/V. The pre-amplification factors of each of the source and radiating panel's sensors were set in order to achieve the desired velocity weighting factors. The black lines in Figure 57 show the radiated sound power spectra when the control system is switched off. The remaining coloured lines show the spectra when the active control system is switched on for different values of the velocity weighting factor. The dashed coloured lines are for values of $0 < \alpha < 0.5$, the blue lines are for $\alpha = 0.5$, and the solid coloured lines are for values of $0.5 < \alpha < 1$. The velocity weighting factor was varied in steps of 0.1.

The reference case with the deep cavity and Honeycomb radiating panel is considered first. As shown by the dashed magenta line, which is for $\alpha = 0$, the radiated sound power is increased at the lowest resonance (63 Hz) when active control is applied. This is because the velocity weighting factor $\alpha = 0$, according to the Nyquist criterion stability analysis given in Chapter 5, results in the low frequency phase lags of the nine sensor-actuator open-loop frequency response functions. Therefore such a feedback configuration generates spillover effects due to the negative real parts of the nine sensor-actuator open-loop FRFs.

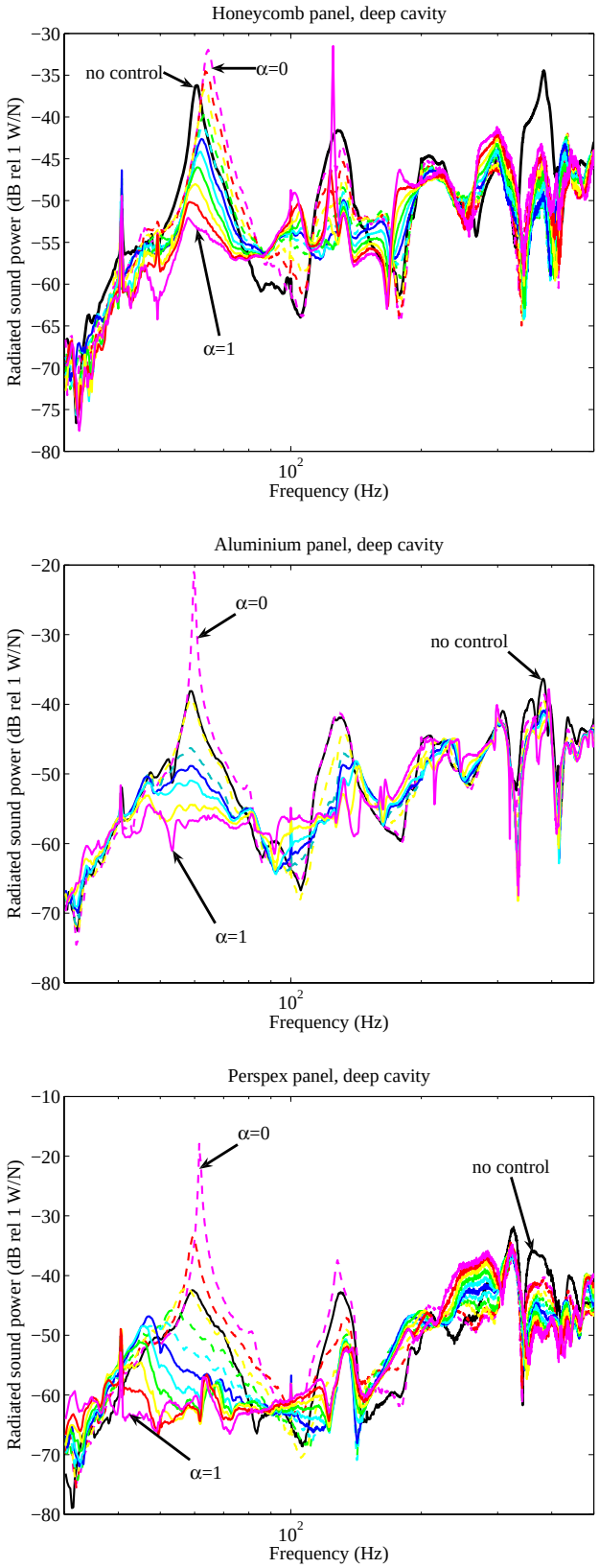

Figure 57: Radiated sound power plotted against frequency in case when Honeycomb (top), aluminium (centre) and Perspex (bottom) radiating panels are used with the deep air cavity. Sound power spectra are shown for velocity weighting factors, α, increasing from 0 to 0.5 (dashed coloured lines) and from 0.5 to 1 (solid coloured lines). Feedback gains equal 100 mV/V. The black lines are when the control is off.

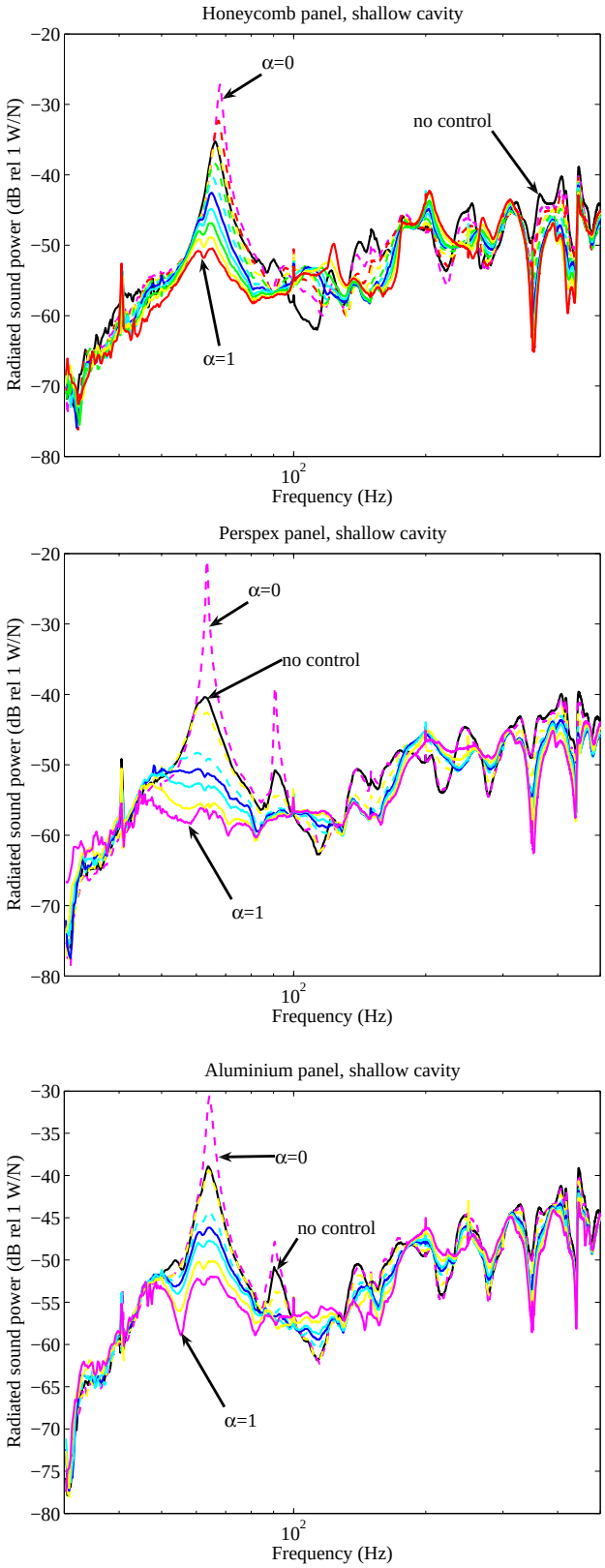

Figure 58: Radiated sound power plotted against frequency in case when Honeycomb (top), aluminium (centre) and Perspex (bottom) radiating panels are used with the shallow air cavity. Sound power spectra are shown for velocity weighting factors, α, increasing from 0 to 0.5 (dashed coloured lines) and from 0.5 to 1 (solid coloured lines). Feedback gains equal 100 mV/V. The black lines are when the control is off.

However, if the weighting factor is increased, as shown by the solid lines in the plots of Figure 57 and Figure 58, the sound radiation at the system lowest resonance decreases monotonically with increasing velocity weighting factor, α. In particular, in comparison to the relative velocity feedback performance, which is shown by the blue lines, the use of $\alpha = 1$ generates an additional 8-10 dB, for all tested double panel configurations. The effect of the velocity weighting factor does not show clear trends at other frequencies. At frequencies close to the mass-air-mass resonance, the use of $\alpha = 1$ still generates good performance if not better than the relative velocity feedback.

Although the active control system performs well in the analysed low frequency range, it is necessary to consider the effects of active control in a broader frequency band. For example, the theoretical performance study presented in Chapter 4 indicated that for very high feedback gains new, lightly damped resonances can occur at frequencies above the mass-air-mass resonance. For that reason the results of the sound power measurements are presented up to 3.2 kHz in the following section.

6.5 Results with optimal weighting factors and feedback gains

In this section sound power measurements with and without active control were considered over a broader frequency band, from 30 Hz to 3.2 kHz. In particular, the spectra of the sound power radiated by the panels equipped with sensor and actuator transducers are compared to the spectra of a double panel with no transducers mounted. This type of analysis was performed because it was suspected that the passive effects generated by the sensors and actuators could have introduced passive damping of the double panel vibration as well as the mass loading of the panel. Also, the purpose is to investigate possible high-frequency spillover effects produced by the control system due to the conditional stability of the feedback loops. The study also includes the assessment of the control system performance in terms of reductions of the spatially averaged radiating panel velocity obtained using the laser vibrometer test facility.

Figure 59 and Figure 60 show the sound power radiated by the smart panel (top plots) and the spatially averaged radiating panel mean velocity (bottom plots) plotted against

frequency up to 3.2 kHz. Figure 59 corresponds to the reference case (Honeycomb radiating panel and the deep cavity). Figure 60 corresponds to the case with Honeycomb radiating panel and the shallow cavity.

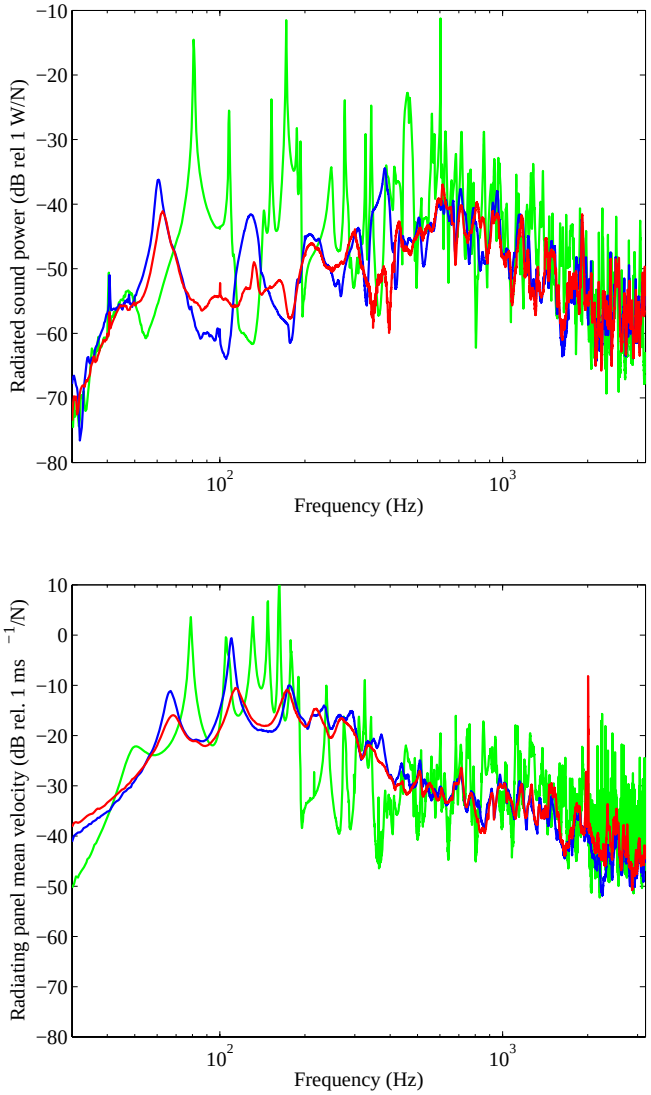

Figure 59: Radiated sound power spectra (top plot) and the spectra of mean velocity of the radiating panel (bottom plot) for the configuration with Honeycomb radiating panel and deep air cavity. Green lines: without sensors and actuators, blue lines: with sensors and actuators open loop, red lines: with sensors and actuators closed loop.

The green lines are representative of the double panel without transducers, whereas the blue lines are for the double panel equipped with the transducers, but with the control system switched off. Therefore the comparison of the blue and the green lines shows the passive effects of the control system transducers.

As can be seen in the two figures, the passive effects are quite large as some of the low frequency resonances are completely damped down when the transducers are mounted onto the panels. This is probably due to internal damping in each of the voice-coil actuators, which is generated by the viscous air flow through a small circular orifice between the actuator coil and magnet.

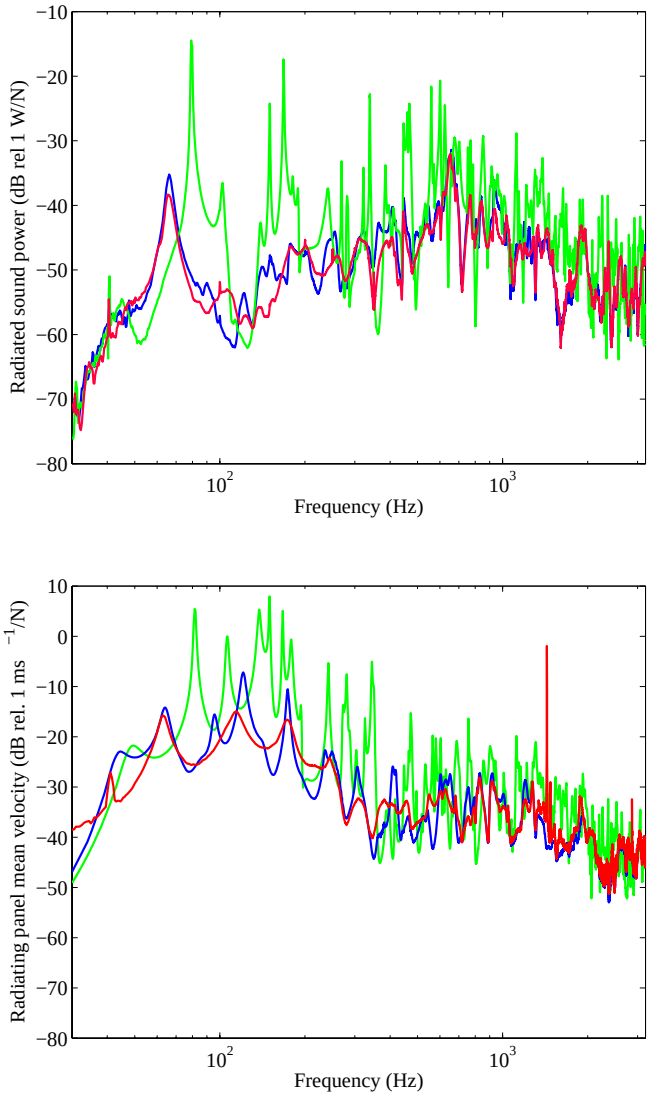

Figure 60: Radiated sound power spectra (top plot) and the spectra of mean velocity of the radiating panel (bottom plot) for the configuration with Honeycomb radiating panel and shallow air cavity. Green lines: without sensors and actuators, blue lines: with sensors and actuators open loop, red lines: with sensors and actuators closed loop.

As the coil windings enter the gap between the two magnet poles, the air is pushed out of the magnet and vice versa. The viscous flow of the air through the small orifice causes the damping of the relative coil-magnet motion. In fact, due to the miniature actuator design and the requirements on the high magnetic flux in the orifice between

the two poles of the magnet, the radial clearance between the coil and the magnet is as low as 0.25 mm. A more practical system would require a larger clearance in order to enable simple and practical mounting of the trim panel. The larger clearance should result in smaller passive damping effects.

The passive mass effects are visible in the mass controlled frequency range, above 500 Hz. Due to the added mass the blue lines are shifted down parallel to the green lines in the four plots at the higher frequencies.

Active control performance is considered next. The feedback gain values and velocity weighting factors were selected to provide the best overall reductions of the radiated sound power in the broad frequency band up to 3.2 kHz. In the reference case this resulted in a velocity weighting factor of 0.4 and feedback gains of 100 mV/V. As shown by the red lines in Figure 59, the implementation of active control generates additional reductions between 5-15 dB at the resonant frequencies of the double panel system. The reductions of the radiating panel transverse velocity are modest, however clear damping effects are generated up to 500 Hz. At approximately 2000 Hz a spillover effect is visible in the bottom plot in Figure 59. This effect is due to the fundamental resonance of the accelerometer sensors which introduce 180 degree phase lags in the open loop frequency response functions, as discussed in Chapter 5. Nevertheless, as shown by the red line in the left hand side plot, the spillover effect is less pronounced in the sound power radiation spectrum, probably because of the weakly radiating mode that dominated the response of the radiating panel.

The two plots in Figure 60 show that similar qualitative passive and active effects are also obtained for the shallow cavity arrangement. The velocity weighting factor and feedback gain that provided the best broadband reductions were respectively 0.3 and 100 mV/V for the Honeycomb radiating panel and the shallow cavity.

In order to complete the study of the broadband active and passive effects, the same type of measurements (with/without transducers and with with/without active control) of the radiated sound power were also performed for the double panels with the aluminium and Perspex radiating panels, with deep and shallow air cavities between source and radiating panels. Figure 61 shows the radiated sound power spectra for Perspex radiating

panel with deep cavity (top plot), and Perspex radiating panel with shallow cavity (bottom plot). Figure 62 shows the radiated sound power spectra for aluminium radiating panel with deep cavity (top plot), and aluminium radiating panel with shallow cavity (bottom plot).

As shown in Figure 61 and Figure 62 large passive effects are also generated by the coil/magnet pairs in these cases. In addition, active control generates additional damping of the low-order vibratory modes, such that the radiated sound power is reduced by 8-10 dB at the low order mode resonances.

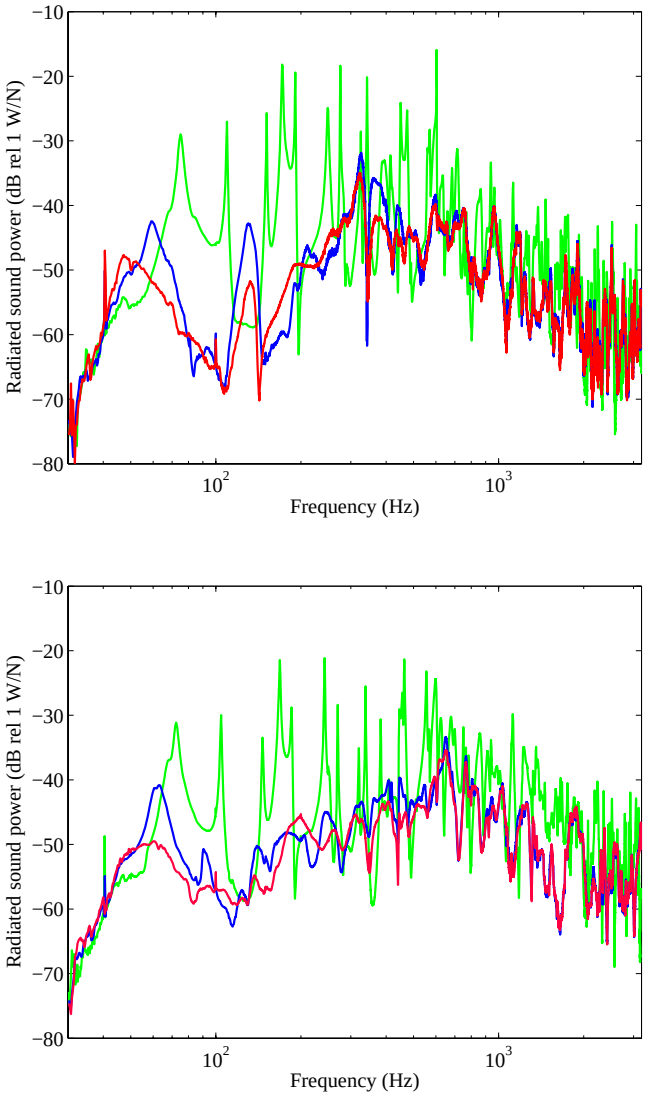

Figure 61: Radiated sound power spectra for Perspex radiating panel with deep cavity (top plot), and Perspex radiating panel with shallow cavity (bottom plot). Green lines: without sensors and actuators, blue lines: with sensors and actuators open loop, red lines: with sensors and actuators closed loop.

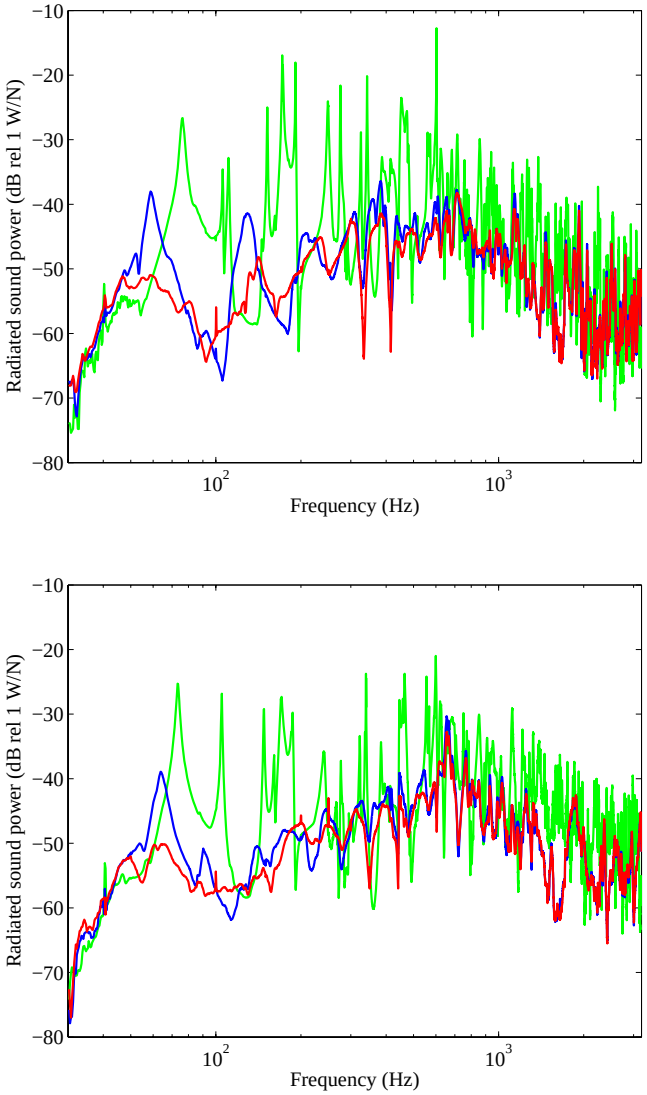

Figure 62: Radiated sound power spectra for aluminium radiating panel with deep cavity (top plot), and aluminium radiating panel with shallow cavity (bottom plot). Green lines: without sensors and actuators, blue lines: with sensors and actuators open loop, red lines: with sensors and actuators closed loop.

6.6 Comparison between active and passive control

The final experiment presented involves active control performance compared to the performance of a passive sound absorbing treatment. The experiment was performed on a double panel with the aluminium radiating panel and with 30 mm deep cavity. The passive treatment used was a high density polyamide foam of dimensions 414×314×25 mm^3, as shown in Figure 63. The mass of the foam was 0.370 kg, and it was attached directly to the source panel, without attaching it to the radiating panel in order to avoid

structure-borne sound transmission between the two plates. For a comparison, the cumulative mass added by the sensor and actuator components was 0.220 kg.

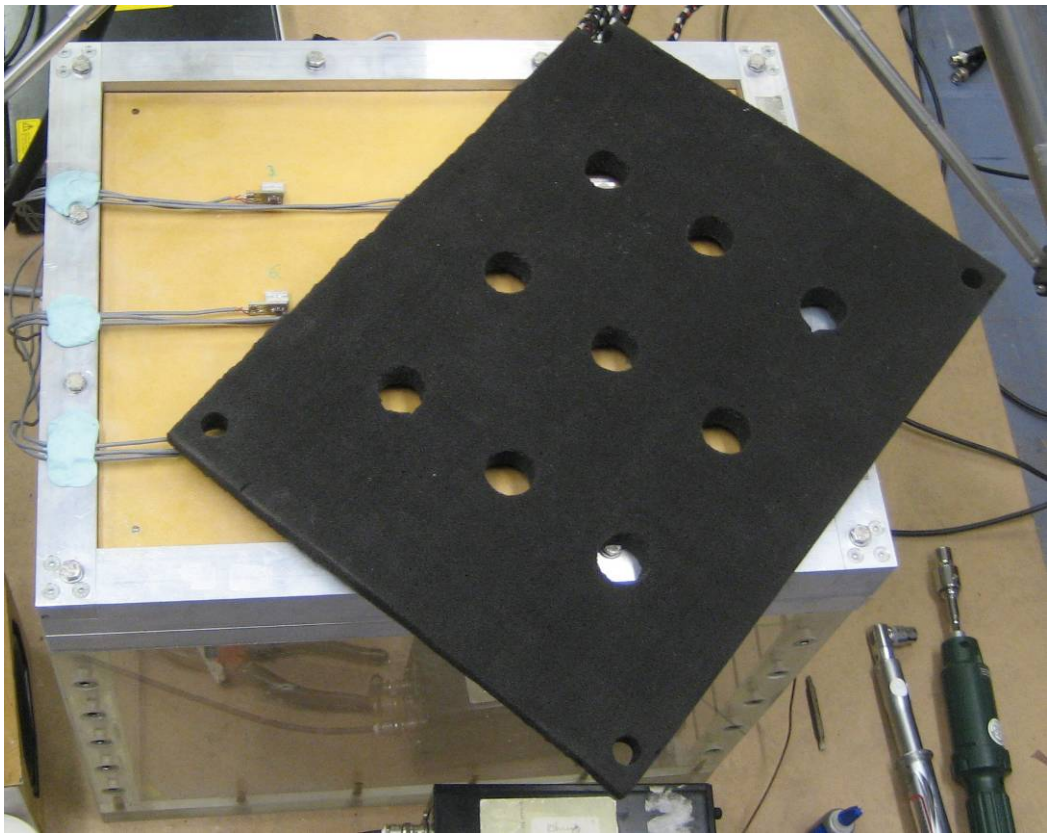

Figure 63: The high density polyamide foam used to asses the effectiveness of a typical passive treatment on the attenuation of the smart panel radiated sound power. The dimensions of the foam are dimensions 414×314×25 mm. The mass of the foam is 0.370 kg.

Figure 64 shows the total radiated sound power plotted against frequency for three cases. The blue line shows the result when neither the passive treatment nor the control transducers are placed onto the double panel. The red line shows the result when the passive treatment is applied to the double panel (without the sensors and actuators), whereas the green line shows the result when the active control system is applied (without the passive treatment). At very low frequencies (below 100 Hz) the passive treatment generates reductions predominantly by adding mass to the panels, as indicated by the downward shift of the first and the second panel resonance. At higher frequencies the passive treatment causes good reductions of the radiated sound power. However, as shown by the green line in Figure 64, active control is able to reduce the radiated sound power even at very low frequencies. In addition, good reductions are also achieved at higher frequencies of the frequency range of interest. In fact, over the frequency range

from 30 Hz to 500 Hz the active control outperforms the passive treatment, despite 68% more weight added to the structure by the passive control arrangement. For example, if the radiated sound power is integrated between 30 and 500 Hz and normalised to the case without transducers (blue line in Figure 64), then the passive treatment (red line) gives a -3.9 dB reduction, whereas the active control (green line) generates -5.3 dB reduction in the radiated sound power. Furthermore, the sensors and actuators can be arranged on shallow cavity double panels without a degradation of the active control performance, whereas the application of thinner sound absorbing layer would result in reduced sound insulation. Thus the active control approach could also yield an additional bonus in terms of saving space.

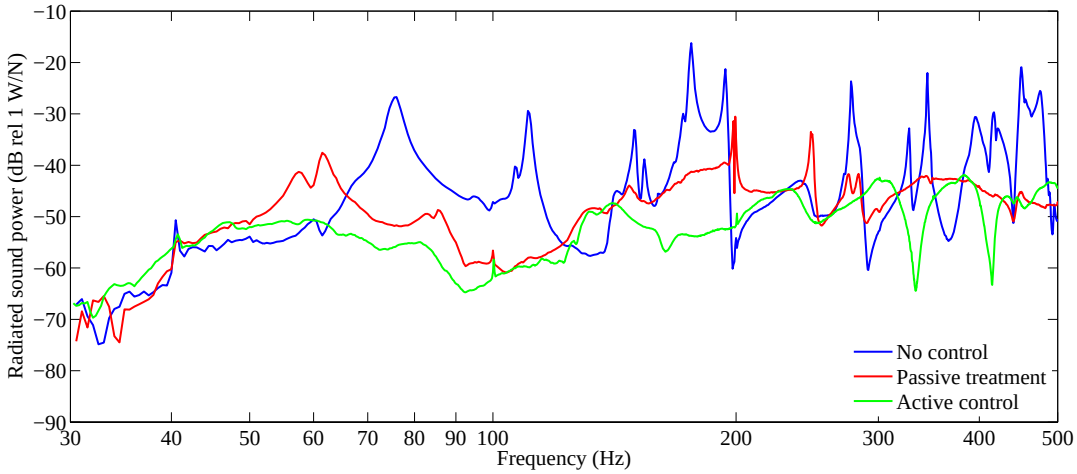

Figure 64: The sound power radiation of the smart double panel with no sensors and actuators (blue line), with the passive sound absorbing foam (red line) and with the active control without the foam (green line). Measurements are performed with the aluminium radiating panel and with the deep air cavity.

6.7 Summary

Chapter 6 presented the experiments carried out in order to test the effectiveness of the smart panel active control. The effectiveness was assessed in terms of reductions in the radiated sound power and the radiating panel spatially averaged velocity.

The experimental procedure was described first. Second, the passive sound radiation was measured with reference to three different radiating panels and two different cavity depths. Third, the effectiveness of the active control system in reducing the radiated

sound power at low frequencies was assessed with respect to the variation of feedback gains. Fourth, the impact of the velocity weighting factor on the radiated sound power was analysed. Fifth, the broadband effects of the active control system on the radiated sound power and the mean velocity of the radiating panel were presented for optimal feedback gains and velocity weighting factors. Finally, the noise reduction performance of the active control system has been compared to the performance of a traditional passive treatment of comparable weight.

It was found that the sensors and actuators generate large passive attenuations of the radiated sound power and mean velocity of the radiating panel, due to passive damping and mass effects. The implementation of active control generated further attenuations of the radiated sound power and the mean velocity of the radiating panel. It was found that the highest gains that still guarantee the feedback system stability should be used in order to generate good active reductions. The use of velocity weighting factor can improve the active control system performance at low frequencies. The active control generates larger reductions than the traditional passive treatment, despite the higher mass of the passive control arrangement.

7 Conclusions

This thesis is concerned with an analysis of a smart aircraft double panel for active vibroacoustic control. The control of the double panel vibration is implemented using Multi-Input-Multi-Output (MIMO) decentralised velocity feedback loops. The loops are applied via an array of electrodynamic force actuators and collocated velocity sensors. The actuators are located in an air cavity between the two panels such that they can react against the two panels. Two velocity sensors per actuator are used. Either sensor is located at the source and radiating panel footprint of an actuator. The error velocity is formed by subtracting weighted sensor outputs. Stability and performance properties of the control system are investigated theoretically and experimentally.

In Chapter two the smart double panel model problem is described first. The model double panel consists of a source and a radiating panel coupled acoustically by the air in the cavity between them and structurally by four elastic mounts. Second, the formulation of the mathematical model for the theoretical analysis is presented. The response and the sound transmission are modelled using an impedance and mobility approach. Third, a parametric study of the passive sound transmission is given. The parametric study included variations of the radiating panel material, air cavity depth and elastic mount stiffness. It has been found that the response and the sound transmission are rather high at frequencies below the mass-air-mass resonance of the double panel. In fact, they are governed by well separated resonances of the low-order acoustical and vibratory modes of the two panels and the air cavity. At frequencies above the mass-air-mass resonance, mass law governs the response and the sound transmission such that they decrease with increase of frequency.

In Chapter three a theoretical performance analysis of three types of MIMO decentralised feedback control systems is given. The performance is assessed in terms of reductions of the radiating panel kinetic energy and the sound transmission ratio. First, the control loops are applied on the source panel using ideal skyhook actuators and velocity sensors. Second, the loops are applied on the radiating panel using ideal skyhook actuators and velocity sensors. Third, reactive actuators, driven with relative

source/radiating panel error velocities are considered. It has been found that the best control performance is obtained with the control of the radiating panel. If very high gains are used, then the performance deteriorates due to effect of pinning the panels at control locations which induces new lightly-damped resonances. The pinning effect is particularly important in case of relative velocity feedback with reactive actuators, because the actuators lock the two panels together and degrade the performance substantially at frequencies above the mass-air-mass resonance.

In Chapter four, a theoretical performance and stability analysis of velocity feedback control systems which utilise reactive actuators driven by the weighted velocity error signals is given. It has been found that feedback loops which use absolute velocities are conditionally stable due to presence of indirect actuation paths. This problem can be solved by using appropriate weighting factors. If fact, there are ranges of weighting factors that guarantee the unconditional stability of the feedback loops. The ranges are limited by critical values of weighting factor where the system stability properties changes from unconditional to conditional. The performance of the active control depends upon the weighing factors used.

In Chapter five the design and experimental testing of a smart double panel demonstrator is presented. Active vibroacoustic control is implemented on the double panel using nine direct velocity feedback loops. Miniature voice coil actuators that react between the two panels with collocated Micro Electro Mechanical Systems (MEMS) accelerometer sensors are used for the decentralised velocity feedback control. The sensor-actuator frequency response function of a single control unit was measured with reference to different velocity weighting factors. The Nyquist stability criterion was then used to determine stability properties of a single control unit. The theoretical predictions of the impact of the velocity weighting factors on system stability were confirmed experimentally. The ranges of velocity weighting factors were determined which help to avoid stability problems related to the indirect actuation paths. However, it has been found that the feedback loops are bound to be conditionally stable due to sensor second order dynamics even if correct velocity weighting factors are used. The analysis is then extended to the stability properties of the array of nine feedback units. A 9×9 matrix of point and transfer mobilities was measured in order do investigate the global stability properties of the smart panel, using the generalised Nyquist criterion.

In Chapter six the effectiveness of the decentralised active control system has been demonstrated experimentally in terms of reductions of the trim panel mean kinetic energy and the radiated sound power. Six different double panel configurations were tested, with three radiating panel materials and two cavity depths. It was found that the passive damping and mass effects of the sensors and actuators are rather high, and reduce the response and sound radiation significantly. It has been demonstrated that the control systems generate additional active damping effects and further reduce resonant response and radiated sound power. Effects of different feedback gains have been studied. It has been found that in practice it is necessary to use as high gains as possible in order to provide good reductions of the radiated sound power and response of the radiating panel. The use of different velocity weighting factors significantly affects the performance of the active control at the lowest resonance of the double panel. Finally, the active control effects are compared to the passive effects produced by a sound absorbing foam sheet, located in the air cavity between the two panels. Although the sound absorbing foam sheet had a weight higher than the weight added by sensor and actuator elements, the active control outperformed the passive control at low frequencies. Moreover the active system can be applied on double panels with shallow air cavities, such that less space is used for noise insulation purposes.

Recommendations for future work

Future work could progress in the directions listed below.

- An analysis of a more realistic aircraft double panel which includes the curvature of the skin and trim panels, the tension effects of the aircraft skin, and the effects of the structural frames and stringers.

- Further miniaturisation of the actuators and the controller units. Although the used actuators are quite small-scale, the cumulative mass added to the structure needs to be reduced.

- An investigation of means to reduce the accelerometer resonance effect on the control system stability. For example, sensors with internal velocity feedback loop for damping down the fundamental sensor resonance can be considered[80].

- A full integration of the control system components into the smart panel, which should provide further savings in space and weight.

- An algorithm to automatically set the optimal control gains and velocity weighting factors.

- Contrast the fully coupled, distributed, and decentralised MIMO feedback control effectiveness.

- A study of a smart double panel excited by a Turbulent Boundary Layer.

Appendix A: Mobility and impedance functions

Appendix A describes the mobility and impedance matrices used in Equations (15,16 and 20) in more detail than then they were described in the Chapter 2 of the thesis. It also gives the expressions for the mobility and impedance functions that the mobility and impedance matrices consist of.

A1 Mobility matrices

The mobility matrix, $\mathbf{Y}_{s1}$, in Equation (15) is used to calculate the contribution to the source panel velocity vector, defined in Equation (7), due to the action of the source panel force vector given in Equation (11). It contains mobility functions between all the possible locations pairs for the elastic mount junction points and centres of source panel elements. The matrix $\mathbf{Y}_{s1}$ is given by the following equation:

$$\mathbf{Y}_{s1} = \begin{bmatrix} \mathbf{Y}_{smm} & \mathbf{Y}_{sme} \\ \mathbf{Y}_{sem} & \mathbf{Y}_{see} \end{bmatrix}, \tag{A1}$$

where the $q \times q$ matrix $\mathbf{Y}_{smm}$ contains the source panel mobility functions between all the points of the elastic mount junctions; the $q \times k$ matrix $\mathbf{Y}_{sme}$ and $k \times q$ matrix $\mathbf{Y}_{sem}$ contain the source plate mobility functions between the centres of elements and points of the elastic mount junctions; the $k \times k$ matrix $\mathbf{Y}_{see}$ contains the source plate mobility functions between all element centres; and where q is the number of elastic mounts, and k is the number of elements on a panel.

In a similar way the mobility matrix $\mathbf{Y}_{r1}$ in Equation (16) is used to calculate the contribution to the radiating panel velocity vector, defined in Equation (8), due to the action of the radiating panel force vector given in Equation (12). It contains mobility functions of the radiating plate between all possible pairs of the elastic mount junction points and element centres. The matrix $\mathbf{Y}_{r1}$ is given by the following equation:

$$\mathbf{Y}_{r1} = \begin{bmatrix} \mathbf{Y}_{rmm} & \mathbf{Y}_{rme} \\ \mathbf{Y}_{rem} & \mathbf{Y}_{ree} \end{bmatrix}, \tag{A2}$$

where the $q \times q$ matrix $\mathbf{Y}_{rmm}$ contains radiating plate mobility functions between all the elastic mount junction points; the $q \times k$ matrix $\mathbf{Y}_{rme}$ and $k \times q$ matrix $\mathbf{Y}_{rem}$ contain the radiating plate mobility functions between the element centres and elastic mount junction points; whereas the $k \times k$ matrix $\mathbf{Y}_{ree}$ contains the radiating plate mobility functions between all the element centres.

The mobility matrix $\mathbf{Y}_{s2}$ in Equation (15) is used to calculate the contribution to the source panel velocity vector, defined in Equation (7), due to the action of the primary excitation force vector $\mathbf{f}_p$, which is a subset of the primary-flanking excitation vector $\mathbf{f}_{pf}$ given in Equation (25). The primary excitation is modelled using out of plane point forces, contained in the primary-flanking excitation vector $\mathbf{f}_{pf}$, which act on the geometrical centres of the elements, but not on the elastic mount junctions. Therefore the matrix $\mathbf{Y}_{s2}$ contains mobility functions between all the possible pairs of points that can be made using the element centres, and between all the possible pairs of points that can be made combining the element centres with the source panel elastic mount junctions. Thus the matrix $\mathbf{Y}_{s2}$, of size $(k+q) \times k$, is given by the following equation:

$$\mathbf{Y}_{s2} = \begin{bmatrix} \mathbf{Y}_{sme} \\ \mathbf{Y}_{see} \end{bmatrix}. \tag{A3}$$

Similarly, the mobility matrix $\mathbf{Y}_{r2}$ in Equation (16) is used to calculate the contribution to the radiating panel velocity vector, defined in Equation (12), due to the action of the flanking excitation force vector $\mathbf{f}_f$, which is a subset of the primary-flanking excitation vector $\mathbf{f}_{pf}$, given in Equation (25). The flanking excitation is again modelled using out of plane point forces, contained in the primary-flanking excitation vector $\mathbf{f}_{pf}$, which act on geometrical centres of the elements, but not on the elastic mount junctions. Therefore the matrix $\mathbf{Y}_{r2}$ contains mobility functions between all possible pairs of points that can

be made using the element centres, and between all the possible pairs of points that can be made combining the element centres with the radiating panel elastic mount junctions. Thus the matrix $\mathbf{Y}_{r2}$ of size $(k+q)\times k$ is given by the following equation:

$$\mathbf{Y}_{r2} = \begin{bmatrix} \mathbf{Y}_{rme} \\ \mathbf{Y}_{ree} \end{bmatrix}. \tag{A4}$$

The mobility matrix $\mathbf{Y}_{s3}$ in Equation (15) is used to calculate the contribution to the source panel velocity vector, defined in Equation (7), due to the action of the control force vector $\mathbf{f}_c$, given in Equation (14). Therefore the matrix $\mathbf{Y}_{s3}$ contains mobility functions between all the possible pairs that can be made combining the source panel element centres and the control force points of action on the source panel as well as mobilities between all the possible pairs that can be made combining the source panel elastic mount junctions and the points of action of the control forces on the source panel.

The matrix $\mathbf{Y}_{s3}$ of size $(k+q)\times 2p$, where p is the number of the control forces, is given by the following equation:

$$\mathbf{Y}_{s3} = \begin{bmatrix} \mathbf{Y}_{smc} & 0 \\ \mathbf{Y}_{sec} & 0 \end{bmatrix}, \tag{A5}$$

where the $q\times p$ matrix $\mathbf{Y}_{smc}$ contains the mobility functions of the source panel between the elastic mount junction points and the points of action of the control forces; and $k\times p$ matrix $\mathbf{Y}_{sec}$ contains the mobility functions of the source plate between the centres of elements and the points of action of the control forces.

Similarly, the mobility matrix $\mathbf{Y}_{r3}$ in Equation (16) is used to calculate the contribution to the radiating panel velocity vector, defined in Equation (7) due to the action of the control force vector $\mathbf{f}_c$, given in Equation (14). Therefore the matrix $\mathbf{Y}_{s3}$ contains mobility functions between all the possible pairs that can be made combining the radiating panel element centres and the radiating panel control force points of action as

well as mobilities between all the possible pairs that can be made combining the radiating panel elastic mount junctions and the points of radiating panel control forces action. The matrix $\mathbf{Y}_{r3}$ of size $(k+q)\times 2p$ is given by the following equation:

$$\mathbf{Y}_{r3} = \begin{bmatrix} 0 & \mathbf{Y}_{rmc} \\ 0 & \mathbf{Y}_{rec} \end{bmatrix}, \tag{A6}$$

where the $q\times p$ matrix $\mathbf{Y}_{rmc}$ contains the radiating panel mobility functions between the points of the elastic mount junctions and the points of action of the control forces, and $k\times p$ matrix $\mathbf{Y}_{rec}$ contains the radiating plate mobility functions between the element centres and the points of action of the control forces.

A2 Mobility functions

In the Section A1 of Appendix A the mobility matrices have been described in such detail so that the elements of each matrix have been defined as mobility functions between two points of either source or radiating panel. In this Section it is explained how to calculate a mobility function between two arbitrary points of the source and the radiating panels.

The mobility function is a frequency dependent complex function that can be defined between two points of a plate and which is given by a ratio of a time harmonic velocity at one point resulting from a time harmonic force acting at some other point on the plate. If the locations of the two points are different, then the mobility function is called the transfer mobility. In contrast, if the two points share the same location then the resulting mobility is called the point mobility. Due to the principle of reciprocity, if the force and the velocity switch their locations then the mobility function does not change. Figure A1 shows a plate excited by an out of plane force N_{zP1} at location *P1*, and the resulting out of plane velocity $\dot{w}_{P2}$ at location *P2*.

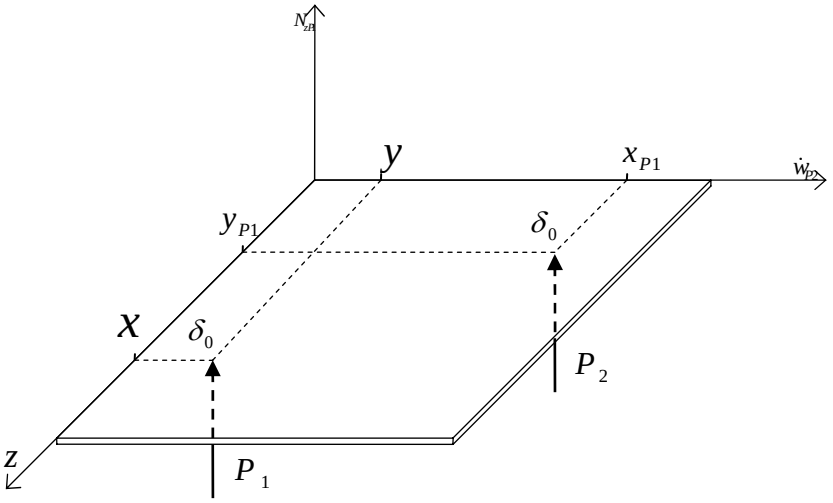

Figure A1: Notation of the velocity $\dot{w}_{P2}$ at position $P2$ when a plate is excited by an out of plane force N_{zP1} at position $P1$.

A mobility function between the points $P1$ and $P2$ is given by[22]:

$$Y_{P1,P2}(x_{P1}, y_{P1}, x_{P2}, y_{P2}, \omega) = \frac{\dot{w}_{P2}}{N_{zP1}} = \frac{\dot{w}_{P1}}{N_{zP2}} \ . \tag{A7}$$

The function in Equation (A7) for a thin lightly damped rectangular plate is given by[22]:

$$Y_{\dot{w},N_z}(x_{P1}, y_{P1}, x_{P2}, y_{P2}, \omega) = j\omega \sum_{m=1}^{\infty} \sum_{n=1}^{\infty} \frac{\phi_{m,n}(x_{P2}, y_{P2}) \phi_{m,n}(x_{P1}, y_{P1})}{\rho\, h\, l_x l_y \left[(\omega_{m,n})^2 (1 + j\eta) - \omega^2 \right]}, \tag{A8}$$

where:

j - imaginary unit,

ω - circular frequency,

$\phi_{m,n}$ - mode shape function,

ρ - mass density of the plate material,

h_s - plate thickness,

l_x - plate length,

l_y - plate width,

$\omega_{m,n}$ - plate natural frequencies, and

η - plate loss factor.

For the source panel (simply supported thin rectangular plate) natural frequencies can be calculated using following equation[22]:

$$\omega_{m,n}^{s} = \sqrt{\frac{E_s I_s}{\rho_s h_s \left(1-\nu_s^{\,2}\right)}}\left[\left(\frac{m\pi}{l_x}\right)^2 + \left(\frac{n\pi}{l_y}\right)^2\right] = \sqrt{\frac{E_s h_s^{\,2}}{12\rho_s \left(1-\nu_s^{\,2}\right)}}\left[\left(\frac{m\pi}{l_x}\right)^2 + \left(\frac{n\pi}{l_y}\right)^2\right], \qquad \text{(A9)}$$

where:

E_s - the Young's modulus of the source panel material,

ν_s - the Poisson's ratio of the source panel material,

ρ_s - density of the source panel material,

h_s - source panel thickness,

I_s - source panel second moment of area ($I_s = \frac{h_s^3}{12}$),

m - mode number in x direction,

n - mode number in x direction,

l_x - double panel system length, and

l_y - double panel system width.

Source panel modal shapes are given by[22]:

$$\phi_{m,n}^{s} = 2\sin\left(\frac{m\pi x}{l_x}\right)\sin\left(\frac{n\pi y}{l_y}\right). \qquad \text{(A10)}$$

For the radiating panel (a thin rectangular plate, with free boundary conditions along all the edges) natural frequencies are given by[22]:

$$\omega_{m,n}^{r} = \sqrt{\frac{E_r h_r}{12\rho_r\left(1-\nu_r{}^2\right)}}\cdot\left(\frac{\pi}{l_x}\right)^2 q_{m,n}, \qquad \text{(A11)}$$

where:

$\omega_{m,n}^{r}$ - radiating panel natural frequencies,

E_r - the Young's modulus of the receiver panel's material,

ν_r - the Poisson's ratio of the receiver panel's material,

ρ_r - density of the receiver panel's material,

h_r - receiver panel thickness, and

$$q_{m,n} = \sqrt{G_x^4(m) + G_y^4(n)\left(\frac{l_x}{l_y}\right)^4 + 2\left(\frac{l_x}{l_y}\right)^2\left[\nu_r H_x(m)H_y(n) + (1-\nu_r)J_x(m)J_y(n)\right]}.$$

The constants G_x, H_x, J_x and G_y, H_y, J_y are given in Table A1.

Table A1 Values for the constants G, H, and J

k	G	H	J
Even mode	0	0	0
Rocking mode	0	0	$12/\pi^2$
1	1.506	1.248	5.017
2, 3, 4, …	$k+1/2$	$(k+1/2)^2\left[1-\frac{4}{(2k+1)\pi}\right]$	$(k+1/2)^2\left[1+\frac{12}{(2k+1)\pi}\right]$

In Table A1 *k* takes the values of *m* or *n* (for calculating values of *G*, *H*, and *J*) for *x* or *y* directions, respectively. Regarding rigid body motion of the plate, there are two non-deforming beam functions as well, and these are designated in the table as an "even" and a "rocking" mode. These must be included in the *m*, *n* combinations as well as

deforming beam functions (i.e. in the modal superposition there are modes with natural frequency $\omega_{rocking,7}$ or $\omega_{even,3}$).

Modal shapes for the radiating panel are given as products of characteristic beam functions:

$$\phi_{m,n}^{r} = \varphi_m(x)\varphi_n(y) \,. \tag{A12}$$

The characteristic beam functions for free boundary condition along all the edges are given in Table A2.

Table A2 Characteristic beam functions for a plate with free edges (after Ref. 22)

$\varphi_{1,3,5,\ldots}(x)$ with $i=(n+1)/2$	$\varphi_{2,4,6,\ldots}(x)$ with $j=n/2$
$\varphi_{even}(x)=1$	
$\varphi_{rocking}(x)=\sqrt{3}(1-2x/l_x)$	
$\varphi_n(x)=\sqrt{2}\left[\cos\gamma_i\left(\frac{x}{l_x}-\frac{1}{2}\right)+k_n\cosh\gamma_i\left(\frac{x}{l_x}-\frac{1}{2}\right)\right]$	$\varphi_n(x)=\sqrt{2}\left[\sin\gamma_j\left(\frac{x}{l_x}-\frac{1}{2}\right)+k_n\sinh\gamma_j\left(\frac{x}{l_x}-\frac{1}{2}\right)\right]$
$k_n=-\frac{\sin\frac{1}{2}\gamma_i}{\sinh\frac{1}{2}\gamma_i}$ with $\tan\frac{1}{2}\gamma_i+\tanh\frac{1}{2}\gamma_i=0$	$k_n=\frac{\sin\frac{1}{2}\gamma_j}{\sinh\frac{1}{2}\gamma_j}$ with $\tan\frac{1}{2}\gamma_j-\tanh\frac{1}{2}\gamma_j=0$

The zeros of the "gamma functions" are given in Table A3.

Table A3 Zeros of the "gamma functions" (γ in Table A2)

	$\tan\frac{1}{2}\gamma_j - \tanh\frac{1}{2}\gamma_j = 0$	$\tan\frac{1}{2}\gamma_i + \tanh\frac{1}{2}\gamma_i = 0$
1	7.8532	4.73004
2	14.13716	10.9956
3	20.4204	17.27876
4	26.7036	23.5620
5	32.9868	29.8452
6, 7, 8, …	$\frac{(4j+1)\pi}{2}$	$\frac{(4i-1)\pi}{2}$

A3 Impedance matrices

The transmission system dynamics in the mobility matrix model formulated in Chapter 2 is modelled using an impedance approach, as given by Equation (20). The matrix $\mathbf{Z}_t$ relates the force vector of the transmission system $\mathbf{f}_t$, defined in Equation (13) to the transmission system velocity vector $\mathbf{v}_t$, which is defined in Equation (9). It can be subdivided into subsets of impedance matrices which contain the impedances of the transmission system at the source panel $\mathbf{Z}_{t11}$, radiating panel $\mathbf{Z}_{t22}$, and the cross coupling impedances of the source to radiating panel $\mathbf{Z}_{t12}$ and the radiating to source panel impedances $\mathbf{Z}_{t21}$:

$$\mathbf{Z}_t = \begin{bmatrix} \mathbf{Z}_{t11} & -\mathbf{Z}_{t12} \\ -\mathbf{Z}_{t21} & \mathbf{Z}_{t22} \end{bmatrix}. \tag{A13}$$

The sub matrices in Equation (A8) can be further subdivided into impedance functions of the structural transmission path and the acoustical transmission path, as given by Equation (A14-A17):

$$\mathbf{Z}_{t11} = \begin{bmatrix} \mathbf{Z}_{tm11} & 0 \\ 0 & \mathbf{Z}_{te11} \end{bmatrix},$$

$$\mathbf{Z}_{t12} = \begin{bmatrix} \mathbf{Z}_{tm12} & 0 \\ 0 & \mathbf{Z}_{te12} \end{bmatrix},$$

$$\mathbf{Z}_{t21} = \begin{bmatrix} \mathbf{Z}_{tm21} & 0 \\ 0 & \mathbf{Z}_{te21} \end{bmatrix}, \quad \text{(A14-A17)}$$

$$\mathbf{Z}_{t22} = \begin{bmatrix} \mathbf{Z}_{tm22} & 0 \\ 0 & \mathbf{Z}_{te22} \end{bmatrix},$$

where the matrices $\mathbf{Z}_{tm11}$, $\mathbf{Z}_{tm12}$, $\mathbf{Z}_{tm21}$, and $\mathbf{Z}_{tm22}$ contain impedance functions for mount junctions on the source panel and the radiating panel, modelling the dynamics of the structural transmission path. The size of each of these matrices is $q \times q$. These matrices are diagonal because a velocity at a mount junction can only cause a force due to elastic deformation of a mount at the junction points of that mount. In contrast, the impedance matrices $\mathbf{Z}_{te11}$, $\mathbf{Z}_{te12}$, $\mathbf{Z}_{te21}$, and $\mathbf{Z}_{te22}$, which model the dynamics of the acoustical transmission path, are fully populated since a velocity of one element will cause pressure fluctuation all over the air cavity, and will therefore generate a force at all other elements on the source and the radiating panel. The size of each of these matrices is $k \times k$.

A4 Impedance functions

In Section A3 of Appendix A the impedance matrices of the transmission system have been described in such detail so that the elements of each matrix have been defined as impedance functions between two points of either acoustical cavity or elastic mount junctions. In this Section it is explained how to calculate these impedance functions.

An impedance function is a frequency dependent complex function that can be defined between two points of a body. It is given by a ratio of a time harmonic force at one point which results from a time harmonic velocity at some other point of the body. The impedance concept can also be used when a rectangular acoustical cavity is driven by an acoustic source causing pressure fluctuations across the cavity. Using elemental subdivisions of the cavity boundaries it is possible to relate pressure fluctuations distributed over element surfaces to resultant point forces at element geometrical centres. It is also possible to relate velocities of element geometrical centres to the strengths of acoustical sources. Therefore, velocity of an element centre located at a cavity boundary can be related to the consequent force at some other boundary element centre. Figure A1 shows a rectangular air cavity excited by a velocity $\dot{w}_{P1}$ of an out of *x,y* plane moving boundary at location *P2*, and the resulting out of plane force N_{zP2} at location *P2*.

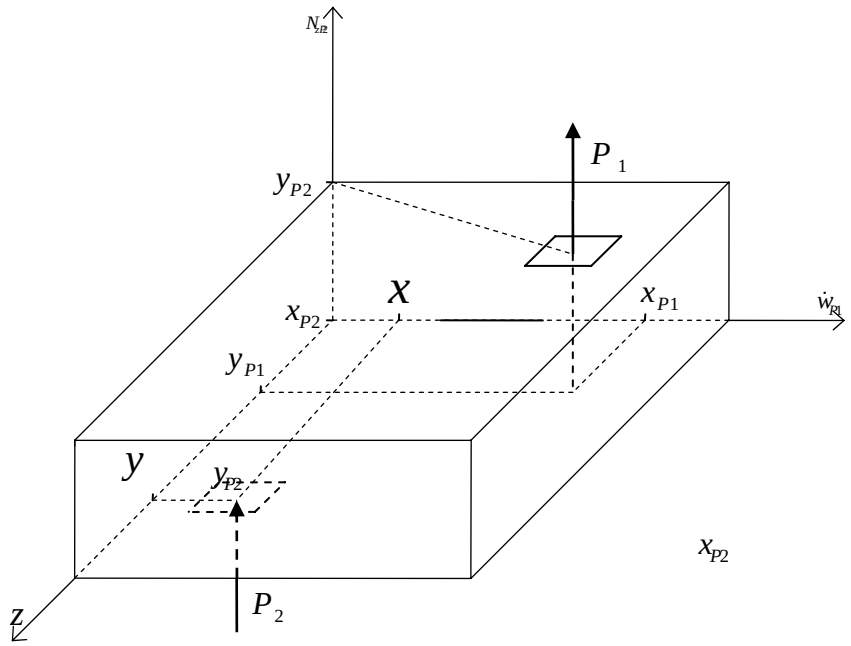

Figure A2: Notation of the force N_{zP2} at position *P*2 when an air cavity is excited by an out of plane velocity $\dot{w}_{P2}$ of the moving boundary at position *P*1.

The impedance function between the points *P*1 and *P*2 is given by:

$$Z_{P1,P2}(x_{P1}, y_{P1}, z_{P1}, x_{P2}, y_{P2}, z_{P2}, \omega) = \frac{N_{zP2}}{\dot{w}_{P1}}. \tag{A18}$$

The impedance function in Equation (A18) for a rectangular acoustical cavity is given by[32]:

$$Z_{N_z,\dot{w}}^{P1,P2}(\omega) = \frac{A_e^2 \rho_{air} \omega c_0^2}{l_x l_y l_z} \sum_{n_1=1}^{\infty} \sum_{n_2=1}^{\infty} \sum_{n_3=1}^{\infty} \frac{\psi_{n_1,n_2,n_3}^{P2}(x_{P2}, y_{P2}, z_{P2}) \psi_{n_1,n_2,n_3}^{P1}(x_{P1}, y_{P1}, z_{P1})}{2\zeta \omega_n^{cav} \omega + j\left[\omega^2 - \left(\omega_{n_1 n_2, n_3}^{cav}\right)^2\right]}, \tag{A19}$$

where:

A_e - area of the surface element,

ρ_{air} - air mass density,

c_0 - speed of sound in the air,

l_z - cavity depth (distance between panels' inner surfaces),

ψ_{n_1,n_2,n_3}^{P1} - natural mode shape function at point *P*1,

ψ_{n_1,n_2,n_3}^{P2} - natural mode shape function at point *P*2,

ζ - air cavity loss factor.

$\omega_{n_1,n_2,n_3}^{cav}$ - air cavity natural frequency,

n_1, n_2, n_3 - mode numbers for, *x*,*y*, and *z* directions.

Natural frequencies of the acoustical cavity can be expressed as[32]:

$$\omega_{n_1,n_2,n_3}^{a} = c_0 \sqrt{\left[\left(\frac{n_1\pi}{l_x}\right)^2 + \left(\frac{n_2\pi}{l_y}\right)^2 + \left(\frac{n_3\pi}{l_z}\right)^2\right]}. \tag{A20}$$

Natural modes of the air cavity are given by[32]:

$$\psi_{n_1,n_2,n_3}(x,y,z) = \sum_{n=0}^{\infty} A_n \cos\frac{n_1\pi x}{l_x}\cos\frac{n_2\pi y}{l_y}\cos\frac{n_3\pi z}{l_z}, \tag{A21}$$

where A_n is an arbitrary complex constant. In order to normalise all the mode shape functions with respect to the volume of the air cavity, this constant has been chosen so that:

$$A_n = \sqrt{\varepsilon_1\varepsilon_2\varepsilon_3}, \tag{A22}$$

where $\varepsilon_k = \begin{vmatrix} 1 \forall n_i = 0 \\ 2 \forall n_i > 0 \end{vmatrix}$.

The impedance function between the two elastic mount junction points is calculated assuming that an elastic mount can be modelled as a spring-damper system. In this case the impedance function in Equation (A18), is given by[22]:

$$Z_{P1,P2}(\omega) = c + \frac{k}{j\omega}, \tag{A23}$$

where:

c -is the viscous damping factor,

k -is the elastic constant.

Appendix B: Convergence

The numerical accuracy of the mathematical model presented in Chapter 2 depends upon the number of elements used for the subdivision of the two panels and adjacent cavity sides, and upon the number of modes used for the modal summation. The number of elements has been determined with respect to the higher modal order used in calculations. Throughout this thesis the simulation results are obtained using two elements per the shortest wavelength in the cavity and the two plates, up to the frequency of interest is 3 kHz. The natural frequency of the highest mode used for modal summation (truncation) is 20 kHz. It is important to have an idea about the sensitivity of the simulation results to the number of elements per wavelength and to the natural frequency of the highest order mode.

Figure B1 shows this sensitivity for the reference case double panel when either one or two elements per wavelength are used in the simulations. The natural frequency of the highest mode that has been used is 20 kHz for all the results plotted. For this result there has been no control action applied.

The largest discrepancies occur at higher frequencies. For example at 2675 Hz the maximal difference of approximately 8dB occurs (plots C and D). Nevertheless, the overall agreement of the two cases is satisfying in the whole frequency band of the interest.

The plots in Figure B2 show the sensitivity to the number of elements in case when 16 decentralised control systems are used, which perform active damping on the radiating panel. The feedback loops use the optimal feedback gain, which provides the largest broadband reductions as explained in Chapter 3.

The largest discrepancies between the results with two and one element per wavelength are approximately four dB, and they occur at frequencies above 2 kHz. Generally, small differences can be noticed between the two cases, which suggest that the accuracy of the simulation using two elements per wavelength is sufficient.

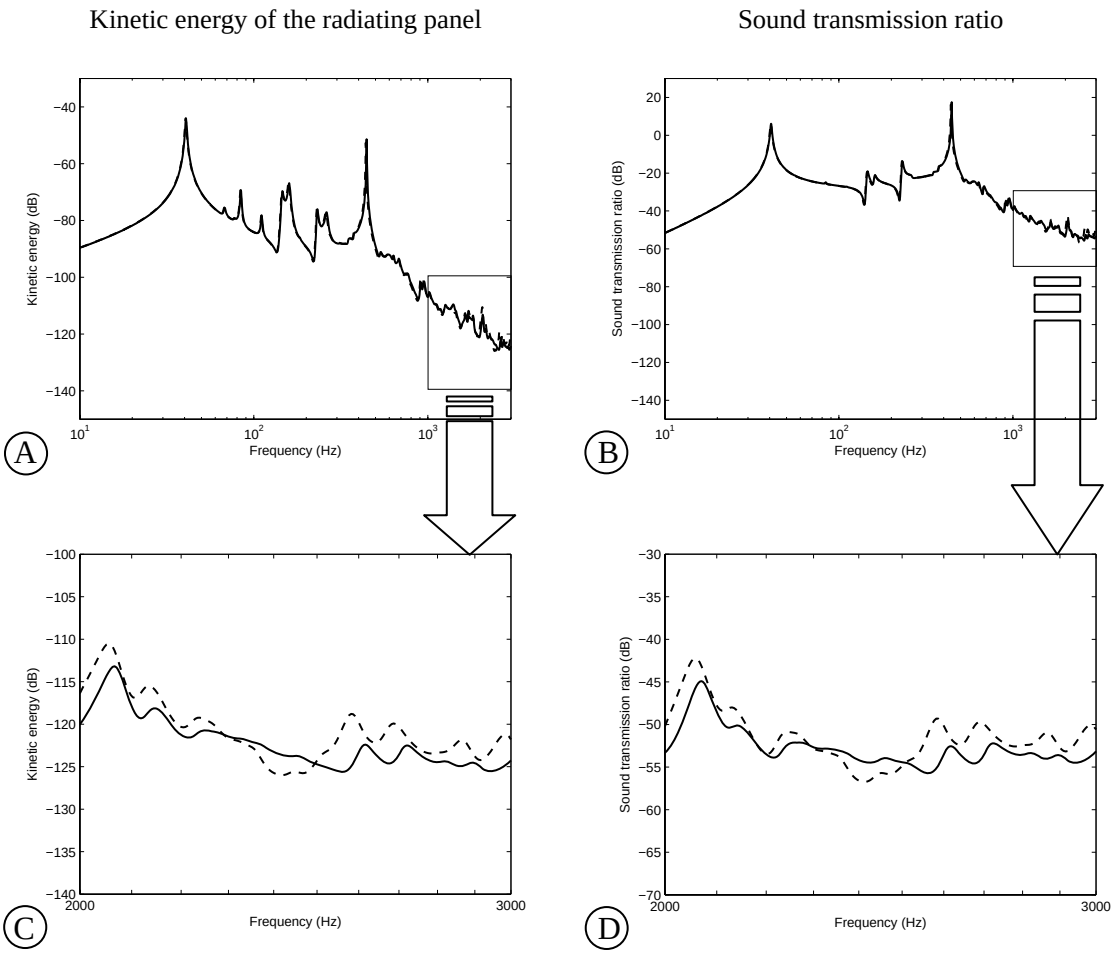

Figure B1: Kinetic energy of the radiating panel (plots A and C) and the sound transmission ratio (plots B and D) of the double panel excited by the plane acoustic wave, without active control. Plots A and B show broadband (10 Hz – 3 kHz) agreement of the results with two elements per wavelength (solid lines) and with one element per wavelength (dashed lines). Plots C and D show the zoomed areas of plots A and B between 1 kHz and 3 kHz, where the differences have the highest values.

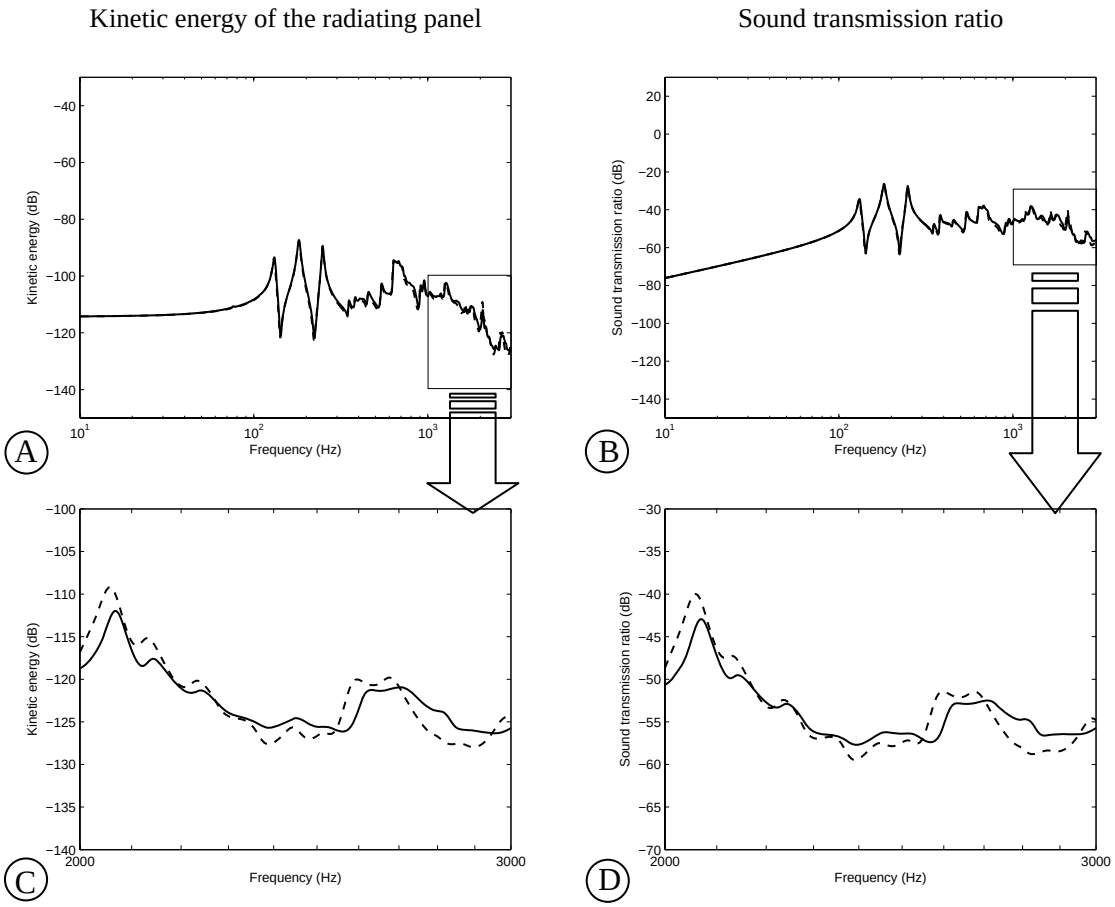

Figure B2: Kinetic energy of the radiating panel (plots A and C) and the sound transmission ratio (plots B and D) of the double panel excited by the plane acoustic wave, with active control systems as in Section 4.1.1. and with optimal feedback gain. Plots A and B show broadband (10 Hz – 3 kHz) agreement of the results with two elements per wavelength (solid lines) and with one element per wavelength (dashed lines). Plots C and D show the zoomed areas of plots A and B between 1 kHz and 3 kHz, where the differences have the highest values.

Figure B3 shows the sensitivity when frequency of 20 kHz, 10 kHz or 3 kHz is used for the highest mode natural frequency in the modal summation. For the results on this plot there has been no control action applied, and the number of elements per wavelength is two.

The curves showing the results with the highest mode natural frequency of 10 kHz and 20 kHz almost overlap over the whole frequency range (solid and faint lines) but the curves with 3 kHz show discrepancies of approximately 11 dB at 3 kHz. This suggests that 20 kHz is sufficiently high cut-off natural frequency. The results shown by dashed lines (3 kHz cut-off), suggest that at least some modes with natural frequencies higher than the maximal frequency of interest need to be used in modal summation.

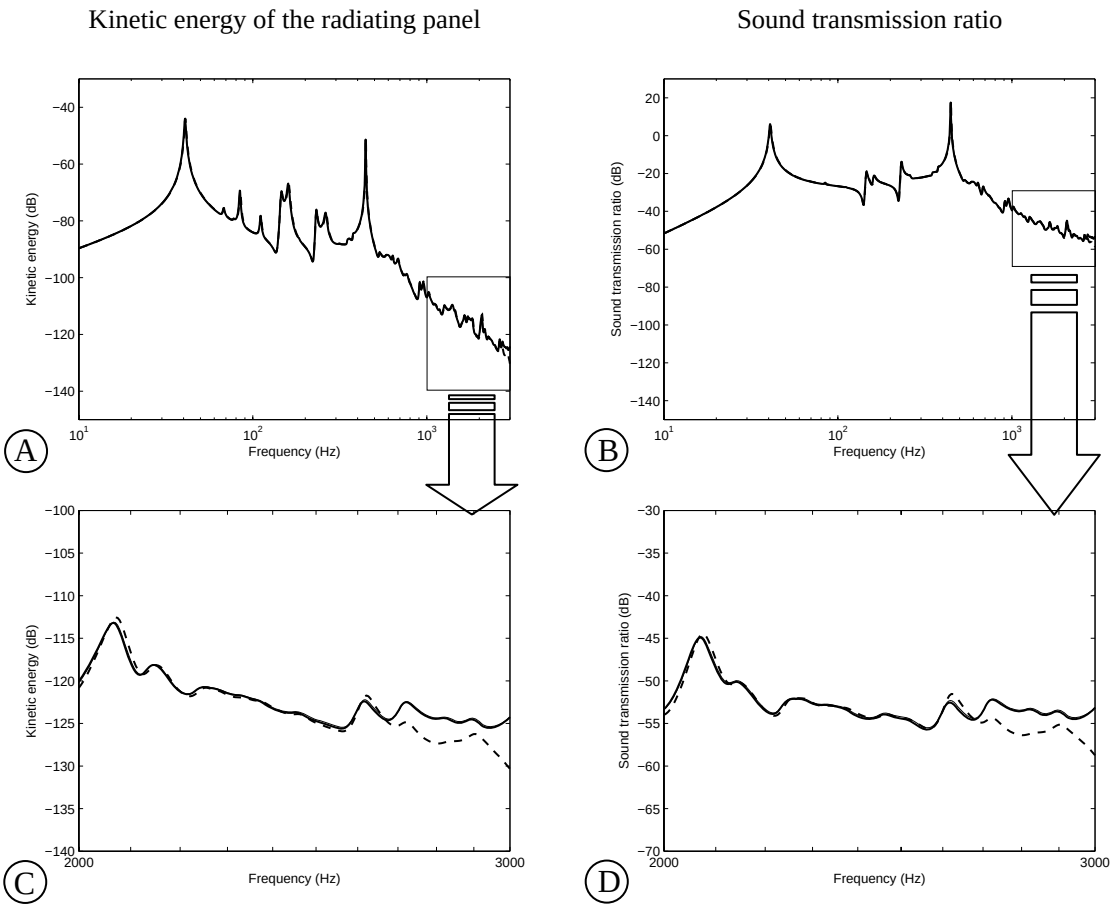

Figure B3: Kinetic energy of the radiating panel (plots A and C) and the sound transmission ratio (plots B and D) of the double panel excited by the plane acoustic wave, without active control. Plots A and B show broadband (10 Hz – 3 kHz) agreement of the results with 20 kHz maximum frequency for modal truncation (solid lines), with 10 kHz maximum frequency for modal truncation (faint lines) and with 3 kHz maximum frequency for modal truncation (dashed lines). Plots C and D show the zoomed areas of plots A and B between 1 kHz and 3 kHz, where the differences have the highest values.

Figure B4 shows the sensitivity when 20 kHz, 10 kHz or 3 kHz cut-off frequency is used. 16 decentralised control systems are used, which perform active damping on the radiating panel, using the optimal feedback gain (the largest broadband reductions) for that case.

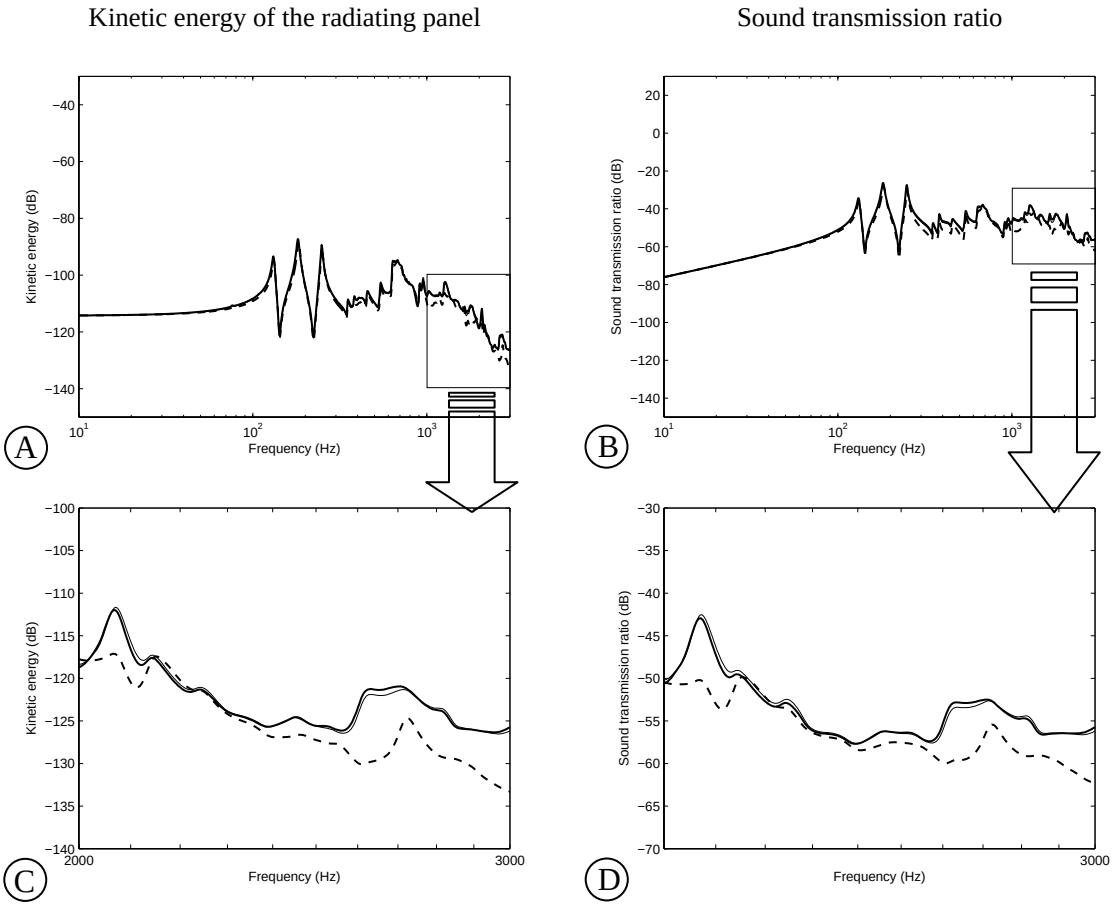

Figure B4: Kinetic energy of the radiating panel (plots A and C) and the sound transmission ratio (plots B and D) of the double panel excited by the plane acoustic wave, with active control systems as in Section 3.2. Plots A and B show broadband (10 Hz – 3 kHz) agreement of the results with 20 kHz maximum frequency for modal truncation (solid lines), with 10 kHz maximum frequency for modal truncation (faint lines) and with 3 kHz maximum frequency for modal truncation (dashed lines). Plots C and D show the zoomed areas of plots A and B between 1 kHz and 3 kHz, where the differences have the highest values.

The curves of 10 kHz and 20 kHz cut-off almost overlap over the whole frequency range (solid and faint lines), but not as closely as in the no control case. The curves with 3 kHz cut-off show more considerable discrepancies of 13 dB at approximately 3 kHz (plots C and D). This suggests that for active control simulations modes with natural frequencies higher than the maximum frequency of interest must be included in order to obtain accurate results.

Appendix C: Data sheets for sensor and actuator transducers

C1 H2W Technologies, voice coil actuator, model NCC01-04-001

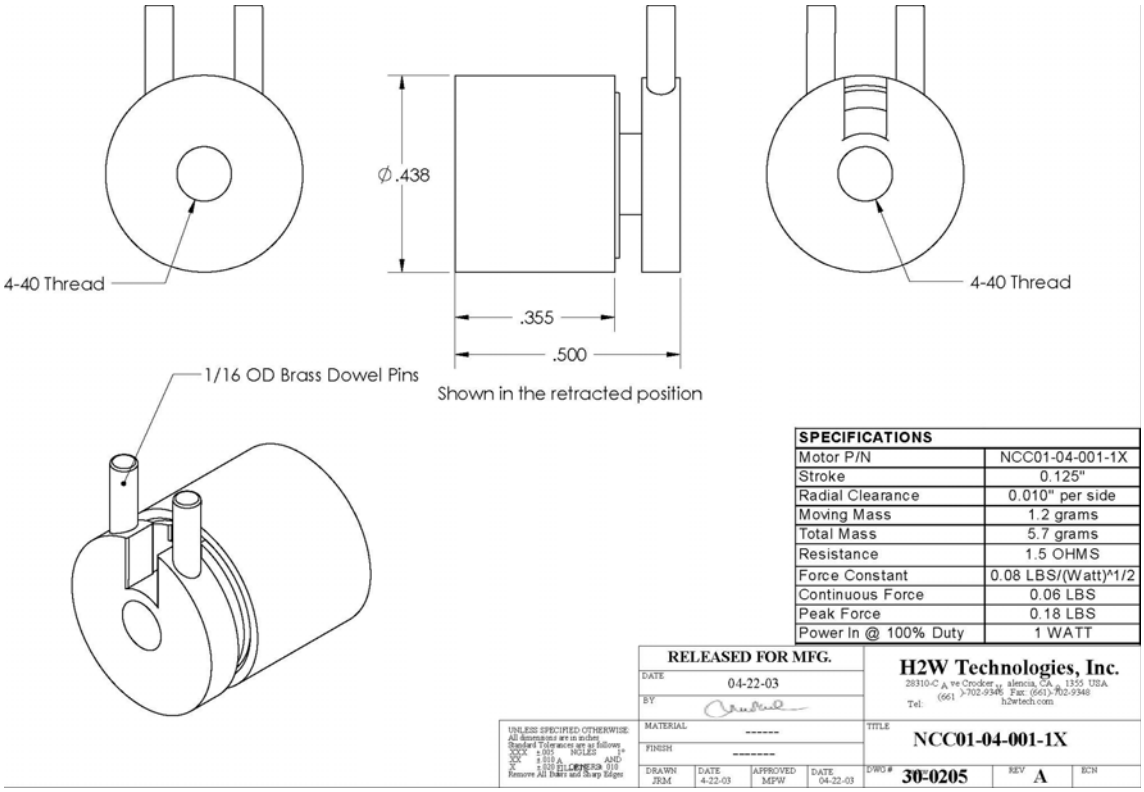

Figure C1: Physical and electrical properties of the voice coil actuator used for the experimental investigations (H2W Technologies, model NCC01-04-001).

C2 Analog Devices, MEMS accelerometer, model ADXL103

ANALOG DEVICES

Precision ±1.7 *g* Single-/Dual-Axis *i*MEMS® Accelerometer

ADXL103/ADXL203

FEATURES

High performance, single-/dual-axis accelerometer on a single IC chip
5 mm × 5 mm × 2 mm LCC package
1 m*g* resolution at 60 Hz
Low power: 700 µA at V_S = 5 V (typical)
High zero *g* bias stability
High sensitivity accuracy
−40°C to +125°C temperature range
X and Y axes aligned to within 0.1° (typical)
BW adjustment with a single capacitor
Single-supply operation
3500 *g* shock survival
RoHS-compliant
Compatible with Sn/Pb- and Pb-free solder processes

APPLICATIONS

Vehicle dynamic control (VDC)/electronic stability program (ESP) systems
Electronic chassis control
Electronic braking
Platform stabilization/leveling
Navigation
Alarms and motion detectors
High accuracy, 2-axis tilt sensing

GENERAL DESCRIPTION

The ADXL103/ADXL203 are high precision, low power, complete single- and dual-axis accelerometers with signal conditioned voltage outputs, all on a single, monolithic IC. The ADXL103/ADXL203 measure acceleration with a full-scale range of ±1.7 *g*. The ADXL103/ADXL203 can measure both dynamic acceleration (for example, vibration) and static acceleration (for example, gravity).

The typical noise floor is 110 µg/√Hz, allowing signals below 1 mg (0.06° of inclination) to be resolved in tilt sensing applications using narrow bandwidths (<60 Hz).

The user selects the bandwidth of the accelerometer using Capacitor C_X and Capacitor C_Y at the X_{OUT} and Y_{OUT} pins. Bandwidths of 0.5 Hz to 2.5 kHz may be selected to suit the application.

The ADXL103 and ADXL203 are available in 5 mm × 5 mm × 2 mm, 8-pad hermetic LCC packages.

FUNCTIONAL BLOCK DIAGRAM

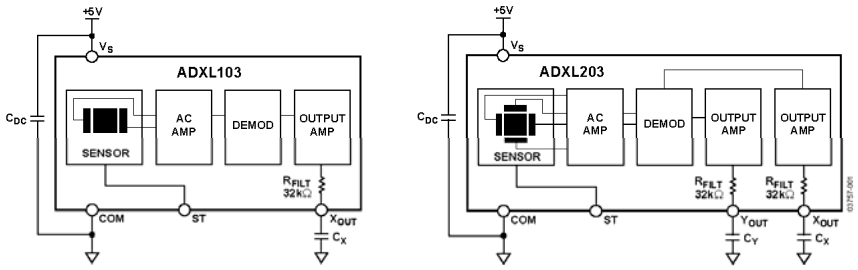

Figure 1.

One Technology Way, P.O. Box 9106, Norwood, MA 02062-9106, U.S.A.
Tel: 781.329.4700 www.analog.com
Fax: 781.461.3113

TABLE OF CONTENTS

Features 1
Applications 1
General Description 1
Specifications 3
Absolute Maximum Ratings 4
ESD Caution 4
Pin Configurations and Function Descriptions 5
Typical Performance Characteristics 6
Theory of Operation 9
Performance 9
Applications 10
Power Supply Decoupling 10
Setting the Bandwidth Using C_X and C_Y 10
Self Test 10
Design Trade-Offs for Selecting Filter Characteristics: The Noise/BW Trade-Off 10
Using the ADXL103/ADXL203 with Operating Voltages Other than 5 V 11
Using the ADXL203 as a Dual-Axis Tilt Sensor 11
Outline Dimensions 12
Ordering Guide 12

REVISION HISTORY

3/06—Rev. 0 to Rev. A

Changes to Features 1
Changes to Table 1 3
Changes to Figure 2 4
Changes to Figure 3 and Figure 4 5
Changes to the Performance Section 9

4/04—Revision 0: Initial Version

SPECIFICATIONS

T_A = −40°C to +125°C, V_S = 5 V, C_X = C_Y = 0.1 µF, acceleration = 0 *g*, unless otherwise noted.

Table 1.

Parameter	Conditions	Min[1]	Typ	Max[1]	Unit
SENSOR INPUT	Each axis				
Measurement Range[2]		±1.7			*g*
Nonlinearity	% of full scale		±0.2	±1.25	%
Package Alignment Error			±1		Degrees
Alignment Error (ADXL203)	X sensor to Y sensor		±0.1		Degrees
Cross-Axis Sensitivity			±1.5	±3	%
SENSITIVITY (RATIOMETRIC)[3]	Each axis				
Sensitivity at X_{OUT}, Y_{OUT}	V_S = 5 V	960	1000	1040	mV/*g*
Sensitivity Change Due to Temperature[4]	V_S = 5 V		±0.3		%
ZERO *g* BIAS LEVEL (RATIOMETRIC)	Each axis				
0 *g* Voltage at X_{OUT}, Y_{OUT}	V_S = 5 V	2.4	2.5	2.6	V
Initial 0 *g* Output Deviation from Ideal	V_S = 5 V, 25°C		±25		m*g*
0 *g* Offset vs. Temperature			±0.1	±0.8	m*g*/°C
NOISE PERFORMANCE					
Output Noise	<4 kHz, V_S = 5 V		1	3	mV rms
Noise Density			110		µ*g*/√Hz rms
FREQUENCY RESPONSE[5]					
C_X, C_Y Range[6]		0.002		10	µF
R_{FILT} Tolerance		24	32	40	kΩ
Sensor Resonant Frequency			5.5		kHz
SELF TEST[7]					
Logic Input Low				1	V
Logic Input High		4			V
ST Input Resistance to Ground		30	50		kΩ
Output Change at X_{OUT}, Y_{OUT}	Self Test 0 to Self Test 1	450	750	1100	mV
OUTPUT AMPLIFIER					
Output Swing Low	No load	0.05	0.2		V
Output Swing High	No load		4.5	4.8	V
POWER SUPPLY					
Operating Voltage Range		3		6	V
Quiescent Supply Current			0.7	1.1	mA
Turn-On Time[8]			20		ms

[1] All minimum and maximum specifications are guaranteed. Typical specifications are not guaranteed.
[2] Guaranteed by measurement of initial offset and sensitivity.
[3] Sensitivity is essentially ratiometric to V_S. For V_S = 4.75 V to 5.25 V, sensitivity is 186 mV/V/*g* to 215 mV/V/*g*.
[4] Defined as the output change from ambient-to-maximum temperature or ambient-to-minimum temperature.
[5] Actual frequency response controlled by user-supplied external capacitor (C_X, C_Y).
[6] Bandwidth = 1/(2 × π × 32 kΩ × C). For C_X, C_Y = 0.002 µF, bandwidth = 2500 Hz. For C_X, C_Y = 10 µF, bandwidth = 0.5 Hz. Minimum/maximum values are not tested.
[7] Self-test response changes cubically with V_S.
[8] Larger values of C_X, C_Y increase turn-on time. Turn-on time is approximately 160 × C_X or C_Y + 4 ms, where C_X, C_Y are in µF.

ABSOLUTE MAXIMUM RATINGS

Table 2.

Parameter	Rating
Acceleration (Any Axis, Unpowered)	3500 *g*
Acceleration (Any Axis, Powered)	3500 *g*
Drop Test (Concrete Surface)	1.2 m
V_S	−0.3 V to +7.0 V
All Other Pins	(COM − 0.3 V) to (V_S + 0.3 V)
Output Short-Circuit Duration (Any Pin to Common)	Indefinite
Temperature Range (Powered)	−55°C to +125°C
Temperature Range (Storage)	−65°C to +150°C

Stresses above those listed under Absolute Maximum Ratings may cause permanent damage to the device. This is a stress rating only; functional operation of the device at these or any other conditions above those indicated in the operational section of this specification is not implied. Exposure to absolute maximum rating conditions for extended periods may affect device reliability.

Table 3. Package Characteristics

Package Type	θ_{JA}	θ_{JC}	Device Weight
8-Lead CLCC	120°C/W	20°C/W	<1.0 gram

ESD CAUTION

ESD (electrostatic discharge) sensitive device. Electrostatic charges as high as 4000 V readily accumulate on the human body and test equipment and can discharge without detection. Although this product features proprietary ESD protection circuitry, permanent damage may occur on devices subjected to high energy electrostatic discharges. Therefore, proper ESD precautions are recommended to avoid performance degradation or loss of functionality.

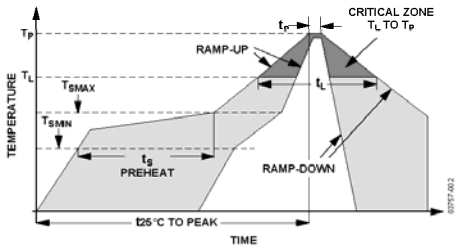

Profile Feature	Condition	
	Sn63/Pb37	Pb-Free
Average Ramp Rate (T_L to T_P)	3°C/second max	
Preheat		
• Minimum Temperature (T_{SMIN})	100°C	150°C
• Maximum Temperature (T_{SMAX})	150°C	200°C
• Time (T_{SMIN} to T_{SMAX}) (t_S)	60 to 120 seconds	60 to 150 seconds
T_{SMAX} to T_L		
• Ramp-Up Rate	3°C/second	
Time Maintained above Liquidous (T_L)		
• Liquidous Temperature (T_L)	183°C	217°C
• Time (t_L)	60 to 150 seconds	60 to 150 seconds
Peak Temperature (T_P)	240°C + 0°C/−5°C	260°C + 0°C/−5°C
Time Within 5°C of Actual Peak Temperature (t_P)	10 to 30 seconds	20 to 40 seconds
Ramp-Down Rate	6°C/second max	
Time 25°C to Peak Temperature	6 minutes max	8 minutes max

Figure 2. Recommended Soldering Profile

PIN CONFIGURATIONS AND FUNCTION DESCRIPTIONS

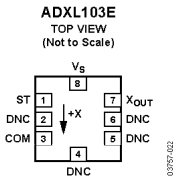

Figure 3. ADXL103 Pin Configuration

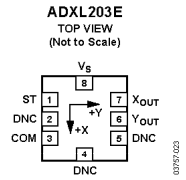

Figure 4. ADXL203 Pin Configuration

Table 4. ADXL103 Pin Function Descriptions

Pin No.	Mnemonic	Description
1	ST	Self Test
2	DNC	Do Not Connect
3	COM	Common
4	DNC	Do Not Connect
5	DNC	Do Not Connect
6	DNC	Do Not Connect
7	X_{OUT}	X Channel Output
8	V_S	3 V to 6 V

Table 5. ADXL203 Pin Function Descriptions

Pin No.	Mnemonic	Description
1	ST	Self Test
2	DNC	Do Not Connect
3	COM	Common
4	DNC	Do Not Connect
5	DNC	Do Not Connect
6	Y_{OUT}	Y Channel Output
7	X_{OUT}	X Channel Output
8	V_S	3 V to 6 V

TYPICAL PERFORMANCE CHARACTERISTICS

V_S = 5 V for all graphs, unless otherwise noted.

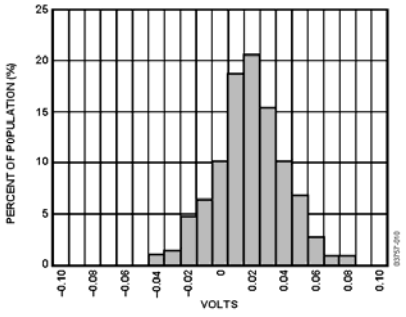

Figure 5. X-Axis Zero g Bias Deviation from Ideal at 25°C

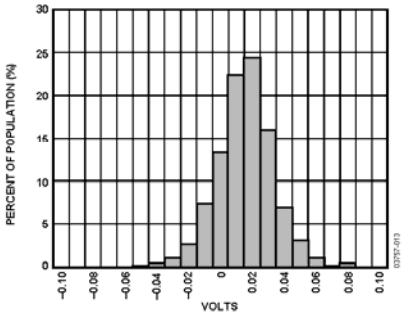

Figure 8. Y-Axis Zero g Bias Deviation from Ideal at 25°C

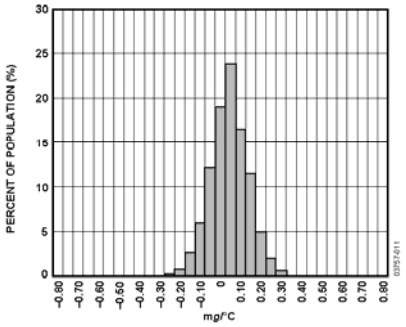

Figure 6. X-Axis Zero g Bias Tempco

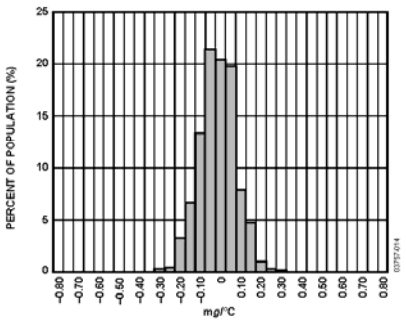

Figure 9. Y-Axis Zero g Bias Tempco

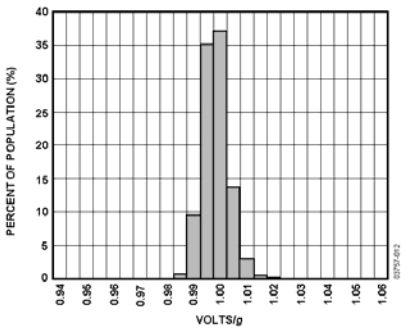

Figure 7. X-Axis Sensitivity at 25°C

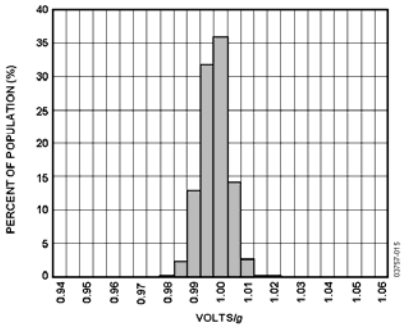

Figure 10. Y-Axis Sensitivity at 25°C

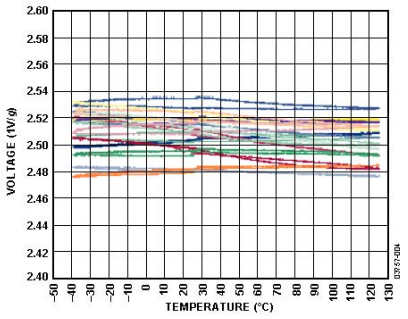

Figure 11. Zero g Bias vs. Temperature; Parts Soldered to PCB

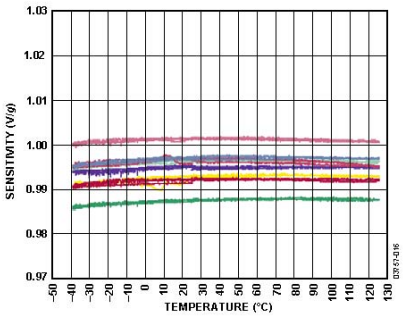

Figure 14. Sensitivity vs. Temperature; Parts Soldered to PCB

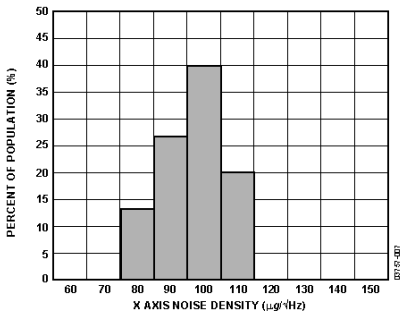

Figure 12. X-Axis Noise Density at 25°C

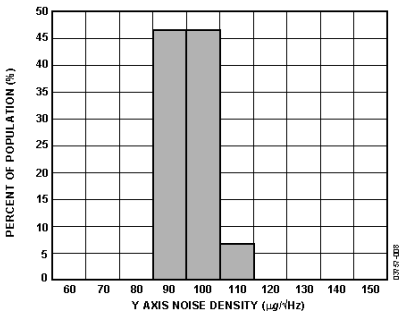

Figure 15. Y-Axis Noise Density at 25°C

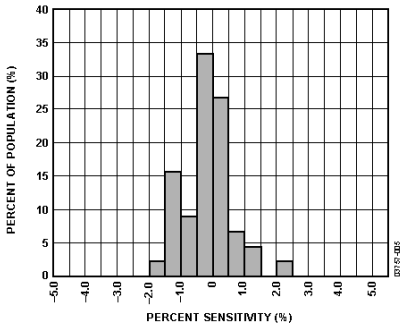

Figure 13. Z vs. X Cross-Axis Sensitivity

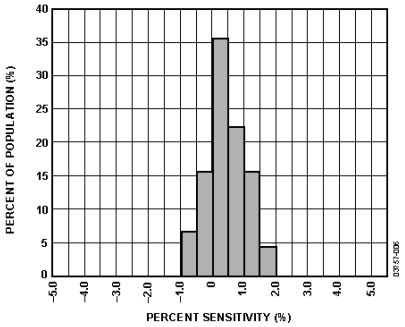

Figure 16. Z vs. Y Cross-Axis Sensitivity

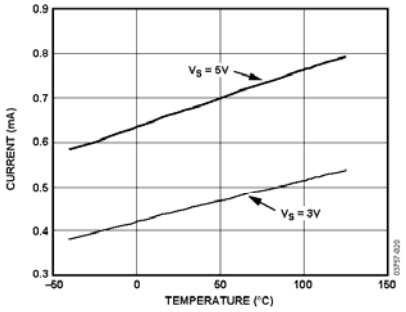

Figure 17. Supply Current vs. Temperature

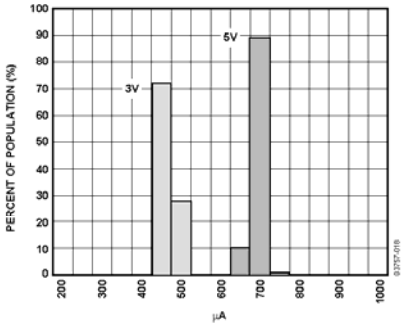

Figure 20. Supply Current at 25°C

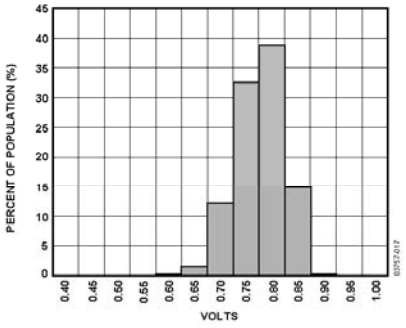

Figure 18. X-Axis Self-Test Response at 25°C

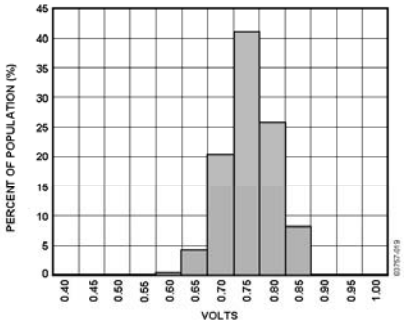

Figure 21. Y-Axis Self-Test Response at 25°C

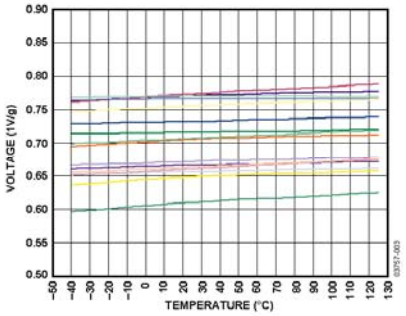

Figure 19. Self-Test Response vs. Temperature

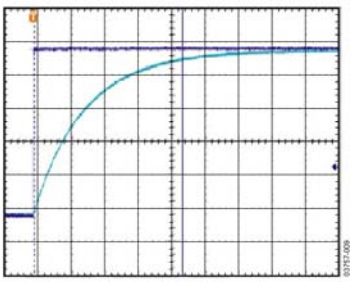

Figure 22. Turn-On Time – C_X, C_Y = 0.1 µF, Time Scale = 2 ms/div

THEORY OF OPERATION

The ADXL103/ADXL203 are complete acceleration measurement systems on a single, monolithic IC. The ADXL103 is a single-axis accelerometer, and the ADXL203 is a dual-axis accelerometer. Both parts contain a polysilicon surface-micromachined sensor and signal conditioning circuitry to implement an open-loop acceleration measurement architecture. The output signals are analog voltages proportional to acceleration. The ADXL103/ADXL203 are capable of measuring both positive and negative accelerations to at least ±1.7 *g*. The accelerometer can measure static acceleration forces such as gravity, allowing it to be used as a tilt sensor.

The sensor is a surface-micromachined polysilicon structure built on top of the silicon wafer. Polysilicon springs suspend the structure over the surface of the wafer and provide a resistance against acceleration forces. Deflection of the structure is measured using a differential capacitor that consists of independent fixed plates and plates attached to the moving mass. The fixed plates are driven by 180° out-of-phase square waves. Acceleration deflects the beam and unbalances the differential capacitor, resulting in an output square wave whose amplitude is proportional to acceleration. Phase-sensitive demodulation techniques are then used to rectify the signal and determine the direction of the acceleration.

The output of the demodulator is amplified and brought off-chip through a 32 kΩ resistor. At this point, the user can set the signal bandwidth of the device by adding a capacitor. This filtering improves measurement resolution and helps prevent aliasing.

PERFORMANCE

Rather than using additional temperature compensation circuitry, innovative design techniques have been used to ensure that high performance is built in. As a result, there is essentially no quantization error or non-monotonic behavior, and temperature hysteresis is very low (typically less than 10 mg over the –40°C to +125°C temperature range).

Figure 11 shows the 0 *g* output performance of eight parts (x and y axes) over a –40°C to +125°C temperature range.

Figure 14 demonstrates the typical sensitivity shift over temperature for V_S = 5 V. Sensitivity stability is optimized for V_S = 5 V but is still very good over the specified range; it is typically better than ±1% over temperature at V_S = 3 V.

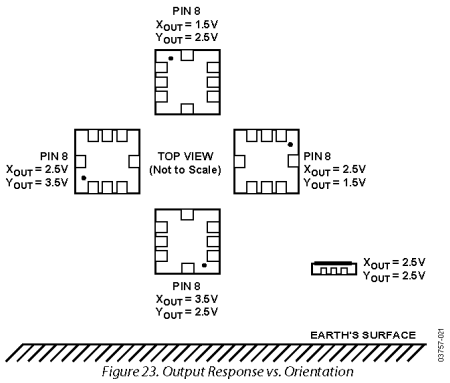

Figure 23. Output Response vs. Orientation

APPLICATIONS

POWER SUPPLY DECOUPLING

For most applications, a single 0.1 µF capacitor, C_{DC}, adequately decouples the accelerometer from noise on the power supply. However in some cases, particularly where noise is present at the 140 kHz internal clock frequency (or any harmonic thereof), noise on the supply can cause interference on the ADXL103/ADXL203 output. If additional decoupling is needed, a 100 Ω (or smaller) resistor or ferrite beads can be inserted in the supply line of the ADXL103/ADXL203. Additionally, a larger bulk bypass capacitor (in the 1 µF to 22 µF range) can be added in parallel to C_{DC}.

SETTING THE BANDWIDTH USING C_X AND C_Y

The ADXL103/ADXL203 has provisions for band limiting the X_{OUT} and Y_{OUT} pins. Capacitors must be added at these pins to implement low-pass filtering for antialiasing and noise reduction. The equation for the 3 dB bandwidth is

$$F_{-3\ dB} = 1/(2\pi(32\ \text{k}\Omega) \times C_{(X,Y)})$$

or more simply,

$$F_{-3\ dB} = 5\ \mu\text{F}/C_{(X,Y)}$$

The tolerance of the internal resistor (R_{FILT}) can vary typically as much as ±25% of its nominal value (32 kΩ); thus, the bandwidth varies accordingly. A minimum capacitance of 2000 pF for C_X and C_Y is required in all cases.

Table 6. Filter Capacitor Selection, C_X and C_Y

Bandwidth (Hz)	Capacitor (µF)
1	4.7
10	0.47
50	0.10
100	0.05
200	0.027
500	0.01

SELF TEST

The ST pin controls the self-test feature. When this pin is set to V_S, an electrostatic force is exerted on the beam of the accelerometer. The resulting movement of the beam allows the user to test if the accelerometer is functional. The typical change in output is 750 mg (corresponding to 750 mV). This pin can be left open-circuit or connected to common in normal use.

The ST pin should never be exposed to voltage greater than V_S + 0.3 V. If the system design is such that this condition cannot be guaranteed (that is, multiple supply voltages are present), a low V_F clamping diode between ST and V_S is recommended.

DESIGN TRADE-OFFS FOR SELECTING FILTER CHARACTERISTICS: THE NOISE/BW TRADE-OFF

The accelerometer bandwidth selected ultimately determines the measurement resolution (smallest detectable acceleration). Filtering can be used to lower the noise floor, improving the resolution of the accelerometer. Resolution is dependent on the analog filter bandwidth at X_{OUT} and Y_{OUT}.

The output of the ADXL103/ADXL203 has a typical bandwidth of 2.5 kHz. The user must filter the signal at this point to limit aliasing errors. The analog bandwidth must be no more than half the analog-to-digital sampling frequency to minimize aliasing. The analog bandwidth can be further decreased to reduce noise and improve resolution.

The ADXL103/ADXL203 noise has the characteristics of white Gaussian noise, which contributes equally at all frequencies and is described in terms of µg/√Hz (that is, the noise is proportional to the square root of the accelerometer bandwidth). The user should limit bandwidth to the lowest frequency needed by the application to maximize the resolution and dynamic range of the accelerometer.

With the single pole roll-off characteristic, the typical noise of the ADXL103/ADXL203 is determined by

$$\text{rmsNoise} = (110\ \mu g/\sqrt{\text{Hz}}) \times (\sqrt{\text{BW} \times 1.6})$$

At 100 Hz, the noise is

$$\text{rmsNoise} = (110\ \mu g/\sqrt{\text{Hz}}) \times (\sqrt{100 \times 1.6}) = 1.4\ \text{mg}$$

Often, the peak value of the noise is desired. Peak-to-peak noise can only be estimated by statistical methods. Table 7 is useful for estimating the probabilities of exceeding various peak values, given the rms value.

Table 7. Estimation of Peak-to-Peak Noise

Peak-to-Peak Value	% of Time That Noise Exceeds Nominal Peak-to-Peak Value
2 × rms	32
4 × rms	4.6
6 × rms	0.27
8 × rms	0.006

Peak-to-peak noise values give the best estimate of the uncertainty in a single measurement; peak-to-peak noise is estimated by 6 × rms. Table 8 gives the typical noise output of the ADXL103/ADXL203 for various C_X and C_Y values.

Table 8. Filter Capacitor Selection (C_X, C_Y)

Bandwidth (Hz)	C_X, C_Y (µF)	RMS Noise (mg)	Peak-to-Peak Noise Estimate (mg)
10	0.47	0.4	2.6
50	0.1	1.0	6
100	0.047	1.4	8.4
500	0.01	3.1	18.7

USING THE ADXL103/ADXL203 WITH OPERATING VOLTAGES OTHER THAN 5 V

The ADXL103/ADXL203 is tested and specified at V_S = 5 V; however, it can be powered with V_S as low as 3 V or as high as 6 V. Some performance parameters change as the supply voltage is varied.

The ADXL103/ADXL203 output is ratiometric, so the output sensitivity (or scale factor) varies proportionally to supply voltage. At V_S = 3 V the output sensitivity is typically 560 mV/*g*.

The zero *g* bias output is also ratiometric, so the zero *g* output is nominally equal to $V_S/2$ at all supply voltages.

The output noise is not ratiometric but is absolute in volts; therefore, the noise density decreases as the supply voltage increases. This is because the scale factor (mV/*g*) increases while the noise voltage remains constant. At V_S = 3 V, the noise density is typically 190 µ*g*/√Hz.

Self-test response in *g* is roughly proportional to the square of the supply voltage. However, when ratiometricity of sensitivity is factored in with supply voltage, self-test response in volts is roughly proportional to the cube of the supply voltage. So at V_S = 3 V, the self-test response is approximately equivalent to 150 mV or equivalent to 270 mg (typical).

The supply current decreases as the supply voltage decreases. Typical current consumption at V_{DD} = 3 V is 450 µA.

USING THE ADXL203 AS A DUAL-AXIS TILT SENSOR

One of the most popular applications of the ADXL203 is tilt measurement. An accelerometer uses the force of gravity as an input vector to determine the orientation of an object in space.

An accelerometer is most sensitive to tilt when its sensitive axis is perpendicular to the force of gravity, that is, parallel to the earth's surface. At this orientation, its sensitivity to changes in tilt is highest. When the accelerometer is oriented on axis to gravity, that is, near its +1 *g* or −1 *g* reading, the change in output acceleration per degree of tilt is negligible. When the accelerometer is perpendicular to gravity, its output changes nearly 17.5 mg per degree of tilt. At 45°, its output changes at only 12.2 mg per degree, and resolution declines.

Dual-Axis Tilt Sensor: Converting Acceleration to Tilt

When the accelerometer is oriented so both its x axis and y axis are parallel to the earth's surface, it can be used as a 2-axis tilt sensor with a roll axis and a pitch axis. Once the output signal from the accelerometer has been converted to an acceleration that varies between −1 *g* and +1 *g*, the output tilt in degrees is calculated as follows:

$$PITCH = ASIN(A_X/1\ g)$$

$$ROLL = ASIN(A_Y/1\ g)$$

Be sure to account for overranges. It is possible for the accelerometers to output a signal greater than ±1 *g* due to vibration, shock, or other accelerations.

OUTLINE DIMENSIONS

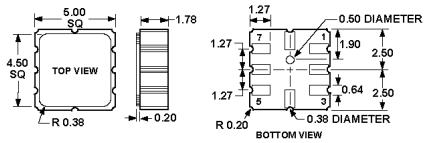

Figure 24. 8-Terminal Ceramic Leadless Chip Carrier [LCC] (E-8)
Dimensions shown in millimeters

ORDERING GUIDE

Model	Number of Axes	Specified Voltage (V)	Temperature Range	Package Description	Package Option
ADXL103CE[1]	1	5	–40°C to +125°C	8-Lead Ceramic Leadless Chip Carrier	E-8
ADXL103CE–REEL[1]	1	5	–40°C to +125°C	8-Lead Ceramic Leadless Chip Carrier	E-8
ADXL203CE[1]	2	5	–40°C to +125°C	8-Lead Ceramic Leadless Chip Carrier	E-8
ADXL203CE–REEL[1]	2	5	–40°C to +125°C	8-Lead Ceramic Leadless Chip Carrier	E-8
ADXL203EB				Evaluation Board	

[1] Lead finish. Gold over nickel over tungsten.

List of references

[1] J.F. Wilby, *Aircraft interior noise*, Journal of Sound and Vibration, 190(3), 1996, pp. 545–564.

[2] J. S. Mixson, J. S. Wilby, *Interior Noise*, in H.H Hubbard, editor, *Aeroacoustics of Flight Vehicles*, Theory and Practice, NASA Langley Research Center, Hampton VA, 1995, Chapter 16, pp. 271-335.

[3] P. Gardonio, *Review of active techniques for aerospace vibroacoustic control*, Journal of Aircraft, 39(2), 2002, pp. 206-214.

[4] J. van Dyke, J. Schendel, C. Gunderson and M. Ballard, *Cabin noise reduction in the DC-9*. AIAA paper 67-401, 1967.

[5] J.F. Wilby, *Noise Transmission into Propeller-Driven Airplanes*, The Shock and Vibration Digest, 21(6), (1989), pp. 3–10.

[6] J. S. Mixson, C. K. Barton, A. G. Piersol and J. F. Wilby, *Characteristics of propeller noise on an aircraft fuselage related to the interior noise transmission* , AIAA paper 79-0646, 1979.

[7] F. G. Pla, R. Ranaudo and R. P. Woodward, *In flight measurements of propeller noise on the fuselage of an airplane*, NASA TM 102285, 1989.

[8] P. L. Spence and P. J. W. Block, *Analysis of the PTA external noise data and comparison with predictions*, AIAA paper 90-3935, 1990.

[9] F. B. Metzger, *Strategies for aircraft interior noise reduction in existing and future propeller aircraft*, SAE paper 810560, 1981.

[10] D. E. Bishop, *Cruise flight noise levels in a turbojet transport airplane*, Noise Control, 7, 1961, pp. 37-42.

[11] J. F. Wilby and F. L. Gloyna, *Vibration measurements of an aircraft fuselage structure, II: Jet noise excitation*. Journal of Sound and Vibration, 23, 1972, 467-486.

[12] H. W. Rudmore and L.L. Beranek, *Noise reduction in aircraft*, Journal of Aeronautical Sciences, 14, 1947, pp. 79-96.

[13] H. H. Bruderlin, *Developments in aircraft sound control*, Journal of the Acoustical Society of America, 8, 1947, pp. 181-184.

[14] J. Sulc, J. Hofer and L. Benda, *Exterior noise on the fuselage of light propeller driven aircraft in flight*, Journal of Sound and Vibration, 84, 1982, pp. 105-120.

[15] R. E. Hayden, B. S. Murray and M. A. Theobald, *A study of interior noise levels, noise sources and transmission paths in light aircraft*, NASA CR-172152, 1983.

[16] F. J. Wilby and E. G. Wilby, *Measurements of propeller noise in a light turboprop airplane*, Journal of Aircraft, 26, 1989, pp. 40-47.

[17] R. B. Tate and E. K. O. Langhout, *Aircraft noise control practises related to ground transport vehicles*, SAE paper 810853, 1981.

[18] G. T. Gebhardt, *Acoustical design features of Boeing model 727*, Journal of Aircraft, 2, 1965, pp. 272-277.

[19] A. H. Marsh, *Noise control features of the DC-10*, Journal of noise control engineering, 4, 1975, pp.130-139.

[20] R. P. Goss, *Acoustic program for the Grumman Golfstream*, AIAA paper 71-783, 1971.

[21] J. B. Large, J. F. Wilby E. Grande and A. O. Anderson, *The development of engineering practises in jet, compressor and boundary layer noise*, in *Aerodynamic Noise*, Toronto, University of Toronto Press, 1969, pp. 43-67.

[22] F.J. Fahy, and P. Gardonio, *Sound and Structural Vibration*, Elsevier, London, 2006.

[23] P. Gardonio and S. J, Elliott, A*ctive control of structure-borne and airborne sound transmission through double panel*, Journal of Aircraft, 36(6), 1999, pp. 1023-1032.

[24] K. Idrisi, M.E. Johnson, J.P. Carneal, *Control of aircraft interior noise using heterogeneous (HG) blankets*, Proceedings of Meetings on Acoustics, Vol. 1, 2008, 065001.

[25] M. A. Simpson, P. H. Druez, A. J. Kimbrough, M. P. Brook, P. L. Burgé, G. P. Mathur, M. R. Connor and B. N. Tran, *UHB demonstrator interior noise control flight tests and analysis*, NASA-CR-181897, 1989.

[26] C. I. Holmer, *Approach to interior noise control, Part I: damped trim panels*, Journal of Aircraft, 22, 1985, pp. 618-623.

[27] D. N. May, K. J. Plotkin, R. G. Selden and B. H. Sharp, *Lightweight sidewalls for aircraft interior noise control*, NASA CR-172490, 1985.

[28] H. L. Kuntz, R. J. Gatineau, R. A. Prydz, and F. J. Balena, *Development and testing of cabin sidewall acoustic resonators for the reduction of cabin tone levels in propfan-powered aircraft*, NASA CR-4388, 1991.

[29] W. G. Halvorsen and U. Emborg, *Interior noise control of the SAAB 340 Aircraft*. SAE paper 891080, 1989.

[30] J. F. Unruh, *Specifications, design and test of aircraft engine isolators for reduced interior noise*, Journal of Aircraft, 21, 1984, pp. 389-396.

[31] B. Magliozzi, *Syncrophasing for cabin noise reduction of propeller-driven airplanes*, AIAA paper 83-0717, 1983.

[32] P. A. Nelson and S. J. Elliott, *Active Control of Sound*, 1st Edition, Academic Press, London, 1992.

[33] S.J. Elliott, P.A. Nelson, I. M. Stothers, and C.C. Boucher, *Preliminary results of in-flight experiments on the active control of propeller-induced cabin noise*, Journal of Sound and Vibration, 128, 1989, pp. 355-357.

[34] S.J. Elliott, P.A. Nelson, I. M. Stothers, and C.C. Boucher, *In-flight experiments on the active control of propeller-induced cabin noise*, Journal of Sound and Vibration, 140, 1990, pp. 219-238.

[35] U. Emborg, S. Leth, F. Samuelson, J. Holmgren, *Active and passive noise control in practice on the SAAB 2000 high speed turboprop*, Fourth AIAA/CEAS Aeroacoustic Conference (19th AIAA Aeroacoustics Conference), Toulouse, France, 1998, AIAA/CEAS Paper 98-2231.

[36] C.F. Ross, M.R. Purver, *Active cabin noise control*, in Proceedings of ACTIVE 97, Budapest, Hungary, 1997, pp. XXXIX-XLVI.

[37] S. M. Hirsh, J. Q. Sun and J. Q. Jolly, *An analytical study of interior noise control using segmented panels, Journal of Sound and Vibration*, 231(4), 1998, pp.1007-1021.

[38] S. M. Hirsh, N. E. Meyer, M. A. Westervelt, P. King, F. J. Li, M. V. Petrova and J. Q. Sun, *Experimental study of smart segmented trim panels for aircraft interior noise control*, Journal of Sound and Vibration, 231(4), 1998, pp. 1023-1037.

[39] M. E. Johnson and S. J. Elliott, *Active control of sound radiation from vibrating surfaces using arrays of discrete actuators*, Journal of Sound and Vibration, 207(5), 1997, pp. 743-759.

[40] D. R. Thomas and P. A. Nelson, *Experiments on the active control of broadband sound radiation from a lightweight partition*, Journal of Sound and Vibration, 202(3), 1997, 438-445.

[41] I. Scott, M. Purver, I. Stothers, *Tonal active control in production on a large turbo-prop aircraft, in Proceedings of ACTIVE 2002*, Southampton, United Kingdom, 2002, pp. 369-376.

[42] S. J. Elliott, *Signal Processing for Active Control*, Academic Press, London, 2000.

[43] S. J. Elliott, I. M. Stothers and P. A. Nelson, *A multiple error LMS algorithm and its application to the active control of sound and vibration*, IEEE Transactions on Acoustics, Speech and Signal Processing, ASSP 35(10), 1987, pp. 1423-1434.

[44] S. J. Elliott, C.C. Boucher, P.A. Nelson, *The behavior of a Multiple Channel Active Control System*, in IEEE Transactions on signal processing, 40(5), May 1992.

[45] C. R. Fuller, J. P. Maillard, M. Mercadal and A. H. von Flotow, *Control of aircraft interior noise using globally detuned vibration absorbers.* Journal of Sound and Vibration, 203(5), 1997, pp. 745-761.

[46] A. H. von Flotow, A. Beard and D. Bailey, *Adaptive tuned vibration absorbers: tuning laws, tracking agility, sizing, and physical implementation,* Proceeding of Noise-Con 94, Institute of Noise Control Engineering of the USA inc., Washington DC, 1994, pp.437-454.

[47] A. H. von Flotow, and T. S. Mixson, *Adaptively tuned vibration absorbers,* U.S. patent 5695027, Dec. 1997.

[48] K. B. Scribner, L. A. Sievers and A. H. von Flotow, *Active narrow-band vibration isolation of machinery noise from resonant substructures,* Journal of Sound and Vibration, 167(1), 1993, pp.17-40.

[49] S. J. Elliott, P. Gardonio, R. J. Pinnington, M. A. David, J. Garcia-Bonito, Goran Pavić, M. Besombes, M. Ohlrich, S. Laugesen, E. Henriksen, *The control of transmitted power in an active isolation system,* Proceedings of Active 97, OPAKFI, Budapest, Hungary, 1997, pp.93-104.

[50] A. H. von Flotow, *An expository overview of active control of machinery mounts,* Proceedings of the 27th conference on decision and control, IEEE publ., 1998, pp. 2029-2032.

[51] M. D. Jenkins, P. A. Nelson, R. J. Pinnington, and S. J. Elliott, *Active isolation of periodic machinery vibrations,* Journal of Sound and Vibration, 166(1), 1993, pp.117-140.

[52] B. Petitjean, and I. Legrain, *Feedback controllers for active vibration suppression*, Journal of Structural Control, 3(1-2), 1996, pp. 111-127.

[53] S. J. Elliott, P. Gardonio, T. C. Sors, and M. J. Brennan, *Active vibroacoustic control with multiple local feedback loops,* The Journal of Acoustical Society of America, 111, 2002, pp. 908-915.

[54] P. Gardonio, E. Bianchi and S. J. Elliott, S*mart panel with multiple decentralised units for the control of sound transmission, Part 1: theoretical predictions,* Journal of Sound and Vibration, 274(1-2), 2004, pp. 163–192.

[55] P. Gardonio, E. Bianchi and S. J. Elliott, *Smart panel with multiple decentralised units for the control of sound transmission, Part 2: Design of the decentralised control units*, Journal of Sound and Vibration, 274(1-2), 2004, pp. 193–213.

[56] P. Gardonio, E. Bianchi and S. J. Elliott, *Smart panel with multiple decentralised units for the control of sound transmission, Part 3: Control system implementation*, Journal of Sound and Vibration, 274(1-2), 2004, pp. 215-232.

[57] P. Gardonio, *Sensor-actuator transducers for smart panels*, Proceedings of ACTIVE 2006, Australia Acoustical Society, Adelaide, Australia, 18–20 Sept. 2006.

[58] P. Gardonio, Y. S. Lee, S. J. Elliott and S. Debost, *Analysis and measure of a matched volume velocity sensor and uniform force actuator for active structural acoustic control*, Journal of the Acoustical Society of America, 110(6), Dec. 2001, pp. 3025–3031.

[59] C. R. Fuller and R. J. Silcox, *Active Structural Acoustic Control*, Journal of the Acoustical Society of America, 91(1), 1992, p. 519.

[60] C. R. Fuller, S. J. Elliott, and P. A. Nelson, *Active Control of Vibration*, Academic Press, London, 1996, pp 223-305, Chapters 8-9.

[61] A. P. Berkhoff, *Piezoelectric sensor configuration for active structural acoustic control*, Journal of sound and vibration, 246 (1), (2001), pp. 175-183.

[62] M. J. Balas, *Direct velocity control of large space structures*, Journal of Guidance and Control, 2(3), 1979, pp. 252, 253.

[63] J. Q. Sun, *Some observations on physical duality and collocation of structural control sensors and actuators*, Journal of Sound and Vibration, 194(5), 1996, pp. 765–770.

[64] V. Jayachandran, J. Q. Sun, *Unconditional stability domains of structural control systems using dual actuator-sensor pairs*, Journal of Sound and Vibration, 208(1), 1997, pp. 159–166.

[65] N. Alujević, P. Gardonio, K.D. Frampton, *Smart double panel with decentralized active damping units for the control of sound transmission*, The American Institute of Aeronautics and Astronautics Journal. 46(6), 2008, 1463-1475

[66] N. Alujević, K.D. Frampton, P. Gardonio, *Stability and performance of a smart double panel with decentralized active dampers*, The American Institute of Aeronautics and Astronautics Journal. 46(7), 2008, 1747-1756.

[67] Y. Aoki. P. Gardonio, and S. J. Elliott, *Rectangular plate with velocity feedback loops using triangularly shaped piezoceramic actuators: Experimental control performance*, Journal of Acoustical Society of America, 123(3), March 2008, pp. 1421–1426.

[68] L. Benassi, S. J. Elliott, *Active Vibration Isolation Using an Inertial Actuator with Local Displacement Feedback Control*, Journal of Sound and Vibration, Vol. 278(4–5), 2004, pp. 705–724.

[69] C. Gonzalez-Diaz, C. Paulitsch, P. Gardonio, *Active damping control unit using a small scale proof mass electrodynamic actuator*, in press, Journal of the Acoustical Society of America, 2007.

[70] C. Gonzalez-Diaz, C. Paulitsch, P. Gardonio, *Smart panel with active damping units. Implementation of decentralised control*, Journal of the Acoustical Society of America, Vol. 124(2), August 2008, pp. 898-910.

[71] C. Paulitsch, P. Gardonio, S.J. Elliott, *Active vibration control using an inertial actuator with internal damping*, Journal of the Acoustical Society of America, 119 (4), April 2006, pp. 2131–2140.

[72] C. Paulitch, *Vibration Control with Electrodynamic Actuators*, PhD Thesis, Institute of Sound and Vibration Research, University of Southampton, September 2005.

[73] A. Preumont, *Vibration Control of Active Structures*, Kluwer Academic, London, 2002.

[74] S. J. Elliott, M. E. Johnson, *Radiation modes and the active control of sound power*, Journal of the Acoustical Society of America, 94(4), 1993, pp. 2194–2204.

[75] L. Cremer, M. Heckl, and E. E Ungar, *Structure-Borne Sound*, Springer Verlag, Berlin, 1988.

[76] R. L. Clark, W. R. Saunders and G. P. Gibbs, *Adaptive Structures*, 1st ed., Wiley, New York, 2002.

[77] L. Meirovitch, *Dynamics and Control of Structures*, Wiley, New York, 1990.

[78] http://www.h2wtech.com/pdfs/30-0205%20Rev%20A%20NCC01-04-001-1X.pdf

[79] http://www.analog.com/static/imported-files/data_sheets/ADXL103_203.pdf

[80] M. Gavagni and P. Gardonio, *Design and Fabrication of a Micro-Velocity Sensor for Direct Velocity Feedback Control Systems*, Active 2006, the 2006 International Symposium on Active Control of Sound and Vibration, Adelaide, Australia, 18 – 20 September 2006.